

# Northumbria Research Link

Citation: Le, Doan Quoc Bao (2021) Micromachining of carbon nanofiller reinforced polymern nanocomposites. Doctoral thesis, Northumbria University.

This version was downloaded from Northumbria Research Link:  
<http://nrl.northumbria.ac.uk/id/eprint/47786/>

Northumbria University has developed Northumbria Research Link (NRL) to enable users to access the University's research output. Copyright © and moral rights for items on NRL are retained by the individual author(s) and/or other copyright owners. Single copies of full items can be reproduced, displayed or performed, and given to third parties in any format or medium for personal research or study, educational, or not-for-profit purposes without prior permission or charge, provided the authors, title and full bibliographic details are given, as well as a hyperlink and/or URL to the original metadata page. The content must not be changed in any way. Full items must not be sold commercially in any format or medium without formal permission of the copyright holder. The full policy is available online: <http://nrl.northumbria.ac.uk/policies.html>

# **Micromachining of Carbon Nanofiller Reinforced Polymer Nanocomposites**

A thesis submitted in partial fulfilment of the requirements for the degree of Doctor of Philosophy

By

Doan Quoc Bao Le

Department of Mechanical and Construction Engineering

Northumbria University

Newcastle upon Tyne NE1 8ST, UK

May 2021



## **Declaration**

The work presented in this thesis is performed entirely by the author during the PhD course at Northumbria University at Newcastle. No portion of the work referred to in this thesis has been submitted in support of an application for another degree or qualification of this or any other university or another institute of learning.

**I declare that the Word Count of this Thesis is 55,112 words**

Doan Quoc Bao Le

## **Abstract**

The modern industry has been observing a growing demand for micro-manufacturing of nanocomposites. This is driven by the miniaturisation trend to obtain products with micro-features, high accuracy and light weight. From an engineering perspective, a miniaturised system can provide many benefits over its predecessors such as precision operation, mobility, or power consumption. Based on these, many techniques of micro-manufacturing have been applied, and micromilling of nanocomposites has shown a huge potential to be applied in this field due to its high capability in producing high-complexity-3D micro-features in a wide variety of workpiece materials, with high dimensional accuracy. However, micromilling of nanocomposites is deemed to be a complicated process due to the anisotropic, heterogeneous structure and advanced mechanical properties of these materials associated with the size effects in micromachining. Also, applying micromachining of nanocomposites is a principal approach to bridge the knowledge gap between macro and micro/nano cuttings which is identified by the so-called “size effect”. This physical phenomenon exhibits by the association between various factors including cutting edge radius, negative tool rake angle, work-piece material microstructure, and minimum uncut chip thickness (MUCT) (or minimum chip load). These lead to unstable cutting regimes, resulting in corrupted chip formation, tool vibration and subsequently, low machined surface quality as well as high tool wear rate.

The enormous potential of applying micromachining of nanocomposites in manufacturing micro-products, as well as the need to fill the knowledge gap of the field of this study, has prompted researchers to uncover the underlying mechanisms and allow appropriate adaption of this technique in industrial applications.

## **Acknowledgements**

I would like to express my profound gratitude to my principal supervisor (from October 2017 to August 2020), Prof. Islam Shyha, for his superb mentoring and continuous support during my PhD project. I would also like to express my gratitude to my co-supervisors, Dr Jibrán Khaliq (who acted as the principal supervisor from September 2020) and Dr Dehong Huo, for their invaluable guidance with critical analysis, expertise and skills during my research. Without their generous supervision, I would not have been able to complete this course.

Dr Pietro Maiello, Phil Donelley, Simon Neville, and Sam Hutchinson, deserve special thanks for the training sessions and constant assistance during the experimental work.

I would also like to thank Northumbria University for providing the financial support and research facilities. My thanks are also extended to my friends and colleagues at the Department of Mechanical Engineering and Construction for their friendship and encouragement.

Finally, I would like to express my appreciation to my family for continuous encouragement to succeed in my profession.

## Table of contents

Declaration .....	i
Abstract .....	ii
Acknowledgements .....	iv
Table of contents .....	v
List of figures .....	vi
List of tables .....	xiv
List of acronyms .....	xvi
List of symbols .....	xviii
Chapter 1: Introduction .....	1
1.1 Background .....	1
1.2 Aims and objectives .....	2
1.3 Thesis outline .....	3
Chapter 2: Literature review .....	6
2.1 Introduction .....	6
2.2 Nanocomposites .....	9
2.3 Mechanical properties of nanocomposites .....	16
2.3.1 CNT-based nanocomposites .....	16
2.3.2 Graphene-based nanocomposites .....	27
2.3.3 Ceramic-based nanocomposites .....	35
2.4 Micromachining of nanocomposites .....	40
2.4.1 Overview of micromachining .....	40
2.4.2 Size effect in micromachining .....	42
2.4.3 Micromachining of nanocomposites .....	52
2.5 Modelling of micromachining of nanocomposites .....	73
2.6 Summary .....	78
Chapter 3: Experimental work .....	79
3.1 Workpiece Materials .....	79
3.1.1 Epoxy .....	79
3.1.2 Graphene .....	79
3.1.3 Multi-walled carbon nanotube .....	80

*Table of contents*

3.1.4	Carbon nanofibre.....	81
3.2	Material fabrication .....	82
3.2.1	Equipment .....	82
3.2.2	Sample preparation .....	85
3.3	Characterisation of workpiece materials .....	88
3.3.1	Tensile test .....	89
3.3.2	Thermal conductivity .....	91
3.3.3	Dynamic mechanical analysis .....	93
3.4	Micromachining experiments.....	95
3.4.1	Micro-machine tool.....	95
3.4.2	Dynamometer.....	96
3.4.3	Micromachining setup.....	96
3.4.4	Scanning electron microscope .....	97
3.4.5	Cutting force measurement .....	98
3.4.6	Surface roughness measurement.....	99
3.4.7	Tool wear measurement.....	100
3.4.8	Dimensional accuracy measurement.....	101
Chapter 4: Machinability of carbon nanofiller reinforced epoxy nanocomposites at micro cutting chip load .....		102
4.1	Introduction .....	102
Part I: Cutting force and surface roughness .....		103
4.2	Machined surface morphology.....	103
4.3	Cutting force.....	104
4.3.1	ANOVA analysis .....	104
4.3.2	Cutting force analysis.....	105
4.4	Surface roughness.....	108
4.4.1	ANOVA analysis .....	108
4.4.2	Surface roughness analysis .....	110
4.5	Summary .....	113
Part II: Tool wear .....		114
4.6	Tool wear analysis.....	114
4.7	Effect of tool wear on cutting force.....	119

*Table of contents*

4.8	Effect of tool wear on surface roughness .....	121
4.9	Effect of tool wear on machined surface morphology .....	124
4.10	Effect of tool wear on dimensional accuracy .....	126
4.11	Summary .....	127
Chapter 5: Machinability of carbon nanofiller reinforced epoxy nanocomposites at nano-micro cutting chip load .....		128
5.1	Introduction .....	128
Part I: Machinability of carbon nanotube reinforced epoxy nanocomposites .....		129
5.2	Tensile properties .....	129
5.3	Thermal conductivity .....	130
5.4	Chip morphology.....	131
5.5	Cutting force.....	133
5.5.1	ANOVA analysis.....	133
5.5.2	Cutting force analysis.....	135
5.6	Machined surface morphology.....	140
5.7	Surface roughness.....	143
5.7.1	ANOVA analysis.....	143
5.7.2	Surface roughness analysis .....	145
5.8	Tool wear.....	146
5.9	Summary .....	148
Part II: Machinability of carbon nanofibre reinforced epoxy nanocomposites .....		150
5.10	Tensile properties .....	150
5.11	SEM analysis of tensile fracture surfaces.....	152
5.12	DMA analysis – Glass transition temperature.....	154
5.13	Chip morphology.....	156
5.14	Cutting force.....	159
5.14.1	ANOVA analysis .....	159
5.14.2	Cutting force analysis.....	160
5.15	Machined surface morphology.....	163
5.16	Machined surface roughness .....	165
5.16.1	ANOVA analysis .....	165
5.16.2	Surface roughness analysis .....	166

*Table of contents*

5.17 Summary .....	172
Chapter 6: Conclusions and future work.....	173
6.1 Conclusions .....	173
6.2 Future work .....	174
References .....	176
List of publications.....	204

## List of figures

Figure 1.1: The schematic diagram of the thesis structure .....	5
Figure 2.1: Micro-features as applications of micromachining of nanocomposites. (a - b) MTA/MWCNT micro-capacitors and micro-resistors made by precise 3D printing [16]; (c) Epoxy/MWCNT wings for MAVs made by moulding [17]; (d) Stainless steel/Al <sub>2</sub> O <sub>3</sub> piston and linkage rod made by soft moulding [18]; (e) PP/SWCNT micro-gear made by injection moulding [19]; (f) Epoxy/SiO <sub>2</sub> micro-wheel made by UV-LIGA methods 7	
Figure 2.2: Nano-filler geometries.....	10
Figure 2.3: Normalised tensile modulus of epoxy-based composites as a function of micro-filler size (adapted from [58], [59], [60], [66]) .....	11
Figure 2.4: Normalised tensile modulus of polymer-based nanocomposites as a function of nano-filler size (adapted from [68, 71]).....	12
Figure 2.5: Graphical representation of the effect of CNT aspect ratio while interacting with polymer chains [72] .....	13
Figure 2.6: Theoretical models representing the micromechanical strengthening mechanism of polymer/CNT nanocomposites via the interfacial stress transfer considering effects of various factors: (a) Effects of polymer matrix density, chemical cross-links and CNT defect [73]; (b) Effects of SWCNT waviness [74]; (c) Effects of tube length and diameter [75]; (d) Effects of nanotube aspect ratio and fibre volume fraction [76].....	14
Figure 2.7: Effect of (a) SWCNT's diameter, thickness and length on the stress transfer efficiency ( $\delta$ ); (b) Young's modulus on the stress transfer efficiency ( $\delta$ ) (Assumed that CF had the same hollow structure with $d=3\text{nm}$ and $t=0.142\text{ nm}$ as SWCNT) (Fibre volume fraction $V_f \sim 0.17\%$ ) [75]; (c) nanotube diameter on stress transfer efficiency ( $V_f = 0.1\%$ ); (d) nanotube volume fraction on stress transfer efficiency ( $d = 0.7086\text{ nm}$ ) [76].....	15
Figure 2.8: (a) Schematic of the microstructure of CNT-reinforced MMCs with dislocation punched zones (DPZs). (b) The entire composite is decomposed into CNT and effective matrix phase, and the effective matrix is comprised of DPZs and pure metal matrix [86].....	16
Figure 2.9: Mechanical properties of polymers reinforced CNTs with corresponding dispersion techniques (adapted from [110, 113-118]) .....	18
Figure 2.10: Effects of dispersion method on mechanical properties of CNT reinforced PMNCs (reproduced from [112]).....	18
Figure 2.11: Effect of CNT structure on mechanical properties of polymer nanocomposites at a filler content of 0.3 wt.% (adapted from [127]) .....	20
Figure 2.12: Effect of CNT alignment on mechanical properties of epoxy-based nanocomposites (adapted from [128, 129]) .....	20



*List of figures*

Figure 2.13: Effect of CNT functionalization on tensile modulus of CNT reinforced epoxy matrix nanocomposites (reproduced from [127, 130, 131]).....21

Figure 2.14: Fracture strain improvement of CNT based polymer nanocomposites as a function of filler content (adapted from [110, 113, 132-136]).....22

Figure 2.15: Schematic representing fracture toughening mechanism of CNT reinforced polymer nanocomposites (reproduced from [139]) .....23

Figure 2.16: Normalised Young’s moduli of thermoplastic polyurethane (TPU)/graphene nanocomposites in different processing methods) (reproduced from [10]).....28

Figure 2.17: Fracture strain improvement of graphene-based PMNCs as a function of filler content (adapted from [194, 200, 201, 205]).....30

Figure 2.18: Comparative fracture toughness improvement of epoxy-based nanocomposites using different nano-fillers [206] .....31

Figure 2.19: Schematic representing fracture toughening mechanism of CNT reinforced PMNCs (adapted from [182]) .....32

Figure 2.20: The formation of carbide when fabricating metal/GO (2 wt.%) nanocomposites [218] .....33

Figure 2.21: The agglomerations of ceramic nano-particles in Al matrices: (a) Al/Al<sub>2</sub>O<sub>3</sub> 4 vol.% [272] and (b) Al/SiC 3 wt.% [271].....37

Figure 2.22: The development of achievable machining accuracy (reproduced from [286]).....40

Figure 2.23: Size effects in micromilling metals and alloys (reproduced from [294-296]) .....42

Figure 2.24: Size effect on specific cutting energy in micromilling as compared to macro-machining [294].....44

Figure 2.25: The schematic representing the differences between macro and micromachining in terms of microstructure ( adapted from [300]) .....44

Figure 2.26: Effect of microstructure on surface quality when micromilling steel [306] .....45

Figure 2.27: Grain size effect on surface roughness and hardness when micromachining W/Cu composite (reproduced from [309]).....46

Figure 2.28: Tool edge radius and feed-rate effects on surface roughness in micromilling (reproduced from [296] [308]).....48

Figure 2.29: MUCT effects on the cutting mechanism in micromachining (adapted from [320]).....49

*List of figures*

Figure 2.30: Effects of MUCT on the shear angle of materials in micromachining: (a) positive effective rake angle; (b) zero effective rake angle; (c) negative effective rake angle (adapted from [323]) .....50

Figure 2.31: Various surface roughness with different nano-fillers and feed rate in micromilling PC-based nanocomposites (reproduced from [331]).....53

Figure 2.32: Effect of CNT addition on chip formation of PC/MWCNT nanocomposite [51].....54

Figure 2.33: Comparison of surface roughness when micromilling PC/ 15 wt.% MWCNT nanocomposite and plain PC (reproduced from [51]) .....54

Figure 2.34: Comparison of the resultant cutting forces for plain PC and PC/CNT nanocomposites (reproduced from [51, 335]).....55

Figure 2.35: Effect of CNT orientation on cutting force when micromilling PC/5 wt.% MWCNT nanocomposites (reproduced from [335]) .....56

Figure 2.36: Effects of CNT loading and feed rate on surface roughness and burr width when micromilling PC/MWCNT nanocomposites at cutting speed = 130 m/min (reproduced from [330]).....57

Figure 2.37: Effects of MUCT (feed rate), cutting speed (strain rate) and CNT loading on cutting force when micromilling PC/MWCNT nanocomposites (reproduced from [330]).....58

Figure 2.38: Schematic of micromilling CNT-based nanocomposite (adapted from [339]).....59

Figure 2.39: Influence of the matrix-fibre bond's strength on the chip formation and surface generation [334].....62

Figure 2.40: Effect of cutting speed on cutting force and surface roughness when micromachining epoxy/0.8 vol.% GF and epoxy/0.8 vol.% GF/0.2 wt.% GPL composites (reproduced from [334]).....62

Figure 2.41: Effect of cutting speed and filler content on cutting force when micromilling different polymer nanocomposites at FPT= 3  $\mu$ m (reproduced from [15, 330]).....63

Figure 2.42: Different trends of cutting forces as a function of graphene addition when micromachining graphene reinforced PMNCs (reproduced from [15, 334, 342]) .....65

Figure 2.43: Quantitative comparison of the standardised effects of various parameters on cutting forces for Mg/graphene nanocomposites (reproduced from [343]).....67

Figure 2.44: Specific cutting energy when micromilling Mg and Mg/10 vol.% SiC nanocomposite (the dash lines represent MUCT boundaries) (reproduced from [344]) 68

Figure 2.45: Effect of SiC content on cutting force when micromilling Mg/SiC nanocomposite (reproduced from [48]) .....69

*List of figures*

Figure 2.46: Effect of feed rate on cutting force when micromachining Mg/ceramic nanocomposites (adapted from [48, 345]) ..... 70

Figure 2.47: Schematic showing the correlations between input variables and the machinability of nanocomposites in micromachining ..... 72

Figure 2.48: Micro-structure-level machining of CNT reinforced PC ([365, 366])..... 74

Figure 2.49: Micro-structure-level machining of CNT reinforced PVA nanocomposite [360]..... 75

Figure 2.50: FE analysis of micromilling PC and PC reinforced GNP nanocomposite: (a) Chip formation of PC/GNP, (b) Cutting forces in simulation and experiment [331] 76

Figure 2.51: FE analysis of micromilling Mg reinforced by 1.5 vol.% SiC nanocomposite (reproduced from [350]) ..... 77

Figure 2.52: Effect of nano-particles on shear zone propagation: (a) direction of shear zone propagation, (b) distorted stress contour caused by particle restricting behaviour [370]..... 77

Figure 3.1: A SEM image of graphene nanoplatelets 79

Figure 3.2: A TEM image of MWCNT NC7000..... 80

Figure 3.3: A SEM image of CNF-110..... 81

Figure 3.4: Three-roll-mill (TRM) 80E EXAKT and the schematic diagram representing the operating principle ..... 85

Figure 3.5: Schematic representing the fabrication of epoxy-based nanocomposites using solution mixing..... 86

Figure 3.6: Schematic representing the fabrication of epoxy-based nanocomposites using three roll milling..... 88

Figure 3.7: Universal Testing machine (INSTRON 3382) ..... 89

Figure 3.8: Tensile test specimen, type V geometry (ASTM D638) (Unit: mm)..... 90

Figure 3.9: Tensile test setup in Instron 3382 universal testing machine (ASTM D638) ..... 91

Figure 3.10: Thermal conductivity test specimen (linear heat conduction) (ASTM D5470) (Unit: mm) ..... 92

Figure 3.11: The schematic representing the calculation of thermal conductivity k ..... 92

Figure 3.12: Thermal conductivity test setup on Hilton H112A linear heat conduction (ASTM D5740)..... 93

Figure 3.13: Dynamic Mechanical Analyzer (DMA) (Model 8000, Perkin Elmer)..... 94

Figure 3.14: Ultra-precision desktop micro-machine tool (Nanowave MTS5R) ..... 95

Figure 3.15: Kistler (9256C2) piezoelectric dynamometer ..... 96

*List of figures*

Figure 3.16: Micro-machining setup.....96

Figure 3.17: (a) Scanning electron microscope (SEM) TESCAN MIRA3 and (b) Quorum Q150R rotary pumped coater.....97

Figure 3.18: Cutting force measurement using Kistler (9256C2) piezoelectric dynamometer in micromilling.....99

Figure 3.19: A representative sample of cutting force signal generated from the dynamometer.....99

Figure 3.20: Surface roughness Ra measurement using Alicona Infinite Focus G4: (a) an Alicona Infinite Focus G4, (b) An example of a 3D scan of the machined slot, (c) An example of the roughness profile ..... 100

Figure 3.21: Surface roughness Ra measurement using Mitutoyo SJ-410 contact style profilometer..... 100

Figure 3.22: Non-uniform flank wear measurement..... 101

Figure 3.23: Stair-formed face wear measurement (with the original cutting-edge outline)..... 101

Figure 3.24: An example of SEM imaging represented tool diameter measurement ... 102

Figure 3.25: An example of SEM imaging represented tool slot width measurement . 102

Figure 4.1: SEM images for a machined slot in graphene/epoxy specimens (at FPT of 5µm and cutting speed of 62.8 m/min)      105

Figure 4.2: Main effect plots for the resultant cutting forces when micromilling epoxy/graphene nanocomposites: (a) Filler content, (b) FPT, and (c) Cutting speed ..107

Figure 4.3. Cutting force results when micromilling of graphene/epoxy nanocomposites at different filler contents: (a) 62.8 m/min, (b) 125.6 m/min, and (c) 188.5 m/min .... 108

Figure 4.4: Effect of cutting speed on the cutting force when micromilling epoxy/graphene nanocomposites at different filler contents (FPT= 15 µm) ..... 109

Figure 4.5 The average surface roughness as a function of FPT when micromilling epoxy/graphene nanocomposites at different filler contents: (a) 62.8 m/min, (b) 125.6 m/min, and (c) 188.5 m/min..... 111

Figure 4.6 The effect of filler content on the average surface roughness at different filler cutting speeds when micromilling epoxy/graphene nanocomposites at FPT of 10µm 113

Figure 4.7: (a) SEM image of tool diameter reduction of the uncoated tool; (b) Effect of tool type and cutting speed on reducing the effective tool diameter. .... 115

Figure 4.8: SEM images of tool wear of different micro-end mills under various cutting speed (after removing 650 mm<sup>3</sup> of material or 500 slots) (left: top view, right: side view)..... 116

*List of figures*

Figure 4.9: SEM images showing tool wear progression of different micro-end mills under the various cutting speed (From left to right: 10 slots, 300 slots and 500 slots) 118

Figure 4.10: Effects of cutting speed and tool coating type on the average cutting force at different cutting stages (from 10 to 500 slots) ..... 121

Figure 4.11: Average surface roughness (Ra) variation as a function of material removal volume at various cutting speeds: (a) 62.8 m/min; (b) 188.4 m/min ..... 123

Figure 4.12: Effect of cutting speed and tool coating type on average surface roughness (in  $\mu\text{m}$ ) at all cutting stages (from 10 to 500 slots)..... 124

Figure 4.13: SEM images of machined surface morphology at two cutting stages (after 10 and 500 slots) using different micro-end mills under various cutting speeds..... 125

Figure 4.14: (a) SEM image of a slot generated by DLC coated tool at 62.8 m/min after 500 slots; (b) Effect of cutting speed and tool coating type on average slot width (in mm) at all cutting stages (from 10 to 500 slots)..... 126

Figure 5.1: Tensile properties of epoxy/MWCNT nanocomposites: (a) Tensile strength, (b) Young's modulus, and (c) Fracture strain 131

Figure 5.2: Thermal conductivity of MWCNT/epoxy nanocomposites at different filler contents ..... 132

Figure 5.3: Chip formations when micromilling at different FPTs and CNT weight contents (Cutting speed = 62.8 m/min; Scale bar is 200  $\mu\text{m}$ ) ..... 133

Figure 5.4: Chip formations at low FPTs at different CNT weight contents (Cutting speed = 62.8 m/min; Scale bar is 50  $\mu\text{m}$ ) ..... 134

Figure 5.5: Cutting force when micromilling epoxy based nanocomposites at different MWCNT contents and FPTs: a) Cutting speed = 62.8 m/min (20,000 rpm); b) Cutting speed = 188.5 m/min (60,000 rpm) ..... 136

Figure 5.6: Cutting force profiles in feed direction at low FPT (0.5 and 1  $\mu\text{m}$ ) (Cutting speed= 62.8 m/min)..... 138

Figure 5.7: Surface morphology of machined surface at different CNT weight contents: (a) Epoxy, (b) 0.1 wt.%, (c) 0.3 wt.%, (d) 0.7 wt.%, and (e) 1 wt.% (FPT = 4  $\mu\text{m}$ ; Cutting speed = 62.8 m/min)..... 139

Figure 5.8: Surface morphology of machined surface at different CNT weight contents and FPTs (Cutting speed = 62.8 m/min; Scale bar is 10  $\mu\text{m}$ ) ..... 140

Figure 5.9: Surface roughness (Ra) when micromilling epoxy-based nanocomposites at different MWCNT contents and FPTs (cutting speed = 62.8 m/min) ..... 142

Figure 5.10: SEM images of tool wear at the end of the micromilling process for each composition (cutting volume of 58.5 mm<sup>3</sup>) (Yellow dashed line indicating wear area)..... 144

*List of figures*

Figure 5.11: Effect of MWCNT content on tool wear when micromilling MWCNT/epoxy nanocomposites ..... 145

Figure 5.12: Tensile properties of epoxy/CNF nanocomposites at different filler contents: (a) Tensile strength, (b) Young’s modulus, (c) Fracture strain ..... 147

Figure 5.13: SEM micrographs of the tensile fracture surfaces of: (a) epoxy/0.1 wt.% CNF, (b) epoxy/0.3 wt.% CNF, (c) epoxy/0.7 wt.% CNF, (a) epoxy/1 wt.% CNF, (e) epoxy ..... 149

Figure 5.14: SEM micrographs at high magnifications of the tensile fracture surfaces of: (a) Epoxy/0.1 wt.% CNF, (b) Epoxy/0.3 wt.% CNF, (c) Epoxy/0.7 wt.% CNF, (a) Epoxy/1 wt.% CNF ..... 150

Figure 5.15: Tan  $\delta$  of epoxy/CNF nanocomposites at different filler contents from DMA analysis ..... 151

Figure 5.16: Chip morphology of epoxy/CNF nanocomposites at different filler contents (Cutting speed= 78.54 m/min) (Scale bar is 200  $\mu\text{m}$ ) ..... 153

Figure 5.17: Chip morphology of epoxy/CNF nanocomposites at different filler contents (Cutting speed= 78.54 m/min) (Scale bar is 50  $\mu\text{m}$ ) ..... 154

Figure 5.18: Cutting force when micromilling epoxy/CNF nanocomposites at different cutting speeds: (a) 31.41 m/min, (b) 78.54 m/min, (c) 125.67 m/min ..... 158

Figure 5.19: Effect of cutting speed on the cutting force when micromilling epoxy/CNF nanocomposites at different filler contents (FPT= 5  $\mu\text{m}$ ) ..... 159

Figure 5.20: Machined surfaces when micromilling epoxy/CNF nanocomposites at the cutting speed of 125.67 m/min (Scale bar is 50  $\mu\text{m}$ ) ..... 161

Figure 5.21: Effect of the filler content and feed rate on the average surface roughness when micromilling epoxy/CNF nanocomposites at different cutting speeds: (a) 31.41 m/min, (b) 78.54 m/min, (c) 125.67 m/min ..... 163

Figure 5.22: Effect of the filler content on the average surface roughness when micromilling epoxy/CNF nanocomposites (FPT= 2  $\mu\text{m}$ ) ..... 165

## **List of tables**

Table 2.1: Nanocomposite manufacturing techniques.....	8
Table 2.2: Fracture toughness of polymer reinforced CNT nanocomposites with the consideration of various factors .....	24
Table 2.3: Mechanical properties of CNT reinforced metal matrix nanocomposites.....	26
Table 2.4: Mechanical properties of graphene reinforced polymer matrix nanocomposites.....	29
Table 2.5: Mechanical properties of graphene reinforced metal matrix nanocomposites .....	34
Table 2.6: Mechanical properties of ceramic nano-fillers reinforced polymer matrix nanocomposites.....	36
Table 2.7: Mechanical properties of ceramic nano-particle reinforced metal matrix nanocomposites.....	39
Table 2.8: The MUCT effects in micromachining – Relevant research .....	51
Table 2.9: Summary of micromachining CNT reinforced polymer matrix nanocomposites.....	60
Table 2.10: Summary of micromachining graphene reinforced polymer matrix nanocomposites.....	66
Table 2.11: Summary of micromachining nano-ceramic-particles reinforced metal matrix nanocomposites .....	71
Table 3.1: Specific characterisation of graphene AO-3 (Source: Graphene Laboratories) 79	
Table 3.2: Specific characterisation of MWCNT NC7000™ (Source: Nanocyl) .....	80
Table 3.3: Specifications of CNF-110 (Source: getnanomaterials.com) .....	81
Table 3.4: OHAUS™ analytical balance specifications (Source: fishersci.com).....	82
Table 3.5: Cole-Palmer lab vacuum oven specifications (Source: colepalmer.co.uk) ...	83
Table 3.6: Ultrasonic processors Vibra-Cell™ VC 750 specifications (Source: sonics.com) .....	83
Table 3.7: IKATM RCT digital magnetic stirrer specifications (Source: fishersci.com) .....	84
Table 3.8: Three-roll milling setup .....	87
Table 3.9: DMA testing parameters for glass transition temperature .....	94
Table 3.10: Main specifications of Ultra-precision desktop micro-machine tool (Nanowave MTS5R).....	95

*List of tables*

Table 4.1: Experimental settings.....	103
Table 4.2: Experimental settings.....	104
Table 4.3: ANOVA result for the resultant cutting force when micromilling epoxy/graphene nanocomposites .....	106
Table 4.4: Effect of filler content on mechanical properties of epoxy/graphene nanocomposites ([375, 385]).....	109
Table 4.5: ANOVA result for the average surface roughness when micromilling epoxy/graphene nanocomposites .....	110
Table 5.1: Experimental settings 128	
Table 5.2: Experimental settings.....	129
Table 5.3: ANOVA result for cutting force when micromilling epoxy/MWCNT nanocomposites.....	135
Table 5.4: ANOVA result for surface roughness when micromilling epoxy/MWCNT nanocomposites .....	141
Table 5.5: Glass transition temperature of epoxy/CNF nanocomposites at different filler contents .....	152
Table 5.6: ANOVA result for the resultant cutting force when micromilling epoxy/CNF nanocomposites.....	156
Table 5.7: ANOVA result for surface roughness when micromilling epoxy/CNF nanocomposites.....	161



## **List of acronyms**

<b>Acronyms</b>	<b>Description</b>
ABS	Acrylonitrile butadiene styrene
Adj MS	Adjusted mean squares
Adj SS	Adjusted sums of squares
ANOVA	Analysis of variance
APTS-GO	Amino functionalised graphene oxide
BET	Surface area analysis
BUE	Built-up edge
bw-GO	Base washed graphene oxide
CCVD	Catalytic chemical vapour deposition
CIP	Cold isotropic pressing
CMNC	Ceramic matrix nanocomposite
CNF/CNT	Carbon nanofibre/ Carbon nanotube
CTE	Thermal expansion coefficients
CVD	Chemical vapour deposition
DF	Degree of freedom
DLC	Diamond-like carbon
DMA	Dynamic mechanical analyzer
DPZ	Dislocation punched zone
DWCNT	Double-walled carbon nanotube
EDM	Electrical discharge machining
EG	Expanded graphite
EGS	Graphene stack
EVA	Ethylene-vinyl acetate
f-CNT	Functionalised carbon nanotube
FLG	Few layer graphene sheet
FPT	Feed per tooth
FSP	Friction stirring processing
GF	Glass fibre
GNF	Graphene nanoflake
GNP	Graphene nano-platelet
GNS	Graphene nano-sheet
GO	Graphene oxide
GPL	Graphene platelet
GPTS-GO	Epoxy functionalised graphene oxide
HDPE	High-density polyethylene
HIP	Hot isostatic pressing
HPU	Hard polyurethane
HRTEM	High-resolution transmission electron microscopy
ICP-MS	Inductively coupled plasma mass spectrometry
ISS	Interfacial shear strength
JC	Johnson-Cook
LDPE	Low-density polyethylene
LIGA	Lithography, electroplating, and moulding

*List of acronyms*

MA	Mechanical alloying
MAV	Micro-air vehicle
MD	Molecular dynamic
MEMs	Micro-electromechanical systems
MMNC	Metal matrix nanocomposite
MMT	Montmorillonite
MRR	Material removal rate
MTA	Thiol acrylate
MUCT	Minimum uncut chip thickness
MWCNT	Multi-walled carbon nanotube
PA	Polyamide/ Nylon
PA6	Polyamide6/ Nylon6
PBO	Poly (p-phenylene benzobisoxazole)
PC	Polycarbonate
p-CNT	Pristine carbon nanotube
PE	polyethylene
PEE	polyester elastomers
PEN	Polyethylene naphthalate
PET	Polyethylene terephthalate
PI	Polyimide
PM	Powder metallurgy
PMMA	Polymethyl methacrylate
PMNC	Polymer matrix nanocomposite
PMP	Poly(4-methyl-2-pentyne)
PP	Polypropylene
PU	Polyurethane
PVA	Polyvinyl alcohol
PVP	Poly-4-vinyl phenol
RGO	Reduced graphene oxide
RVE	Representative volume element
SEM	Scanning electron microscope
Seq SS	Sequential sums of squares
SMC	Silane modified clay
SPS	Spark plasma sintering
SPU	Soft polyurethane
SWCNT	Single-walled carbon nanotube
TEGO	Thermal expanded graphite oxide
TEM	Transmission electron microscopy
TGA	Thermogravimetric analysis
TPU	Thermoplastic polyurethane
TRM	Three roll mill
UCT	Uncut chip thickness

## List of symbols

<b>Symbol</b>	<b>Description</b>	<b>Unit</b>
$V_f$	Fibre volume fraction	%
$k_c$	Specific cutting force	GPa
$f$	Feed rate	$\mu\text{m}$
$r$	Tool edge radius	$\mu\text{m}$
DoC	Depth of Cut	$\mu\text{m}$
$v$	Cutting speed	m/min
$R_a$	Surface roughness	$\mu\text{m}$
$F$	Cutting force/ Resultant cutting force	N
$\varphi$	Shearing angle	$^\circ$
$\gamma$	Clearance angle	$^\circ$
$\lambda_n$	Normalised minimum chip thickness	
$\alpha$	Effective rake angle	$^\circ$
$h$	Uncut chip thickness	$\mu\text{m}$
$h_m$	Minimum uncut chip thickness	$\mu\text{m}$
$W$	Maximum load	N
$A_0$	Original cross-sectional area	$\text{m}^2$
$\sigma_u$	Tensile strength	MPa
$E$	Young's modulus	GPa
$\varepsilon$	Strain	
$K_{\text{int}}$	Thermal conductivity of the specimen (intermediate section)	W/mK
$Q$	Heat transfer rate	W
$A_{\text{int}}$	Area of the contacting surface of the specimen	$\text{m}^2$
$\Delta x_{\text{int}}$	Specimen thickness	m
$\Delta T_{\text{int}}$	Temperature difference between hot face and cold face	K
$V$	Electrical voltage	V
$I$	Electrical current	A
$F_x$	Cutting Force element (perpendicular to feed direction)	N
$F_y$	Cutting Force element (feed direction)	N
$F_z$	Cutting Force element (axial to tool central line)	N
$V_B$	Flank wear	$\mu\text{m}$
$T_g$	Glass transition temperature	$^\circ\text{C}$
$E_f$	Specific cutting energy	J/mm <sup>3</sup>
$H$	Height of feed mark without plastic deformation	$\mu\text{m}$
$h_p$	Depth of plastic deformation	$\mu\text{m}$
$h_e$	Depth of elastic recovery	$\mu\text{m}$
$F_s$	Surface stress	N
$\delta$	Stress transfer efficiency	
Ti	Titanium	
C	Carbon	
Cu	Copper	
Ni	Nickel	
Al	Aluminium	

*List of symbols*

Si	Silicon
Mg	Magnesium
W	Tungsten
O	Oxygen

## **Chapter 1: Introduction**

### **1.1 Background**

The discovery of nanocomposites in 1961 [1] has led to an emerging trend to apply nano-reinforcement materials in the industry. Due to the high strength-to-weight ratio and high specific surface area, the nano-fillers show enormous potential to replace conventional fillers (i.e., carbon fibre) in reinforcing composites [2], leading to a new class of lightweight engineering materials. Nowadays, many nanocomposites have been commercially applied in aerospace [3], automobile [4], and medicine [5] due to their superior properties over conventional composites, namely mechanical [6], thermal [7], electrical [8], electrochemical, electromagnetic [9], and gas barrier properties [10]. Furthermore, nanocomposites have found potential applications in micro-manufacturing such as microelectronics [11] or micromechanical devices [12]. However, the fabrication of nanocomposites has been primarily implemented using near-net-shape (NSS) manufacturing (i.e., mould casting, additive manufacturing) which are mainly applied when time-cost efficiency is the main objective. However, the accuracy generated from these methods is unlikely to meet the requirement of producing micro-features (i.e., surface quality, dimensional accuracy) in micro-manufacturing due. For example, the shrinkage of materials can lead to low dimensional accuracy in mould casting, hence post-processing (i.e., machining and finishing) is deemed required. Therefore, it leads to the requirement of applying mechanical micromachining (hereafter, called micromachining) of nanocomposites. This method shows high capability in producing high-complexity-3D micro-features in a large range of workpiece materials, with acceptable accuracy and time-cost efficiency compared to those of other techniques (i.e., lithography-based method, micro-electro-discharge machining) [13]. However, the main challenges of micromachining nanocomposites are the tool performance associated with the complex structure of nanocomposites. Due to the inherent low chip load in micro/nano-cutting, extremely high cutting speeds need to be employed in micro-cutting to compensate the low material removal rate (MRR). Given such small micro-tools being used to remove heterogeneous nanocomposites, it resulted in high tool vibration due to micro-structure effect. Subsequently, it increased tool wear rate, particularly when cutting though strong, abrasive

nano-fillers (i.e., ceramic nanoparticles). The tool wear acceleration may consequently affect cutting force, surface roughness, and dimensional accuracy. Moreover, the enhancement of thermomechanical properties due to nano-reinforcements may also result in the low micro-machinability of nanocomposites such as an increase of cutting force and surface roughness. Therefore, the investigation of nanocomposites' micromachining behaviour is deemed to be necessary to attain optimal cutting conditions with low cutting forces, surface roughness, and tool wear rate generated.

Also, applying micromachining of nanocomposites is a principal approach to bridge the knowledge gap between macro and micro/nano-cutting that is contributed by the so-called "size effect". The size effect indicates the main challenge when reducing the cutting chip load from macro to micro/nano scales making the well-informed knowledge from conventional material cutting (at macro-scale) may not be directly adapted to micromachining. This physical phenomenon exhibits by the association between various factors including cutting edge radius, negative tool rake angle, workpiece material microstructure, and minimum uncut chip thickness (MUCT) (or minimum chip load). These lead to unstable cutting regimes including debris chip formation, tool vibration and subsequently low machined surface quality, and high tool wear rate. Therefore, it leads to the need of investigating the size effect when micromachining of nanocomposites at minimal chip load below the MUCT, hence eliminating their adverse effects on the micro-machinability of these materials.

The vast potential of applying micromachining in fabricating nanocomposite micro-products and, consequently, filling the knowledge gap between macromachining and micromachining nanocomposites have inspired researchers to reveal the underlying mechanisms and enable suitable adaption of this technique in industrial domains.

## **1.2 Aims and objectives**

This research aimed to experimentally investigate and characterise the machinability of carbon nano-filler reinforced epoxy nanocomposites through the micromilling process. The micromachining experiments were performed on epoxy-based nanocomposites reinforced by different allotropies of carbon nano-fillers including carbon nanoplatelets (graphene), carbon nanotubes (CNTs) and carbon nanofibres (CNFs) at

## *Chapter 1: Introduction*

various chip loads at nano/micro-scale. These provided a comprehensive view of the machinability of carbon nano-filler reinforced epoxy nanocomposites. The detailed objectives to fulfil the aim of this study are as follows:

- To critically review the current literature regarding thermomechanical characterisation and micromachining of nanocomposites. Subsequently, indicate the knowledge gap between micromachining and macromachining nanocomposites.
- To propose procedures for fabricating epoxy-based nanocomposites with the consideration of suitable mixing methods for each type of carbon nano-fillers to attain a high dispersion rate.
- To characterise the nanocomposites' thermomechanical properties and microstructure which affect their micro-machinability.
- To investigate and define the key process variables when micromachining nanocomposites. Based on that, recommended cutting conditions will be suggested.
- To find out the differences of nanocomposites' machinability between micromachining and macromachining nanocomposites when reducing chip load from macro to nano/micro scales.
- To investigate the size effect when micromachining of nanocomposites at low chip loads and its influences on the machinability of the workpiece materials.

### **1.3 Thesis outline**

This thesis is divided into six chapters introducing the research conducted within the scope of a PhD course as shown in Figure 1.1.

#### **Chapter 1: Introduction**

This chapter provides the background, critical overview of knowledge, and the importance of the study. Based on these, the aim and objectives of the research are indicated.

#### **Chapter 2: Literature Review**

This chapter presents a critical review of past and current research in the fields of physical characterisations and micromachining of nanocomposites. It focuses on the micro-

machinability in the consideration the effects of micro-structure and thermo-mechanical properties of nanocomposites. Based on that, the knowledge gap is revealed in detail.

### **Chapter 3: Experimental Work**

This chapter first shows the procedure of fabricating carbon nano-fillers reinforced epoxy nanocomposites and subsequently, the thermo-mechanical characterisations of these materials. The general micromachining experiment setups are then presented. In addition, the specifications of equipment, materials, and cutting tools as well as the measurement methods are also provided.

### **Chapter 4: Machinability of carbon nanofiller reinforced epoxy nanocomposites at micro cutting chip load**

#### **Chapter 4-Part I: Cutting force and surface roughness**

The machinability of graphene reinforced epoxy nanocomposites under microchip load from 5 to 15  $\mu\text{m}$  is investigated in this part. This chapter aims to look at how cutting force and surface roughness change as cutting speeds, feed rates, and graphene loadings change

#### **Chapter 4-Part II: Tool wear**

The tool wear behaviour of different uncoated and coated micro-end mills when micromilling graphene reinforced epoxy nanocomposites at various microchip loads is the subject of this chapter. To account for the impact of tool wear progress, other machinability indicators such as cutting force, surface roughness, and dimensional accuracy are examined.

### **Chapter 5: Machinability of carbon nanofiller reinforced epoxy nanocomposites at nano-micro cutting chip load**

#### **Chapter 5-Part I: Machinability of carbon nanotube reinforced epoxy nanocomposites**

The machinability of carbon nanotube (CNT) reinforced epoxy nanocomposites at nano/microchip-load (from 0.2 to 4  $\mu\text{m}$ ) is investigated in this part. Cutting speed, feed rate, and filler content are all input variables. Cutting force and surface roughness are the study's two key process measures; other measures such as chip morphology and machined surface morphology are also examined. Since the thermomechanical properties and



microstructure of workpiece materials may affect machinability, they are also characterised.

**Chapter 5-Part II: Machinability of carbon nanofibre reinforced epoxy nanocomposites**

This part includes the experimental results for the machinability of carbon nanofibre (CNF) reinforced epoxy nanocomposites at nano/micro-chip load (from 0.2 to 5  $\mu\text{m}$ ). Different levels of cutting speed, feed rate, and filler content are used to characterise the cutting force and surface roughness's variations. Chip formation, machined surface morphology, as well as thermomechanical and microstructure characterisations of nanocomposites are all discussed to aid in the analysis of these variations.

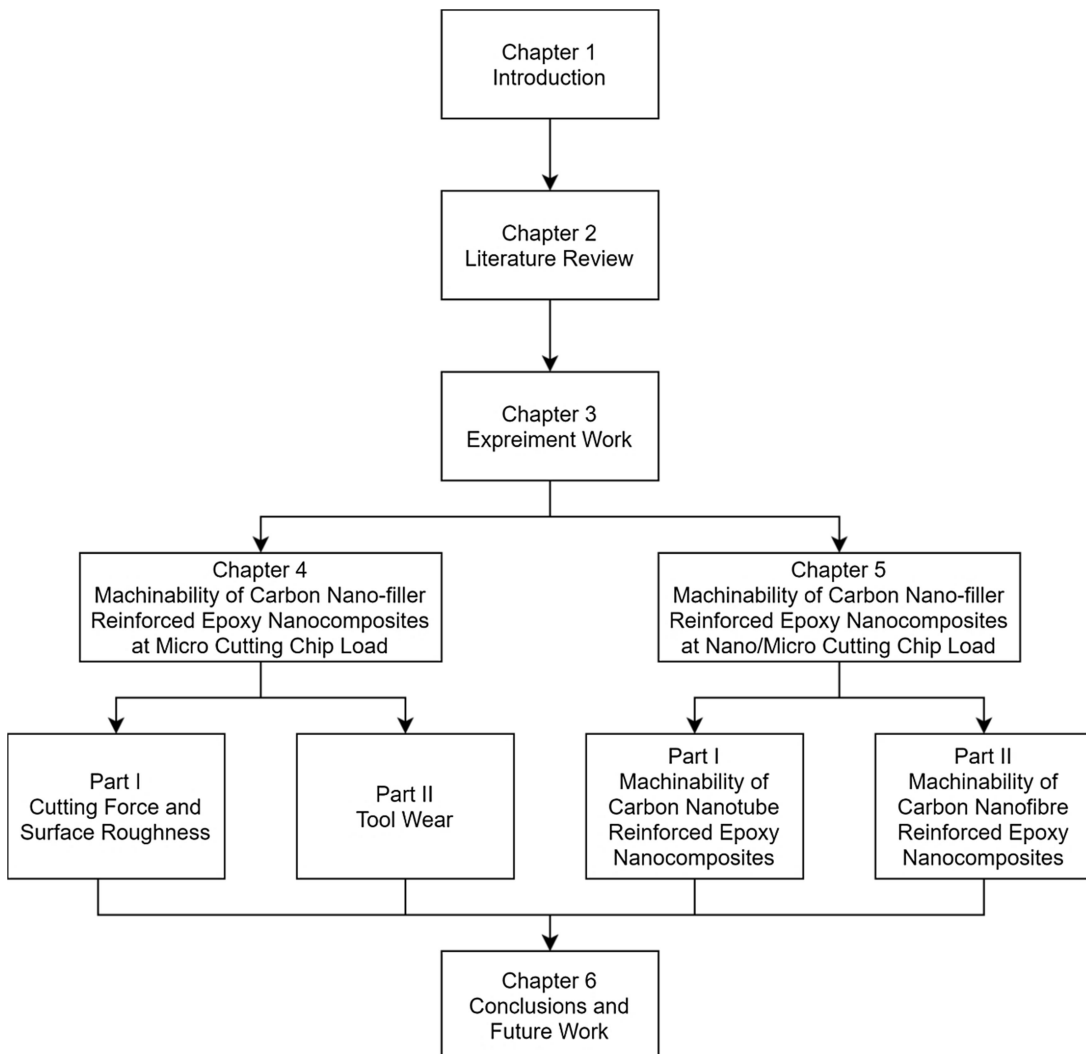


Figure 1.1: The schematic diagram of the thesis structure

## **Chapter 2: Literature review**

### **2.1 Introduction**

Micromachining of nanocomposites is deemed a complicated process due to the anisotropic, heterogeneous structure and advanced mechanical properties of these materials associated with the size effects in micromachining. It leads to poorer machinability in terms of high cutting force, low surface quality and high rate of tool wear. This literature review starts with a comprehensive review of the mechanical properties of various nanocomposites. Their subsequent micro-machining processes are critically discussed based on relevant studies from both experimental and modelling approaches. The main findings and limitations of these micro-machining methods in processing nanocomposites have been highlighted together with prospects.

The word "nanocomposite" was first introduced by Blumstein in 1961[1]. The primitive nanocomposite was investigated to improve the thermal stability of nano-silicate reinforced polymethyl methacrylate (PMMA) [14] in 1965. Nanocomposites share similar terminologies as conventional composites in terms of their constituents except for the reinforcement size typically in the range of hundreds of nanometres. The reduction from micro-range to nano-range of fillers provides remarkable reinforcements in nanocomposites while requiring much lower filler content than the composites with conventional sizes (hereafter, call composites or conventional composites for short), hence leading to considerable increases in weight [15]. Nowadays, many nanocomposites have been discovered and commercially applied in various industrial areas including (and not limited to) aerospace [3], automobile [4] and medicine [5] due to their superior properties, namely mechanical [6], thermal [7], electrical [8], electrochemical, electromagnetic [9], and gas barrier properties [10]. Due to these superior properties, further applications of nanocomposites have been found in terms of manufacturing micro-structured components following the miniaturisation trend of modern production. These nanocomposites have found many applications in microelectronics (Figure 2.1a, b).

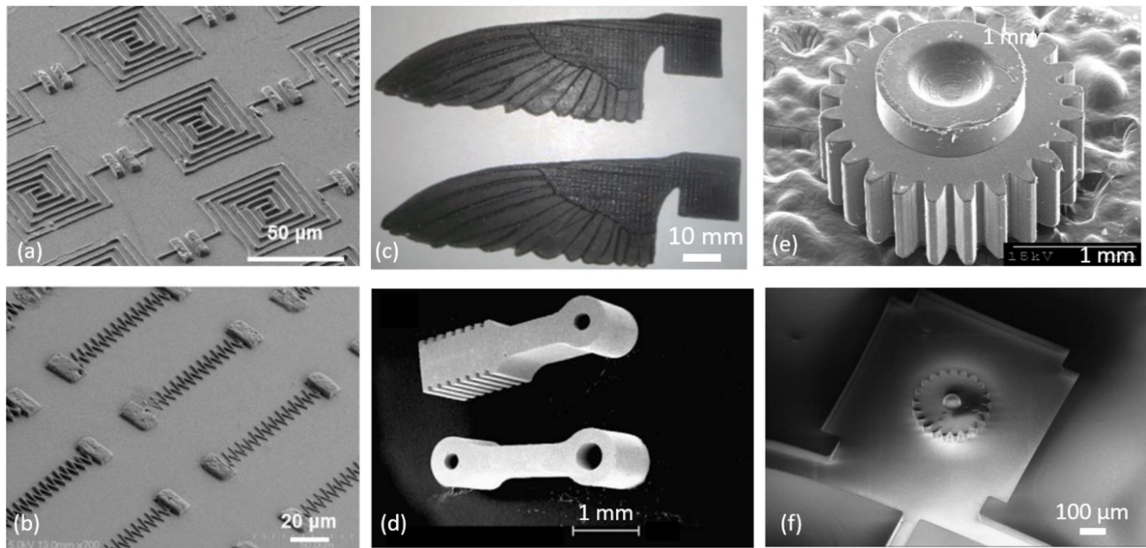


Figure 2.1: Micro-features as applications of micromachining of nanocomposites. (a - b) MTA/MWCNT micro-capacitors and micro-resistors made by precise 3D printing [16]; (c) Epoxy/MWCNT wings for MAVs made by moulding [17]; (d) Stainless steel/ $\text{Al}_2\text{O}_3$  piston and linkage rod made by soft moulding [18]; (e) PP/SWCNT micro-gear made by injection moulding [19]; (f) Epoxy/ $\text{SiO}_2$  micro-wheel made by UV-LIGA methods

(MTA: thiol-acrylate; MWCNT: multi-walled carbon nanotube; SWCNT: single-walled carbon nanotube; PP: polypropylene; LIGA: Lithography, Electro-plating, and Moulding; MAV: micro-air vehicle)

CNTs reinforced polyimide nanocomposites (PI/CNT) are applicable for microelectronics devices due to their ideal electrical conductivity, storage modulus and environmental stability [20]. Other applications such as high-performance transistors from poly-4-vinyl phenol (PVP)/  $\text{TiO}_2$  nanocomposite [21] or high energy density capacitor from poly-vinylidene-fluoride/ $\text{TiO}_2$  nanocomposite [11] have exhibited better operations than their neat matrix counterparts. Moreover, this miniaturisation trend has covered not only microelectronics but also micromechanical devices. Nanocomposites can be considered as alternatives to composites and alloys in manufacturing micro-products [22]. For example, manufacturing airframe [23] or wings [24] of MAVs using conventional composites [25] such as carbon fibre, glass fibre or Kevlar reinforced plastics could be replaced by CNTs or CNF nanocomposites which have higher strength-to-weight ratio and flexibility. The artificial wings for MAVs have been developed using CNT/Epoxy and CNT/PP nanocomposites [12] (Figure 2.1c). Additionally, the additions of ceramic nanoparticles

improved the tribological property, wear-resistance and overall mechanical properties of metal nanocomposites [26]. Therefore, these nanocomposites could be used in manufacturing micro-gear [27], piston or linkage rod [18] (Figure 2.1d-f).

Due to their huge potentials to produce micro-products, it would be necessary to investigate the thermomechanical properties as well as feasible processing methods to fabricate nanocomposites. Most of the recent techniques (Table 2.1) to manufacture nanocomposites are incapable of producing a final product (in terms of dimensional and geometrical accuracies as well as surface quality). Instead, a near-net-shape is produced.

Table 2.1: Nanocomposite manufacturing techniques

Nanocomposites	Manufacturing method	Ref.
Polymer matrix nanocomposites (PMNCs)	Melt mixing	[28]
	Solution mixing	[29]
	In situ polymerisation	[30]
	In situ formation	[31]
	Sol-Gel	[32]
Metal matrix nanocomposites (MMNCs)	Spray pyrolysis	[33]
	Infiltration	[34]
	Rapid solidification	[35]
	High energy ball milling and powder metallurgy (PM) (consolidation)	[36]
	Chemical vapour deposition	[37]
	Physical vapour deposition	[38]
	Colloidal suspension	[39]
Ceramic matrix nanocomposites  (CMNCs)	Powder processing (Compression, rolling, and extrusion)	[41]
	Polymer precursor	[42]
	Sol-Gel and consolidation	[43]

Therefore, post-processing or finishing technologies will be always required. Some manufacturing processes such as LIGA [44], laser micromachining [45], micro-extrusion additive manufacturing [46], micro-EDM (Electrical Discharge Machining) [47], and mechanical micromachining [48] have been used to generate small precision component and micro-structured parts [49].

Among micromachining techniques, mechanical micromachining exhibits high performance in terms of surface quality, dimension accuracy and a wide range of materials. However, the addition of reinforcements leads to the complex structure of nanocomposites (multiple phases, homogeneity, anisotropy, etc.), and their advanced mechanical properties (high tensile properties, hardness, wear resistance, etc.) could reduce the machinability of these materials. Moreover, micromachining also complicates the material removal process. It contains some fundamental differences from conventional machining such as cutting edge radius, MUCT, micro-structure that are generally called size effects. All these factors make the micromachining of nanocomposites challenging to adapt. Additionally, there is a scarcity of data related to the micromachining of nanocomposites. That is why only a few reports on micromachining of nanocomposites available in providing in-depth analyses on micromachining of nanocomposites.

## **2.2 Nanocomposites**

In general, nanocomposites keep the distinct characteristics of both matrix and fillers that make them different from alloys. At the same time, their final properties depend on their matrix-filler interface bonding, the arrangement of fillers inside the matrix and the geometry and content of the fillers. Nanocomposites are also distinguished from composites in which one of the filler's dimensions is in the range of 1-100 nm. Figure 2.2 demonstrates a few fundamental geometries of typical nano-fillers. The specific properties of each category, as well as the effect of filler phases on them, will be discussed in section 2.3. Based on the unique properties of different nanocomposites, their potential or commercial applications will be given. In parallel with the discussion about nanocomposites, a comparison between nanocomposites and composites will be addressed to identify the basic differences in terms of the influences of the filler's size, content and properties on their properties.

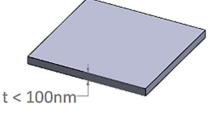
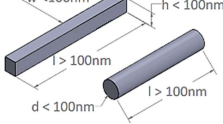

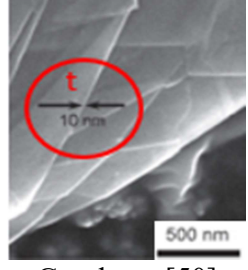
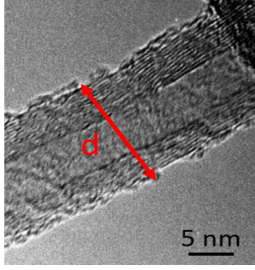
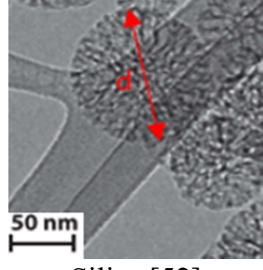
1D-Planar shape	2D-Tubular shape	3D- Spherical shape
		
at least one dimension $\leq 100 \text{ nm}$	at least two dimensions $\leq 100 \text{ nm}$	all three dimensions $\leq 100 \text{ nm}$
 Graphene [50]	 CNT [51]	 Silica [52]

Figure 2.2: Nano-filler geometries

The main difference between nanocomposites and traditional composites is the size of fillers. The revolution of composites took place with the size reduction of the fillers from few millimetres in traditional composites to micro-scale (1-999  $\mu\text{m}$ ) in modern composites and recently, nanocomposites with the fillers having dimensions in nano-scale. The original for size reduction of filler is to attain a homogenous distribution of filler within the matrix hence reduce the stress concentrations within the composite structure [53] that subsequently improve its mechanical properties.

Furthermore, smaller fillers can obtain higher surface energy that makes stronger bonding with the matrix [54], which in turn improves the stiffness and strength of the system [55]. In essence, the reinforcing mechanism of composite could be divided into two main types based on the filler scale. For micro-fillers, when the filler-matrix interface is larger than atomic level, the continuum mechanics is employed to indicate that the micro-fillers bear a fraction of transferred load from the matrix hence the efficiency of reinforcement depends on the adhesion of the matrix-filler interface [56]. This model considers materials exist as continuum, and continuously distributed in the entire region of space, hence providing high accuracy when applied at micro-scale. For nano-fillers (1-999 nm), the strengthening mechanism is applied when the matrix-filler interaction is at the molecular level. This mechanism proclaims that the nano-fillers restrict the plastic

deformation of the matrix by impeding its dislocations, subsequently leading to the improvement of tensile strength and hardness.

The influence of filler size on the mechanical properties of polymer composites has been investigated. It was observed that in the micro-range of fillers, their size effect on the tensile modulus of composites was unobvious. Some experimental results indicated that the moduli of epoxy-based composites were not considerably improved, or even decreased [57] while using various particle size of Al<sub>2</sub>O<sub>3</sub> (1-12 μm) [58], glass (4.5-62 μm) [59], or silica (2-47 μm) [60]. The same trend could be seen with PP/ CaCO<sub>3</sub> [61], polybenzoxazine/CaCO<sub>3</sub> [62] or polyester/ Al [63] (Figure 2.3). Also, the relation between the filler size and tensile strength of composite was not clear. While some studies reported that tensile strengths of composites remarkably increased with the size reduction of fillers, using micro silica particles to reinforce epoxy [60, 64], another result showed no trend of tensile strength variation of epoxy/Al<sub>2</sub>O<sub>3</sub> when decreasing the filler size [58]. In general, it could be seen that the influence of filler size in micro-scale on mechanical properties of composite is unremarkable.

However, when the fillers' size is reduced to the nanoscale, their influences on the mechanical properties of composites are more sensitive than the micro-counterparts. For example, tensile modulus, flexural strength and impact strength of snail shell reinforced PP composites were observed to be improved with the decrease of filler size (150, 300 and 420 nm) [65].

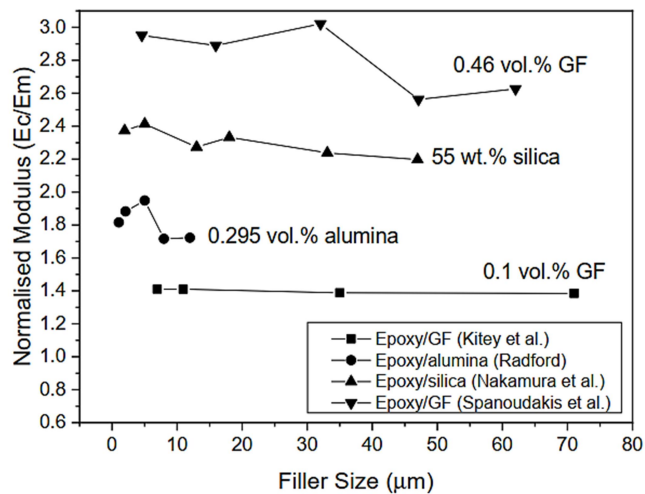


Figure 2.3: Normalised tensile modulus of epoxy-based composites as a function of micro-filler size (adapted from [58], [59], [60], [66])

However, those improvements were not considerable. Tensile strengths increased by around 5% when decreasing the filler size from 300 to 150 nm for every weight fraction. The improvements of the mechanical properties of composites became considerable at the size of filler below 100 nm. This phenomenon was verified when a comparative study between micro and nano-fillers in terms of mechanical performance of polymer composites was given by Devaprakasam et al. [67]. In this research, micro-silica (100 nm – 4  $\mu$ m) and nano-silica (40 – 60 nm) were employed. The results exhibited less variation in the modulus and hardness of the nanocomposite than the composite while applying different loadings. It can be explained by the homogenous distribution of nano-fillers, strong interfacial matrix-filler bonding compared with micro-fillers. The dominant effect of filler sizes on mechanical properties of composites was exhibited when they were reduced below 20 nm [68] (Figure 2.4) while other researchers claimed that a high degree of reinforcement could be achieved using the fillers with sizes below 100 nm [69]. This threshold of filler size in which the mechanical properties of composites increase remarkably is called ‘critical size’, according to [70].

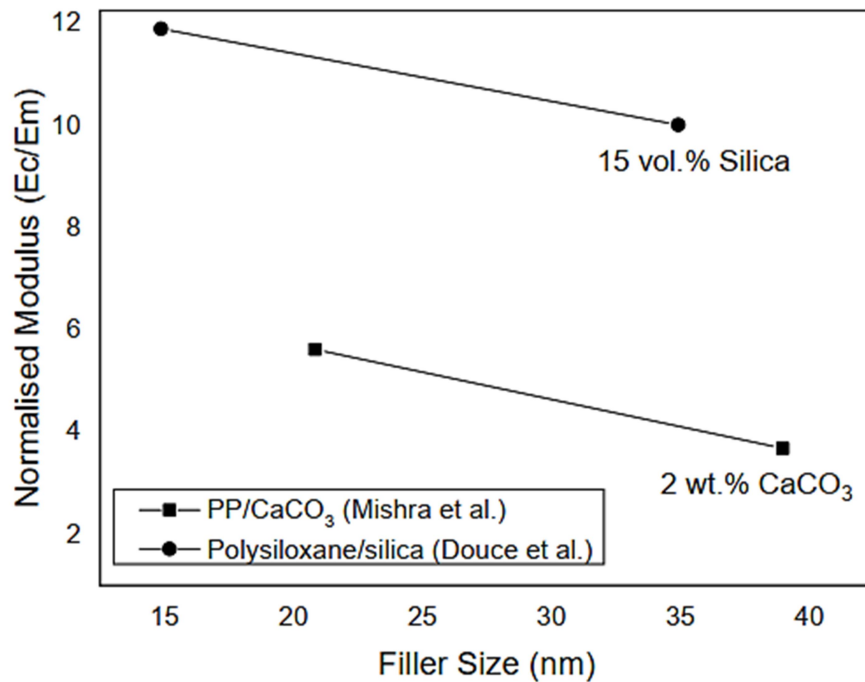


Figure 2.4: Normalised tensile modulus of polymer-based nanocomposites as a function of nano-filler size (adapted from [68, 71])



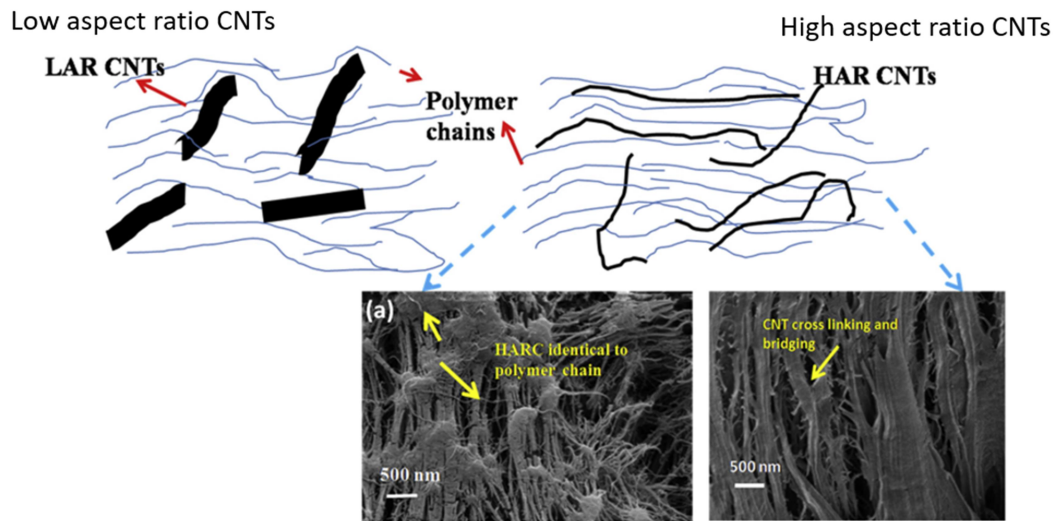


Figure 2.5: Graphical representation of the effect of CNT aspect ratio while interacting with polymer chains [72]

The application of nano-fillers with high aspect ratios such as CNTs can efficiently improve the hardness and elastic modulus of polymer nanocomposites due to increased contact surface area (of nano-fillers) and strong interfacial bonding of CNT-polymer. Also, mechanical locking was more frequent in terms of high-aspect-ratio CNTs (Figure 2.5).

However, most of the relevant studies only focused on experimental works while a few theoretical models or simulations were found (Figure 2.6). Constitutive models would be essential to provide quantitative analysis and explanation in terms of strengthening mechanism. The molecular dynamic (MD) method have been applied to investigate the effect of matrix density, chemical cross-links on the interface and geometrical defect of CNTs on interfacial shear strength (ISS) and consequently, CNT pull-out (Figure 2.6a) [73].

The simulation concluded that high matrix density, presence of cross-link and small cross-link switching contributed to high ISS. Additionally, a 3D representative volume element (RVE) method has also been applied to assess the effects of CNT waviness, diameter, volume fraction, Poisson's ratio and matrix modulus on interfacial strength of polymer/SWCNT [74] (Figure 2.6b). Based on these, investigating the interfacial bonding between nano-fibre and matrix seemed to play a critical role in load transfer assessment and consequently, the mechanical strengthening efficiency of the reinforcement. The Cox model has also been applied to study the stress transfer ( $\delta$ ) behaviour of SWCNT in the

epoxy matrix [75] (Figure 2.6c). The results showed a remarkable improvement of  $\delta$  (128%) in the case of epoxy/SWCNT compared to that in epoxy/CF composite. The increase in Young's modulus and structural change (from solid to hollow structure) contributed 69% and 31%, respectively to this enhancement (Figure 2.7a, b). The improvement of stress transfer efficiency  $\delta$  due to the nanotube's diameter increase has also been confirmed by Li and Saigal [76] using shear-lag analysis and the RVE (Figure 2.6d). Besides, they also considered the effect of fibre volume fraction as it has not been evaluated in previous studies. Based on these, it could be seen that nano-fibres with higher aspect ratio and tensile properties can provide higher reinforcing efficiency compared to their micro-counterpart.

The strengthening efficiency of nano-fillers such as CNT in MMNCs was also investigated and its mechanism is following load transfer [77], Orowan strengthening [78] and thermal expansion mismatch [79]. The strength improvement that is contributed by metal matrix grain size refinement [80], which resulted from the addition of CNT has been found by [81]. Similar to polymer-based nanocomposites, the effect of reinforcement size also significantly contributed to the strengthening behaviour of MMNCs [82-84].

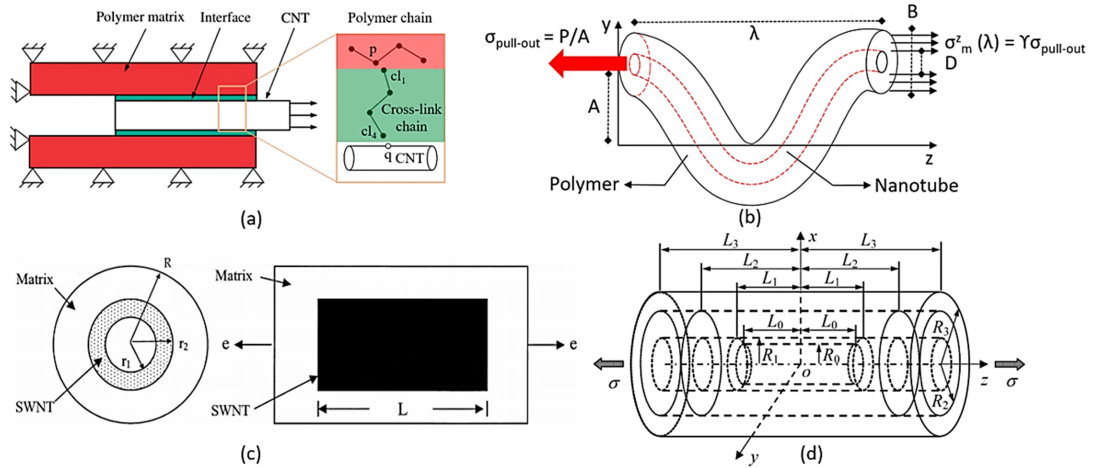


Figure 2.6: Theoretical models representing the micromechanical strengthening mechanism of polymer/CNT nanocomposites via the interfacial stress transfer considering effects of various factors: (a) Effects of polymer matrix density, chemical cross-links and CNT defect [73]; (b) Effects of SWCNT waviness [74]; (c) Effects of tube length and diameter [75]; (d) Effects of nanotube aspect ratio and fibre volume fraction [76]

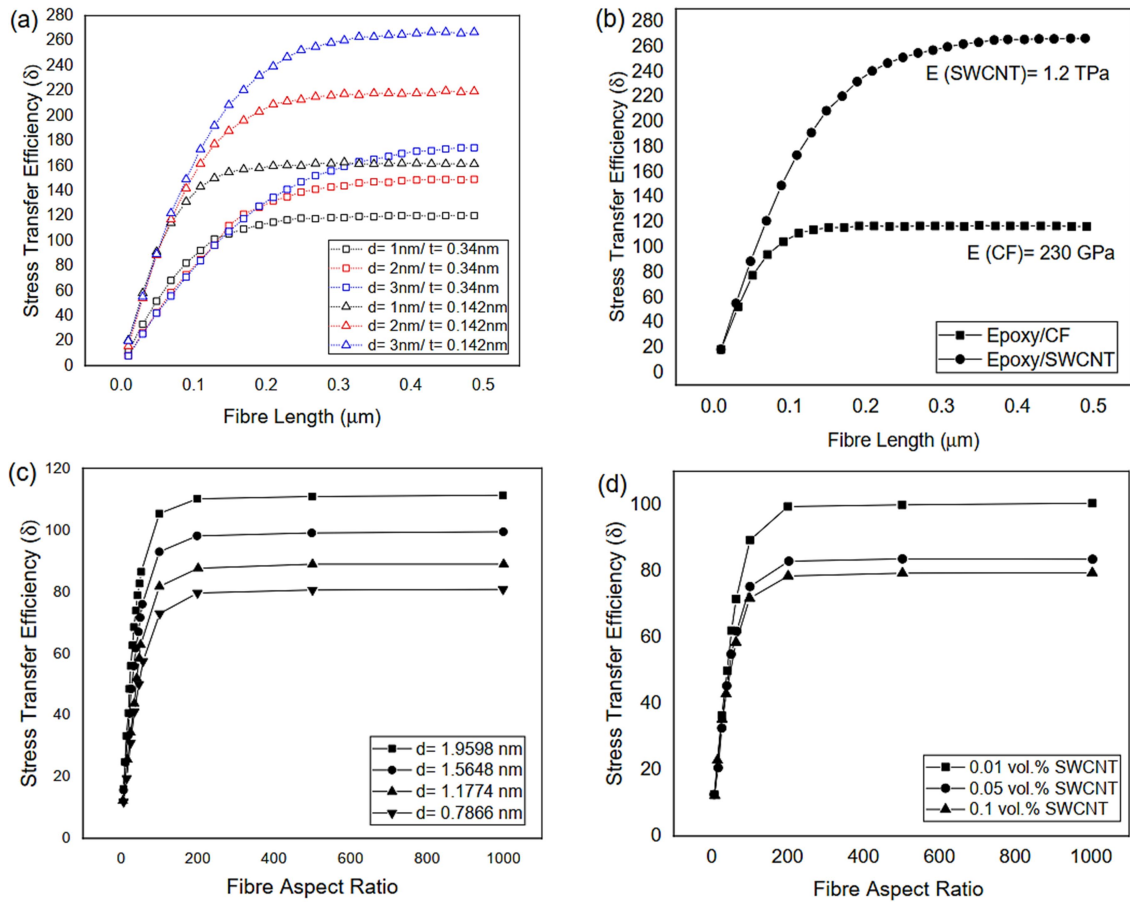


Figure 2.7: Effect of (a) SWCNT's diameter, thickness and length on the stress transfer efficiency ( $\delta$ ); (b) Young's modulus on the stress transfer efficiency ( $\delta$ ) (Assumed that CF had the same hollow structure with  $d=3\text{nm}$  and  $t=0.142\text{nm}$  as SWCNT) (Fibre volume fraction  $V_f \sim 0.17\%$ ) [75]; (c) nanotube diameter on stress transfer efficiency ( $V_f = 0.1\%$ ); (d) nanotube volume fraction on stress transfer efficiency ( $d = 0.7086\text{nm}$ ) [76]

However, only a few models published have provided a comprehensive explanation of the strengthening mechanism of CNT reinforced MMNCs. Barai and Weng [85] have developed a two-scale model to analyse the elastoplastic behaviour of CNT reinforced MMNCs that considered CNT agglomeration and interface properties as two main factors affecting the load transfer. Dong et al. [86] have built a dislocation model that combined the effect of both matrix grain size and filler size on the strengthening mechanism of metal/CNT nanocomposites (Figure 2.8). They claimed that the load transfer effect was improved at small grain size and high volume of CNT.

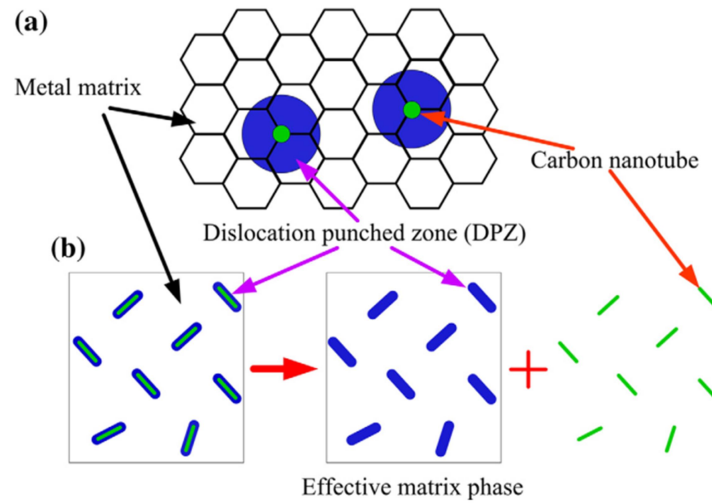


Figure 2.8: (a) Schematic of the microstructure of CNT-reinforced MMCs with dislocation punched zones (DPZs). (b) The entire composite is decomposed into CNT and effective matrix phase, and the effective matrix is comprised of DPZs and pure metal matrix [86]

## 2.3 Mechanical properties of nanocomposites

From the discussions of the differences between nanocomposites and composites in section 2.2, it could be seen that reinforcing a matrix material by nano-fillers could lead to higher effectiveness of reinforcement than micro-fillers due to their advanced mechanical properties and novel nanostructures. Within the scope of this micromachining-aimed review, the mechanical properties of nanocomposites that have been applied in micromachining are addressed including CNT, graphene, and ceramic-based nanocomposites.

### 2.3.1 CNT-based nanocomposites

CNTs are allotropes of carbon that made of a cylindrical rolled-up single layer of the carbon atom. The diameters and lengths of CNTs range from 1-100 nm and 0.1 – 100  $\mu\text{m}$ , respectively [87] with the tubular structure make them very high aspect ratio materials with surface areas are in the range of 200–900  $\text{m}^2/\text{g}$  [88]. CNT was first discovered by Iijima in the transmission electron microscopy (TEM) image in 1991 [89] and the first SWCNT was synthesized in 1993 by the same author [90]. Many applications have been found for CNT in different domains such as drug delivery [91], health care [92], electronics

[93], electrical and thermal applications [94]. Due to their high strength-to-weight ratio, aspect ratio, thermal and electrical properties [95], CNTs have found huge potential applications in composite reinforcement.

### **2.3.1.1 CNT reinforced Polymer Nanocomposites**

CNTs have been employed to reinforce polymers due to their better interfacial interaction in comparison to ceramic [96] or metal matrix [97] and the similar characteristic of organic structure. Therefore, there were some polymer/CNTs nanocomposites with tensile strengths ranging from 0.1 to 5 GPa and Young's modulus from 5 to 200 GPa [98]. Generally, the mechanical properties were improved when using CNTs as reinforcement in some polymers such as epoxy [99], polystyrene (PS) [100], polyethylene (PE) [101], PMMA [102], poly (p-phenylene benzobisoxazole) (PBO) [103], polyvinyl alcohol (PVA) [104], polyester elastomer (PEE) [105], polycarbonate (PC) [106], polyamide-6 [107] and nylon-6 [108]. The loading of CNTs was considered carefully to avoid agglomerations that negatively affect the mechanical properties of PMNCs, usually when CNTs content exceeds 2-3% [109]. Figure 2.9 shows some improvements of Young's moduli and tensile strengths when reinforcing polymer by CNTs. Generally, it could be seen that the level of CNTs distribution in polymer matrixes, their interfacial interaction and processing methods significantly affect the load transfer from the matrix to CNTs, hence decide their effectiveness of reinforcement in terms of mechanical properties of polymer-based nanocomposites. From Figure 2.9, both Young's modulus and tensile strength of nanocomposites improved with the addition of CNTs. However, there are different thresholds of CNTs loading at which the tensile strengths decrease or even lower than pristine polymers. The re-agglomeration [110] of CNTs due to insufficient dispersion techniques, high loading of fillers hence creating the more stress concentration and reducing the effectiveness of CNT as reinforcement. Specifically, the poor interfacial interaction between CNT and polyester even leads to the negative influence on tensile strength of nanocomposite [111]. In terms of dispersion methods, solution mixing, in situ polymerization, dry mixing, and melt mixing are the most common methods for fabricating polymer-based nanocomposites. Esawi et al. [112] have investigated the effects of dispersion methods on the mechanical properties of PP/CNT nanocomposites (Figure 2.10).

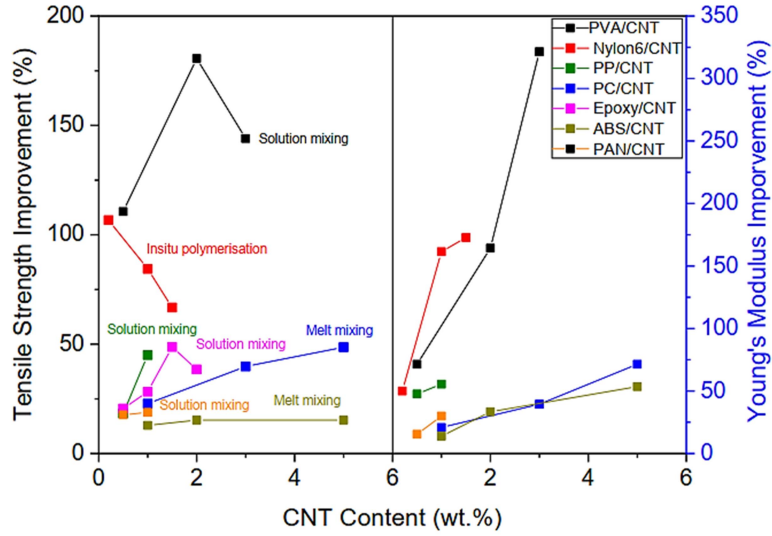


Figure 2.9: Mechanical properties of polymers reinforced CNTs with corresponding dispersion techniques (adapted from [110, 113-118])

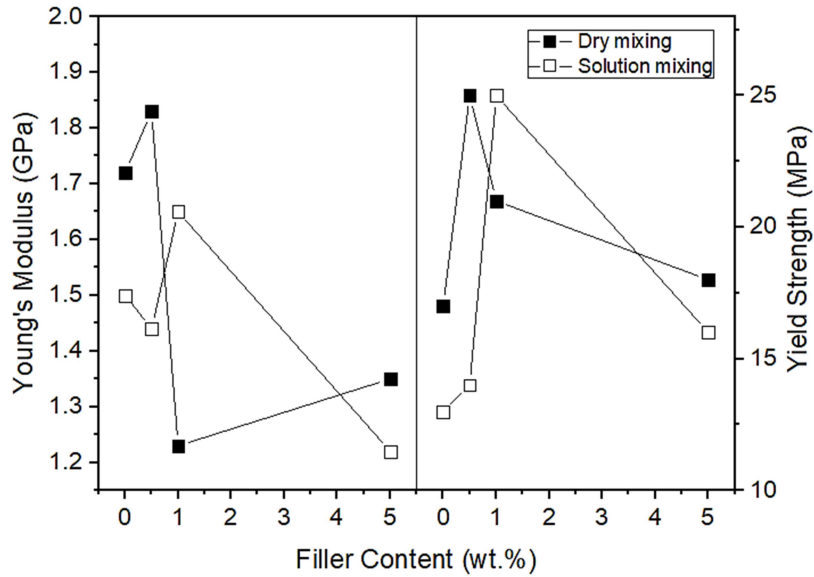


Figure 2.10: Effects of dispersion method on mechanical properties of CNT reinforced PMNCs (reproduced from [112])

The results have indicated a higher level of CNT distribution when using dry-mixing in comparison with solution-mixing. The degradation of the polymer, high viscosity due to the addition of solutions that limited the CNT distribution contributed to the lower improvements of mechanical properties when applying solution-mixing. Additionally, employing ultra-sonication in solution-mixing might damage the CNT structure, hence also

contributed to the low mechanical properties of nanocomposites [119]. Associated with the effect of CNT content, the influence of CNT structure on the mechanical properties of CNT-based nanocomposites has been also indicated considerable. Since CNTs have various types: single-walled carbon nanotubes (SWCNTs), double-walled carbon nanotubes (DWCNTs), and multi-walled carbon nanotube (MWCNTs), their different structures and properties lead to various efficiencies in terms of mechanical reinforcement. Figure 2.11 shows the improvements in tensile properties when reinforcing epoxy with different types of CNTs. Theoretically, the addition of SWCNTs and DWCNTs exhibited higher reinforcement of mechanical properties than MWCNTs due to their higher mechanical properties, aspect ratio and specific surface area. Also, the multi-layer structure of MWCNTs leads to a low effective surface area in comparison with less-layer structure CNTs. However, this reinforcing effectiveness also depends on how homogenous the CNTs distribute within the polymer matrix. In this case, DWCNTs showed no agglomeration as SWCNTs that explained a higher improvement of tensile properties. This phenomenon was also verified by Fornes et al. [115] and Sennett et al. [120] that the dispersion of MWCNTs within the PC matrix was much more effective than SWCNT regardless of the fabricating routes. They explained that SWCNT had a high propensity to re-agglomerate during the synthesis making the exfoliation more difficult in comparison with MWCNT.

Besides the structure, CNTs alignment also has a dominant effect on the mechanical properties of polymer-based nanocomposites. This feature could be attained using several methods such as shear flows [121], ex-situ alignment [122], force field-induced alignment [123], magnetic field-induced alignment [124], electrospinning-induced alignment [125] and liquid crystalline phase-induced alignment [126]. Figure 2.12 shows some experimental results that exhibited the improvements of tensile properties of CNT based nanocomposites with aligned CNTs in comparison with non-aligned CNTs. It could be explained by the isotropic nature of nanocomposites when CNT alignment was employed and leading to better distribution and reducing agglomeration of CNT when filling into the polymer matrix. In addition, functionalization has been considered as an effective treatment of CNTs to improve their interactive adhesions with polymer matrix, hence enhance the reinforcing effectiveness of mechanical properties through load transferring.

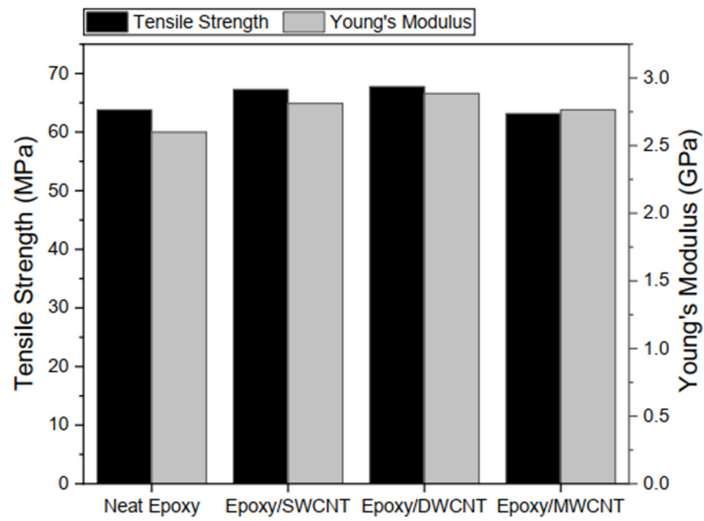


Figure 2.11: Effect of CNT structure on mechanical properties of polymer nanocomposites at a filler content of 0.3 wt.% (adapted from [127])

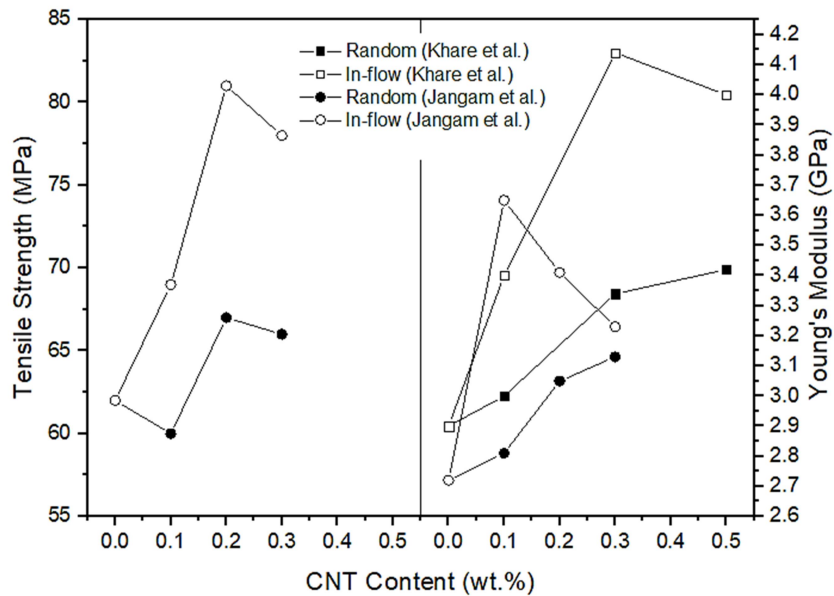


Figure 2.12: Effect of CNT alignment on mechanical properties of epoxy-based nanocomposites (adapted from [128, 129])

Reinforcing epoxy by amido-anime functionalised carbon nanotubes (f-CNTs) led to a higher improvement of mechanical properties in comparison with pristine carbon nanotubes (p-CNTs) (~ 51% of Young's modulus) [130]. It was due to the lower interphase compression, matrix structure integrity, suppression of matrix mobility, stable-covalent bonds of epoxy/f-CNTs and subsequent facilitation of load transfer (Figure 2.13).



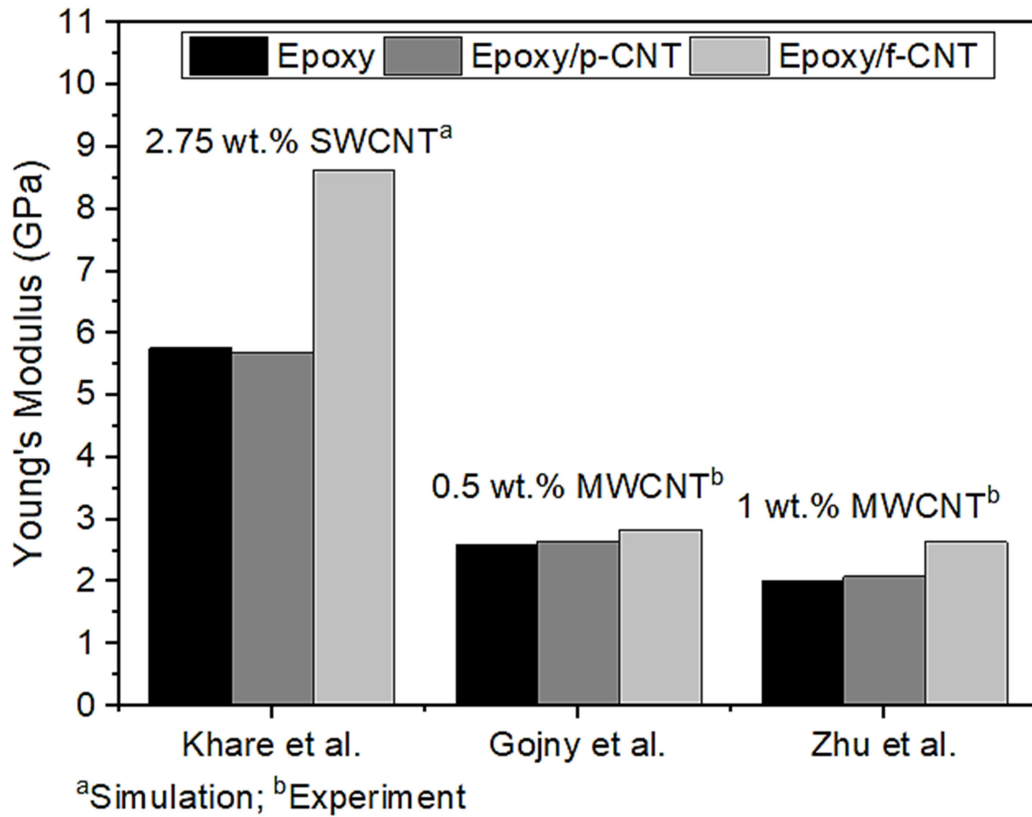


Figure 2.13: Effect of CNT functionalization on tensile modulus of CNT reinforced epoxy matrix nanocomposites (reproduced from [127, 130, 131])

Unlike the improvements of tensile strength and Young's modulus, the addition of CNTs exhibited different variations of fracture strain and toughness. Figure 2.14 shows the different trends of fracture strain improvement between thermoplastic and thermosetting reinforced by CNTs at various weight contents. It could be seen that the flexibility of thermoplastic nanocomposites was significantly decreased at all filler loadings. Although relevant studies have shown this phenomenon, a comprehensive mechanism to explain it has been not proposed. Wang et al. [132] claimed that the degradation of flexibility when adding MWCNT-NH<sub>2</sub> into PI was possibly due to strong interface interaction between matrix and filler. Consequently, the movement of polymer chains under loading could be restricted and hence, decreasing the flexibility of this material. However, the characterisation of interfacial strength has not been made to support this claim. On the other hand, the fracture strains of thermosets could be enhanced by the addition of CNTs at certain levels of contents which is different from thermoplastic nanocomposites.

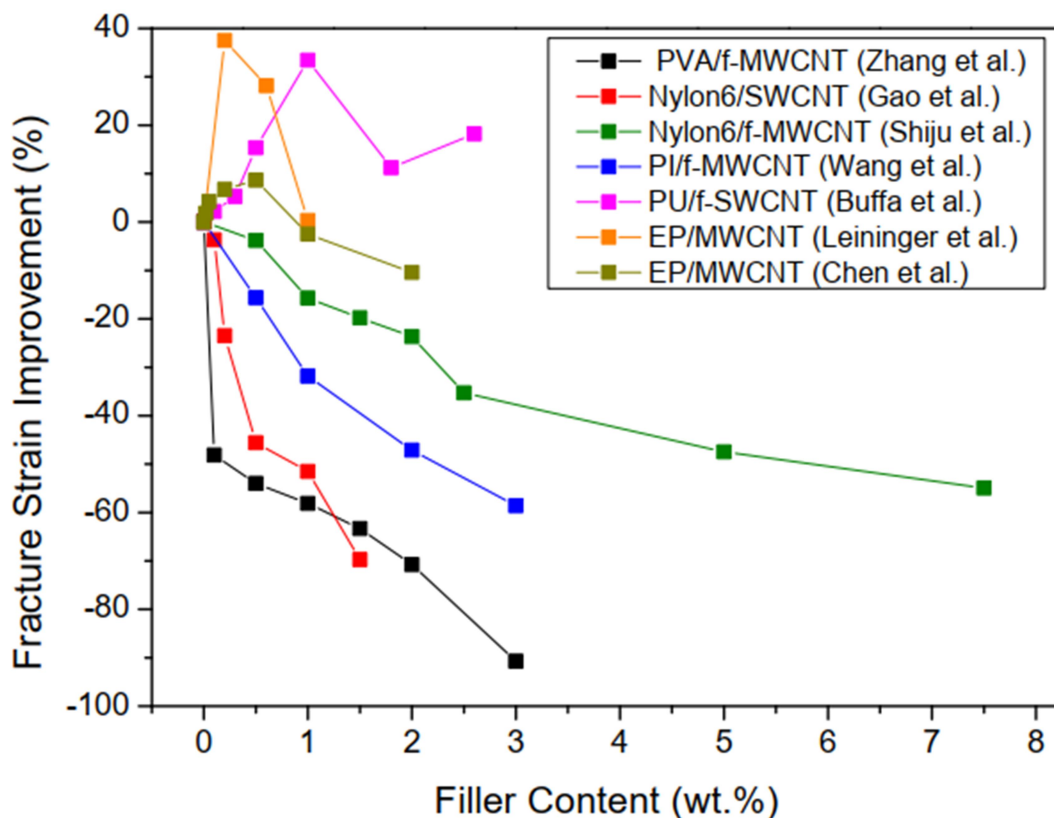


Figure 2.14: Fracture strain improvement of CNT based polymer nanocomposites as a function of filler content (adapted from [110, 113, 132-136])

When reinforcing epoxy by MWCNT, Chen et al. [136] indicated that the brittle epoxy phase was toughened by dispersed CNT. This enhancement of failure strain at certain low filler loadings (below 1 wt.%) was confirmed by Gojny et al. [137]. At higher CNT loadings, CNT agglomeration led to stress concentration and weaken the interfacial interaction of polymer-CNT, hence reducing the fracture strain. Scanning electron microscope (SEM) imaging was employed to demonstrate these explanations in terms of CNT distribution at different filler contents.

Regarding fracture toughness, CNTs have been qualified as a potential reinforcing candidate to replace glass fibre (GF) or CF to attain higher toughening efficiency due to their high aspect ratio and stiffness [138]. The micro-mechanical toughening mechanism of polymer reinforced CNT nanocomposites can be expressed as follows: (1) crack bridging by CNTs and (2) CNTs de-bonding and pull-out or breaking depends on the interface strength and applied load [139, 140] (Figure 2.15).

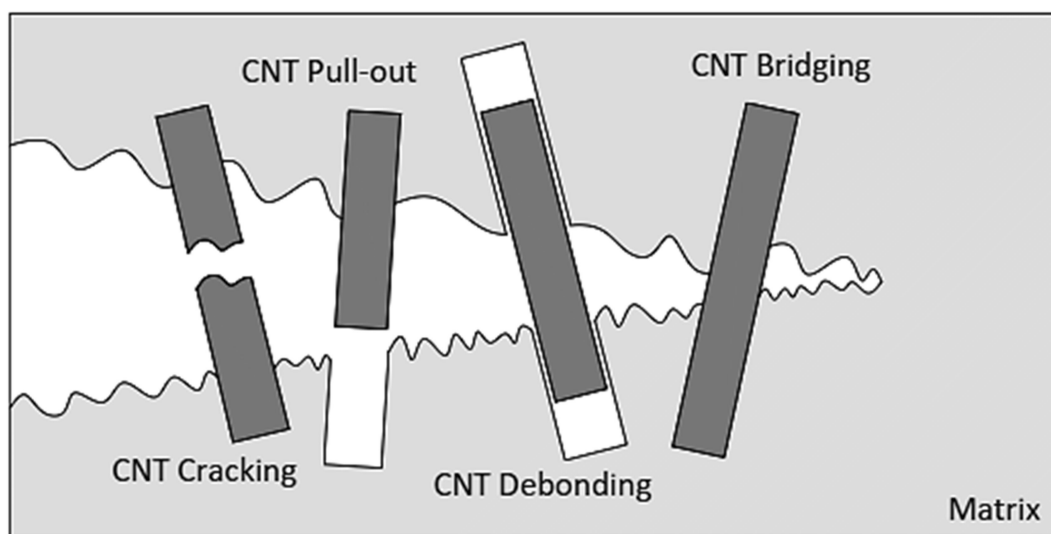


Figure 2.15: Schematic representing fracture toughening mechanism of CNT reinforced polymer nanocomposites (reproduced from [139])

Based on this schematic, it could be seen that the highest fracture toughness could be achieved if CNTs are oriented transversely with the propagated cracks in which the bridging mechanism takes effect. Otherwise, it will not have a considerable influence on fracture toughness in the case of longitudinal or random distribution of CNTs [141]. Besides, the effect of transverse alignment could be only effective at a low loading of CNTs. Some studies have shown a maximum enhancement of fracture toughness (around 51%) of polymer/CNT nanocomposites at 3 wt.% of fillers was used and decreased when exceeded this threshold due to filler agglomeration [141]. On the other hand, the random distribution of CNTs did not show considerable enhancement in toughness at low filler content (< 1wt.%) [127].

Chen et al. [140] have analysed the effect of CNT length and interface strength on fracture toughness. They claimed that the fracture toughness could not be improved with the consideration of interface chemical bond density or fibre length only but combined them. The optimal values of these indicators were around 5-10% and 100 nm, respectively. Optimal CNT-bridging from their experiment has confirmed this theoretical analysis. Generally, reinforcing polymers by long CNT can achieve high fracture toughness due to its high load transfer and hence, improving the interface shear strength [142]. The structure of CNTs has also influenced the fracture toughness of nanocomposites. Low contents of

DWCNT (<0.5 wt.%) have shown a remarkable improvement of fracture toughness of epoxy-based nanocomposites due to its high compatibility with epoxy matrix.

However, using suitable dispersion methods and functionalization could make MWCNT a better reinforcing candidate to enhance fracture toughness than other types of CNTs. In general, the fracture toughness improvement when reinforcing polymer by CNTs has shown a complicated correlation between various factors including CNT content, structure, alignment, treatment as well processing technique. Table 2.2 shows some fracture toughness improvements of polymer reinforced CNT nanocomposites with the consideration of the aforementioned factors.

Table 2.2: Fracture toughness of polymer reinforced CNT nanocomposites with the consideration of various factors

Matrix	Factors	Variables	Filler content (wt.%)	Fracture toughness improvement (%)	Ref.
Epoxy	- CNT structure - Functionalisation - Filler content	SWCNT	0.05	10.8	[127]
			0.1	23.0	
			0.3	12.3	
		DWCNT	0.1	16.9	
			0.3	30.8	
			0.5	30.7	
		MWCNT	0.1	21.5	
			0.3	23.0	
		Epoxy	- CNT diameter	20-30 nm	
30-40 nm	26.4				
40-50 nm	24.2				
50-60 nm	21.2				
Epoxy	- CNT length	2091 nm	0.1	46.6	[144]
		1689 nm		43.3	
		1332 nm		8.7	
		992 nm		2.0	
		503 nm		-14.7	
Epoxy	- CNT alignment - Filler content	Random orientation	0.05	6.2	[128]
			0.1	11.6	
			0.3	16.9	
			0.5	13.8	
		Aligned orientation	0.05	23.3	
			0.1	36.1	
			0.3	53.0	
			0.5	31.1	
Epoxy	- Processing technique	Three-Roll Milling (TRM)	0.1	58.3	[145]
			0.5	64.5	
			1	68.5	
			1.5	60.0	
		HPH (High Pressure Homogenization)	2	57.7	
			0.1	48.3	
			0.5	56.4	
			1	64.2	
			1.5	56.0	
			2	42.0	

### 2.3.1.2 CNT reinforced metal nanocomposites

Although CNTs are theoretically considered an effective reinforcement for high strength-to-weight materials, few studies have concerned about using them to reinforce metals. The incorporation of CNTs in metals has some difficulties due to the inherent characteristics of both CNTs and metals, the fabricating conditions that negatively affect the interfacial adhesion as well as CNTs defects and subsequently, the improvement of mechanical properties of metal reinforced CNT nanocomposites. In general, two main challenges hinder CNTs from achieving high effectiveness of reinforcement in the metal matrix. The first challenge is the poor interfacial adhesion between CNTs and metals. It is due to the nature of CNTs such as low compatibility with high surface energy ( $72.8 \text{ mJ}\cdot\text{m}^{-2}$ ) [146] high surface tension ( $721 \text{ mN/m}$ ) [147], low wettability or hydrophobicity [148] and high possibility of agglomeration because of Van der Waals forces [149]. Because chemical bonding between CNT-metal is neglected, these physical factors are dominant in the interfacial interaction [147]. Secondly, the undesirable chemical reactions between CNTs and metals at high temperature, pressure from fabricating conditions such as sintering, hot milling. It leads to the formation of intermetallic such as  $\text{Al}_4\text{C}_3$  [150],  $\text{TiC}$  [151],  $\text{Al}_2\text{MgC}_2$  [152]. Generally, a minor formation of carbide can positively improve the interfacial adhesion while an uncontrolled process could lead to serious damages of CNTs and in situ carbide formations [153] or enhance CNTs amorphization as well as their thermal decomposition [154]. Some solutions have been adapted to improve the wettability and distribution of CNTs as well as their interfacial strength with a metal matrix such as chemical functionalization [155], surfactant [156], coating CNTs with Ni [157], Si [158] or in situ synthesis CNTs within metal matrix [159]. Table 2.3 shows the mechanical properties of CNT reinforced metal matrix nanocomposites. The improvements in mechanical properties depend on the homogenous distribution of CNTs [160], interfacial strength of metal/CNT [161], thermal expansion mismatch between metal and CNTs [162], grain refinement effect [157], CNTs structure retention of plastic deformations of metal matrixes [161], that all contributed to strengthening mechanism. The two last ones also contribute to the hardness improvement of metal/CNT nanocomposites.

Table 2.3: Mechanical properties of CNT reinforced metal matrix nanocomposites

Material	$\sigma_u$ (MPa)	E (GPa)	Hardness (GPa)	Reasons	Fabricating methods
Al/MWCNT 1wt.% [163]	521.7 (35.7%)	102.2 (41.3%)	0.136 (30.8%)	Good interfacial bonding, homogenous distribution, high elastic behaviour of CNT, the integrity of Al	PM cold isostatic press, hot extrusion
Al/MWCNT 0.5wt.% [164]	130 (9.2%)	60 (20%)	--	Good distribution of CNT due to the rolling process	Mechanical mixing, hot rolling
Al/(Si) MWCNT 10wt.% [165]	83.1 (4%)	120.4 (78%)	--	Strengthening by retained CNT and nano-crystalline structure	Thermal spray, plasma spraying
Al/(Si) CNT 10wt.% [166]	--	125 (39%)	2.1 (141%)	Good distribution of CNTs due to Si-coating and dispersing method	Spark plasma sintering (SPS)
Al/(Ni) CNT 5wt.% [167]	213 (52%)	--	3200 (113.3%)	Homogenous dispersion, CNT structure retention, strong interfacial strength due to molecular mixing in in-situ CVD synthesis as compared to ball milling	Ball milling
	398 (184%)	--	6.5 (333%)		In situ CVD synthesis
Cu/MWCNT 20 vol.% [160]	--	106.5 (108%)	1.304 (72%)	Homogenous distribution and reduction of MWCNT agglomerations	SPS and electroless deposition
Cu/MWCNT 10 vol.% [168]	196 (45%)	135 (95%)	1.75 (207%)	Homogenous distribution of CNT	SPS, cold rolling
Cu/(Ni) CNT 12 vol.% [169]	--	--	21.5 <sup>a</sup> (111%)	Highest mechanical reinforcement at 12 vol.% of CNT	Mechanical mixing and hot pressing
Cu/(Ni) MWCNT 0.75wt.% [161]	279 (76%)	--	1.383 (54%)	CNTs resist plastic deformation, thermal expansion mismatch, homogenous distribution, good interfacial bonding, high hardness of Ni	Ball milling and hot pressing
Cu/MWCNT 0.5 vol.% [170]	307.4 (81.6%)	--	106 (14.7%)	Well dispersed of MWCNTs Stable interface blocks dislocation	Ball milling and hot pressing
Ni-P/MWCNT 0.21wt.% [171]	--	665.9 (303%)	28.9 (331%)	Strengthening effects due to MWCNT presence	Electroless deposition
Ni/MWCNT 0.1wt.% [172]	1140.7 (14.2%)	--	4.824 (74.5%)	High quality dispersion and integrity of MWCNT due to surfactant treatment	SPS
Mg-Zn/CNT 1 vol.% [173]	321 (13.6%)	52 (42.5%)	--	Homogenous, single distribution of CNTs, no reaction at the interface, grain refinement	Melting and solidification
Mg/(Si)MWCNT 5 vol.% [158]	296 (44.4%)	--	1.569 (100%)	High wettability of MWCNTs due to Si-coating leads to good distribution, bonding strength	Ball mill and hot pressing
Mg/CNT 1.3wt.% [174]	210 (9%)	--	46 <sup>b</sup> (2.2%)	The coefficient mismatch of thermal expansion and elastic modulus of Mg-CNT	Melt deposition and hot extrusion
Mg/(Ni) MWCNT 0.3wt.% [157]	237 (38.6%)	--	0.54 (41%)	Improved adhesion of Mg-(Ni) MWCNT due to Ni coating leading to Mg <sub>2</sub> Ni intermetallic formation, grain refinement	PM, microwave-assisted sintering
Mg alloy/MWCNT 2wt.% [175]	297 (6.1%)	--	0.8 (0.37%)	Strengthening mechanism, thermal mismatch of CNT-Mg alloy	Ball mill, hot compact

CVD: chemical vapour deposition, PM: powder metallurgy, (<sup>a</sup>: HRB; <sup>b</sup>: HR15T)

### **2.3.2 Graphene-based nanocomposites**

Graphene is a planar sheet of a single layer of sp<sup>2</sup>-bonded carbon atoms that are considered as an original structure element of other carbon allotropes such as CNTs, graphite and diamond. This two-dimensional (2D) structure provides graphene with a much larger specific surface area of ~ 2600 m<sup>2</sup>/g than other carbon allotropes such as carbon black (CB) or CNTs [176]. Graphene exhibits exceptional mechanical properties such as Young's modulus (~1 TPa) or strength (130 GPa) [177] hence considered as the strongest material [177]. Moreover, this material is also an excellent conductor with high thermal and electrical conductivity of ~4000 WmK<sup>-1</sup> [178] and ~ 6000 S.cm<sup>-1</sup> [179], respectively and other properties such as gas impermeability, optical transmittance. Therefore, graphene has high potential in a wide range of applications such as flexible electronic devices, transparent coating material, energy storage, and especially, nanocomposites [180].

#### **2.3.2.1 Graphene reinforced polymer nanocomposites**

Many researchers have attempted to investigate the reinforcing efficiency of graphene in nanocomposites by considering various factors such as the effective modulus, filler dispersion [181], alignment [182], agglomeration [183] or fabricating methods [10]. All these factors have certain influences on the filler distribution and graphene-matrix interfacial adhesion or stress transfer that subsequently affect the reinforcing effectiveness of graphene-based fillers.

The effective modulus of thermal expanded graphite oxide (TEGO) has been measured when it was mixed with PC and PE. Only a slight improvement of modulus was experimentally observed in comparison with graphite-based composites while its effective modulus was around 70 GPa-7% of the value for defect-free graphene (~1 TPa) [184]. This low effective modulus of graphene is explained by its wrinkled geometry once dispersed in the matrix [185], which consequently unfold under tensile load instead of stretching. The incomplete exfoliation could also lead to the aspect ratio reduction of graphene [186] that contributes to this phenomenon.

Graphene-matrix interfacial adhesion is considered as another crucial factor that affects the effective reinforcement [187] since it makes ineffective dispersion as well as

load transfer, hence resulting in a low modulus of nanocomposites [188]. Some significant increases of composite tensile moduli were observed when using graphene as reinforcement due to the roughness of the platelets [189] that attribute to mechanical interlocking within the matrix and hence, strong interfacial bonding.

In addition, the reinforcing effectiveness of graphene also depends on the processing method. For instance, melt mixing has been found less suitable in graphene-based nanocomposites since this method causes particle attrition [190] that possibly decrease the filler ratio. In situ polymerization, on the other hand, can generate good dispersion but it also causes polymer chain extension by graphene, resulting in a less modulus improvement of composites than the solution-mixing method [10]. This comparison between different processing methods can be seen in Figure 2.16. Table 2.4 summarises some improvements in mechanical properties when reinforcing polymers with graphene. In general, the elastic moduli increased with the addition of graphene while the tensile strengths decreased. It is explained by the improvement of interfacial interaction of matrix-filler due to the high aspect ratio of graphene [191] that effectively bridging with the matrix molecules and leading to a high stiffening effect [192]

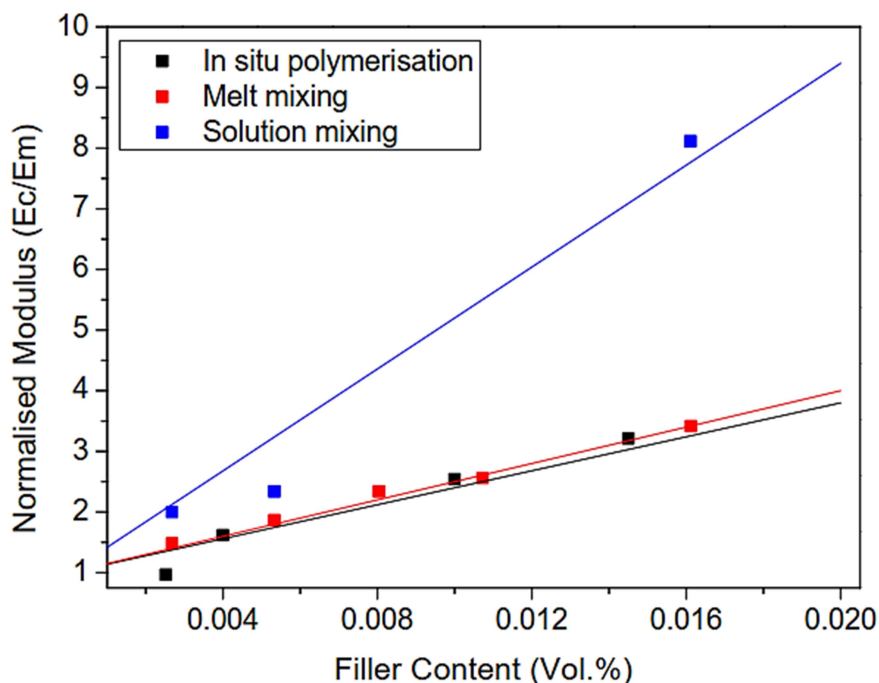


Figure 2.16: Normalised Young's moduli of thermoplastic polyurethane (TPU)/graphene nanocomposites in different processing methods) (reproduced from [10])



Table 2.4: Mechanical properties of graphene reinforced polymer matrix nanocomposites

Material	$\sigma_u$ (MPa)	E (GPa)	Reasons	Fabricating methods
EP/GNP 0.3 wt.% [193]	64.4 (12.6%)	2.16 (30%)	The high temperature in low viscosity system, low concentration of Gr leading to low agglomeration and uniform distribution of Graphene	Solution mixing
EP/APTS-GO 0.2 wt.% [194]	81.2 (16%)	3.3 (32%)	Uniformly distributed APTS-GO, strong interfacial stress	Solution mixing
EP/NH <sub>2</sub> -GNP 4 wt.% [195]	66 (1.5%)	3.4 (17%)	GNP aggregation, poor GNP dispersion	Solution mixing
EP/EGS 3 wt.% [196]	41 (20%)	3.7 (25%)	High aspect ratio and uniformly distributed EGS, good interfacial adhesion of EP-EGS	Solution mixing
EP/RGO 0.2 wt.% [197]	52.6 (-0.8%)	3.1 (7%)	Weak interfacial bond of EP-RGO, RGO agglomeration, RGO curvature	Solution mixing
EP/GNP 0.1 wt.% [198]	78 (40%)	3.7 (31%)	The high specific surface area of GNPs, strong matrix-filler adhesion/interlocking due to wrinkled surface of GNPs	Solution mixing
EP/GNP 0.3 wt.% [199]	70.4 (23%)	1.28 (47%)	High effect of Sodium Dodecyl Sulphate as the solution on GNP dispersion, the effect of surfactants	Solution mixing
ABS/CO(OH) <sub>2</sub> / GNS 4 wt.% [200]	43.2 (50%)	--	High modulus GNS, homogenous dispersion	Melt mixing
PMMA/GO 1 wt.% [201]	70.9 (22%)	4.39 (28%)	High aspect ratios and good dispersions of GO at low loading, wrinkled platelets	In situ polymerization
PC/FLG 1 wt.% [202]	60 (10%)	1.45 (26%)	Optimizing the aspect ratio of the graphene flakes	Solution mixing
HDPE/GNS 3 wt.% [203]	47 (77%)	2.033 (87%)	High specific area and flat-structure of GNS, HDPE-GNS mechanical interlocking	Melt mixing
LDPE/RGO 5 wt.% [204]	--	10.1 (60.7%)	Homogeneous distribution of exfoliated carbon sheets in functionalised PE	Solution mixing/ melt compounding
TPU/EG 10 wt.% [205]	9 (-84%)	0.091 (237%)	Homogenous distribution, HS crystallization, EG hindering the amorphous phase, weak interfacial interaction of TPU-EG, EG agglomerations	Melt mixing
PVA/GNS 3 wt.% [191]	43.2 (122%)	1.186 (155%)	Homogenous distributed Gr and strong bond of PVA-GNP. GNP restricting polymer chain movements	Solution mixing

(ABS: Acrylonitrile butadiene styrene; HDPE: high-density polyethylene; LDPE: low-density polyethylene; APTS-GO: amino-functionalised – graphene oxide; EGS: Graphene stack; FLG: Few layer graphene sheets; EG: Expanded graphite; GO: Graphene oxide; RGO: Reduced graphene oxide; GNP: Graphene nano-platelet; GNS: Graphene nano-sheet)

Consequently, the tensile strength of nanocomposites would be reduced. Moreover, this reduction is also due to the fabricating methods, re-agglomeration of graphene that constitutes some defects in the polymer matrix. The presence of graphene also opposes the flow of the amorphous phase and increase the crystallization of the hard segment of a polymer matrix that subsequently contributes to the elastic modulus improvement and the tensile strength reduction of polymer-based nanocomposites [205].

Like CNTs, the addition of graphene into the polymer matrix leads to different variations in terms of fracture strain and toughness. Fracture strain showed a significant reduction in the case of thermoplastic/graphene nanocomposite while this property was improved for thermoset plastic reinforced with low loading of graphene (Figure 2.17). However, the fracture toughness improvement when using graphene seems to be higher than CNT. Domun et al. [206] have collected experimental values of fracture toughness when using graphene to reinforce epoxy from relevant studies (Figure 2.18). They claimed that among common nano-fillers (CNTs, graphene, and nano-clay), graphene exhibited higher fracture toughness enhancement in epoxy-based nanocomposites, mostly at low filler loadings (<1 wt.%). It is due to the higher surface area, aspect ratio of graphene, as well as its exceptional stiffness and strength, compared to CNT as aforementioned.

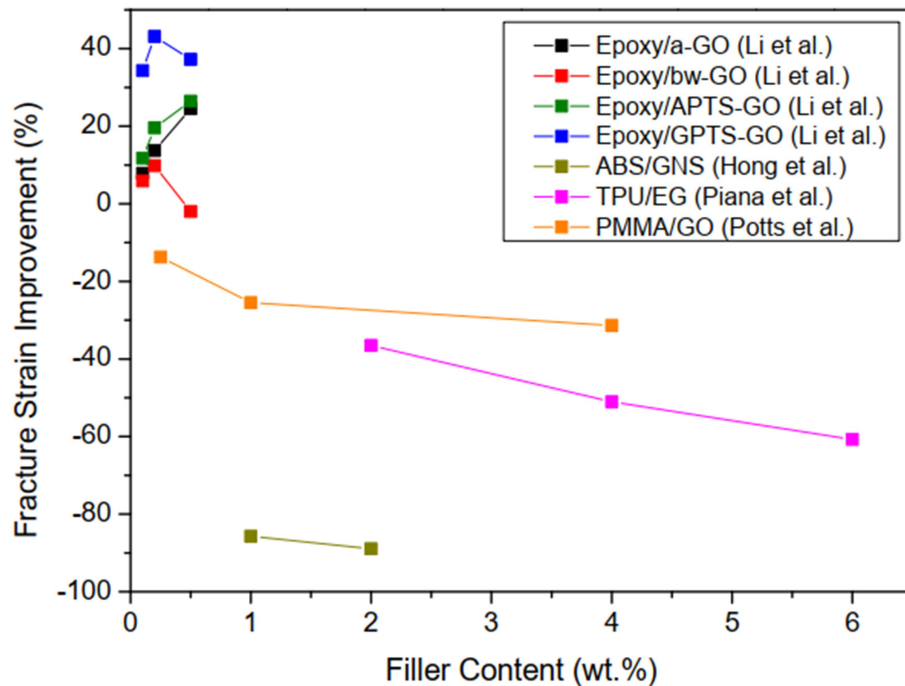


Figure 2.17: Fracture strain improvement of graphene-based PMNCs as a function of filler content (adapted from [194, 200, 201, 205])

(GPTS-GO: epoxy-functionalised – graphene oxide; bw-GO: based washed-graphene oxide)

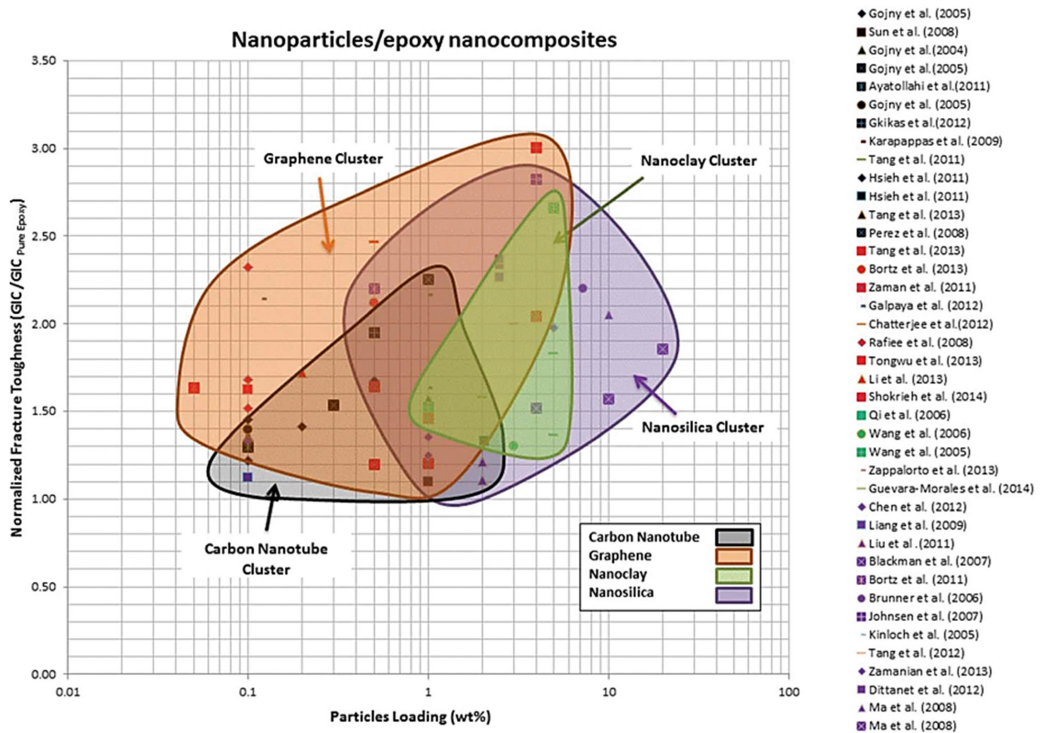


Figure 2.18: Comparative fracture toughness improvement of epoxy-based nanocomposites using different nano-fillers [206]

Rafiee et al [207]., in a comparative study, have claimed that graphene exhibited better mechanical reinforcement including Young's modulus, tensile strength and toughness than MWCNT. It was due to poor interfacial contact area, wetting and adhesion of MWCNT that showed ineffective reinforcing epoxy-based nanocomposites. On the other hand, a higher aspect ratio allowed more interfacial contact between graphene and epoxy matrix in contrast with the only outer tube of MWCNT. Also, wrinkled sheets of graphene contributed to better interfacial binding, hence improving the toughening mechanism in epoxy/graphene nanocomposites. The micro-mechanical toughening mechanism of polymer reinforced graphene is also different from that in CNTs. While filler pull-out and de-bonding still exhibit along the cracks, there is no presence of graphene cracking. When the crack reaches the graphene surface, it will be deflected and bifurcated then propagating around the filler. The ease of shearing between graphene sheets also allows the crack propagation to go through or penetrates within layers (Figure 2.19).

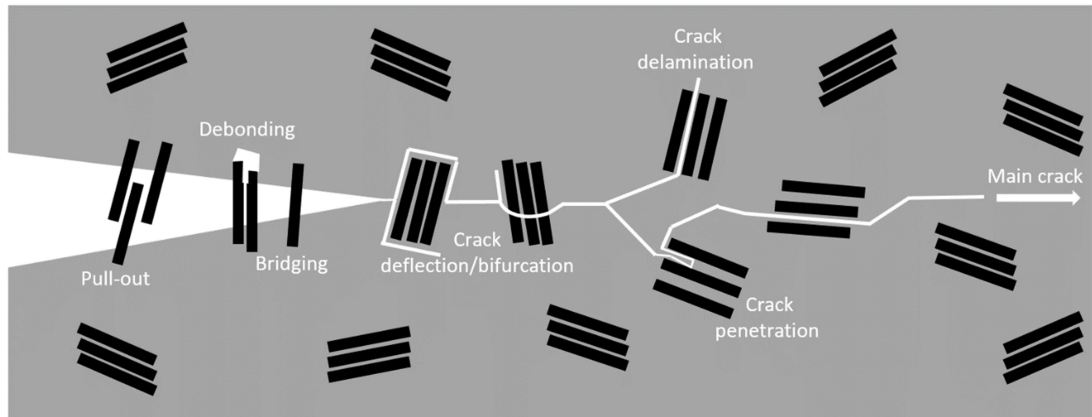


Figure 2.19: Schematic representing fracture toughening mechanism of CNT reinforced PMNCs (adapted from [182])

### 2.3.2.2 Graphene reinforced metal nanocomposites

Graphene has been also applied to reinforce metal to improve their stiffness but subsequently leads to the reduction of ductility that was called ‘strengthening mechanism’. However, tensile strengths have been increased [208] possibly due to the straightening of wrinkled graphene during the plastic deformation or ball milling process [209]. In general, the strengthening mechanism is related to the improvements of yield strength [210], elongation [208], flexural strength [211], but Young’s modulus and hardness are the most fundamental objectives. The improvements of Young’s modulus when reinforcing metal with graphene is ascribed to the homogenous distribution of graphene [212], compact interfacial bonding of metal-graphene [213] that lead to effective load transfer [214]. On the other hand, the improvements of hardness in nanocomposites are possibly due to the mismatch of thermal expansion coefficient [215] between graphene and metal matrix as well as the restriction or obstruction of graphene in plastic deformation [216]. Besides, the formation of metal carbide due to the chemical reaction between graphene and metal during synthesis contributes to the strengthening effectiveness. Al carbide ( $Al_4C_3$ ) has been observed in Al/graphene nanocomposite synthesis using hot extrusion [210]. However, its role in terms of improvement of hardness has been still controversial whether it leads to the reduction of strength, hardness [210] or enhancement of bonding strength, load transfer [217]. The interfacial reaction can be improved by the formation of carbide because it decreases the contact angle of liquid alloy hence increase the wetting [218]. Furthermore,

using metal powder through ball milling and sintering processes at a high temperature can cause oxidation or the formation of metal oxide. Song et al. [219] reported that the hardness of Cu/ graphene nanocomposite was improved due to the presence of Cu<sub>2</sub>O during the synthesis but it was reduced when increasing graphene loading. Similarly, Lin et al. [218] indicated that the formation of Fe<sub>3</sub>C after sintering decreased the contact angle between liquid-alloy and GO, hence increasing GO wettability (Figure 2.20).

In case no carbide is formed, the interfacial bonding of metal-graphene strongly depends on matrix nature (contact angle and cohesive energy of liquid-metal and filler) that has been addressed in the case of Mg matrix [220]. Hwang et al. [221] have confirmed the compatibility between Mg and graphene with their high adhesion energy. Also, pre-coating metals such as Ni on graphene surfaces have shown similar effects on improving the wettability of fillers in the Cu matrix [222] as compared to CNT cases [223]. Xu and Buehler [224] have pointed out that Ni-graphene has higher cohesive energy and interfacial strength than Cu-graphene.

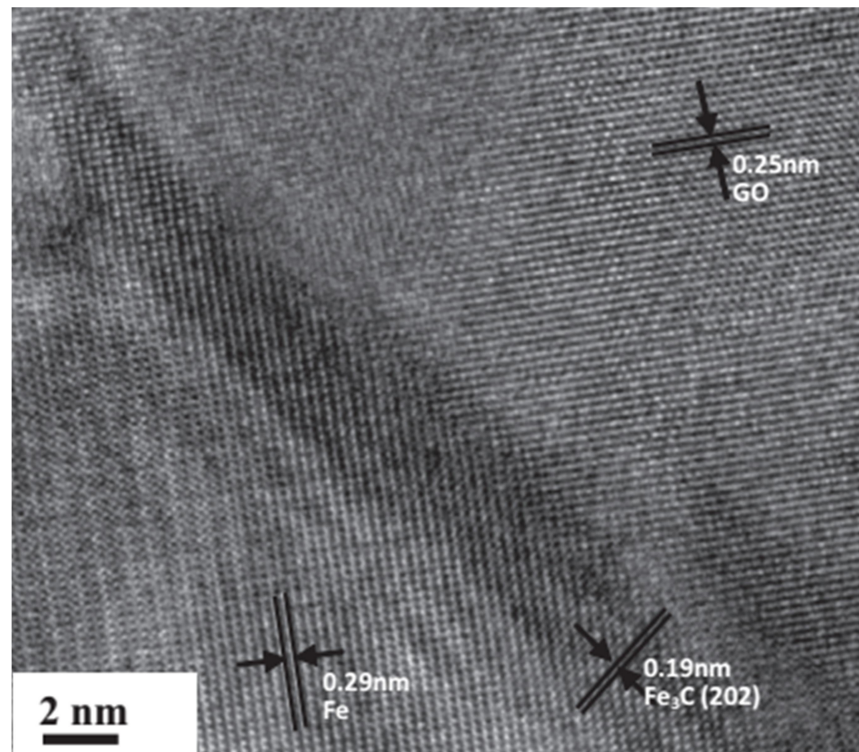


Figure 2.20: The formation of carbide when fabricating metal/GO (2 wt.%) nanocomposites [218]

The improvements of mechanical properties of metal/graphene nanocomposites have shown their dependences on the integrity of graphene [211], graphene exfoliation [225] and distribution [212], interfacial bonding [211], prevention of metal dislocation [226] beside the aforementioned roles of intermetallic formation due to sintering process (Table 2.5). These formations of metal carbide, metal oxide through the synthesis might contribute to these improvements but cannot be evaluated whether they have positive or negative effects on mechanical properties of graphene reinforced metal nanocomposites.

Table 2.5: Mechanical properties of graphene reinforced metal matrix nanocomposites

Material	$\sigma_u$ (MPa)	E (GPa)	Hardness (GPa)	Reasons	Fabricating methods
Al/RGO 0.3wt.% [211]	--	90.1 (18%)	1.59 (17%)	High quality and uniformly dispersed RGO, strong bonding of Al-RGO	Compacting and hot pressing
Al-Mg-Cu/Gr 0.3wt.% [227]	454 (25%)	72 (-1%)	--	Evenly distributed of Gr, good interfacial bonding, Gr structure retention	Ball milling, hot isostatic pressing (HIP) and extruding
Al/GO 15 mg ml <sup>-1</sup> [228]	192 (-7%)	--	--	Dynamic recrystallization of matrix phase due to shear deformation, heat from FSP and grain refinement	Friction stirring processing (FSP)
Al/GNS 1 wt.% [229]	248 (68.7%)	--	--	Homogenous distribution of GNFs, no metallurgical at interfaces of Al-GNF	Blending, cryo-milling, degassing and hot extrusion
Cu/FLG 3 wt.% [230]	--	--	0.46 (39%)	Disruption of graphene layers, Gr partly hinder grain growth	Rolling
Cu/RGO 2.5 vol.% [221]	335 (30%)	131 (30%)	--	Strong interfacial bonding of Cu-RGO	Compacting and SPS
Cu/GO 0.5 gL <sup>-1</sup> [231]	--	137 (30%)	2.5 (96%)	Uniform distribution of Gr, grain size refinement	Pulse reverse electrodeposition
Cu/(Ni)GPL 0.8 vol.% [232]	245 (42%)	--	--	Good dispersion of GPL and strong interfacial bonding Cu-GPL (Ni), covalent interaction of Ni-GPL	Solution, sonication, SPS
Cu/GNP 1.3 wt.% [233]	485 (107%)	104 (21%)	--	Homogenous dispersion of GNPs due to pre-coating of Cu on GNPs	Electroless plating, SPS tensile
Cu/RGO 0.3 wt.% [234]	308 (41%)	109 (12%)	--	Less structural damage on RGO, randomly oriented of RGO benefit the load transfer of nanocomposite	Hot pressing
Ni/GO 0.12wt.% [213]	--	252.76 (51.6%)	6.85 (278.4%)	Compact interfacial bonding of Ni-GO, homogenous dispersion of GO	Electrodeposition
Ni/Gr 0.05 gL <sup>-1</sup> [226]	--	240 (70%)	4.6 (20%)	High interaction of Ni-Gr, Gr preventing Ni dislocation	Electrochemical deposition
Mg/Ti/GNP 0.18wt.% [225]	230 (8.5%)	--	--	High specific area and adhesion of Gr	Semi powder metallurgy
Mg/GNP 0.3 wt.% [212]	246 (32.2%)	13.84 (131%)	55HV (34%)	The high specific surface area of GNPs, uniform dispersion	Compaction, sintering, extruding

(GNF: graphene nanoflake; GPL: graphene platelet)

### **2.3.3 Ceramic-based nanocomposites**

In this section, the other nano-filler based nanocomposites will be reviewed in terms of their mechanical properties. There were many types of nano-fillers instead of CNTs and graphene that make the discussion in detail for all of them not feasible within the scope of this review section. Therefore, some common nano-filler based nanocomposites will be taken into consideration including polymer/nano-clay, polymer/ceramic and metal/ceramic nanocomposites. These selections are also based on the effective reinforcements of nano-fillers with their corresponding matrices as well as their important applications as engineering materials.

Besides of CNTs and graphene, nano-clay and ceramic nanoparticles have also been applied as reinforcement in polymer materials due to their advanced tensile properties. Nanoclays are potential candidates for nanocomposite reinforcements, especially in terms of mechanical properties. The most common type of nanoclays that has been applied in reinforcing nanocomposites is montmorillonite (MMT). It is derived from absorbent aluminium phyllosilicate clay called "bentonite" and thus named "organoclays". MMT has been applied for reinforcing polymers due to their high aspect ratio and unique intercalation/exfoliation natures [235]. The incorporation of organoclays into polymer matrices has exhibited superior strength and modulus [236]. The most applied polymers by nanoclay reinforcements are polystyrene [237], epoxy resin [238], poly(methyl methacrylate) [239], poly( $\epsilon$ -caprolactone) [240], PP [241], PU [242], PI [243]. However, nanoclays mostly require pre-exfoliation to attain homogenous distribution due to higher specific area and hence higher effectiveness of load transfer could be achieved [244]. In general, the effectiveness of nanoclay reinforcements have been indicated strongly depend on intercalation methods [245], exfoliation nanoclays [246], the integrity of nanoclays [247] or matrices [248], and most importantly, the level of distribution of nanoclays [249] or interaction of polymer-nanoclays [250]. However, the addition of nanoclays in polymer exhibited some negative effects on the tensile strength of nanocomposites in some cases but no explanation was given [249].

On the other hands, silica nanoparticles are also common nano-fillers that have been applied to reinforce polymers due to their high mechanical properties. The processing

methods to fabricate these materials are similar to other polymer-based nanocomposites such as melt mixing for PP [251], PE [252], Polyethylene naphthalate (PEN) [253], Polyethylene terephthalate (PET) [254], solution mixing for epoxy [255], poly(4-methyl-2-pentyne) (PMP) [256], or sol-gel processing for epoxy [257]. In general, the additions of nano-silica in polymer matrices lead to the improvements of stiffness mostly due to the homogenous distribution, high aspect ratio and stiffness of silica nanoparticles. However, it could be seen that their effectiveness of stiffness improvement is not high as CNTs, graphene or nano-clays (Table 2.6).

Table 2.6: Mechanical properties of ceramic nano-fillers reinforced polymer matrix nanocomposites

Material	$\sigma_u$ (MPa)	E (GPa)	Reasons	Fabricating methods
PP/MMT 15 wt.% [258]	38 (13%)	3.36 (100%)	Well-dispersed MMTs	Melt mixing, injection moulding
PP/MMT 10 wt.% [245]	41.6 (38.7%)	--	The intercalation of MMT layers in the matrix due to the presence of MAPP compatibilization	Melt mixing, injection moulding
PP/MMT 2 wt.% [247]	32 (18%)	0.9 (82%)	The persistence of silicate layers, modification of PP structure, partially immobilized polymer segments	Melt mixing
PA6/MMT 7.2 wt.% [248]	--	5.7 (107%)	High molecular weight and integrity of the matrix	Melt mixing
SPU/30B 7 wt.% [249]	21 (-53.3%)	0.024 (220%)	Well-dispersed and delaminated of Cloisite 30B, good interaction of PU-clay, preferable solution mixing due to PU and surfactant degradations from melt mixing, improvements of the stiffness of SPU due to higher fraction of soft segment	Solution mixing Melt mixing
SPU/30B 7 wt.% [249]	7 (-66.7%)	0.0193 (168%)		
HPU/30B 7 wt.% [249]	15 (-66%)	0.119 (95%)		
EVA/ Cloisite Na 3 wt.% [250]	25.9 (-8.8%)	0.0135 (10.7%)	The dominant effect of exfoliation on tensile properties of nanocomposites, high interaction between EVA and Cloisite 30B	Melt mixing, compression moulding
EVA/ Cloisite 20A 3 wt.% [250]	25.8 (-9.2%)	0.0249 (104.1%)		
Epoxy/SMC 2 wt.% [259]	57 (25%)	3.3 (10%)	Homogenous distribution and high exfoliation of SMCs	Solution mixing
Epoxy/SiO <sub>2</sub> 3.72 vol.% [255]	--	3.96 (12%)	Less agglomeration, well dispersed and high aspect ratio of Silica at low loadings	Solution mixing
Epoxy/SiO <sub>2</sub> 4 wt.% [260]	42.3 (30.57%)	--	The optimal interaction of EP-SiO <sub>2</sub> at 4 wt.%	Solution mixing
Epoxy/SiO <sub>2</sub> 13.4 vol.% [257]	--	3.85 (30%)	High modulus, well dispersion and no agglomeration of Silica	Sol-gel mixing
Epoxy/SiO <sub>2</sub> 20 wt.% [261]	--	3.97 (26.4%)	The high stiffness of silica	Solution mixing
EP/SiO <sub>2</sub> 20.2 wt.% [262]	--	3.85 (30%)	Well-dispersed silica	Solution mixing

(SMC: Silane-modified clay; SPU: Soft polyurethane; HPU: Hard polyurethane; PA6: Polyamide6/Nylon6)



In the case of ceramic reinforced MMNCs, the main challenge is the incorporation of ceramic nanoparticles into molten metal matrices due to their poor wettability. Besides high wetting could be seen in some metal/ceramic systems with strong (chemical) reactions and low contact angles ( $\theta$ ) such as Cu/WC ( $\theta = 200$ ) or Au/ZrB<sub>2</sub> ( $\theta = 250$ ), most of the other ceramic nano-fillers generate non-covalent (physical) bonds with liquid metals with low wettability such as Ag/Al<sub>2</sub>O<sub>3</sub>, Cu/SiO<sub>2</sub> ( $\theta = 120^\circ$ – $140^\circ$ ); Au/BN( $\theta = 135^\circ$ – $150^\circ$ ) at high temperature [263]. The inhomogeneous distribution of ceramic nano-particles and their agglomerations within the metal matrix have been indicated resulting from their low wettability associated with high specific surface areas. Some dispersion routes have been employed to overcome these obstacles including ex-situ and in-situ techniques [264]. The basic difference between these two methods is whether the reinforcements (ceramic nano-particles) are fabricated within the matrices (in-situ) [265] or separately synthesized outside by CVD [266], spray conversion process [267] or laser-induced gas-phase reaction [268] and then subsequently incorporated into metal matrices via PM [269] or mechanical alloying (MA) [270]. Although the traditional PM method has been successfully applied to synthesis metal/ceramic nanocomposites, especially in aluminium-based matrices, it still exhibited obvious agglomerations of ceramic nano-particles and hence their inhomogeneous distribution [271] (Figure 2.21).

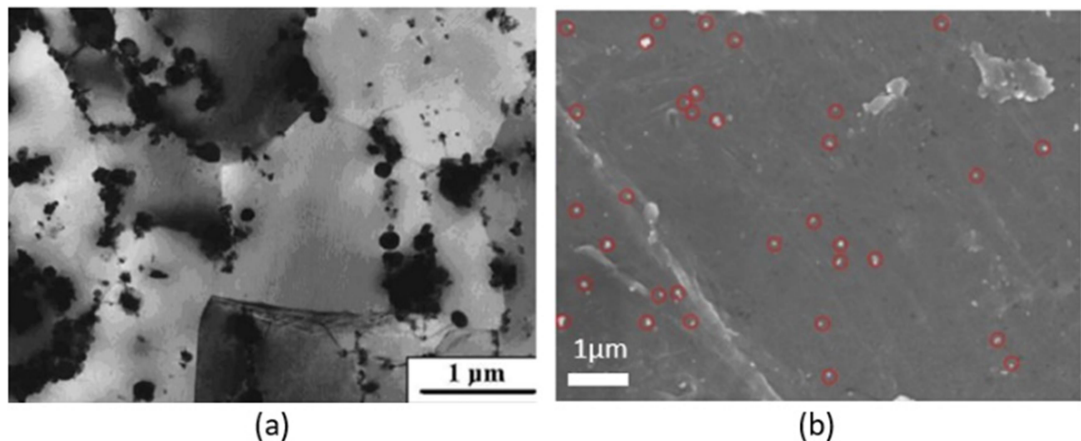


Figure 2.21: The agglomerations of ceramic nano-particles in Al matrices: (a) Al/Al<sub>2</sub>O<sub>3</sub> 4 vol.% [272] and (b) Al/SiC 3 wt.% [271]

The low wettability of as-produced ceramic nanoparticles, as well as their high specific surface area, have indicated the main reasons for this drawback. It could be improved by employing MA methods with better dispersion of ceramic nano-fillers with significant grain size reduction [273]. Also, the densification of MA is mainly conducted by hot pressing, HIP or extrusion. On the other hand, the In-situ route has been claimed more suitable than the aforementioned methods in terms of generating the homogenous distribution of ceramic nano-particles such as  $\text{Al}_3\text{Ti}$  [274] or  $\text{TiC}$  [275] at high loadings (50 vol.% and 18 vol.%, respectively) and subsequent ultrafine microstructures.

In general, the additions of ceramic nanoparticles lead to the improvements of tensile strength, yield strength and hardness associated with the sacrifice of ductility. All these changes in tensile properties follow strengthening mechanisms including Orowan strengthening, mismatch of thermal expansion coefficients between matrix and filler (CTE) and grain size refinement. Besides, the reductions of ductility have been claimed due to the presence of porosities within the system or brittle nano-fillers [271] although some improvements of ductility could be seen when using Mg-based matrices [276] without sufficient explanation. The role of ceramic nano-fillers in hindering the matrix dislocations and the effect of grain size reduction have discussed in most relevant research that was the main reason for hardness increments [271]. Table 2.7 summarises the mechanical properties of some common ceramic nanoparticles reinforced MMNCs with their corresponding fabricating methods and discussion.

Table 2.7: Mechanical properties of ceramic nano-particle reinforced metal matrix nanocomposites

Material	Hardness (GPa)	Tensile strength (MPa)	Reasons	Fabricating methods
Al/SiC 3 wt.% [271]	0.55 (39.5%)	164.4 (29.3%)	Homogenous distribution of SiC, Orowan strengthening, grain size refinement, the thermal mismatch between Al and SiC. Porosities lead to a reduction of ductility. SiC hindered metal matrix dislocation (increasing hardness)	PM, ultrasound-assisted stirring and planetary agitation, hot compressing
Al/SiC 6.5 vol.% [273]	--	807 (26.5%)	Homogenous dispersed SiC, grain size refinement, Orowan strengthening	Mechanical alloying, cryo-milling, HIP consolidation
Al/SiC 1.25 vol.% [277]	-- (69%)	-- (109%)	Homogenous distribution of SiC and CTE strengthening at low loading, residual stresses, high dislocation density and grain size reduction, agglomeration and porosity at a high loading of SiC. Hard particles reduced ductility.	Mechanical alloying, ultra-sonication
Al/SiC 2 wt.% [278]	--	301 (12%)	Uniformly dispersed SiC, CTE, high dislocation density, restriction of dislocations	Mechanical alloying, ultra-sonication
Al/Al <sub>2</sub> O <sub>3</sub> 4 vol.% [272]	66.6 (109.5%)	245.5 (67%)	Evenly distributed Al <sub>2</sub> O <sub>3</sub> , Orowan strengthening and grain size refinement effects	PM, wet mixing, cold isotropic pressing and sintering
Al alloy/SiC 10 wt.% [279]	87.2 BHN (9%)	265 (12.3%)	Density reduction, SiC hindered alloy dislocations, uniform distribution of SiC and their high wettability due to Mg coating	Stir casting
Al alloy/SiC 10 wt.% [280]	78 BHN (28%)	188 (0.53%)	Non-homogenous distribution of SiC due to improper stirring led to the low improvement of tensile strength, hard SiC hindered dislocations that contributed to hardness improvement	PM, mechanical mixing
Al alloy/SiC 6 wt.% [281]	116 BHN (62%)	267 (29%)	SiC possessed advanced hardness, the strong interface of Al alloy - SiC	Liquid metallurgy
Mg alloy/SiC 1.5 wt.% [276]	--	199.3 (90%)	Grain size refinement, the strong bond of Mg/Zn-SiC, SiC clusters, no reason for ductility improvement	MA, ultrasonic cavitation
Mg/SiC 3 vol.% [282]	0.58 (180%)	288 (21.5%)	Grain size refinement, dispersion hardening, strain hardening due to extrusion, dislocation hindering	PM, ball milling
Mg/SiC 1.84 wt.% [283]	0.42 (10%)	203 (18%)	The high constraint of matrix deformation that improved hardness, dislocation density, internal stresses formation due to thermal expansion mismatch, Orowan strengthening and the mismatch of elastic reinforcing phase - plastic matrix phase, SiC-Mg interfacial integrity led to ductility improvement	MA, pressing, microwave hot sintering
Mg/SiO <sub>2</sub> 10 vol.% [284]	1.03 (75%)	251 (32%)	Uniform distribution of SiO <sub>2</sub> , grain size refinement, Mg <sub>2</sub> Si, MgO formations during FSP	FSP
Al/TiC 10 wt.% [275]	44.17 HV5 (143.6%)	--	Strong TiC particles, grain size refinement	In situ

## 2.4 Micromachining of nanocomposites

### 2.4.1 Overview of micromachining

The motivation of product miniaturisation with high precision is to make multifunctional products with lightweight, high mobility, less energy consumption and higher efficiency. Along with the discovery of advanced materials (i.e., super alloys, composites, ceramics, etc.) with outstanding ratios of strength to weight, the development of advanced machining techniques with ultra-high precision makes the miniaturisation of components feasible [285]. Taniguchi [286] has modified machining advancement by the achievement of machining accuracy from conventional machining (1 to 100  $\mu\text{m}$ ) to ultra-precision machining (1 nm) (Figure 2.22). In other perspectives, micromachining has been defined by its product dimensions (at least two dimensions ranging from 1 to 500  $\mu\text{m}$ ) that are extremely small to be fabricated by conventional machining [287]. The difference between precision machining and micromachining is identified by their objectives. While precision machining highlights the machining accuracy with the ratio of size to tolerance higher than 10,000:1, micromachining intends to make micro-parts that are typically in the range of 1 to 100  $\mu\text{m}$  [288].

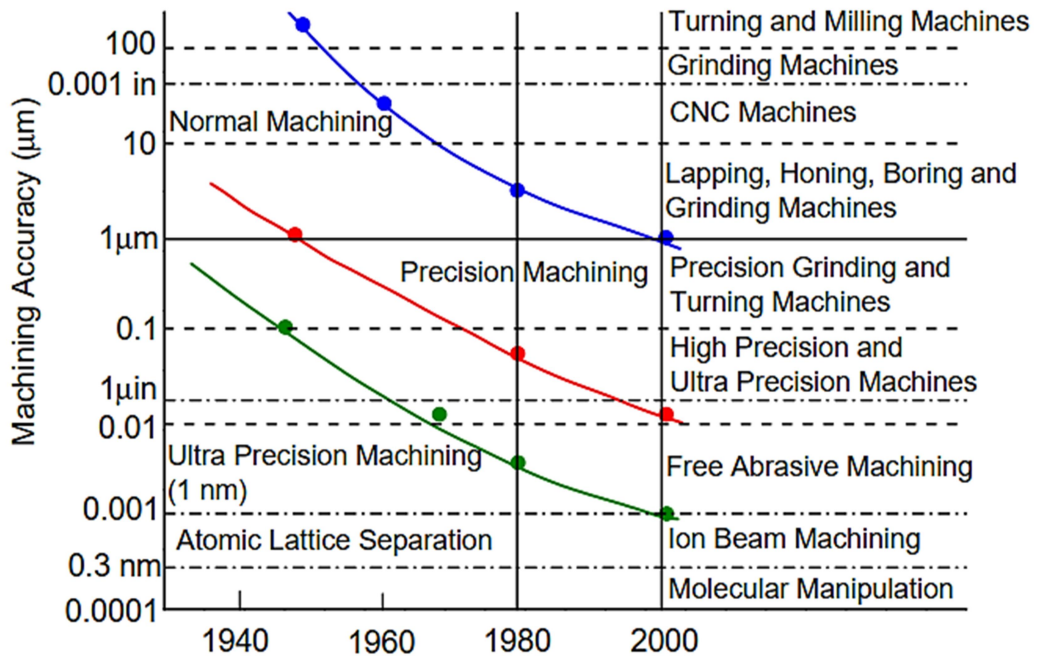


Figure 2.22: The development of achievable machining accuracy (reproduced from [286])

Micromachining is also defined by the uncut chip thickness (UCT) measurement when it becomes smaller than the mean value of grain size [289] or in the range of 0.1 to 200  $\mu\text{m}$  [290]. However, with the continuous development of machining, this border would be narrowed.

There are many micro-machining techniques with their capabilities in terms of machining accuracy, part size, workpiece material and geometrical complexity. Classification in an attempt to identify the distinct principles between some basic micromachining process, generally based on whether micro-electromechanical systems (MEMS) or non-MEMS mechanism. MEMS are manufactured by micromachining processes which use lithography-based techniques to make the near net shape in semiconductors such as sensors, transducers, actuator, and other electrical devices on a silicon substrate. MEMS-based techniques are usually employed to fabricate the products in sizes ranging from 1 to 100  $\mu\text{m}$ . The remarkable advantages of these kinds of micro-manufacturing are the high accuracy of machined products without burr formation on the machined edges, low cost and feasible mass-producing applications due to their short processing time.

However, their applications are limited by workpiece material, mostly silicon, a small range of metals and ceramics because of high requirements of materials for MEMS such as deposition ability in thin films, high definition and reproduction. Additionally, the geometrical complexity of micro-components is also a considerable disadvantage of MEMS-based micromachining whilst they can only be effectively managed with 2D or 2.5D machined subjects. Micromechanical machining, on the other hand, is a miniaturized version of conventional machining that employs a geometrical micro cutting tool to remove material. Although MEMS can achieve smaller feature size, this adaption in micro-fabrication has high potential in terms of machining accuracy, surface quality, a wide range of workpiece materials, and high complex geometry of products (3D). Moreover, the gap between macro and micro mechanical machining is also bridged while studying this approach [291] by discussing the size effect issue.

### 2.4.2 Size effect in micromachining

Although micromachining has the same principle as conventional machining in terms of material removal mechanism, there are, however, some critical differences due to size effects when adapting from macro to micro-scale machining. Size effects make the relationship between inputs (micromachining parameters) and outputs (surface quality, chip formation, cutting forces, tool wear) distinct from conventional machining. Therefore, it could be seen that size effects are the key issues as well as the basis to explain the unusual aspects that micromachining processes have achieved [292]. Size effects are the results of extrapolated-value aberration from macro to micromachining. These effects are expressed by the dramatic, nonlinear increase of specific cutting energy when the UCT ( $h$ ) decreases [293]. Experimental results to support this phenomenon have been achieved when metal and alloys were cut taking into consideration the ratio between UCT to cutting edge radius [294]. The specific cutting forces ( $k_c$ ) in micromilling are hyper-proportionally increased when micromilling at a feed rate ( $f$ ) value lower than tool edge radius ( $r$ ) [294], especially when reaching grinding levels ( $f/r=0.1$ ), the specific cutting force could achieve maximum value of 70 GPa (Figure 2.23).

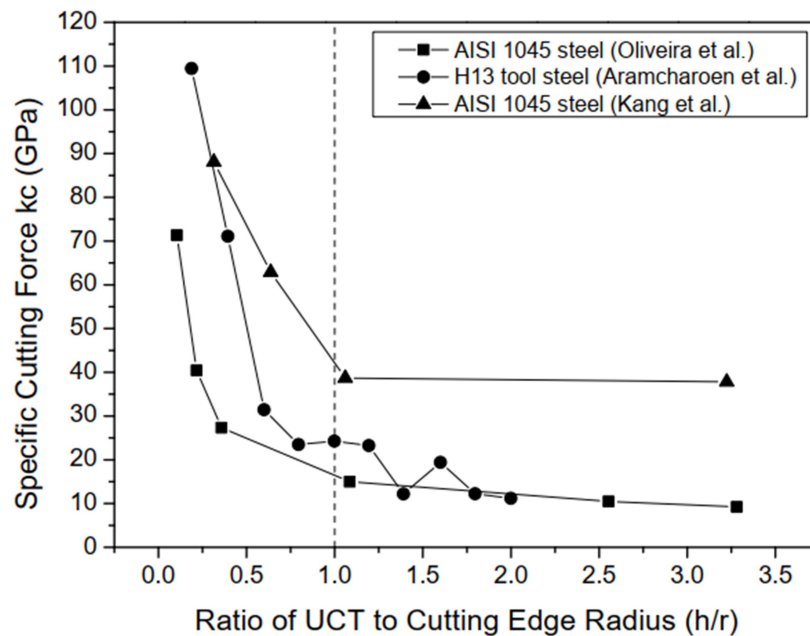


Figure 2.23: Size effects in micromilling metals and alloys (reproduced from [294-296])

In general, size effects in micromachining are related to different aspects that are usually neglected in conventional machining including:

- A dramatic non-linear increase of specific cutting force when the UCT adapts the cutting edge radius.
- A consideration of the microstructure effect on the machining process when cutting parameters (depth of cut, feed rate) adapt grain size or strengthening effects.
- A critical threshold so-called MUCT sets the lowest limit for feasible cutting operation and decides the state of the cutting mechanism (shearing, sliding or ploughing).
- A complex analysis of cutting force and surface roughness due to high spindle speeds, tool deflection/chatter and run-out [297].
- Different design of the micro-tool to ensure rigidity and stability, high tool wear and tool failure possibility when miniatures tool parameters.
- Finally, the combination of those factors makes a comprehensive explanation for the differences in terms of surface generation between macro-machining and micromachining.

Based on that the above, those aspects will be expressed in more detail in section 2.4.3. However, the influences of size effects on micromachining have been still unobvious and need more experimental investigation to support [298]. The most specific exhibition of size effect is the higher specific cutting energy in micromachining compared to macro-machining (Figure 2.24).

#### **2.4.2.1 Microstructure effect**

In macro-machining, when the material volume or the removal rate of the material for one route is relatively high, the material structure, in that case, is considered homogenous and isotropic. Although, it still has a certain tolerance in this assumption but could be acceptable due to the high ratio between tool edge radius and grain size. On the other hand, when micromachining using micro-tools, the tool edge radius approaches the grain size, homogenous and isotropic assumptions are no longer valid.

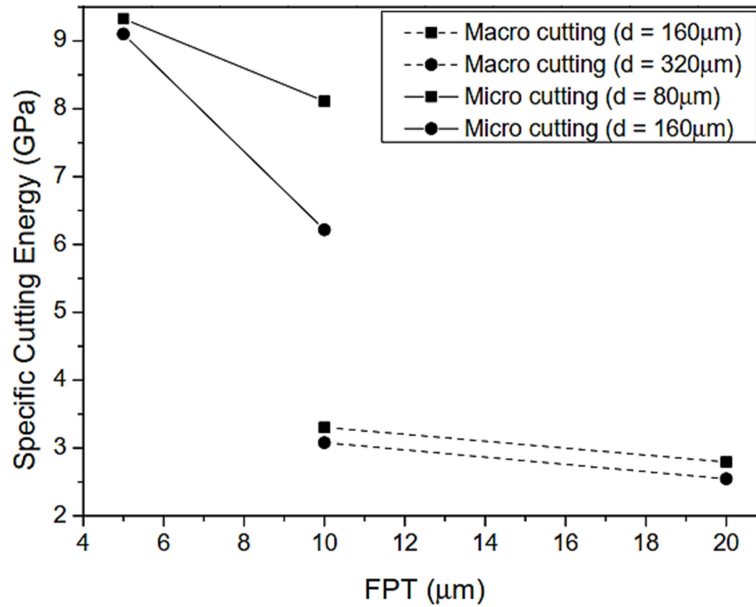


Figure 2.24: Size effect on specific cutting energy in micromilling as compared to macro-machining [294]

Workpiece material structure is now considered as an assemblage of distinct grains with random distribution within the material system or anisotropic characteristic. Therefore, in this case, the cutting mechanism takes place by breaking each individual grain that requires more specific cutting energies or forces and mean flow stress due to atom bonds [299] (Figure 2.25).

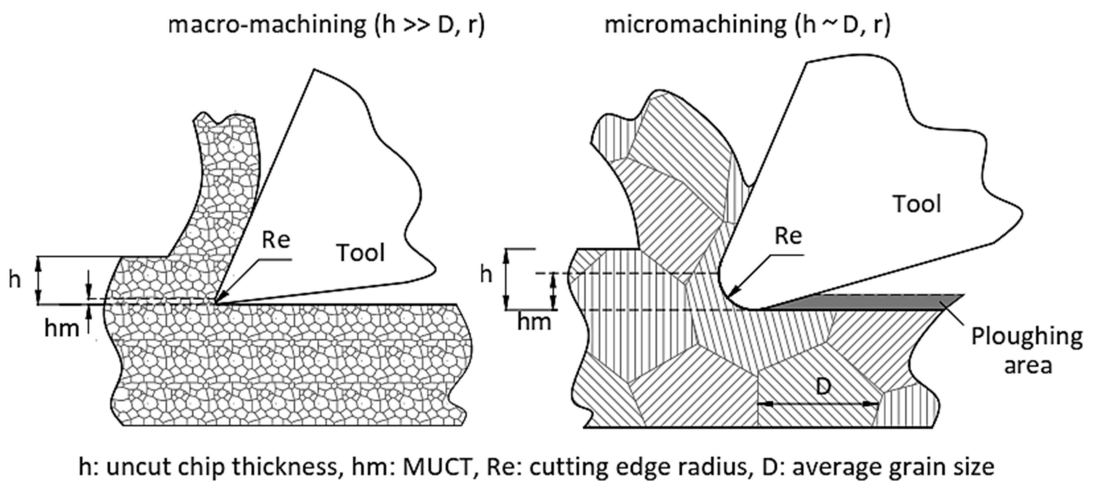


Figure 2.25: The schematic representing the differences between macro and micromachining in terms of microstructure ( adapted from [300])



The effect of microstructure in micromachining exhibited in the case of multi-phase material. Vogler et al. [301] have studied a mechanistic force modelling that using microstructure mapping for the micro-end milling multi-phase ductile iron. It is observed that more than 35% cutting energy increase due to microstructural effects when micro-end-milling multiphase ductile iron and higher frequency of cutting forces in comparison with macro-machining. The cutting forces, as well as other cutting conditions, vary when the cutting tool moves along two adjacent grains that have different mechanical properties. A ‘two-grain model’ has been used to study the grain boundary influences on cutting forces [302] or surface generation [303]. Additionally, elastic recovery in micromachining is also an important factor of microstructure effects [304]. Furukawa and Moronuki [305] gave some experimental results to support the grain boundary effect on cutting force variation in single-phase and multiple-phase as well as in brittle and ductile materials (pure copper, aluminium alloy, PMMA, CaF<sub>2</sub>, and germanium). Mian et al. [306] have conducted a comparative study when micromilling single-phase material (AISI 1005 steel) and multi-phase material (AISI 1045 steel). They claimed that the surface quality after micromilling AISI 1005 was better than AISI 1045 due to the minimisation of the differential elastic recovery in single-phase material (Figure 2.26).

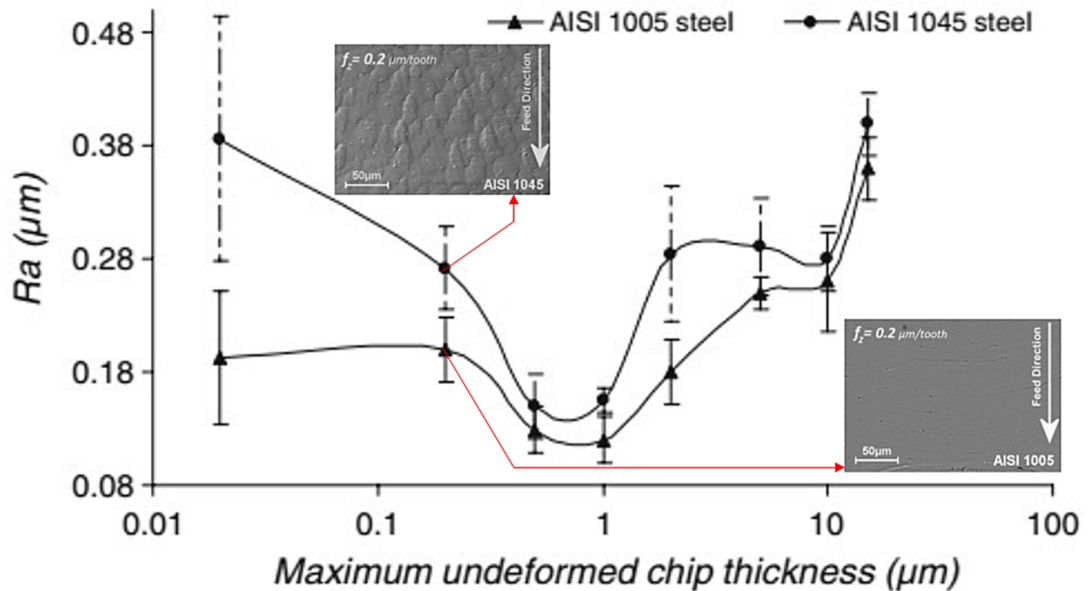


Figure 2.26: Effect of microstructure on surface quality when micromilling steel [306]

Micromachining of multi-phase materials also leads to the unbalance of plastic strain that contributes to low surface quality and high cutting force variation [307]. The burr formation at the grain boundary areas also leads to higher surface roughness when micromachining multi-phase material. This burr formation is due to chip formation interrupting when tool adapts the grain boundary [308]. Nevertheless, in general, the chip loads is recommended to be ten times higher than the grain size to obtain high surface quality [305].

Furthermore, it could be seen that a homogenous and isotropic material is considered the ideal condition for achieving high surface quality. This grain size effect has been indicated by Uhlmann et al. [309] when high machined surface, as well as hardness, could be positively affected by the high levels of material homogeneous property (Figure 2.27).

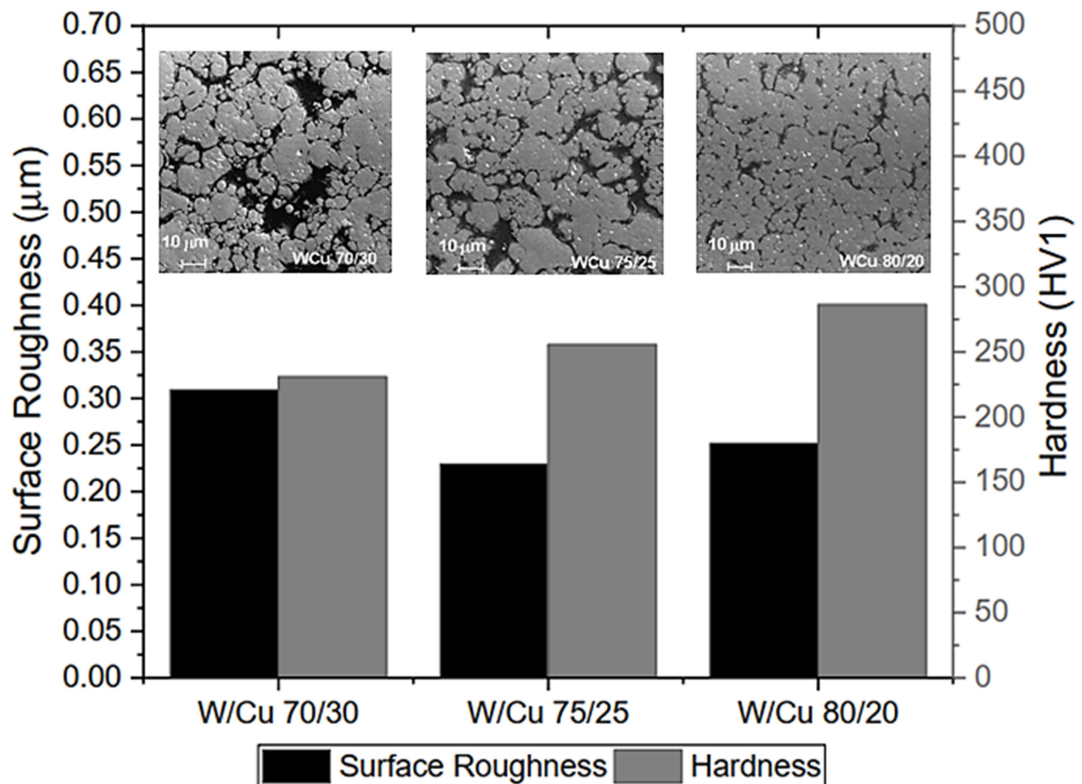


Figure 2.27: Grain size effect on surface roughness and hardness when micromachining W/Cu composite (reproduced from [309])

However, the surface roughness when micromilling W/Cu 80/20 was still higher than W/Cu 75/25 that had a lower level of homogeneity. Popov et al. [310] have indicated that a remarkable improvement of surface quality can be feasible through the refinement of grain size to make higher homogeneity and isotropy and the grain size, in the case of micromilling aluminium alloy, have a significant influence on surface roughness. In details, with the decrease of the anisotropy and grain size of workpiece material from 100-200 $\mu\text{m}$  into 0.6 $\mu\text{m}$ , the surface roughness decreased more than three times compared to non-refinement material. They also suggested the optimal cutting condition with narrow grain distribution associated with certain cutting direction could achieve the highest quality of machined surface, but due to the limit of certain refinement process, this was still a target for further research.

Lauro et al. [311] in the similar adaption, indicated that with the small grain size (39.9 $\mu\text{m}$ ), the variation of surface roughness will be reduced to 2% compared to larger grain size (51.1% when using grain size of 497 $\mu\text{m}$ ). A similar explanation about the heterogeneous microstructure effect of multiphase material on surface roughness has been given by Weule et al. [304]. Therefore, it could be seen that reduce grain size tends to improve the machined surface quality and its role seems to be dominant in micromachining. Furthermore, the microstructure effect also exhibited by changing cutting directions and/or crystal orientation due to the anisotropic structure of materials when micromachining. Komanduri et al. [312] used an MD model to study cutting forces variation when specifically combining crystal orientation and cutting directions. To et al. [313] identified the higher surface quality can be achieved when micro-cutting single-crystal aluminium along (100) plane than (110) and (111) planes but Zhou and Ngoi [314] have claimed that the dominant factor was not cutting direction but the plastic behaviour of single crystal. However, Moriwaki et al. [315] neglected the effect of crystallographic orientation when micromachining polycrystalline copper. They claimed that surface quality degradation is caused by the formation of the amorphous damaged layer due to the ploughing effect when the UCT is at 0.1  $\mu\text{m}$ . In general, the microstructure effects on the micro-machinability are indicated by the inhomogeneity (grain size effect), anisotropic (different cutting directions) and structure (different phases) that lead to the variation of surface roughness, cutting forces and burr formations.

### 2.4.2.2 Minimum uncut chip thickness and cutting edge radius

The chip removal mechanism is among the principal differences between micro and conventional machining due to size effects. The contact between the cutting tool clearance face and workpiece surface is usually ignored and the tool edge is considered sharp in the case of macro-machining. It could be explained by the high ratio of the MUCT to the cutting edge radius. When down-scaling into the micro-cutting mechanism, they become comparable to the tool edge radius and hence change the chip formation mechanism.

In micromachining, the MUCT could range from submicron to a few microns and the depth of cut and feed rate varies from a few microns to maybe 100 $\mu\text{m}$ , hence the cutting edge radius and the grain size become comparable [316]. In that case, tool edge radius becomes a dominant factor as well as feed rate that affect the surface roughness. Moreover, the surface roughness tends to increase with the feed rate decrease exceeds a lower minimum chip thickness [308] (Figure 2.28). That means MUCT has an inverse effect on surface roughness in the case of micro-machining. A decrease of UCT below the magnitude of edge radius (10-60 nm) leads to a significant increase of surface roughness for various levels of cutting speeds (10 and 150 m/min) [317].

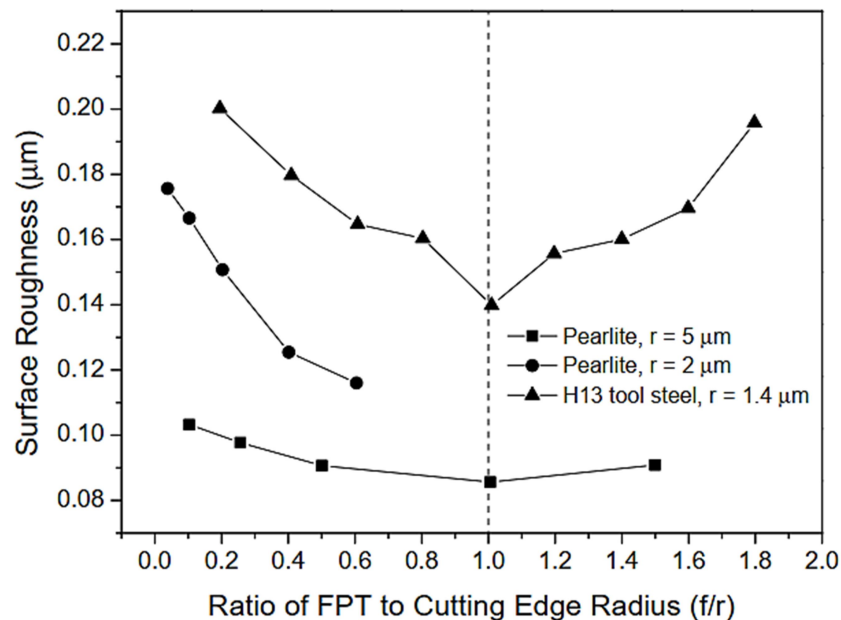
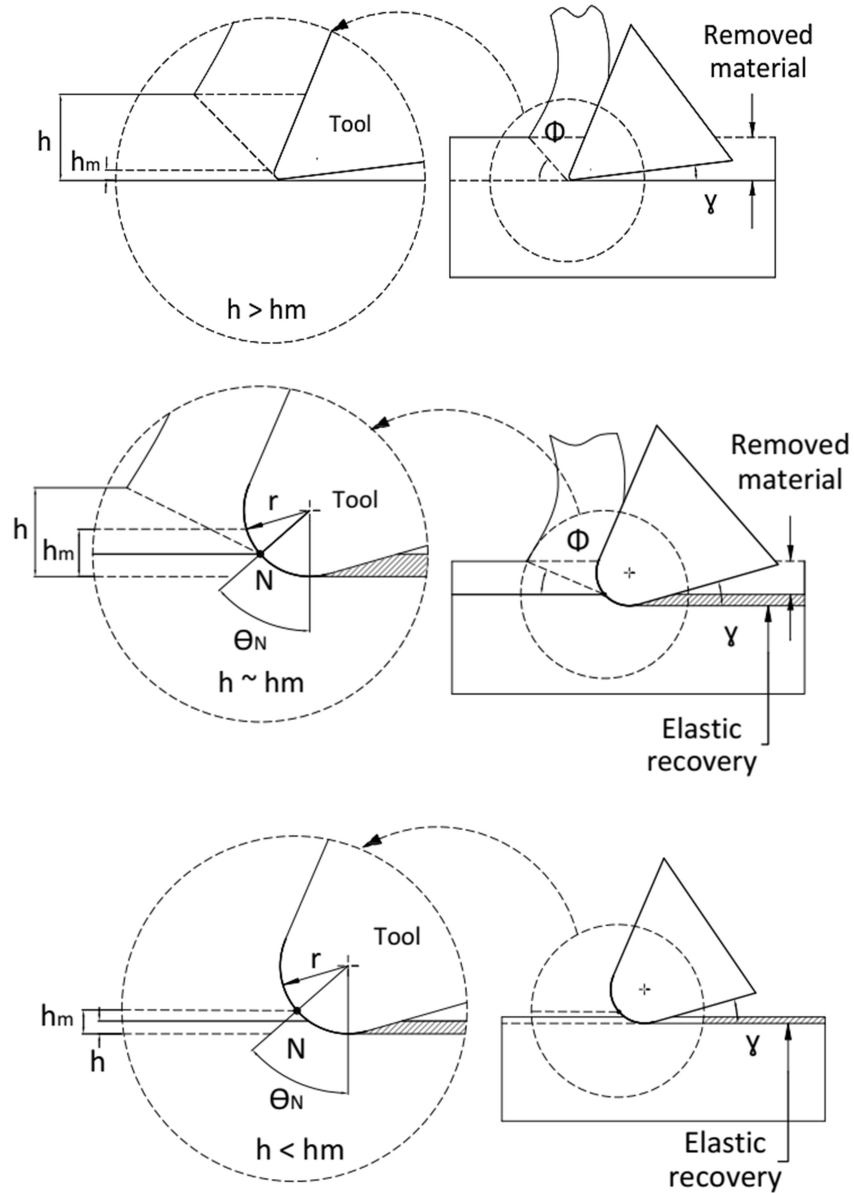


Figure 2.28: Tool edge radius and feed-rate effects on surface roughness in micromilling (reproduced from [296] [308])

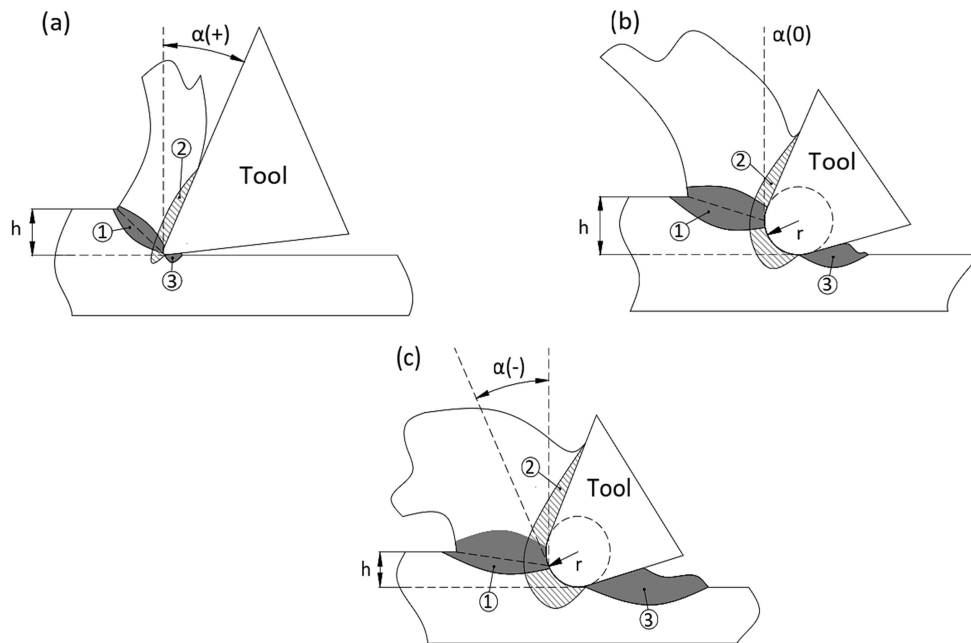
In micromachining, shear stress increases around the cutting edge instead of along the shear plane [299], and the workpiece is ploughed rather than being sheared [318] when cutting depth and feed-rate below a threshold so-called ‘minimum uncut chip thickness’. It was defined as a lower limit of minimum under form chip thickness that can be feasible to be removed [319] (Figure 2.29).



$\phi$ : shearing angle;  $\gamma$ : clearance angle;  $\theta_N$ : neutral angle;  $h$ : UCT;  $h_m$ : MUCT;  $r$ : cutting edge radius;  $N$ : neutral point

Figure 2.29: MUCT effects on the cutting mechanism in micromachining (adapted from [320])

The negative effect of UCT on surface roughness is also related to the plastic deformation of materials during the machining process. The surface quality is reduced when decreasing the ratio of UCT/edge radius due to the plastic accumulation of workpiece material on the tool surface [321] and the adhesive workpiece material on the machined surface [322] caused by material strengthening. Furthermore, the shear angle decreases along with the MUCT leading to deformation areas expanded and hence increasing the mean friction that negatively affects the surface quality. Furthermore, elastic deformation of materials in micromachining is also negatively affected the surface quality. When the cutting depth adapts to the tool edge radius magnitude, the effective rake angle of the micro-cutting tool transforms from positive to zero or even negative. This transformation makes the cutting more stable but also leads to some negative effects, such as more elastic deformation due to shear zone expanding, higher stress, strain, cutting forces, and energy consumption. It also leads to a high ratio of ploughing/shearing in the cutting mechanism, making the cutting mechanism becomes less efficient (Figure 2.30).



$\alpha$ : effective rake angle;  $r$ : cutting edge radius;  $h$ : UCT; 1: plastic deformation in the shear zone; 2: plastic deformation along tool rake face; 3: Elastic recovery

Figure 2.30: Effects of MUCT on the shear angle of materials in micromachining: (a) positive effective rake angle; (b) zero effective rake angle; (c) negative effective rake angle (adapted from [323])

Therefore, the identification of MUCT in micromachining is significantly important to attain an optimal machining process. L'vov [320] considered the influence of MUCT as a function of the tool edge radius and recommended that the depth of cut should be above 29.3% of the tool edge radius to avoid ploughing and elastic deformation when micro-cutting 1045 steel. Other researchers identified the minimum chip thickness by studying the cutting mechanism along with various feed rate levels in micromilling 360 brass, and the minimum chip thickness is approximately 30% of the tool edge radius [324]. Liu et al. [325] provided experimental results when identifying the ratios of chip thickness/tool edge radius  $\lambda_n$  (normalised minimum chip thickness) of 0.35-0.4 for micro-end-milling Al 6082-T6 and 0.2-0.3 for micro-end-milling AISI 1018 steel over a range of cutting velocity (84,000 to 150,000 rpm) and feed-rate (0.5 to 4  $\mu\text{m}/\text{flute}$ ).

In general, the size effects exhibited by the ratio of MUCT/cutting edge radius in the range of about 0.05 to 0.4 depending on materials and cutting parameters that have been supported by experimental, theoretical, and modelling results that were published in many studies when micromachining metals and alloys (Table 2.8).

Table 2.8: The MUCT effects in micromachining – Relevant research

Approach	Remarks	Ref.
Micromilling lead, aluminium, and mild steel.	The critical DoC ranges from 0.1 to 0.23 mm along with different edge radius (from 0.025 into 0.06 in), and a neutral point angle of $37.6^\circ$ at a cutting speed of 240 mm/min.	[326]
Ultra-precision turning aluminium alloys	The MUCT is 0.05-0.2 $\mu\text{m}$ while the cutting edge radius is 0.2-0.6 $\mu\text{m}$	[327]
Micromilling pure copper 101	Various cutting speed (40, 80, and 120m/min), feed-rate (0.75, 1.5,3, and 6 $\mu\text{m}/\text{flute}$ ), and DoC of 30 $\mu\text{m}$ . The highest burr formation, largest tool wear and cutting forces were shown at the lowest ratio of feed rate/edge radius (approximately 0.4).	[328]

### **2.4.3 Micromachining of nanocomposites**

Micromachining nanocomposites are significantly different from the process with metals, alloys. The low machinability due to their advanced mechanical properties and the extensive cutting conditions (extreme small chip load and high cutting speed) are the main challenges when micromachining nanocomposites. Additionally, the effects of heterogeneity, anisotropic of materials, volume fraction and distribution of nano-fillers make the cutting mechanism even more complicated. For example, Deng et al [329] indicated that interface failure could contribute around 35% to cutting forces increase when micromilling Al/45 vol.% SiC composites besides the shearing - ploughing factor. This part of the paper will be focused on the cutting mechanism when micromachining nanocomposites in terms of cutting forces, surface generation, chip morphology and tool wear. As mentioned, micromachining has been focused extensively on metals and their alloys while machining of nanocomposites, on the other hand, is still limited [51, 330]. The following sections will discuss in detail the most common objectives of current researches related to micromachining of different types of nanocomposites as well as their limitations.

#### **2.4.3.1 Micromachining of CNT-based nanocomposites**

PMNCs are widely applied in micromachining due to their huge potential applications in the industry. The mechanical, thermal and electrical properties of polymers are significantly improved when reinforcing with CNT that leads to the requirement of machinability investigation when micromachining these materials. Additionally, the mechanical properties of CNT reinforced polymer nanocomposites (PMNC/CNTs) for instance: tensile strength, Young's modulus or hardness are considered feasible for mechanical micromachining applications hence make this study area more adaptable. Cutting force, surface roughness, chip formation, and tool wear are the most common objectives that take the effects of nanomaterial properties and cutting parameters into account.

Kumar et al. [331] have investigated the machinability when micromilling PC/GNP/MWCNT nanocomposites in terms of cutting force, dimensional accuracy, chip morphology and surface roughness. Cutting forces were higher when micromilling PC/GNP/MWCNT than plain PC (~ 22% at 4  $\mu\text{m}$ /tooth feed rate) that suggesting the



dominant of strengthening effects due to higher mechanical properties and the decrease of thermal softening effect due to the thermal conductivity improvement when reinforcing PC with MWCNT (and GNP).

The thermomechanical properties also lead to higher dimensional accuracy and surface quality (~197% at a feed rate of 3  $\mu\text{m}/\text{tooth}$ ) (Figure 2.31) when micromilling PC/GNP/MWCNT, especially at a high feed rate where the effect of softening is minimized. These explanations were validated by the consideration of chip morphology with discontinuous forms when micromilling PC/GNP/MWCNT that reconfirmed the role of CNT in chip breakage. However, the effects of size effects, filler loading and cutting speed on the micro-machinability have not been addressed. The chip formation due to the presence of CNT has also been investigated by Samuel et al. [51] with different forms and explanations. Instead of being broken, the chip formation tends to be continuous and curly when micromilling PC/CNT nanocomposites for the entire range of feed rates. It is possibly due to the good rake face lubrication [332] that could attain from reducing the friction coefficient of CNT along the rake face in comparison with plain PC [333]. Also, the presence of adiabatic shear bands on plain PC chip surfaces as well as their absence in the case of PC/CNT indicated the effect of thermal conductivity of materials on chip morphology (Figure 2.32).

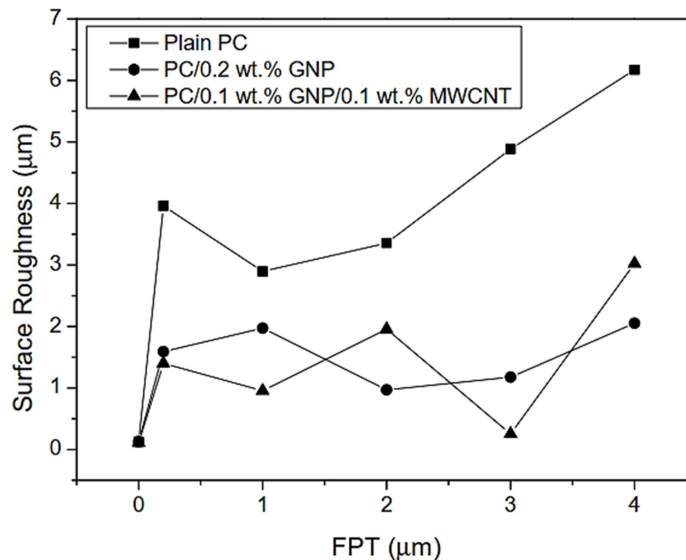


Figure 2.31: Various surface roughness with different nano-fillers and feed rate in micromilling PC-based nanocomposites (reproduced from [331])

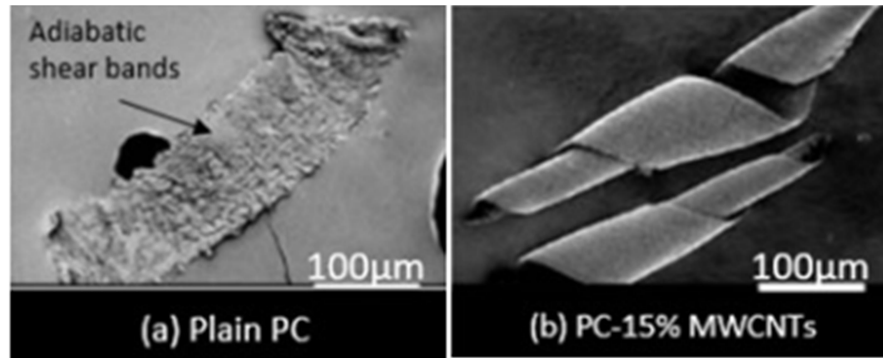


Figure 2.32: Effect of CNT addition on chip formation of PC/MWCNT nanocomposite [51]

Heat concentration at the cutting interface due to poor thermal properties also led to built-up-edge (BUE) formation on the tool face, resulting in a poor surface finish in the case of micromilling plain PC as compared to PC/MWCNT nanocomposite (Figure 2.33). Besides, the infestation of CNT and polymer smearing on the machined surface also contributed to its high surface quality. The cutting forces when micromachining PC/CNT nanocomposites were also lower in this case due to the reduction of shear strength for failure than plain PC or the low-quality bonding of PC-CNT [334], especially when high feed rates (shearing-dominated regime) were applied (Figure 2.34).

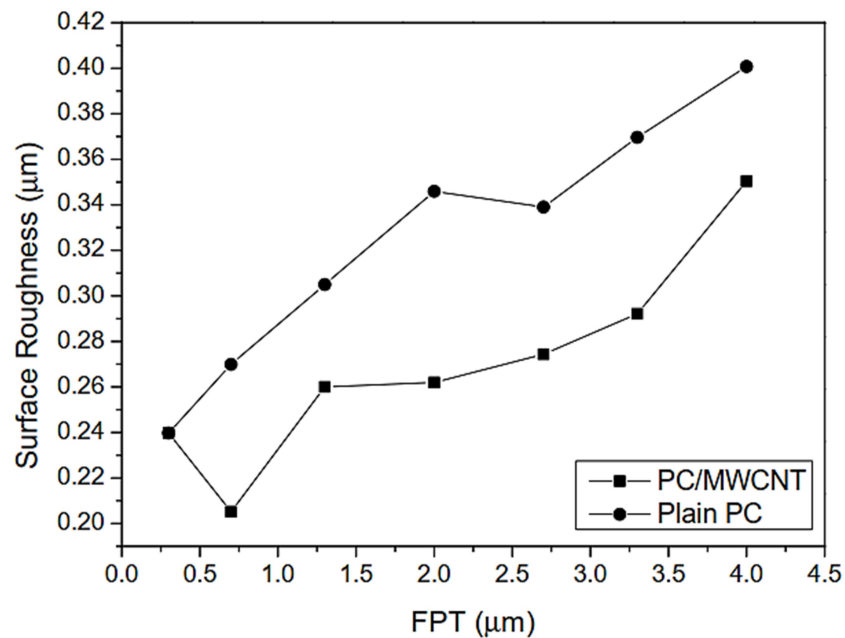


Figure 2.33: Comparison of surface roughness when micromilling PC/ 15 wt.% MWCNT nanocomposite and plain PC (reproduced from [51])

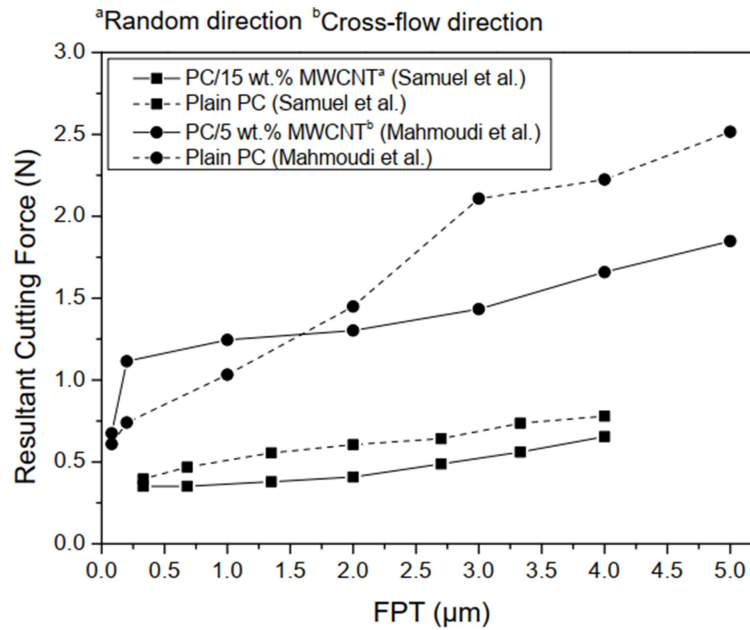


Figure 2.34: Comparison of the resultant cutting forces for plain PC and PC/CNT nanocomposites (reproduced from [51, 335])

The lower friction coefficient of PC/CNT might also play a key role in cutting forces reduction [336] that has not been addressed by the authors. Mahmoudi et al. [335] also confirmed the important roles of thermal-mechanical properties and microstructure effects on cutting force variations. However, the experimental results showed higher cutting forces when micromilling PC/MWCNT nanocomposite than plain PC only when the feed rate ( $2 \mu\text{m}$ ) was lower than edge radius ( $\sim 3 \mu\text{m}$ ) as a result of ploughing dominance in cutting mechanism due to MUCT effects. Therefore, it could be seen that the strengthening effects seem to be dominant on cutting forces when size effects are considered. The effect of CNT orientation has been also investigated with the significant increase when micromilling in the inflow direction as compared to the cross-flow direction (Figure 2.35). It was explained based on strengthening-dominated effects due to higher thermomechanical properties of inflow nanocomposite. Additionally, the surface quality of PC/MWCNT specimens after micromilling seemed to be better than a plain PC. However, no experimental results or explanation related to surface roughness was given.

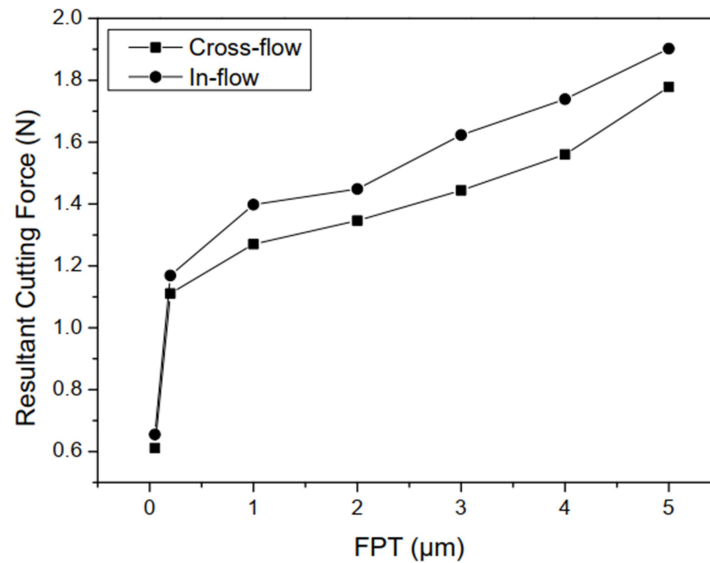


Figure 2.35: Effect of CNT orientation on cutting force when micromilling PC/5 wt.% MWCNT nanocomposites (reproduced from [335])

Stress concentration and crack formation ahead of the tooltip due to CNT agglomeration was indicated as the main reasons for cutting force reduction of cross-flow machining. The study has neglected the effects of filler content, cutting speed on the machinability when micromachining of nanocomposites as well as the investigation of chip formation that is necessary to support the discussion. The influences of cutting speed on surface roughness when micromachining HDPE/MWCNT nanocomposites have been experimentally claimed less significant than feed rate [337] due to the obvious feed marks on the specimen surfaces but no detailed discussion was expressed. This has been reconfirmed by Zinati et al. [338] in an investigation on surface roughness with variations of cutting speed, feed rate and MWCNT content. The Analysis of Variance (ANOVA) has also exhibited the least effect of filler loading on surface roughness generation. However, surface roughness variation, in this case, was only explained by tool-workpiece interaction when changing feed rates and cutting speeds without concerning about the thermomechanical properties of PA6/MWCNT nanocomposites.

The effect of filler loading on the micro-machinability of polymer/CNT nanocomposites has been only investigated by Samuel et al. [330]. The study highlighted the basic role of CNT addition in different chip formations as well as a cutting mechanism when micromilling PC/CNT nanocomposite and plain PC. Reinforcing CNT changed the

stress-strain behaviour of PC based materials, exhibiting by the reduction in strain-to-failure that indicated a ductile-to-brittle transition when the CNT loading reached 5 wt.%. When micromilling at low feed rates were applied, the chips were still continuously formed even in extremely low feed rate (0.3  $\mu\text{m}/\text{tooth}$ ) with high-content CNT nanocomposites (5 wt.%, 15 wt.%). The plain PC or PC/5 wt.% CNT, on the other hand, showed discontinuous chip formation. Therefore, it could be seen that the addition of CNT reduced the MUCTs of the PC/CNT nanocomposites that also indicated the size effects in micromachining. The improvement of machined surface quality associated with burr width reduction due to the addition of CNTs that leads to thermal conductivity improvement has been observed (especially at a high cutting speed of 130 m/min) with similar explanations as to their previous study [51] (Figure 2.36).

However, CNT content did not show considerable influence on cutting force in this case. Its effect became less dominant with the increase of cutting speed that indicated high sensitivity of strain rate (cutting speed) regarding cutting force variation instead (Figure 2.37). Cutting force exhibited significant reduction when increasing cutting speed regardless of the filler content, but the reasons for those changes were different between PC, PC/1.75 wt.% MWCNT and PC/5 wt.% MWCNT, PC/15 wt.% MWCNT.

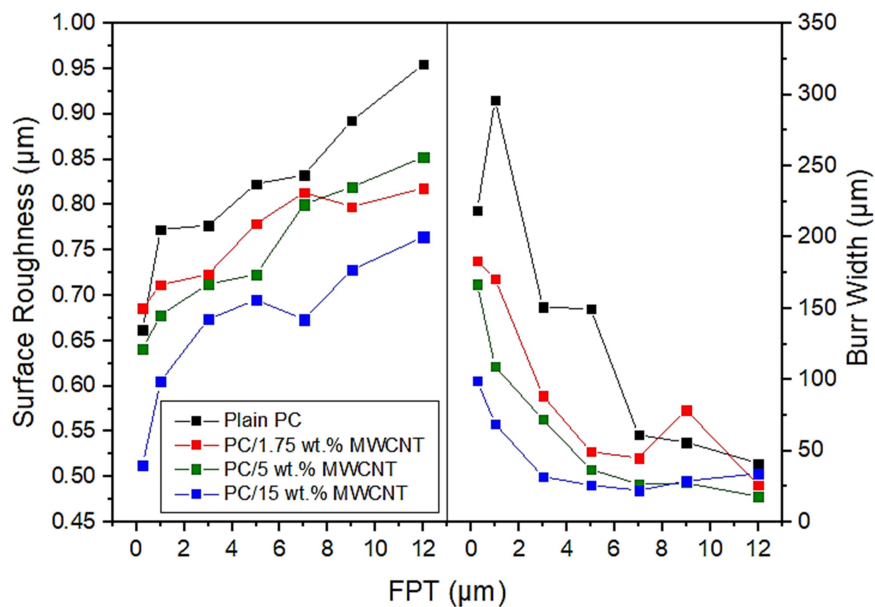


Figure 2.36: Effects of CNT loading and feed rate on surface roughness and burr width when micromilling PC/MWCNT nanocomposites at cutting speed = 130 m/min (reproduced from [330])

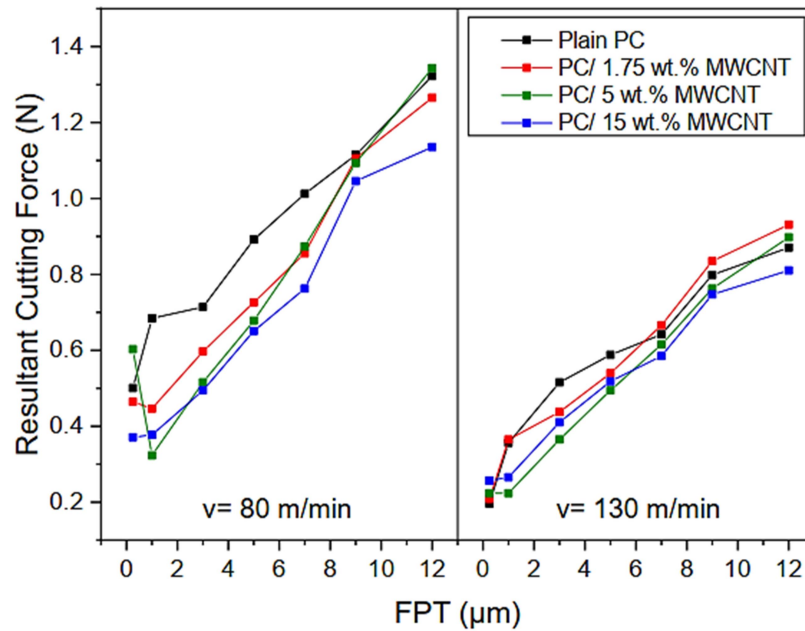


Figure 2.37: Effects of MUCT (feed rate), cutting speed (strain rate) and CNT loading on cutting force when micromilling PC/MWCNT nanocomposites (reproduced from [330])

While the advancement of cutting speed leads to the thermal softening-dominated regime of micromachining PC and the low-loading CNT, it is likely due to the interface failure or crack propagation from low interfacial bonding of CNT-PC when dealing with a higher content of CNT. The influence of heat transferring improvement due to the addition of CNT on cutting force when micromachining CNT reinforced polymer nanocomposites has been also investigated by Mahmoodi et al. [339]. Cutting force was considered as a function of cutting and edge coefficients in this case. The two main factors that were considered affecting these coefficients included: CNT content and CNT orientation. The radial and tangential have been considered as two components of cutting force (Figure 2.38). Optimization of instantaneous force method has been applied to identify the cutting force coefficient. Based on that, it could be seen that when micromilling at feed rates below MUCT, cutting forces were much higher than that of higher feed rates due to the much higher values of ploughing coefficients than cutting coefficients. However, the experimental results from this study did not exhibit the same trend as expected with low cutting forces at a low feed rate (ploughing-dominated regime at feed rates below 2 μm).

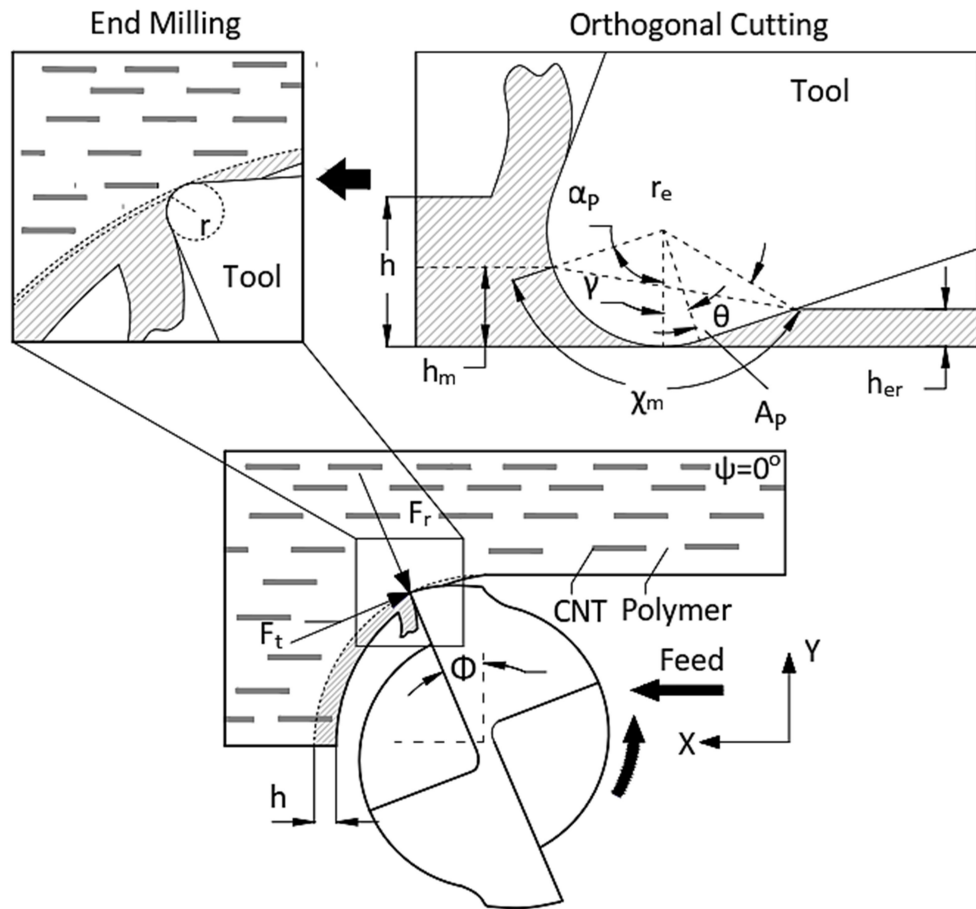


Figure 2.38: Schematic of micromilling CNT-based nanocomposite (adapted from [339])

The influence of CNT orientation on cutting force has also been exhibited with slight reductions of cutting coefficients when changing from in-flow to cross-flow cutting that indicated lower values of cutting forces. However, there was also no experimental result to validate this proposal. In general, the effect of CNT addition on micro-machinability in terms of improving thermomechanical properties of CNT based polymer nanocomposites has been the most important factor. Associated with MUCT and microstructure effects, CNT addition influences the cutting mechanism and chip formation, hence affecting cutting force, surface roughness and dimensional accuracy. However, recent studies have still exhibited different results (outputs) and the dominances of various input factors with distinct explanations (Table 2.9) that reconfirmed the high complexity when micromachining nanocomposites. Also, most of those researches have been only focused on the effect of feed rate while the roles of CNT type, filler content, fibre orientation and a

cutting tool were almost neglected. In terms of machinability, no study has addressed tool wear that is a highly important criterion, especially in micromachining nanocomposites.

Table 2.9: Summary of micromachining CNT reinforced polymer matrix nanocomposites

Inputs					Outputs						Ref.
CNTs		Cutting condition		Tool	Chip	Cutting force	Surface roughness	Dimension accuracy	Tool wear	Burr	
Loading	Direction	Feed	Speed								
--	--	X	--	--	X	X	X	X	--	--	[331]
Conclusions					Reasons						
High cutting force, dimensional accuracy and surface roughness when micromilling PC/CNT with discontinuous chip forms, especially at high feed rates.					The improvement of thermomechanical properties due to the presence of CNT leading to strengthening-dominated and thermal-softening-neglected regimes when micromilling PC/CNT nanocomposite.						
--	--	X	--	--	X	X	X	--	--	--	[51]
Conclusions					Reasons						
Continuous, curly and smooth chip forms when micromilling PC/CNT nanocomposites as compared to broken forms with adiabatic shear bands in the case of plain PC chips					Adding CNT reduce friction coefficient along the rake face and the effect of thermal softening in contrast with BUE formations due to poor thermal conduction of plain PC						
High surface quality when micromilling PC/CNT nanocomposite					Improvement of thermomechanical properties due to the addition of CNT into the PC matrix. CNT infestation and polymer smearing on machined surfaces						
Low cutting force when micromilling PC/CNT nanocomposite, especially at high feed rates					Low-quality bonding of PC-CNT leading to the reduction of failure shear strength along with the interface areas						
--	X	X	--	--	--	X	--	--	--	--	[335]
Conclusions					Reasons						
Higher cutting forces when micromilling PC/MWCNT nanocomposite than that of plain PC only at a low feed rate (2 μm)					Strengthening-dominated and microstructure effects associated with ploughing cutting mechanism when micromilling PC/CNT below MUCT.						
Significant increase of cutting force when micromilling in inflow direction in comparison with that of crossflow direction					Stress concentration and crack formation ahead of the tooltip due to CNT agglomeration						
--	--	X	X	--	--	--	X	--	--	--	[337]
Conclusions					Reasons						
Surface roughness decreased as cutting speed decreased and feed rate decreased with the more dominant effect of feed rate when micromilling HDPE/MWCNT					Visco-elasticity nature of HDPE matrix and feed marks						
X	--	X	X	--	X	X	X	--	--	X	[330]
Conclusions					Reasons						
The feasible chip formation when micromilling PC/CNT nanocomposites at a low feed rate (below tool edge radius).					Reinforcing CNT changed the stress-strain behaviour of PC based materials, exhibiting by the reduction in strain-to-failure that indicated a ductile-to-brittle transition						
High surface quality and low burr width when micromilling PC/CNT nanocomposite.					Addition of CNTs that leads to thermal conductivity improvement of nanocomposite						
Cutting force exhibited significant reduction when increasing cutting speed regardless of the filler content					The thermal softening-dominated regime of micromachining PC, low-loading CNT nanocomposites and crack propagation from low interfacial bonding of CNT-PC when adding higher loading of CNT.						



### **2.4.3.2 Micromachining of graphene-based nanocomposites**

Although graphene has high potential in terms of reinforcing various matrix materials such as polymers, metals or ceramics, it has been seen that few studies have investigated these graphene-based nanocomposites recently. One of the early studies about the micro-machinability of graphene-based nanocomposite has employed GPLs (Graphene platelets) as the secondary filler [334]. The main objective of this study is to consider the differences in micromachining responses between two-phase composite (epoxy/GF) and three-phase composite (epoxy/GF/GPL). The addition of GPL has remarkably revealed a better micro-machinability of hierarchical composite in terms of lower cutting forces, surface roughness and tool wear than the baseline composite. It was explained by the improvement of thermal conductivity of epoxy when adding GPL and the reduction of friction along with the tool-chip interface that reducing BUE of polymer and tool wear subsequently. This explanation is similar to those of the micromachining polymer/CNT nanocomposites that have been aforementioned. Moreover, the influences of GPL on reducing surface roughness have been also analysed by considering the concept of effective fibre length (Figure 2.39).

It was explained by the enhancement of interfacial strength of GPL- epoxy, making a longer effective fibre length and subsequent shearing-dominated cutting regime. In the case of baseline composite (epoxy/GF), glass fibre tended to bend and extrude on chips and machined surfaces indicating the lower effective fibre length, subsequent bending-dominated regime. The effects of cutting speed on machined surface roughness have also been concerned with preferable high cutting speed for both materials to attain low cutting forces and surface roughness, but no explanation has been given. The effect of feed rate on the micro-machinability, however, has been not concerned (Figure 2.40).

The reduction of cutting force due to the effect of strain rate (cutting velocity) and MUCT because of GPL addition has been also investigated by Arora et al. [15] with a similar discussion to the case of micromilling PC/MWCNT [51]. The alternation of thermal softening and strain hardening due to ductile-to-brittle transition associating with minimum chip thickness effects have been applied to explain the cutting force variations when increasing cutting speed.

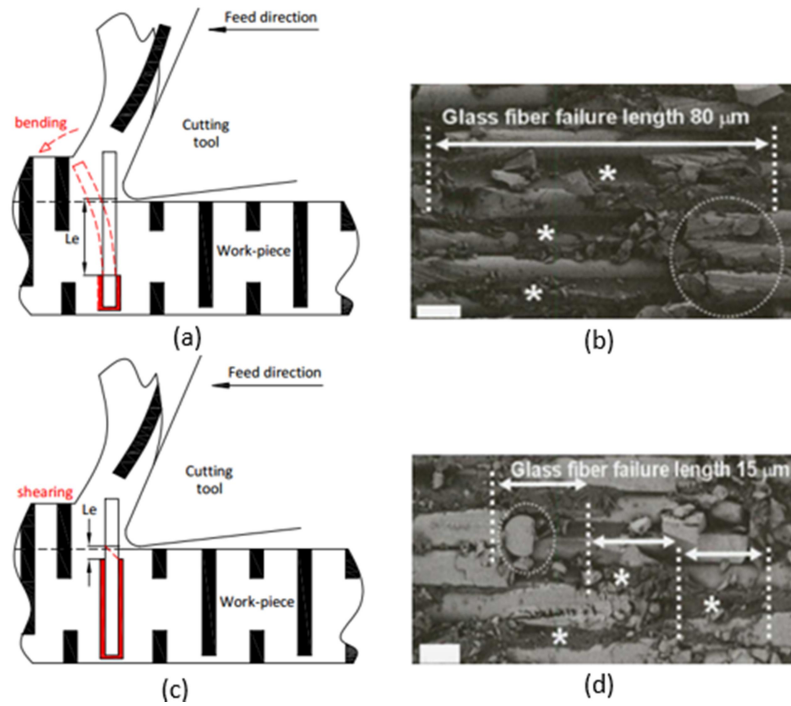


Figure 2.39: Influence of the matrix-fibre bond's strength on the chip formation and surface generation [334]

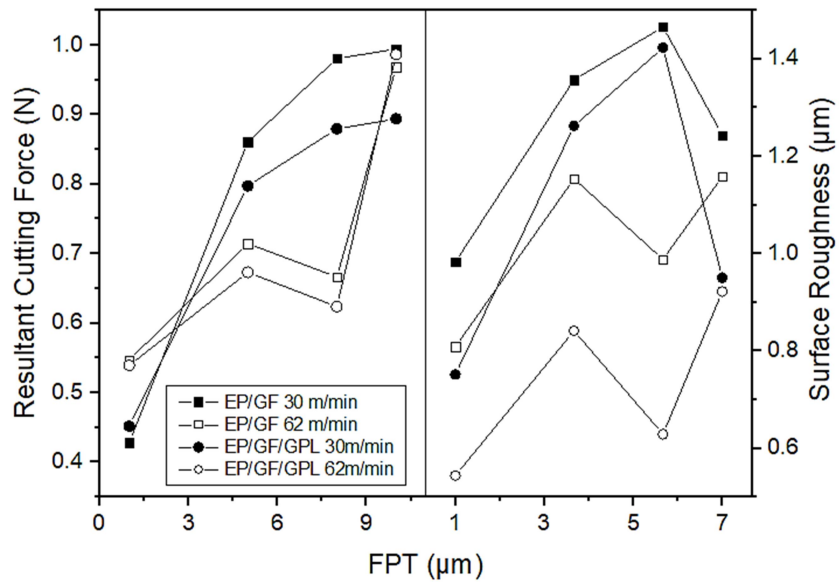


Figure 2.40: Effect of cutting speed on cutting force and surface roughness when micromachining epoxy/0.8 vol.% GF and epoxy/0.8 vol.% GF/0.2 wt.% GPL composites (reproduced from [334])

However, a different trend in terms of cutting force variation could be seen between the two studies. From Figure 2.41, it was observed that there were some fluctuations of cutting force when micromilling epoxy and epoxy/GPL (0.1 wt.%) at low cutting speeds (7.5 – 17.5 mm/min) while they constantly decreased in the case of PC/MWCNT. This difference comes from the different natures between epoxy (thermoset) and PC (thermoplastic) and the applied range of cutting speeds. In such a low cutting speed, the thermal softening mechanism has not still taken effect on reducing cutting forces yet, especially with thermoset polymers (epoxy) that have higher heat resistance than thermoplastics (PC). Therefore, the ploughing cutting mechanism is now dominated at a low feed rate (3  $\mu\text{m}$ ) instead that contributed to cutting force increase. The lack of rising portion in the case of epoxy/GPL (0.2 wt.%) might be due to the reduction of minimum chip thickness leading to the dominance of ploughing at lower cutting speeds (<7.5 mm/min). The highest cutting forces at 0.2 wt.% GPL were also due to the highest improvement in the mechanical properties of the nanocomposite. Tool wear has also been investigated in this study with the optimum when micromilling at 0.2 wt.% of GPL due to the lubricant nature of GPL and its role in reducing the elastic recovery of the matrix phase. At higher loading of GPL, their agglomerations were considered to accelerate the tool wear [340].

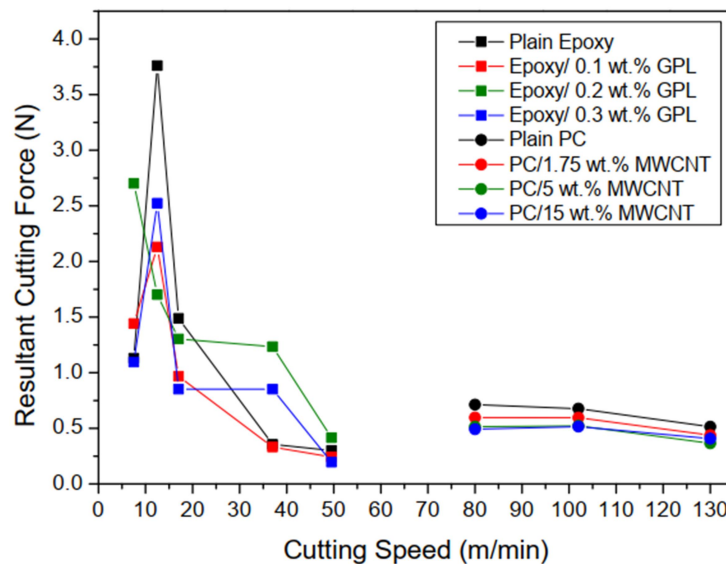


Figure 2.41: Effect of cutting speed and filler content on cutting force when micromilling different polymer nanocomposites at FPT= 3  $\mu\text{m}$  (reproduced from [15, 330])

However, graphene loading's effect on dimensional accuracy in micromachining polymer-based nanocomposites has not been considered sufficiently. Among relevant studies, only Kumar et al. [331] discussed the improvement of dimensional accuracy when micromilling PC/MWCNT in comparison with the plain matrix. The effect of thermomechanical properties is again the main reason for this phenomenon that leading to the strengthening-dominated mechanism when cutting CNT-based polymer nanocomposite instead of the thermal softening regime in that of its plain counterpart. Besides, an elevation of cutting force has been observed in this case that was different from the previous studies. While adding graphene [334] or CNTs [51] have in a polymer matrix have been indicated the main factor for cutting forces reduction due to two reasons: reduce friction coefficient in tool-chip interaction that leads to superior rake face lubrication and low interfacial failure strength between polymers and nano-fillers, this study, however, differently claimed a high specific surface area of GPL increasing tool-GPL interaction associated with its rough/wrinkled morphology enhancing mechanical interlock within PC matrix were two reasons that leading to cutting forces rise.

The strain-hardening-dominated effect when adding GPL into a polymer matrix that leads to high cutting force has also been confirmed by Arora et al. [15] at 0.2 wt.% GPL. The highest cutting forces confirm the most effective reinforcement of mechanical properties at a certain threshold of graphene content that if exceed this limit, the influence of filler agglomeration will accelerate crack propagation or reduce shear strength to failure of polymer-graphene bonding [341]. These different trends of cutting force variation in a consideration of graphene loading can be seen in Figure 2.42. Like micromachining-polymer/CNT studies, the most common objectives of that in polymer/graphene are also about cutting force, surface roughness and chip formation.

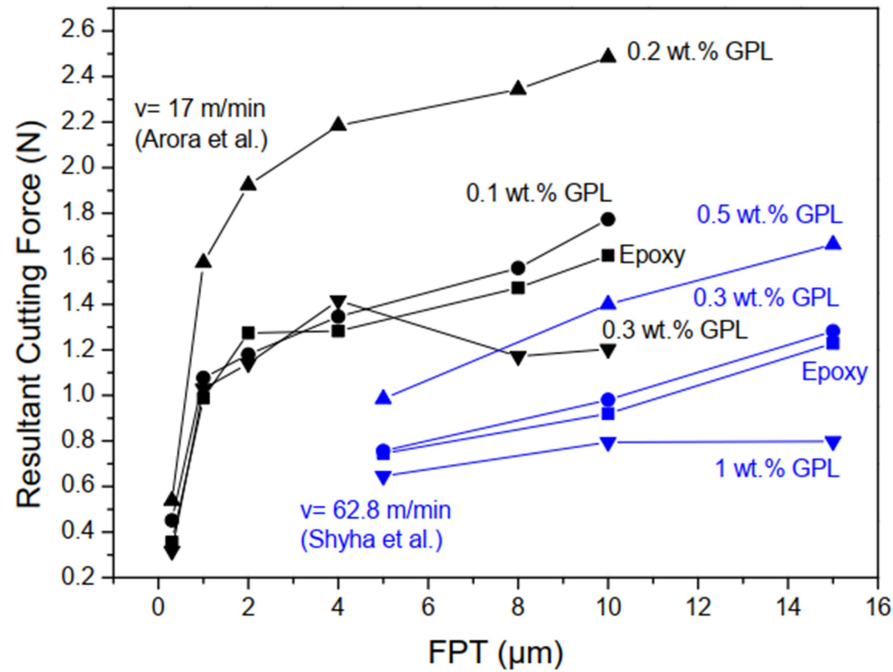


Figure 2.42: Different trends of cutting forces as a function of graphene addition when micromachining graphene reinforced PMNCs (reproduced from [15, 334, 342])

On the other hand, tool wear has been received more attention in the case of micromachining polymer/graphene nanocomposites [342] that indicated its importance as a machinability indicator. By discussing relevant studies, it could be seen that effects of graphene addition associated with cutting speed and feed rate have been considered changing the thermo-mechanical properties of the based polymer matrix, hence affecting the cutting mechanism, chip formation and subsequent cutting force, surface roughness and tool wear. However, the effect of material and geometry of micro-tool has not been investigated (Table 2.10).

Other gaps related to micromachining of graphene-based nanocomposites proposing through the discussion of relevant studies are the lack of attention in micromachining metal matrix and ceramic matrix-based material. Only Gao and Jia [343] has proposed simulated results in terms of the standardised effects of various inputs (DoC, cutting speed, tool rake angle, edge radius, graphene content and size) on cutting force only without sufficient explanations (Figure 2.43).

Table 2.10: Summary of micromachining graphene reinforced polymer matrix nanocomposites

Inputs					Outputs						Ref.
Graphene		Cutting condition		Tool	Chip	Cutting force	Surface roughness	Dimension accuracy	Tool wear	Burr	
Type	Loading	Feed	Speed								
--	X	X	X	--	X	X	X	--	X	--	[15]
Conclusions					Reasons						
Reduction of MCT with GPL addition					Ductile-to-brittle transition when adding GPL into epoxy						
Highest cutting forces at 0.2 wt.% GPL					Most effective reinforcement of GPL in terms of mechanical properties						
Cracks and debris on the machined surface at high content of GPL					Agglomeration of GPL, low interfacial interaction of GPL-epoxy leading to a strength-to-failure reduction						
Optimum tool wear at 0.2 wt.% GPL					Lubricant effect of GPL at the tool-chip interface and its role in minimizing sliding of polymer chains, subsequently reducing rubbing on the tool clearance face.						
--	--	X	X	--	X	X	X	--	X	--	[334]
Conclusions					Reasons						
Low cutting force, surface roughness and tool wear when adding GPL into epoxy/GF system					Improvement of thermal conductivity and lubrication at the tool-chip interface led to BUE reduction and tool wear. Shearing-dominated regime due to superior interface strength of GPL-epoxy, leading to low glass fibre extrusion on the machined surface.						
The sensitive influence of cutting speed on surface quality improvement regardless of the material types					The dominance of strain hardening effect at high cutting speeds						
X	--	X	--	--	X	X	X	X	--	--	[331]
Conclusions					Reasons						
Discontinuous chip formation, high surface quality and cutting forces when micromilling PC/GPL					Reduction of BUE due to the improvement thermomechanical properties when adding GPL filler into PC matrix						
--	X	X	X	--	--	X	X	--	X	--	[342]
Conclusions					Reasons						
Highest cutting forces at 0.5wt.% GPL with the dominance of feed rate instead of cutting speed.					Most effective reinforcement of GPL in terms of mechanical properties of epoxy/GPL leads to mechanical strengthening dominance when micromilling epoxy/GPL						

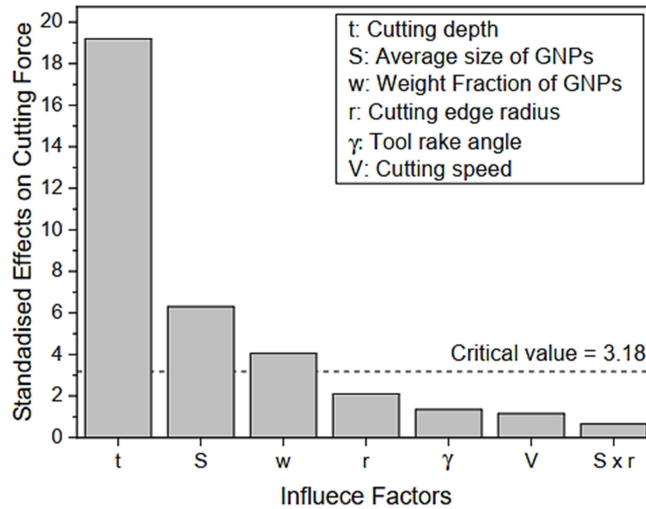


Figure 2.43: Quantitative comparison of the standardised effects of various parameters on cutting forces for Mg/graphene nanocomposites (reproduced from [343])

### 2.4.3.3 Micromachining of nano-ceramic based nanocomposites

Metallic materials are the most common matrices that have received more attention in terms of their micro-machinability when reinforcing with nano-ceramic particles. It comes from the requirement to fabricate high-toughness, corrosion than their metallic counterparts. One of the early studies that have investigated the micro-machinability of metal/ceramic nanocomposites was published by [344] with the considerations of cutting force variations as a function of filler loading, feed rate and cutting speed while micromilling Mg/SiC nanocomposites. Interestingly, the size effect has been applied to explain the non-linear correlation between specific cutting forces and feed rates with larger ploughing zone in the case of micromachining Mg/SiC nanocomposite (Figure 2.44).

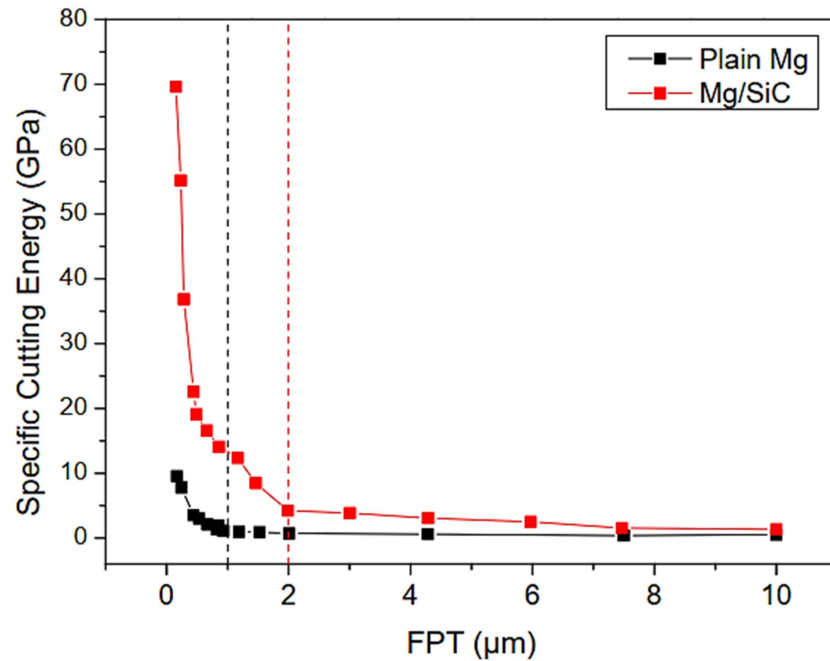


Figure 2.44: Specific cutting energy when micromilling Mg and Mg/10 vol.% SiC nanocomposite (the dash lines represent MUCT boundaries) (reproduced from [344])

It is different from the case of micromachining polymer-based nanocomposites. The main reason is the predominance of thermal softening due to the reduction of thermal conductivity when micromilling Mg/SiC at low feed rates. Additionally, its high specific cutting energies in the ploughing zone and high cutting forces also indicated the influences of strengthening and microstructure effects when micromachining inhomogeneous materials. Those influences also exhibited on the complex profiles of cutting force variations when micromachining Mg/SiC nanocomposite. The effect of filler content has been significantly affected cutting forces at 5-10 vol % of SiC due to its highest efficiency of reinforcement at this certain level [48] (Figure 2.45) that was similar to some experimental results in the case of micromachining of polymer/CNT [330] and polymer/GNP [15, 342]. The complex cutting mechanisms in micro-range parameters due to other factors such as tool deflection or microstructure effect neglected the role of feed rate on surface roughness as well as leading unobvious correlations between filler content-cutting speed and surface roughness.



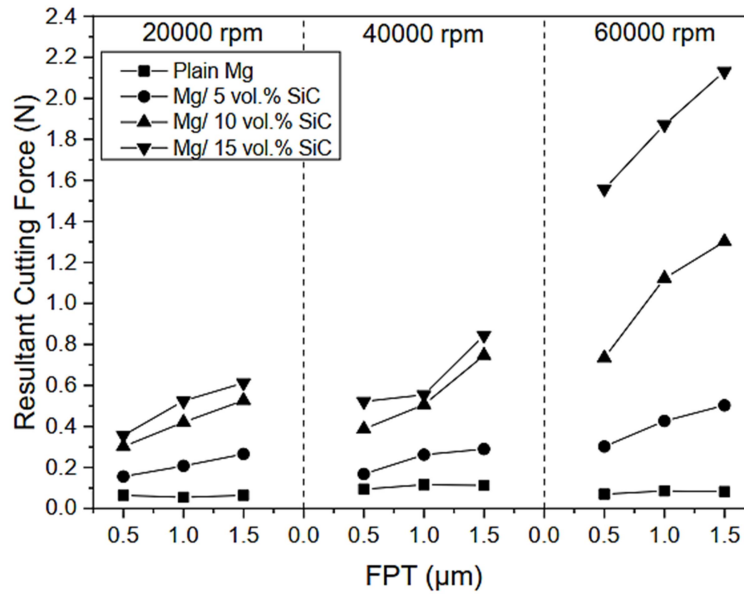


Figure 2.45: Effect of SiC content on cutting force when micromilling Mg/SiC nanocomposite (reproduced from [48])

With the micromachining of metal/ceramic nanocomposites, tool wear has been received more attention than that of CNT and graphene-based polymer nanocomposite. It is possibly due to the high improvement of corrosion resistance and mechanical properties of those nanocomposites due to the presence of nano-ceramic particles. Teng et al. [345], in a comparative study of micro-machinability between Mg/TiB<sub>2</sub> and Mg/Ti, have claimed the effect of nano-filler additions on tool wear as well as cutting force and surface quality. The roles of thermomechanical properties due to the presence of nano-fillers in micro-machinability of particle reinforced metal-based nanocomposites seem to be like polymer/CNT and polymer/graphene nanocomposites. It exhibited by the higher tool wear rate when micromilling Mg/TiB<sub>2</sub> with tool coating peeling in comparison with that of Mg/Ti. Due to the size effect, the associated effects of DoC and feed rate on cutting force increase were only available in the shearing region. On the other hand, thermal softening-dominated effect when increasing cutting speed and DoC has been claimed the main reason for surface roughness variations. Also, the high ductility of Mg/Ti led to more chip adherence on the tool surface that increasing cutting forces and subsequent surface roughness. However, no explanation related to thermal softening or strain hardening effects was given as compared to [48] (Figure 2.46).

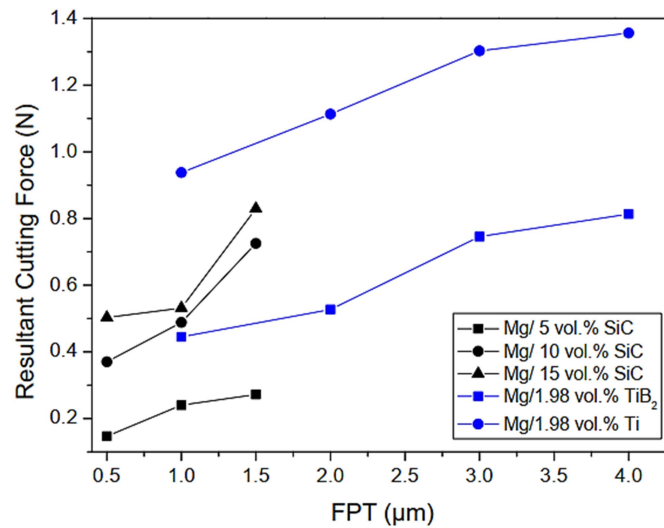


Figure 2.46: Effect of feed rate on cutting force when micromachining Mg/ceramic nanocomposites (adapted from [48, 345])

The application of micromachining or the investigation of micro-machinability of nanocomposites mostly focused on three main materials: CNTs or graphene reinforced polymer matrix and nano-ceramic-particles reinforced MMNCs. While micromachining the first two materials have similar features due to the similarities between CNTs and graphene properties, the last one exhibited different trends of micro-machinability, especially chip formation and cutting force. A summary of relevant studies of micromachining of nano-ceramic-particles MMNCs is given in Table 2.11. However, micromachining of ceramic-based nanocomposites have not been applied recently although there was one study has mentioned micromachining SiO<sub>2</sub>/GNPs nanocomposite using EDM [346]. It was possibly due to the low micro-machinability (high tool wear, cutting force or low surface quality) of these materials.

Based on the discussion of relevant studies, it could be seen that micromachining of nanocomposites is a complicated process with the associations of many factors such as microstructure effects, MUCT, cutting edge radius or the thermomechanical properties of nanocomposites (Figure 2.47). In general, the influences of nano-fillers on micro-machinability of nanocomposites have been confirmed while feed rate, cutting speed, depth of cut have exhibited some different levels of effect on machinability of nanocomposites from conventional machining in some specific cases due to size effect. However, the

relevant studies mostly focused on CNTs or graphene reinforced polymer matrix or nano-ceramic particles reinforced MMNCs. It leads to a lack of sufficient information to analyse the micro-machinability variations of these materials.

Table 2.11: Summary of micromachining nano-ceramic-particles reinforced metal matrix nanocomposites

Inputs						Outputs						Ref
Material	Filler loading	Cutting condition			Tool	Chip	Cutting force	Surface roughness	Dimension accuracy	Tool wear	Burr	
		Feed	Speed	DoC								
Mg/SiC	X	X	X	--	--	--	X	--	--	--	--	[344]
Conclusions						Reasons						
Non-linear increase of specific cutting energy when reducing feed rate below MUCT.						Size effect in micromachining						
Wider ploughing zone when micromilling Mg/SiC indicates higher MUCT with more SiC content						The predominance of thermal softening due to the reduction of thermal conductivity when micromilling Mg/SiC at low feed rates						
Higher specific cutting forces when micromilling Mg/SiC in ploughing zone						Strengthening effect and microstructure effect of inhomogeneous nanocomposite						
Highest cutting forces when micromilling Mg/SiC (10 vol %).						Improvement of yield strength and fracture strength due to SiC addition						
Complex force profiles of micromilling Mg/SiC						Microstructure effect						
Mg/SiC	X	X	X	--	--	--	X	X	--	--	--	[48]
Conclusions						Reasons						
The predominance of filler contents on cutting forces, especially at 5-10 vol% of SiC						Improvement of mechanical properties when adding more SiC in Mg matrix						
Unremarkable effect of feed rate on surface roughness while unobvious correlations between filler content-cutting speed and surface roughness were seen.						Complex microcutting mechanism while tool deflection and microstructure are also dominant						
Mg/TiB <sub>2</sub> Mg/Ti	--	X	X	X	--	--	X	X	--	X	--	[345]
Conclusions						Reasons						
High tool wear rate when micromilling Mg/TiB <sub>2</sub> with tool coating peeling						High mechanical properties and thermal load of Mg/TiB <sub>2</sub>						
Higher cutting force when micromilling Mg/Ti than Mg/TiB <sub>2</sub>						Chip adherence effect in case of micromilling Mg/Ti						
Higher surface quality when micromilling Mg/TiB <sub>2</sub> than Mg/Ti						Lower cutting forces when micromilling Mg/TiB <sub>2</sub>						
In the shearing region, cutting forces increased with DoC and feed rate						More resistance on tool-chip interface due to higher contacting surface						
Cutting speed and DoC have more dominant effects on surface roughness than the feed rate						The thermal softening effect when changing cutting speed and DoC						
Al/TiB <sub>2</sub>	--	X	X	X	--	--	X	--	--	--	--	[347]
Conclusions						Reasons						
Feed rate has the most dominant effects on cutting force when micromilling Al/TiB <sub>2</sub>						Shear angle increase and friction angle decrease when increasing feed rate						
Al/SiC	--	X	X	--	--	X	X	X	--	--	--	[348]
Conclusions						Reasons						
Unobvious effect of nano-filler addition on machined surface quality						The absence of particle pull-out or failure when micromilling Al/SiC						
The low predominance of feed rate effect on the surface finish at high cutting speed						Thermal softening effect						

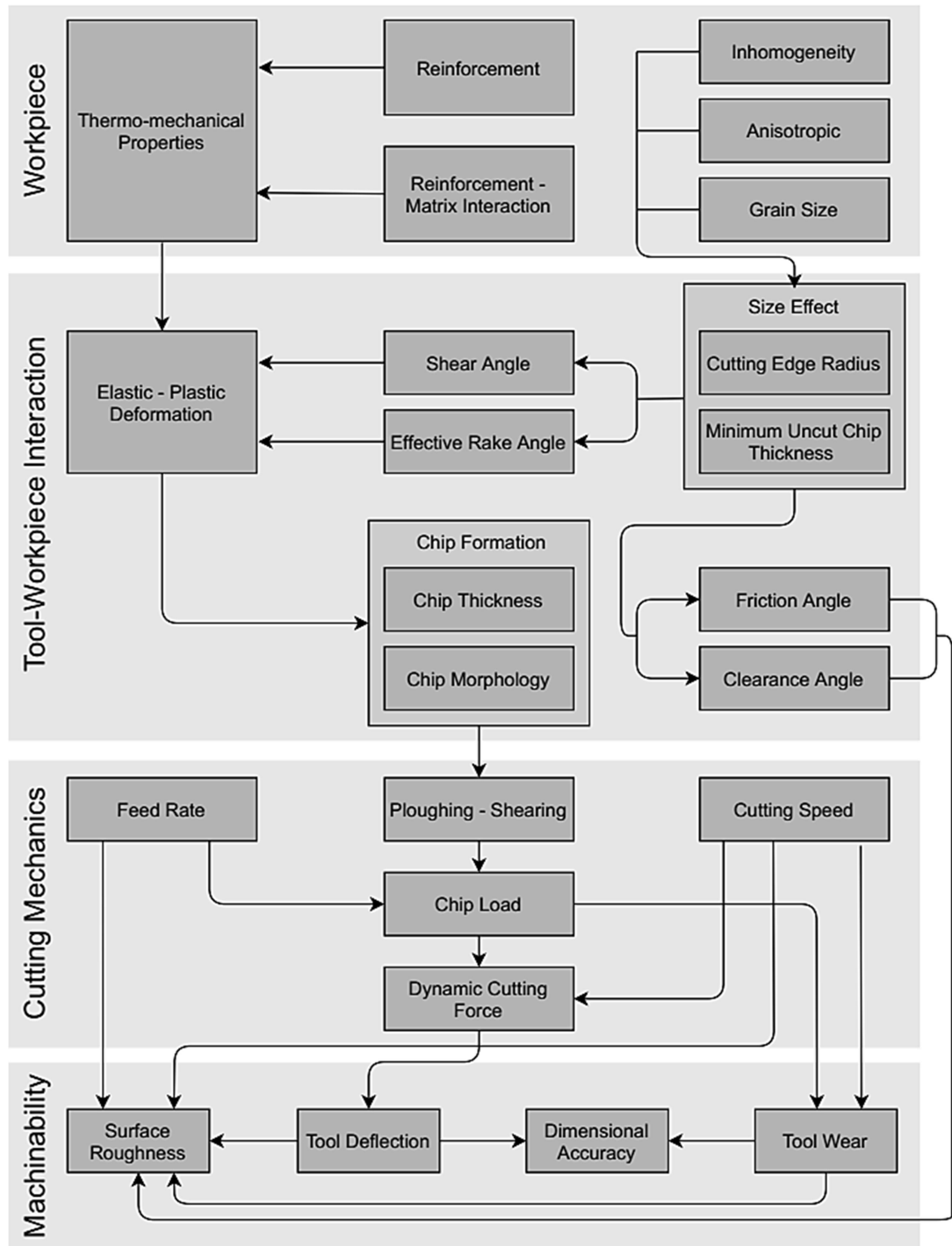


Figure 2.47: Schematic showing the correlations between input variables and the machinability of nanocomposites in micromachining

## **2.5 Modelling of micromachining of nanocomposites**

There are various models available to analyse the machinability of nanocomposites using micromachining. Those models include analytical [349], mechanistic models [301], finite element (FE) models [350] and MD models [351]. Analytical modelling simulate the machining responses based on analytical solutions of mathematical modelling [352]. This method is based on classical models in macro-cutting with the kinematics from empirical observation. Due to the high complexity in terms of elastic/plastic deformation and fracture at high strain rate in micromachining, the applications of this model have been limited. The mechanistic models provide the machine responses by investigated material [353], however, require validations from experiments that more complex with various content of nano-fillers. MD simulations are applied in micromachining [354] however due to limitations of time/length-scale, computational effort, and complex formulas, they seem to be unsuitable for a high number of atom models [355]. On the other hand, FE is one of the most common methods that has been applied in micromachining [356]. The different materials of both tool and workpiece are capable to be assigned. Furthermore, this method is also suitable for multi-phase material (i.e., nanocomposites) in predicting cutting forces, stress, strain, temperature distribution, chip formation and tool wear.

A microstructure-level model to simulate the micromachining process of PC reinforced with CNT has been applied by DeVor and Kapoor [357] appeared to accurately predict cutting forces (error 8%), thrust force (error 13.4%) and chip thickness ( error 10%). In general, the material structure was separated into main phases: matrix (PC) and reinforcing (CNT) phase. Based on the TEM images of the nanocomposites, the CNT distribution within the matrix would be characterized for length, curvature, slope, and orientation [358]. Similarly, the failure modes were also separately identified for two phases. Plastic stretch was applied as the ductile failure and hydrostatic tension was employed for brittle failure [359] in the matrix phase while a simple strain-to-fracture was used for CNT failure.

The results of chip formations, subsurface damage of the simulation can be seen in Figure 2.48. Based on that, Jiang [360] have developed a new microstructure-level model in micromachining polymer reinforced CNT nanocomposite. The principal difference was

that they indicated the failure mechanism of the micromachining process was primarily affected by the CNT- polymer interface. This idea was supported by subsequent numerical and experimental results from [361, 362]. Therefore, this polymer-CNT interface should be modelled as a third phase in the nanocomposite structure related to the load transfer from matrix to reinforcing phase [363]. They also showed that the characterisation of the interface properties was based on two main parameters: strength and fracture energy. Some nano-indentation tests have been conducted to identify these values.

Figure 2.49 shows the simulation results of this model. Other similar adaption in terms of simulation of micromachining polymer reinforced CNT has been conducted by Kumar et al. [331] in an attempt to investigate the heterogeneity of polymer-based nanocomposite with the addition of graphene. The PC matrix properties were characterized by the Johnson-Cook (JC) constitutive material model [364] with the consideration of flow stress at high temperature and high strain rates.

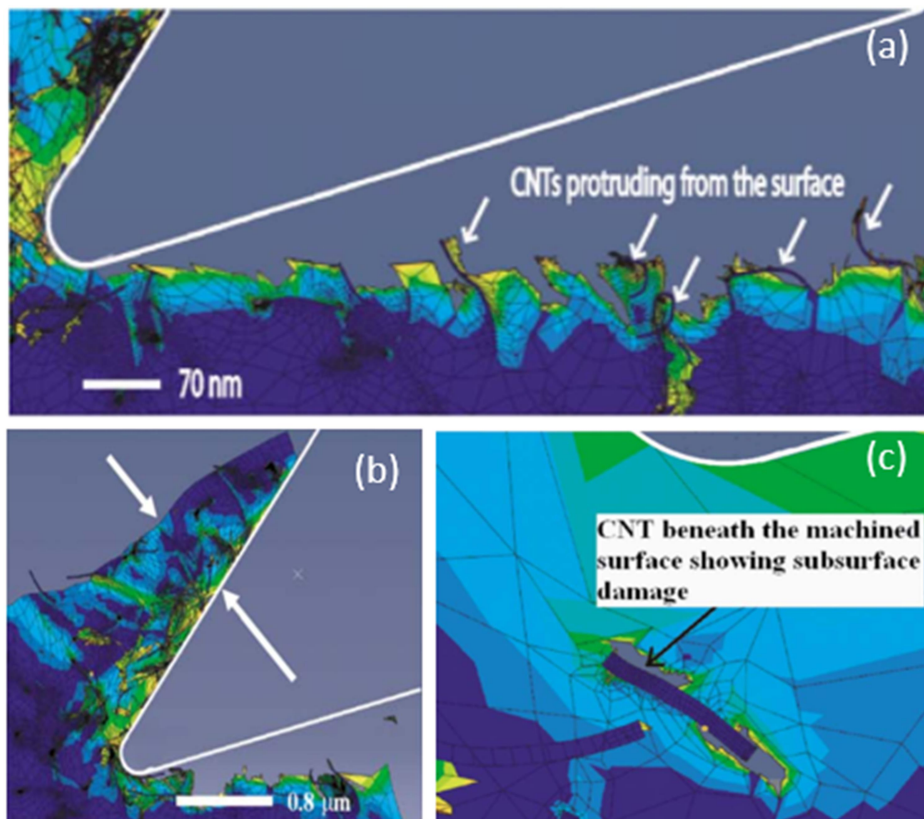


Figure 2.48: Micro-structure-level machining of CNT reinforced PC ([365, 366])

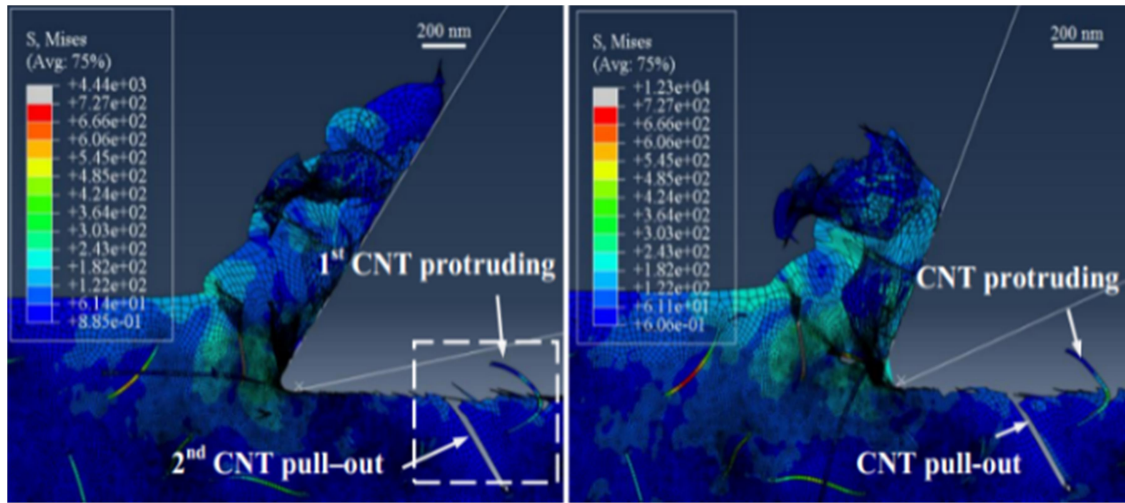


Figure 2.49: Micro-structure-level machining of CNT reinforced PVA nanocomposite [360]

The value of JC coefficients was provided by Dwivedi et al. [367]. The failure mode of the PC matrix was ductile damage for material separation and chip formation. The filler (GNP) was considered isotropic [368]. The mechanical characterisation was identified from the experimental validation of Tiejun [369]. From the simulation, the chip formation and cutting forces seemed to be similar to the experimental results. Discontinuous chip due to the presence of GNP seemed to appear in the PC-GNP interface that was supposed to be the weakest location. Besides, the strengthening effect due to the addition of GNP led to a higher cutting force when micromilling PC/GNP nanocomposites. Although there were some differences between simulated and experimental results due to various filler distributions, the model was indicated to be able to simulate the chip morphology and the trend of cutting forces accurately (Figure 2.50).

Teng et al. [350] have developed another FE model that employed the same filler (nano SiC particles) of 1.5 vol% when considering the effect of UCT and cutting edge radius on cutting force and chip morphology. It was concluded that the cutting forces in simulation increased along with the UCT. However, the percentage error seemed to be higher at low UCT and only improved when its value exceeded  $0.1 \mu\text{m}$ . The lower values of simulated results in terms of cutting force were due to the assumptions such as sharp cutting edge, rigid cutting tool and without tool wear consideration.

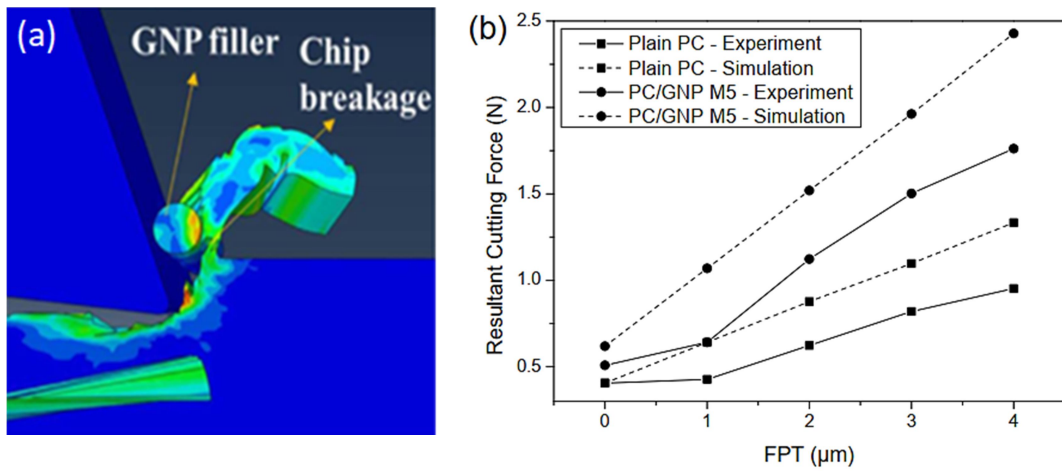


Figure 2.50: FE analysis of micromilling PC and PC reinforced GNP nanocomposite: (a) Chip formation of PC/GNP, (b) Cutting forces in simulation and experiment [331]

Similarly, the chip formation was also different while changing the UCT. When the UCT was from 0.1 to 0.2  $\mu\text{m}$ , the chip formation could not take place due to ploughing with elastic deformation. Exceed that limit, the chip was formed irregularly that could be seen at the minimum chip thickness of about 0.5  $\mu\text{m}$  (0.5R) (Figure 2.51).

In their later work [370], two FE models were established to comparing the machinability between micro-particles and nano-particles reinforced MMCs in terms of stress/strain distribution within the workpiece, chip formation, surface generation and tool wear. It was found that the particles reinforced within the matrix act as a barrier restricting the stress propagation during the machining process (Figure 2.52). The nano-particles were found to be intact during the machining process which is different from the micro-sized reinforced counterpart. It was explained by the better mobility of nano-particles caused by the significantly reduced particle size which bear evenly distributed stress and less kinetic energy.



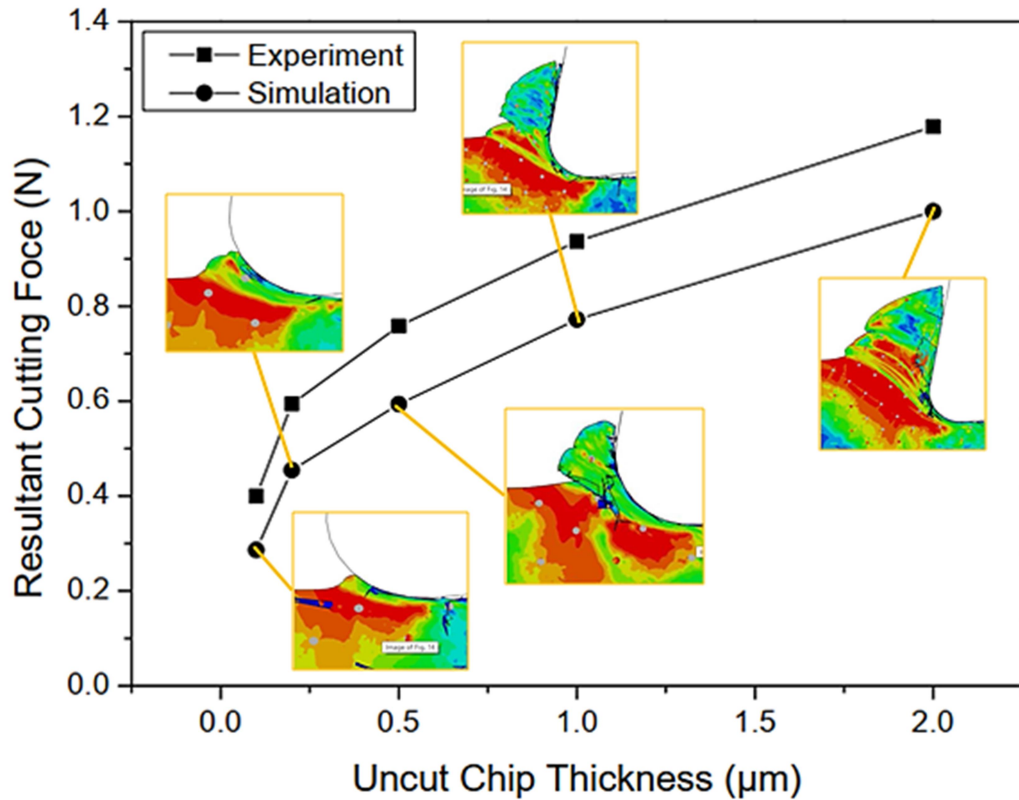


Figure 2.51: FE analysis of micromilling Mg reinforced by 1.5 vol.% SiC nanocomposite (reproduced from [350])

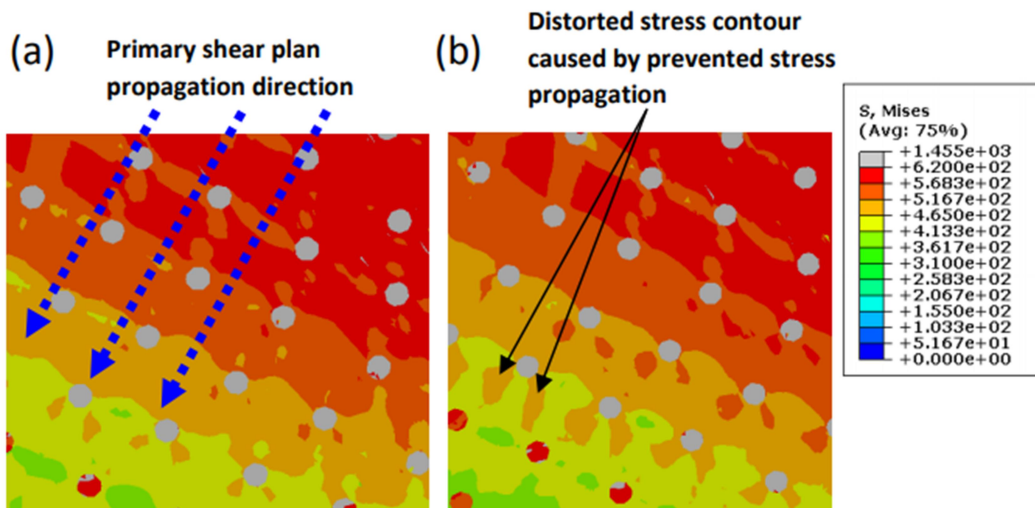


Figure 2.52: Effect of nano-particles on shear zone propagation: (a) direction of shear zone propagation, (b) distorted stress contour caused by particle restricting behaviour [370]

## **2.6 Summary**

Based on the relevant studies that have been addressed, it has been observed that although most nanocomposites fabrication and characterisation have been conducted and discussed, their machinability investigations in micromachining have still been limited, predominantly to the polymer matrix and metal matrix and nanocomposites reinforced by CNTs, graphene or ceramic nano-particle reinforced. It is possibly due to material integrity/defect, micromachining feasibility (tool wear, vibration, etc.) and most importantly, the high complexity of micromachining nanocomposites.

The associations of many factors including microstructure (homogeneity, anisotropic, grain size), improvements of thermomechanical properties (filler distribution, loading) of nanocomposites and size effects of micromachining complicate the manufacturing process as well as significantly decrease the machinability of these materials. In the case of fibre reinforcement, the distribution of nano-fibre (i.e., CNT) and fibre/cutting orientation were also important factors in micromachining. Subsequently, the intricate micromachining process leads to unobvious relations between variable inputs such as feed rate, cutting speed and corresponding outputs (i.e., cutting force, surface roughness, chip formation) with different explanations. In some cases, the cutting parameters showed inverse influences on the machinability compared to other conventional machining processes. Most studies have been concerned about the effects of filler content, feed rate and cutting speed on chip formation, cutting force and surface roughness. However, the micro-machinability of polymer nanocomposites has not been sufficiently investigated. Additionally, the effects of micro-cutting tool's material and tool wear on the micro-machinability of nanocomposites have been rarely mentioned. Besides, the analysis of size effect when micromachining nanocomposites have been still under-researched although it has been addressed extensively when micromachining metals and alloys.

Nevertheless, through the discussion of both mechanical properties and mechanical micromachining of nanocomposites, a general view about their micro-machinability has been given. It would be the basic knowledge for further studies in this area in future. However, the gap of knowledge has also led to the requirement for more efforts for collecting quantitative data and sufficient information on this area.

## Chapter 3: Experimental work

### 3.1 Workpiece materials

#### 3.1.1 Epoxy

A two-component Bisphenol A-epichlorohydrin (BPA) based epoxy was used in this research. EPOPHEN EL5 (resin) and EPOPHENTM EHA 57 (hardener) were purchased from Polyfibre UK Ltd (Birmingham, UK). Resin has a density of  $\sim 1.3 \text{ g/cm}^3$  and a viscosity of 12,000-15,000 cps while hardener has a viscosity of 45 cps.

#### 3.1.2 Graphene

Graphene AO-3 was purchased from Graphene Laboratories Inc., USA. The specifications of graphene AO-3 are shown in Table 3.1. Figure 3.1 shows the SEM image of as-received graphene nanoplatelets.

Table 3.1: Specific characterisation of graphene AO-3 (Source: Graphene Laboratories)

Properties	Unit	Value
Average flake thickness	nm	12
Average particle size	nm	$\sim 4500$ (1500 – 10000)
Carbon purity	%	99.2
Specific surface area	$\text{m}^2/\text{g}$	80

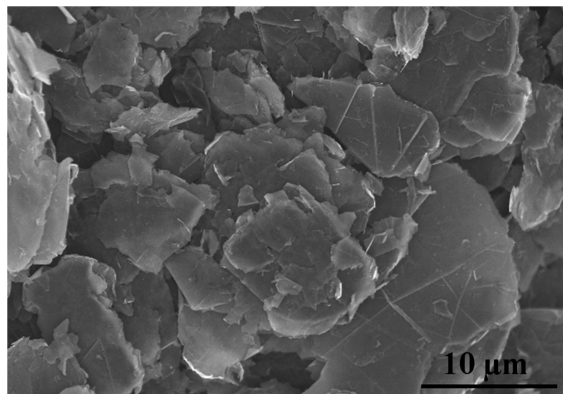


Figure 3.1: A SEM image of graphene nanoplatelets

### 3.1.3 Multi-walled carbon nanotube

NANOCYL® NC7000™ thin MWCNTs were purchased from Nanocyl that were produced via the catalytic chemical vapour deposition (CCVD) process. The specifications of MWCNT NC7000™ are shown in Table 3.2. The high aspect ratio of NC7000™ leads to the higher efficiency of properties improvement of nanocomposites than other fillers such as graphite or carbon blacks (CB). Figure 3.2 shows the TEM image of the as-received MWCNT NC7000.

Table 3.2: Specific characterisation of MWCNT NC7000™ (Source: Nanocyl)

Properties	Value	Unit	Measuring method
Average diameter	9.5	nm	TEM
Average length	1.5	µm	TEM
Carbon purity	90	%	Thermogravimetric analysis (TGA)
Transition metal oxide	<1	%	Inductively Coupled Plasma Mass Spectrometry (ICP-MS)
Specific surface area	250-300	m <sup>2</sup> /g	Surface area analysis (BET)
Volume resistivity	10 <sup>-4</sup>	Ω.cm	Internal test method (resistivity on powder)

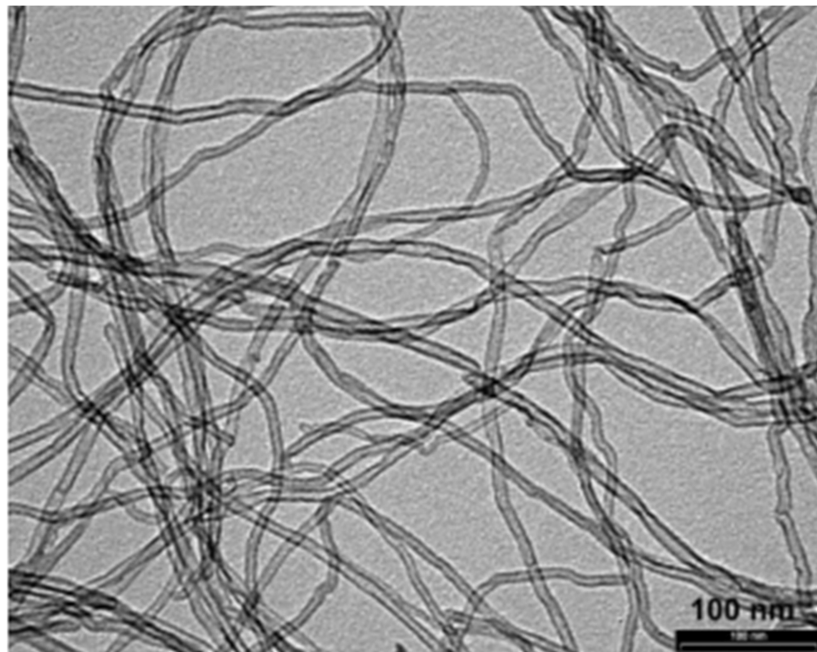


Figure 3.2: A TEM image of MWCNT NC7000

### 3.1.4 Carbon nanofibre

Carbon nanofibre CNF-110 was purchased from GNM that are produced via the CVD process. The specifications of CNF-110 are depicted in Table 3.3. Figure 3.3 shows the SEM image of the as-received CNF-110.

Table 3.3: Specifications of CNF-110 (Source: getnanomaterials.com)

Properties	Unit	Value	Measuring method
Outer diameter	nm	200 - 600	High resolution TEM (HRTEM)
Length	$\mu\text{m}$	5 - 50	TEM
Carbon purity	%	>70	TGA, TEM
Specific surface area	$\text{m}^2/\text{g}$	> 18	BET
Tap density	$\text{g}/\text{cm}^3$	0.043	N/A

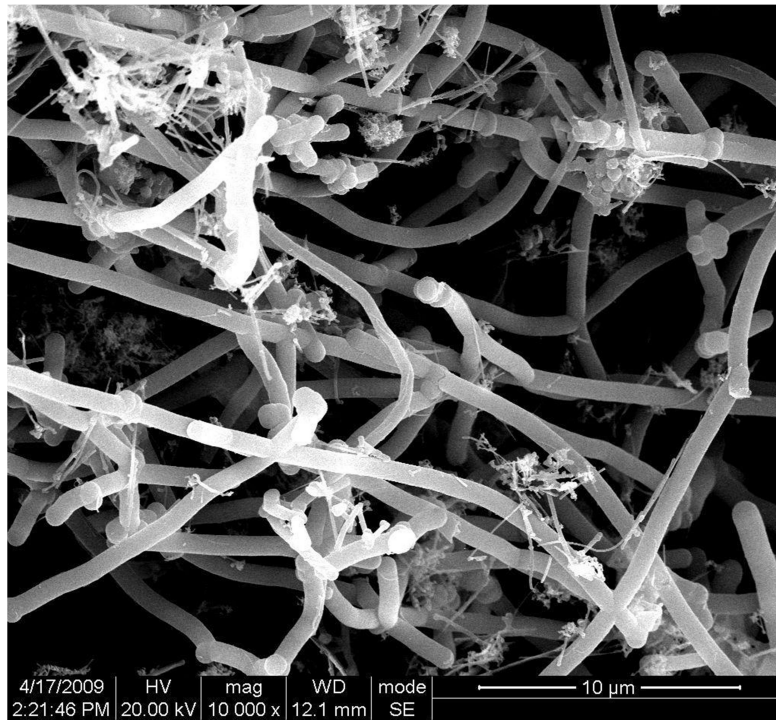


Figure 3.3: A SEM image of CNF-110


## 3.2 Material fabrication

### 3.2.1 Equipment

#### 3.2.1.1 Analytical balance

Due to the requirement of high accuracy of weight measurements for nanomaterial fabrication, it was considered that analytical balance OHAUS™ PA224C was suitable equipment for material weights with the resolution up to 0.1 mg and its specification (Table 3.4) was also appropriate for laboratory scale with an uncomplicated operation for most of the basic weighing requirements. In this study, this analytical balance was employed for all processes of nanocomposite preparation.


Table 3.4: OHAUS™ analytical balance specifications (Source: fishersci.com)

Specifications	Unit	Value	Image
Capacity	g	200	
Readability/resolution	mg	0.1	
Linearity	mg	0.3	
Repeatability	mg	0.1	
Dimension (D x W x H)	cm	32 x 19.6 x 28.7	
Weight	kg	4.5	
Stabilization time	sec	3	
Model	N/A	PA224C	

#### 3.2.1.2 Vacuum oven

A vacuum oven was required for degassing, especially after a stirring process because it could generate entrapped bubbles within the liquids that could negatively affect the final properties of the material. Cole-Palmer lab vacuum oven (Table 3.5) was employed in this study for degassing and post-curing when the solution mixing process was employed (Figure 3.5). In the case of three roll milling, this device was used for post-curing only (Figure 3.6).


Table 3.5: Cole-Palmer lab vacuum oven specifications (Source: colepalmer.co.uk)

Specifications	Unit	Value	Image
Chamber Dimension	cm	40 x 40 x 40	
Temperature uniformity	°C	≤ ± 1.5 (at 150 °C)	
Temperature range	°C	5 to 250	
Vacuum range	MPa	0 - 0.1	
Capacity	L	29	
Frequency	Hz	50/60	

### 3.2.1.3 Ultrasonic probe

Ultrasonic processors VC 750 (750 W – Vibra-Cell™ model) was employed to disperse CNT into epoxy resin in this study. This apparatus was considered suitable for nano-fillers dispersion, homogenisation and disaggregation with a wide range of organic and inorganic materials. The specifications of this device are depicted in Table 3.6. In this study, ultrasonic processors VC 750 was used to provide a homogenous mixture of epoxy hardener and nanofillers in the solution mixing process (Figure 3.5).

Table 3.6: Ultrasonic processors Vibra-Cell™ VC 750 specifications (Source: sonics.com)


Specifications	Unit	Value	Image
Sample volume	ml	10 – 250 (standard probe)	
Dimension	mm	Ø 63.5 x 183	
(w x d x h)	mm	190 x 340 x 235	
Power display	N/A	Digital	
Max. output power	W	750	
Frequency	Hz	20	
Interval time	s	1 – 59	
Timer (sonics)	s	1 – 36,000	
Probe	mm	136	
(Ti -6Al -4V)	mm	13	

### 3.2.1.4 Magnetic hot plate stirrer

Hardener- catalyst incorporation required homogenous mixing without more bubbles generation within the mixture during the agitation. It was due to the limitation of the curing time of epoxy (20 minutes after adding hardener in the case of EPOPHEN EL5)

hence a gentle mixing in a short time was needed. Hand mixing or mechanical stirring could be feasible but using magnetic stirring with a hot plate, in this case, seemed to be more sufficient in providing a homogenous mixture. Although a magnetic stirrer was not suitable for mixing high viscosity liquids as epoxy resin this drawback could be resolved with a hot plate since it could reduce the viscosity of epoxy at high temperature. Besides, magnetic stirrer generates less bubble than mechanical mixing and this apparatus is also available in the laboratory recently. Therefore, IKA<sup>TM</sup> RCT - a basic digital magnetic stirrer was chosen with the specifications are shown in Table 3.7. In this study, IKA<sup>TM</sup> RCT magnetic stirrer was used to provide the mixture of epoxy resin, hardener, and nano-fillers in three roll milling process (Figure 3.6).

Table 3.7: IKATM RCT digital magnetic stirrer specifications (Source: fishersci.com)

Specifications	Unit	Value	Image
Stirring capacity	L	20	
Temperature range	°C	310	
Speed range	rpm	0/50 to 1500	
Dimension (w x d x h)	mm	160 x 135 x 85	
Weight	kg	2.5	
Model	N/A	RTC basic digital	
Top plate material	N/A	Aluminium alloy	
Frequency	Hz	50/60	
Power	W	650	
Voltage	V	220 to 230/115/100	

### 3.2.1.5 Three roll mill

A TRM (80E EXAKT GmbH, Germany) was employed to incorporate nano-filler into epoxy resin. This method contributed to the uniform distribution of fillers as the raw nano-fillers are usually in bundle form. Agglomerates and powder clumps could be exfoliated and subsequently homogenized due to the shear force between rollers [371] (Figure 3.4). The shear rate was controlled by roller gap ( $\delta$ ) and circumferential speed ( $\omega$ ). This shear intensity and the number of rolling cycles have been determined as decisive factors for the nano-fillers dispersion [372]. In this study, TRM 80E EXAKT was used to create a homogenous mixture of epoxy resin and fillers in three roll milling process (Figure 3.6).



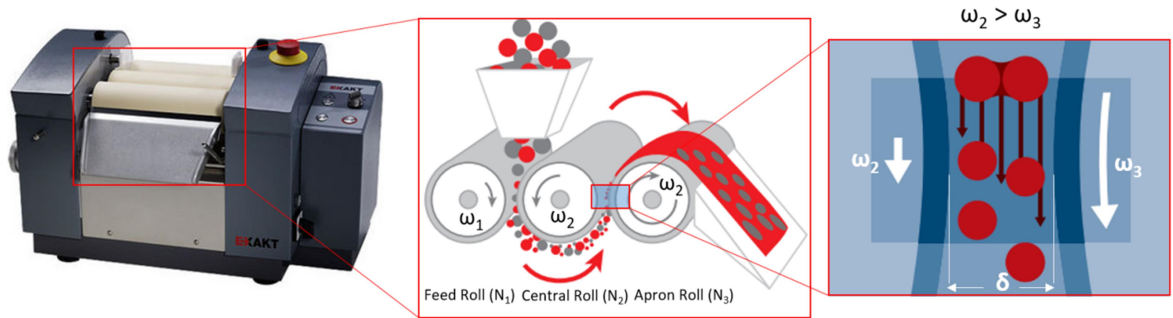


Figure 3.4: Three-roll-mill (TRM) 80E EXAKT and the schematic diagram representing the operating principle

### 3.2.2 Sample preparation

This study employed two different processes to synthesize carbon nanofiller reinforced epoxy nanocomposites. The solution mixing was used to fabricate graphene and carbon nanofibre reinforced epoxy nanocomposites. Due to the agglomeration nature of MWCNTs, three roll milling was used to synthesize epoxy/MWCNT nanocomposites due to the high performance of this technique in exfoliating fillers' agglomerates and homogenizing their distribution within the matrix.

#### 3.2.2.1 Solution mixing

The fabrication of epoxy-based nanocomposites using solution mixing is shown in Figure 3.5. The fractions of constituents comprising epoxy resin, nano-filler, and catalyst were measured using OHAUSTM PA224C analytical balance. The weighing and hand-mixing of the hardener and the nano-fillers were first implemented inside the glove box to eliminate the nano-fillers exposure. This first step was to create the initial mixture for the fabrication. The first mixture (hardener and nano-fillers) was then sonicated after moved out from the glove box. The sonication process was employed to make homogenous dispersion of the nano-fillers. Due to the low viscosity of the hardener (compared to the epoxy resin), it was mixed with the nano-filler first to assure a well-dispersed mixture. The ultrasonic processor VC750 was applied for this process due to its capability in producing better dispersion of nano-fillers at low loadings (less than 1 wt.%) without any surface treatment required compared to another mechanical mixing [373]. To avoid defects on nano-fillers' surfaces due to overheating through the operation of the ultrasonic processor,

the sonication performed at 60% of the maximum power (around 643 W) and a frequency of 250 kHz for 10 minutes, each 5-second break was taken after every 10 seconds of operation. It was also important to maintain a low temperature of the mixture (hardener and the nano-fillers) after the sonication process to slow the curing process (after adding epoxy resin). Therefore, an ice bath was also employed to reduce the heat generated from the sonication process [374]. Once the sonication was completed, the epoxy resin was incorporated using hand mixing. The final mixture (hardener, nano-fillers, and epoxy resin) was degassed using a vacuum chamber to remove entrapped air bubbles generated from the previous mixing steps (sonication and hand mixing). It was then poured into silicone moulds for mould casting. The specimens were also post-cured in 80°C [375] in an oven for fully cross-linking of the polymer.

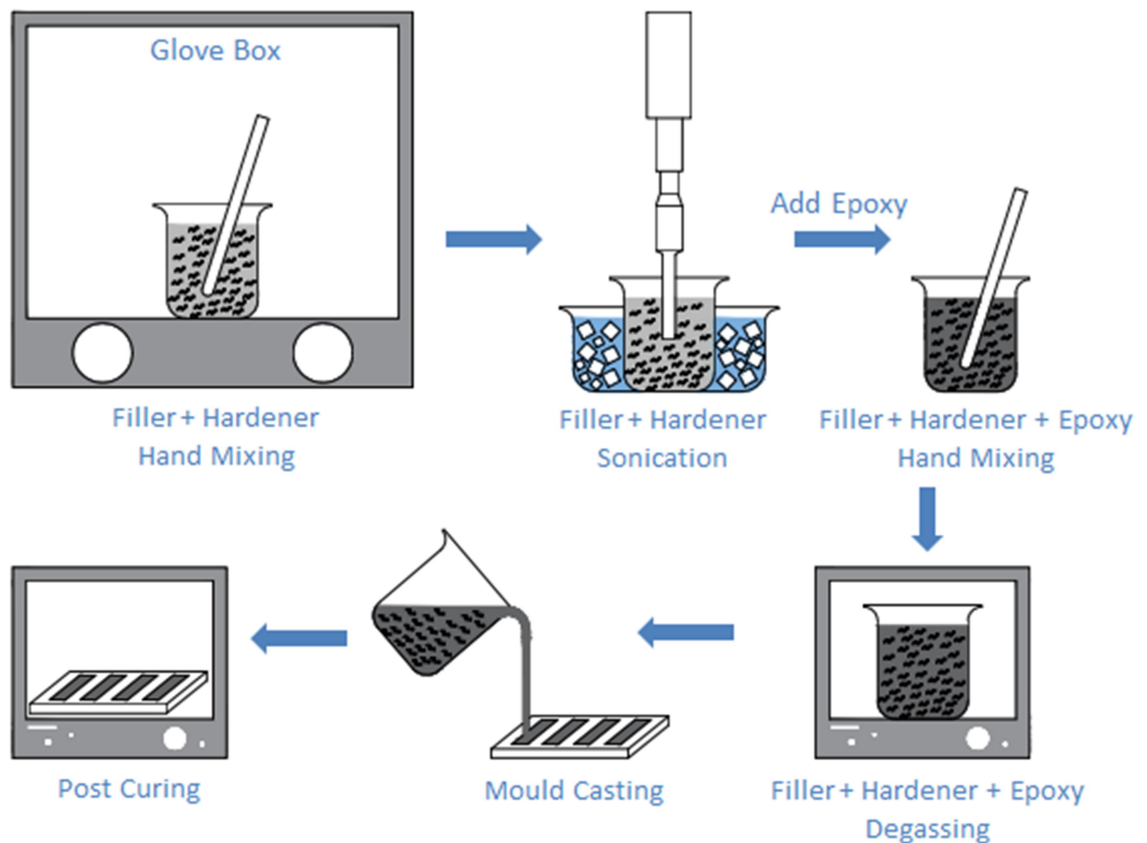


Figure 3.5: Schematic representing the fabrication of epoxy-based nanocomposites using solution mixing

### 3.2.2.2 Three Roll Milling

The fabrication of epoxy-based nanocomposites using three roll milling is shown in Figure 3.6. The mixtures of nano-fillers and epoxy resin were first prepared by manual mixing for 5 minutes to attain homogenous solution. A TRM (80E EXAKT GmbH, Germany) was then used to incorporate nano-fillers into epoxy resin. This method contributed to the uniform distribution of fillers, especially in bundled forms. Agglomerates and powder clumps could be exfoliated and subsequently homogenized due to the shear force between rollers [371]. The shear rate was controlled by roller gap ( $\delta$ ) and circumferential speed ( $\omega$ ). This shear intensity and the number of rolling cycles were determined as decisive factors for the nanotube dispersion [372]. Using shear mixing from TRM has shown high degrees of filler distribution within the matrix [376]. In this study, the mixture of nano-fillers and epoxy resin was passed six consecutive cycles through TRM in gap mode (fixed roll-to-roll distance), with the same rotational speed of the apron roller (200 rpm). The speed ratio between rollers was fixed at 1:3:9 ( $\omega_1$ -Feed roller:  $\omega_2$ -Central roller:  $\omega_3$ -Apron roller). Two gaps of  $N_1-N_2 = 90 \mu\text{m}$  and  $N_2-N_3 = 30 \mu\text{m}$  were applied for the first two cycles to exfoliate CNT bundles. After finer filler exfoliations were achieved, these gaps will be reduced to attain a uniform mixture. Therefore, the gaps of  $N_1-N_2 = 45 \mu\text{m}$ ,  $N_2-N_3 = 15 \mu\text{m}$  and  $N_1-N_2 = 15 \mu\text{m}$ ,  $N_2-N_3 = 5 \mu\text{m}$  will then be used for the second and last two cycles, respectively (Table 3.8). After a homogenous mixture of nano-fillers and epoxy resin was attained by TRM, the epoxy hardener was added by manual mixing for 5 minutes. Subsequently, this mixture was degassed in a vacuum chamber (pressure of - 1 bar) at  $50^\circ\text{C}$  for 1 hour. In the meanwhile, magnetic stirring was also applied at a speed of 1000 rpm. This combination was to eliminate trapped air bubbles inside and produce uniform mixtures simultaneously.

Table 3.8: Three-roll milling setup

Mode	Gap mode (fixed roll-to-roll distance)		
Apron roll speed	200 rpm		
Speed ratio	1 : 3 :9 ( $\omega_1$ : $\omega_2$ : $\omega_3$ )		
Gap	$N_1-N_2 = 90 \mu\text{m}$	$N_1-N_2 = 45 \mu\text{m}$	$N_1-N_2 = 15 \mu\text{m}$
	$N_2-N_3 = 30 \mu\text{m}$	$N_2-N_3 = 15 \mu\text{m}$	$N_2-N_3 = 5 \mu\text{m}$
Number of cycles	2	2	2

All parameters used in this experiment were based on the literature [377] with some properly adjustments to be adaptable for epoxy/MWCNT fabrication. The mixture was then poured into silicone moulds at room temperature (RT). To attain full crosslinking of epoxy, the mixture was cured in a chamber at 120°C for 12 hours, as recommended by the supplier. The procedure to fabricate epoxy-based nanocomposites using TRM is shown in Figure 3.6.

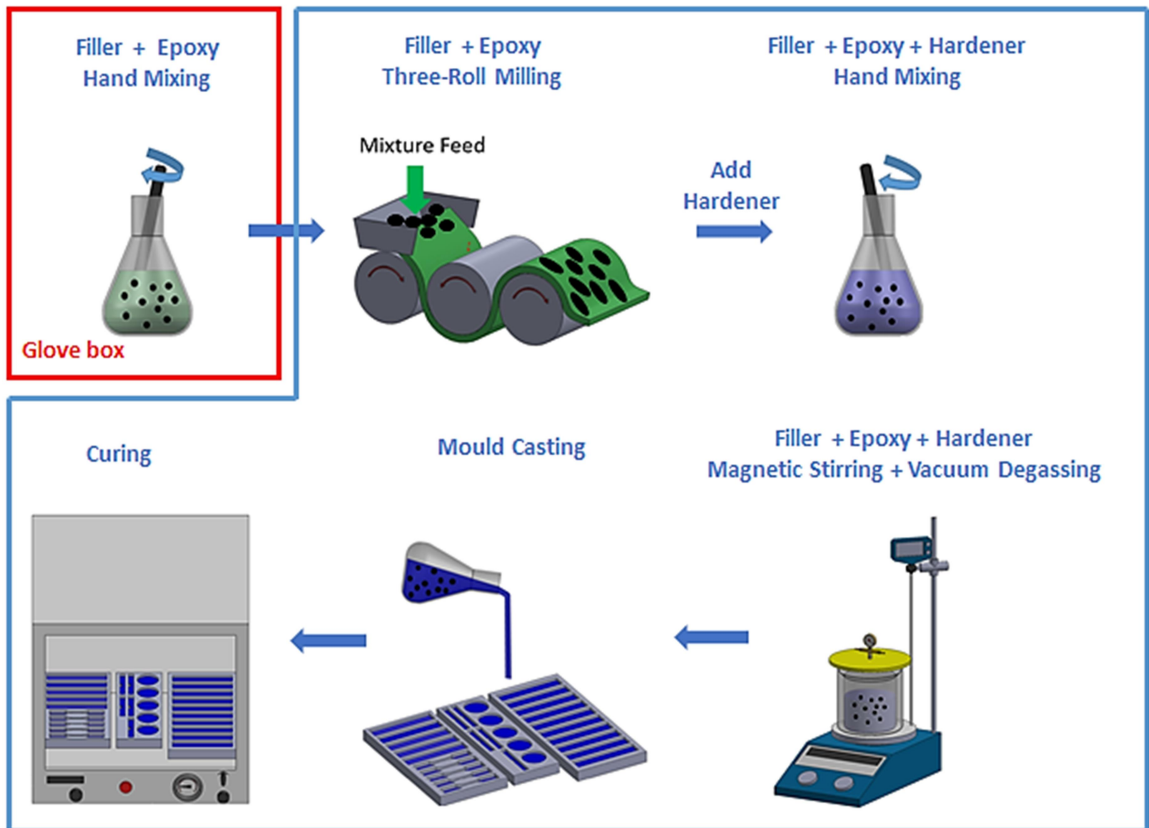


Figure 3.6: Schematic representing the fabrication of epoxy-based nanocomposites using three roll milling

### 3.3 Characterisation of workpiece materials

For characterisation of the nanocomposite samples manufactured by different techniques, the following characterisation was used including tensile properties (tensile strength, modulus, and fracture strain), thermal conductivity, and glass transition temperature. The repeatability and reliability of the measurement were undertaken

throughout the experiments and all measurements were repeated five times to get the average values as the final results.

### 3.3.1 Tensile test

Tensile tests were implemented on a Universal Testing Machine (INSTRON 3382) (Figure 3.7). This device provided wide ranges of load-displacement (maximum of 100 kN) and speed (up to 500 mm/min) with high accuracy. The minimum load could reach 1% (1 kN) without accuracy loss (100:1 force range). Following the ASTM standards, 5 specimens were used for each test with the displacement rate of 0.5 mm/min and their specifications were indicated in detail including specimen geometries, dimensions, and testing conditions.



Figure 3.7: Universal Testing machine (INSTRON 3382)

Tensile properties are one the most important criteria to evaluate the material characteristics. It is also used to assess the efficiency of filler reinforcement in the case of epoxy-based nanocomposites. Additionally, these properties were expected to have significant effects on the micro-machining process. The standard test method ASTM D638 was applied for the tensile characterisation of material in terms of measuring tensile stress and strain, Young's modulus. Tensile strength was calculated by dividing the maximum load by the average original cross-sectional area in the gage length segment of the specimen that was expressed in equation (3.1):

$$\sigma = W/A_0 \quad (3.1)$$

Where  $W$  is the maximum load (N) and  $A_0$  is the original cross-sectional area ( $m^2$ ). The results were expressed in MPa. In the case of Young's modulus, it was calculated by extending the initial portion of the load–extension curve and dividing the difference in stress corresponding to any segment of the section on the straight line by the corresponding difference in strain. Equation  $E = \sigma/\epsilon$  (3.2) was applied in Young's modulus calculation and its unit is MPa:

$$E = \sigma/\epsilon \quad (3.2)$$

Following the ASTM D638 standard, the test specimen that was prepared by moulding shall be  $3.2 \pm 0.4$  mm. The type V specimen was chosen due to the high strength of testing material that made the evaluation available with limited material. The thickness of the specimen, in this case, was 4 mm. Therefore, the specimen dimension was 63.5 x 9.53 x 4 mm (L x W x B) that is depicted in Figure 3.8. The setup of tensile characterisation is shown in Figure 3.9.

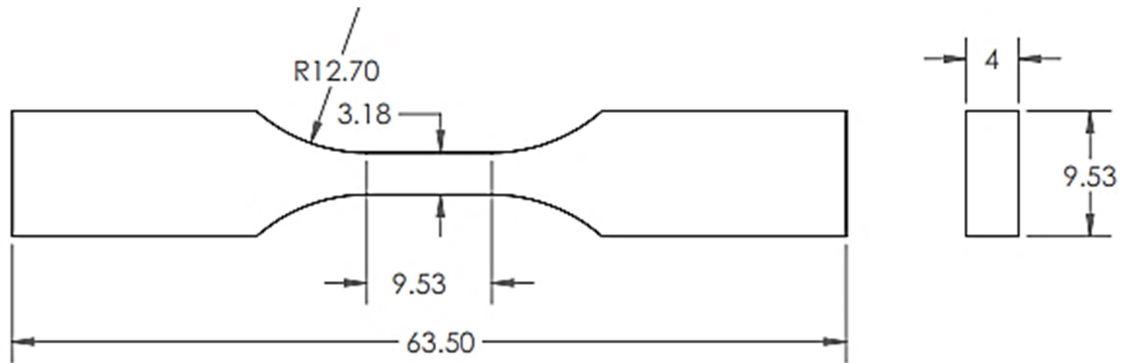


Figure 3.8: Tensile test specimen, type V geometry (ASTM D638) (Unit: mm)

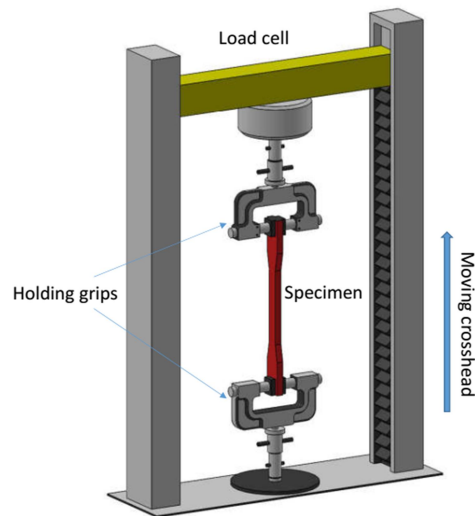


Figure 3.9: Tensile test setup in Instron 3382 universal testing machine (ASTM D638)

### 3.3.2 Thermal conductivity

Epoxy is considered a thermal insulator due to its low thermal conductivity (around 0.19 W/mK) [378]. However, the thermal conductivity of epoxy-based nanocomposites could be enhanced with the additions of nano-fillers (i.e., CNF, CNT). Therefore, it was important to investigate the thermal conductivity of the workpiece materials since it related to thermal softening that affected the machining behaviour of epoxy-based nanocomposites during the micro-machining process. ASTM D5470 standard was employed for thermal conductivity characterisation of epoxy-based nanocomposites with the prepared specimens of the same area as the contacting test surfaces and the thickness depends on the toggle clamp. In this study, the Hilton H112A device for linear heat conduction was employed. Following the ASTM D5470, the geometry of the specimen was circular with its diameter and thickness of 25 mm and 3 mm, respectively (Figure 3.10).

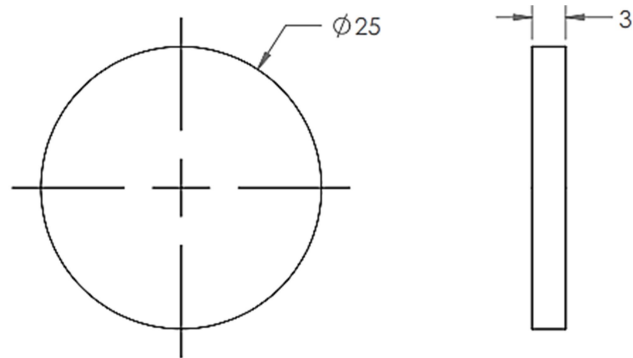


Figure 3.10: Thermal conductivity test specimen (linear heat conduction) (ASTM D5470)  
(Unit: mm)

The hot and cold meter bars were tightly clamped with the specimen to provide good thermal contact between them. The temperature distribution was considered linear without any heat loss to the surroundings (Figure 3.11), and then the thermal conductivity of the specimen could be calculated by applying Fourier's law in this case:

$$K_{\text{int}} = \frac{Q}{A_{\text{int}}} \cdot \frac{\Delta X_{\text{int}}}{\Delta T_{\text{int}}} \quad (3.3)$$

$$Q = V \times I$$

$$\Delta T_{\text{int}} = (T_{\text{hot-face}} - T_{\text{cold-face}}) \quad (3.4)$$

$$T_{\text{hot-face}} = T_3 - (T_2 - T_3)/2 \quad (3.5)$$

$$T_{\text{Cold-face}} = T_6 + (T_6 - T_7)/2 \quad (3.6)$$

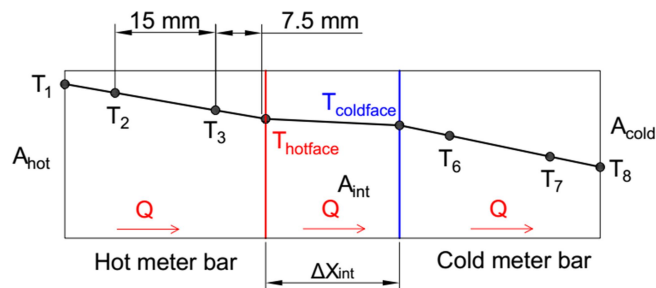


Figure 3.11: The schematic representing the calculation of thermal conductivity k



Where:

- $K_{int}$  is the thermal conductivity of the specimen (intermediate section) (W/mK)
- $Q$  is the heat transfer rate (W)
- $A_{int}$  is the area of the contacting surface of the specimen ( $m^2$ )
- $\Delta X_{int}$  is the thickness of the specimen (m)
- $\Delta T_{int}$  is the temperature difference between hot face and cold face (K)
- $V$  is the voltage of electrical power (V)
- $I$  is the current of the electrical power (A)

The characterisation setup of thermal conductivity is shown in Figure 3.12.

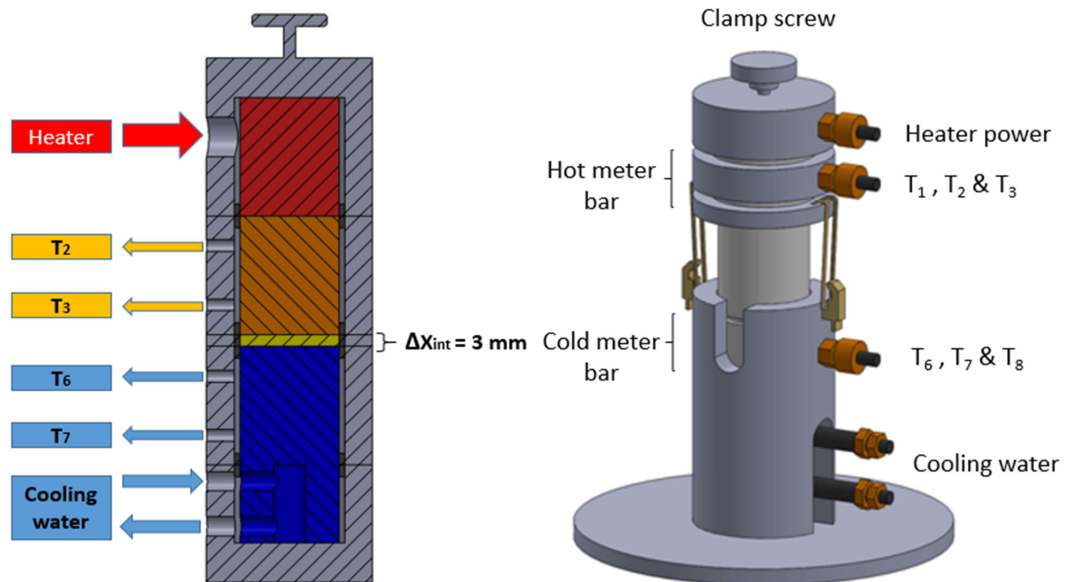


Figure 3.12: Thermal conductivity test setup on Hilton H112A linear heat conduction (ASTM D5740)

### 3.3.3 Dynamic mechanical analysis

Dynamic Mechanical Analyzer (DMA) (Model 8000, Perkin Elmer) (Figure 3.13) was used to identify the glass transition temperature  $T_g$  of the epoxy-based nanocomposites. This temperature indicates the lower threshold at which the polymer chains begin to move, causing a transition from a stiff (glassy) to a soft (rubbery) state of epoxy systems. The addition of nano-fillers was expected to hinder these movements of polymer chains, hence improving the glass transition temperature of epoxy-based nanocomposites. These

variations of  $T_g$  might contribute to the thermal softening effect that consequently affecting the machining behaviour of these nanocomposites.



Figure 3.13: Dynamic Mechanical Analyzer (DMA) (Model 8000, Perkin Elmer)

From DMA, three properties of materials could be identified including storage modulus, loss modulus, and tangent delta ( $\tan \delta$ ). The storage and loss modulus in viscoelastic materials identify the stored energy. The storage modulus represents the elastic portion of the material whereas the loss modulus indicates the viscous portion (the energy dissipated/lost at increased heat).  $\tan \delta$  is the ratio between loss and storage modulus.

The glass transition temperature could be identified based on the storage modulus (tangent lines intersect) or loss modulus (peak). However, this study determined  $T_g$  by the peak of  $\tan \delta$  curve as it showed high sensitivity to thermal change. ASTM E1640-13 was applied in the DMA test to identify glass transition temperature. The dimension of the specimen and testing conditions is shown in Table 3.9.

Table 3.9: DMA testing parameters for glass transition temperature

Specimen (L x W x T)	20 x 5 x 1 (mm)
Test Mode	Single cantilever
Test Frequency	1 Hz
Oscillation Amplitude	0.05% strain
Initial temperature	45 °C
Heating rate	Ramp 5°C/min to 150°C
Preload	0.01 N

### 3.4 Micromachining experiments

#### 3.4.1 Micro-machine tool

An ultra-precision desktop micro-machine tool (Nanowave MTS5R) (Figure 3.14) was employed to perform micromilling experiments in this study. High-speed cutting in micromachining was generated by a high-speed spindle driven by a power of 100W (240V). This spindle used an air bearing to provide high stability when cutting at high speeds. A wide range of rotational speed (20,000 to 80,000 rpm) could be applied using this micromachine tool. These three axes (X, Y, Z) were controlled by DC servo motors with high accuracy. Also, the high rigidity of the machine stage allowed stable operations during the micromachining process at such an extremely low feed rate (0.1  $\mu\text{m}$ ). Ultra-precision collets were also employed to minimise the negative effects of tool run-out. The main specifications of this ultra-precision desktop micro-machine tool (Nanowave MTS5R) are shown in Table 3.10.

Table 3.10: Main specifications of Ultra-precision desktop micro-machine tool (Nanowave MTS5R)

Machine size	413 x 450 x 470mm	
Max. cutting size	X: 50mm / Y: 50mm / Z: 30mm	
Main spindle	Max. speed	80000 rpm
	Min. speed	20000rpm
XYZ table	Smallest feed	0.1 $\mu\text{m}$
	Fast feed speed	3,000mm/min



Figure 3.14: Ultra-precision desktop micro-machine tool (Nanowave MTS5R)

### 3.4.2 Dynamometer

The piezoelectric dynamometer Kistler (9256C2) (Figure 3.15) was employed to measure the cutting force generating from the micromilling process in all three axes (X, Y, Z). This dynamometer was suitable for cutting force measurements in micromachining due to its low threshold ( $<0.002\text{N}$ ) that allowed measuring extremely small cutting forces with high accuracy.



Figure 3.15: Kistler (9256C2) piezoelectric dynamometer

### 3.4.3 Micromachining setup

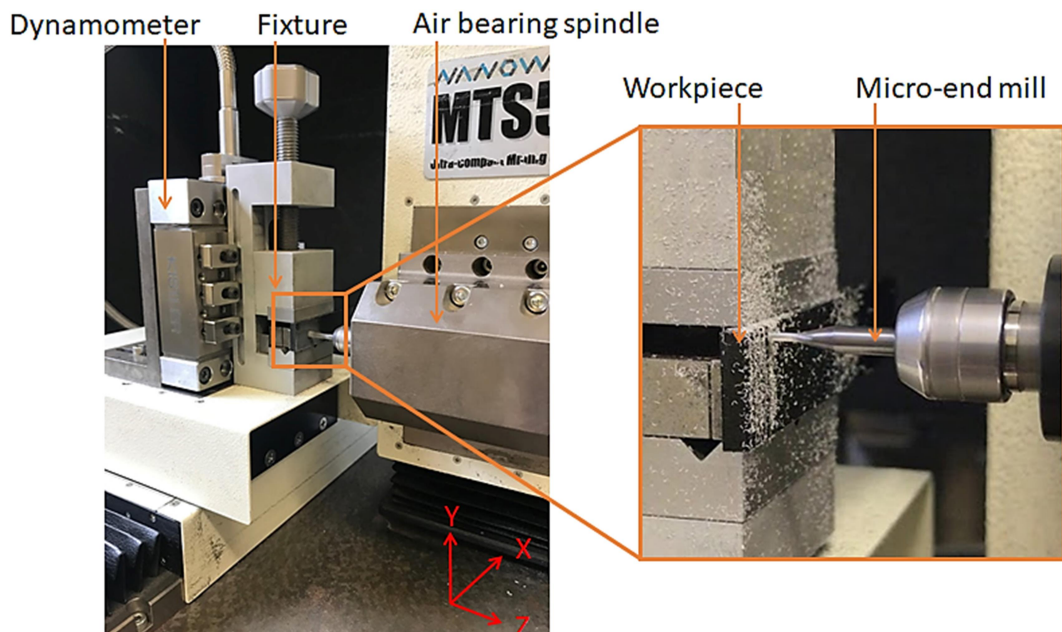


Figure 3.16: Micro-machining setup

Micro-end milling experiments were performed on the ultra-precision desktop micro-machine tool (Nanowave MTS5R). The experimental setup (Figure 3.16) shows the main components including nanocomposite specimen, spindle, micro-end mill as well as the coordinate system and feed direction. Kistler piezoelectric dynamometer (9256C2) was attached behind the fixture to measure cutting forces in X, Y, and Z directions. Dry cutting was applied for all experiments due to its simple setup. Also, it could be expected to generate obvious tool wear during the micromachining of polymer nanocomposites. The rectangular specimens with dimensions of 70x13x3 mm were applied for the micromachining trials to generate slots.

#### 3.4.4 Scanning electron microscope

SEM TESCAN MIRA3 (Figure 3.17a) was employed to examine tensile fracture surfaces, chip formation, and machined surface morphology. To attain high-quality images, the samples were first coated with platinum (5nm thickness) using Quorum Q150R rotary pumped coater (Figure 3.17b).

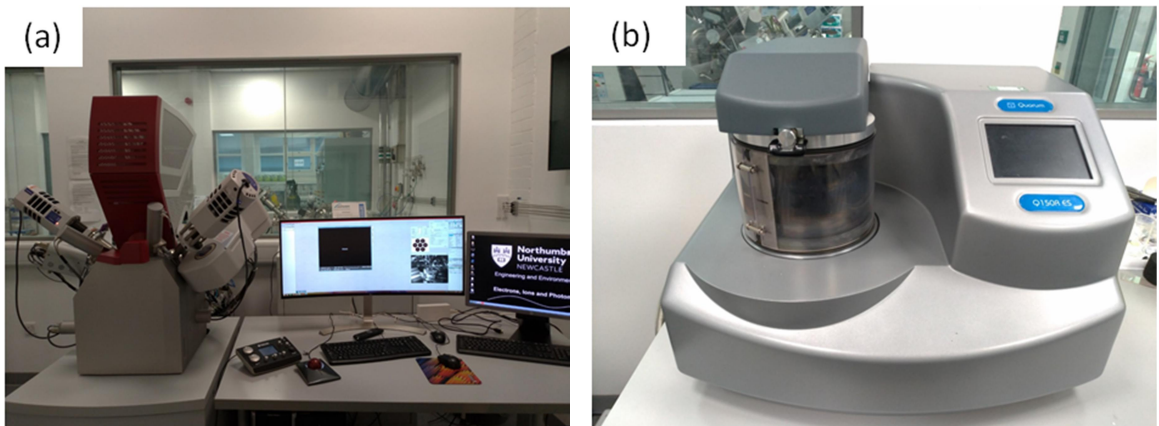


Figure 3.17: (a) Scanning electron microscope (SEM) TESCAN MIRA3 and (b) Quorum Q150R rotary pumped coater

The tensile fracture surface provided the fracture pattern of each composition (i.e., 0.1 wt.%) and the nano-fillers' distribution and failure (i.e., pull-out, de-bonding) (at high magnification). The results could be used to support the tensile characterisation and machining behaviour's analyses. Therefore, it needed to be examined before micromachining trials. After the tensile test finished, the broken pieces of each composition

would be collected for the SEM imaging.

SEM was also used to examine chip morphology generated from the micromilling process. Based on the analysis of chip formation the cutting mechanism (i.e., ploughing, shearing) and MUCT could be revealed. The chips generated from each cutting condition were collected using conductive carbon tape.

Additionally, the machined surface morphology was also investigated using SEM imaging. Based on that, the integrity of these surfaces was examined. Also, these results could be used to support the surface roughness analysis in the considerations of feed mark formation, chip adhesion, or defects, The SEM imaging of the machined surfaces would be conducted after surface roughness measurements.

### 3.4.5 Cutting force measurement

Kistler (9256C2) piezoelectric dynamometer with high frequency (up to 4.8 kHz) was attached behind the fixture to measure the micro-cutting forces in  $X$ ,  $Y$ , and  $Z$  directions. In this case,  $F_y$  is the feed force ( $F_f$ ) and was measured in the feed direction of the tool.  $F_x$  is the feed normal force ( $F_{fn}$ ) (perpendicular to  $F_f$ ), while  $F_z$  is the passive cutting force ( $F_p$ ) (axial to the central tool line) The signals generated from the force sensor were transferred to the charge amplifier (Kistler 5070A) then showed by Dynoware software for measuring cutting forces (Figure 3.18).

The cutting force measurements were replicated three times for each cutting conditions and workpiece materials. Based on the cutting force signals (Figure 3.19), the transient areas were identified and then eliminated. Only steady cutting areas were chosen for measurement. Five sub-sectors would be extracted from these steady areas. The peak values of each cutting force component on the three directions ( $X$ ,  $Y$ , and  $Z$ ) would be intercepted, respectively and their average values were identified. Based on that, resultant cutting forces ( $F$ ) were calculated.

$$F_x = \max|F_{xi}| - \bar{F}_{xi} \quad (3.7)$$

$$F_y = \max|F_{yi}| - \bar{F}_{yi} \quad (3.8)$$

$$F_z = \max|F_{zi}| - \bar{F}_{zi} \quad (3.9)$$

$$F = \sqrt{F_x^2 + F_y^2 + F_z^2} \quad (3.10)$$

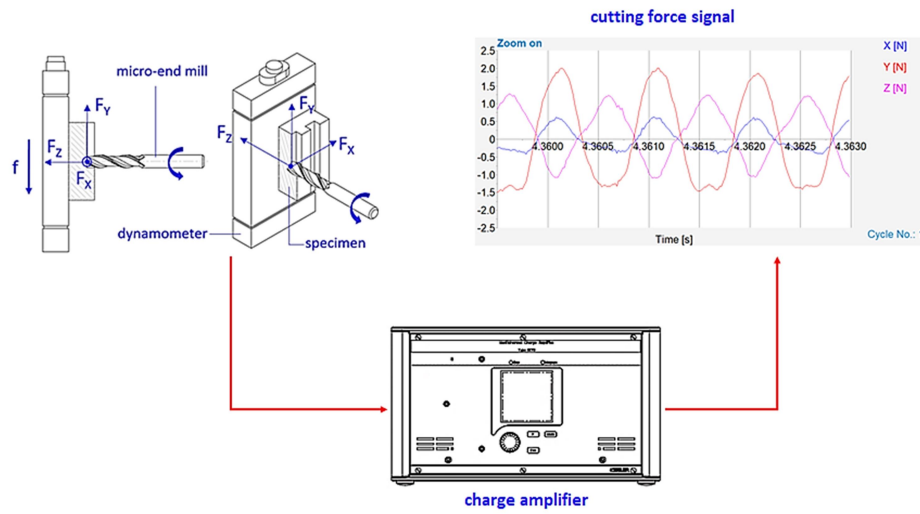


Figure 3.18: Cutting force measurement using Kistler (9256C2) piezoelectric dynamometer in micromilling

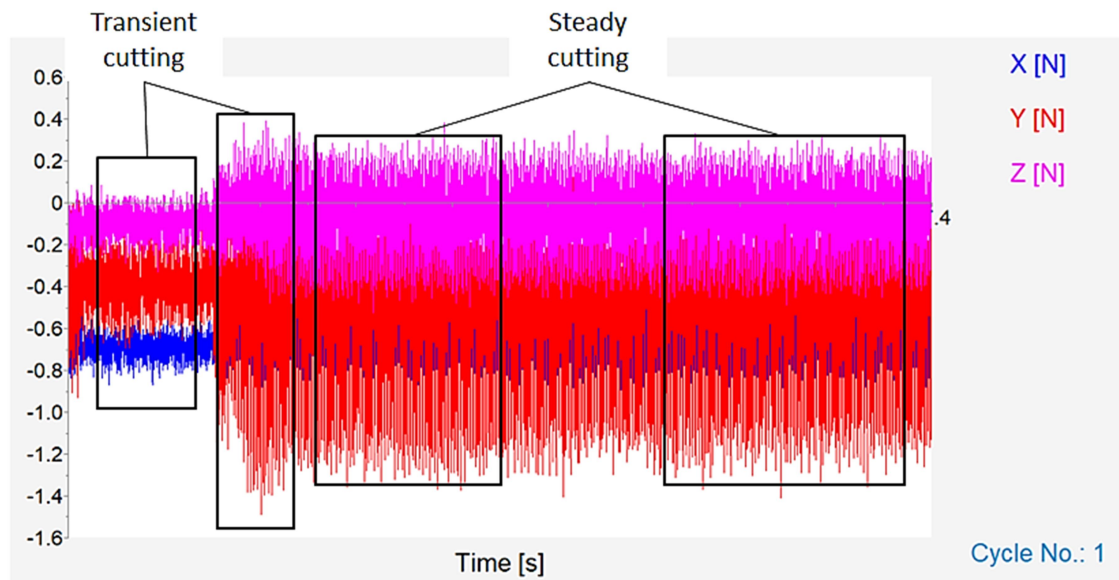


Figure 3.19: A representative sample of cutting force signal generated from the dynamometer

### 3.4.6 Surface roughness measurement

Surface roughness  $R_a$  measurements were performed on an Alicona Infinite Focus G4 (Figure 3.20) at the central line of the machined slot. Average values were obtained from



five measurements at different positions (entry, middle, and exit) in the feed direction.

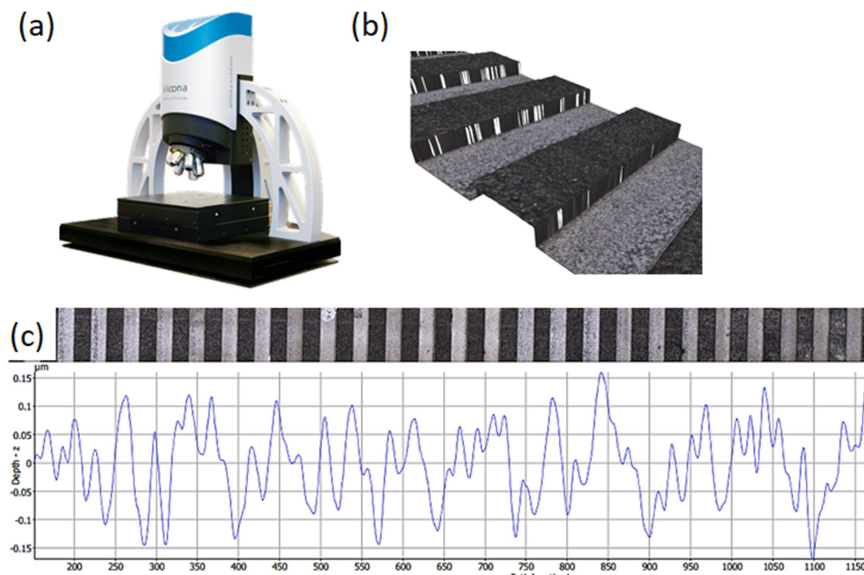


Figure 3.20: Surface roughness Ra measurement using Alicona Infinite Focus G4: (a) an Alicona Infinite Focus G4, (b) An example of a 3D scan of the machined slot, (c) An example of the roughness profile

The surface roughness Ra was also measured using Mitutoyo Surftest SJ-410 (0.25 mm and 2.5 mm cut off and measurement length, respectively) (Figure 3.21) at the centre line of each slot. Average values were also obtained from five measurements at different positions (entry, middle, and exit) that were similar to those of Alicona Ra measurements. These Ra measurements were used to validate the results from the contactless method (using Alicona microscope).



Figure 3.21: Surface roughness Ra measurement using Mitutoyo SJ-410 contact style profilometer



### 3.4.7 Tool wear measurement

The scanning electron microscope (SEM) TESCAN MIRA3 was used to investigate tool wear. The geometry of new tools was first considered by SEM imaging. The non-uniform flank wear (VB 2) and the stair-formed face wear (KT 2) were used as the main criteria tool wear assessment that was based on ISO 8688-2 standard [379]. The flank wear VB2 was the maximum bandwidth in the perpendicular direction to the original cutting edge on the side view (Figure 3.22). The face wear KT 2 occurred at the intersection of the wear scar and the major flank surface was measured perpendicular to the tool face (Figure 3.23). Tool wear was also assessed by identifying the tool diameter's reduction between new and used tool (Figure 3.24).

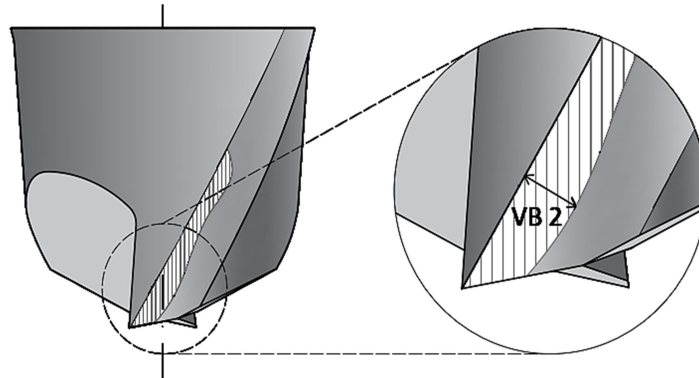


Figure 3.22: Non-uniform flank wear measurement

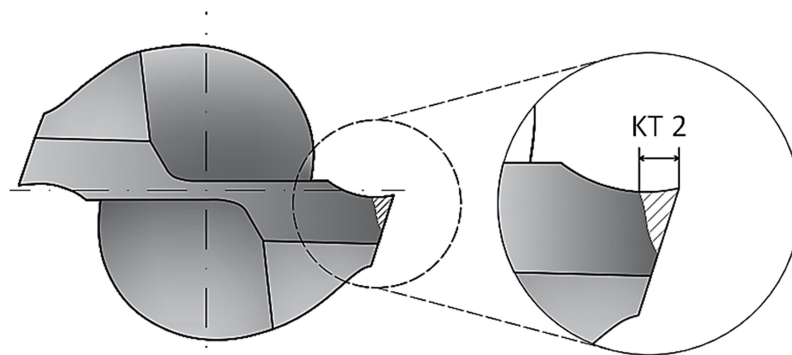


Figure 3.23: Stair-formed face wear measurement (with the original cutting-edge outline)

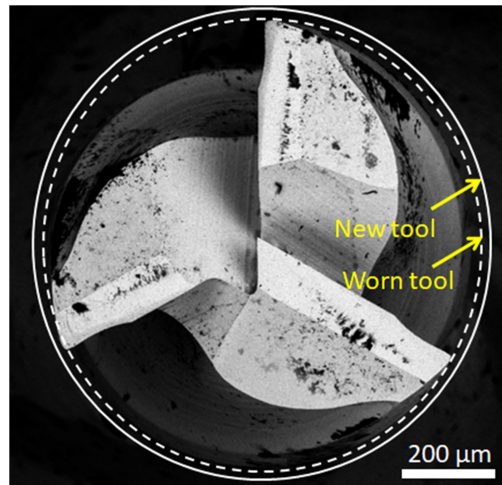


Figure 3.24: An example of SEM imaging represented tool diameter measurement

### 3.4.8 Dimensional accuracy measurement

Similar to tool wear measurement, SEM imaging was also employed to assess the dimensional accuracy when micromilling of epoxy-based nanocomposites. The assessment was implemented based on the slot width measurement at each cutting condition and filler content. Figure 3.25 shows an example of slot width measurement using SEM imaging. Five measurements were conducted in the same slot from the entry to the exit and the average values represented the slot width.

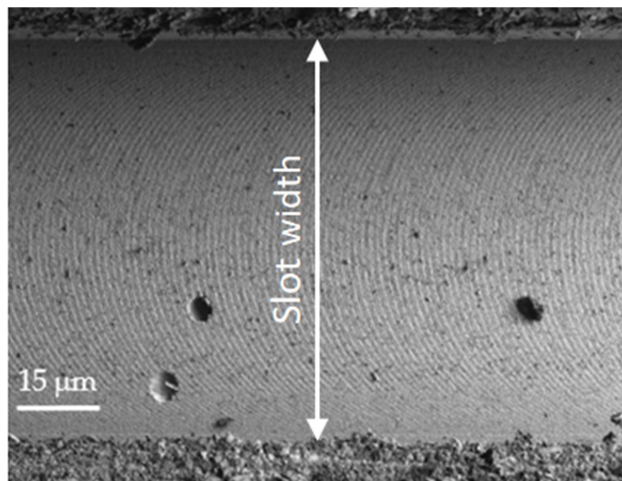


Figure 3.25: An example of SEM imaging represented tool slot width measurement

## Chapter 4: Machinability of carbon nanofiller reinforced epoxy nanocomposites at micro cutting chip load

### 4.1 Introduction

This chapter represented the investigation on the machinability of graphene reinforced epoxy nanocomposites (epoxy/graphene) in micromilling that was divided into two parts.

The main objectives of part I were cutting force and surface roughness in the considerations of FPT, cutting speed, and graphene loading. Three different compositions were used in this study including 0.1 wt.%, 0.5 wt.%, and 1.0 wt.% graphene. Additionally, plain epoxy was also employed for comparative purpose. In the consideration of the cutting conditions, the DoC remained the same at 100µm during the cutting process while various cutting speed and feed per tooth (FPT) are applied as input variables. Three different levels were chosen for both cutting speed (from 62.8 to 188.5 m/min) and FPT (5 to 15 µm). The uncoated micro-end milling tools used in this study had some main features as follows: micro-grain carbide substrate, two flutes, cutting diameter of 1 mm and helix angle of 30°. The characterisation of thermomechanical properties was also addressed to support the machinability analysis. The details of experimental works including cutting parameters, tool and workpiece material are summarised in Table 4.1.

Table 4.1: Experimental settings

Filler loading (wt.%)	0, 0.1, 0.5, 1	
Cutting tool	Material	Micro grain carbide Co 10%
	Number of flutes	2
	Cutting diameter (mm)	0.5
	Flute length (mm)	1.8
	Helix angle	20 <sup>0</sup>
Cutting conditions	Cutting speed (m/min)	62.8, 125.6, and 188.5
	Feed rate (µm/tooth)	5, 10, 15
	Depth of cut (DoC) (µm)	100

In part 2, the tool wear behaviour of the micro-end mill was investigated. The effect of material's microstructure (i.e., anisotropy, heterogeneity) thermomechanical properties

associated with the size effects [380] contributed to accelerated tool wear. Additionally, the increases of MUCT [381], cutting edge radius, and flank wear due to tool wear acceleration could result in cutting force rising in micromachining nanocomposites [380]. Moreover, the use of micro-tools in high-cutting-speed conditions in micromachining could significantly reduce tool life. It was also necessary to address the effects of thermomechanical properties of nanocomposite materials and their microstructures on the cutting mechanism (i.e., shearing, ploughing) and the chip adhesion. However, the investigations on tool wear behaviour have been still limited, especially in the micromachining of polymer nanocomposites. Therefore, the investigation on tool wear behaviour when micromilling of epoxy/graphene nanocomposites was necessary. This study performed the micromilling epoxy/0.3 wt.% graphene nanocomposites at a feed rate of 20 $\mu\text{m}/\text{rev}$  (or FPT of 6.7 $\mu\text{m}$ ), 100 $\mu\text{m}$  axial DoC and under dry cutting conditions. Three different 3 flute-micro-tools including uncoated, Diamond-Like Carbon (DLC) and diamond were employed with some main features: micro-grain carbide Co 10%, helix angle of 30°. The main objective of the investigation was tool wear behaviour. The effect of tool wear on the variations of cutting force, surface roughness, and dimensional accuracy was also addressed. The details of experimental works including cutting parameters, tool and workpiece material are summarised in Table 4.2.

Table 4.2: Experimental settings

Filler loading (wt.%)	0, 0.3	
Cutting tool	Substrate material	Micro grain carbide Co 10%
	Number of flutes	3
	Cutting diameter (mm)	1
	Flute length (mm)	4
	Helix angle	30°
	Coating materials	Diamond and DLC
Cutting conditions	Cutting speed (m/min)	62.8 and 188.4
	Feed rate ( $\mu\text{m}/\text{rev}$ )	20
	Depth of cut (DoC) ( $\mu\text{m}$ )	100

## Part I: Cutting force and surface roughness

### 4.2 Machined surface morphology

Figure 4.1 shows the SEM images of the machined surface morphology of epoxy/1 wt.% graphene polymer nanocomposites after micromilling processes at FPT of  $5\mu\text{m}$  and cutting speed of  $62.8\text{ m/min}$ . The addition of graphene was expected to improve the thermal conductivity of epoxy nanocomposite [382], hence encouraging heat dissipation in the cutting area. It consequently led to the reduction of the thermal softening effect that might contribute to less chip adhesion on the machined surface, hence resulting in surface quality improvement. This was confirmed by the negligible burr formation on the slot edges and chip debris adhesion as seen in Figure 4.1a, b. This result was identical to those of micromilling PC nanocomposites [331]. However, the SEM evaluation revealed that graphene pull-out and smearing were the main patterns of the machined surfaces (Figure 4.1c, d, e, and f). Graphene smearing also led to the obscuration of the feed marks (Figure 4.1b). The pre-machined material damage in terms of internal porosity (Figure 4.1a) due to insufficient processing method in producing the as-received material might contribute to this.

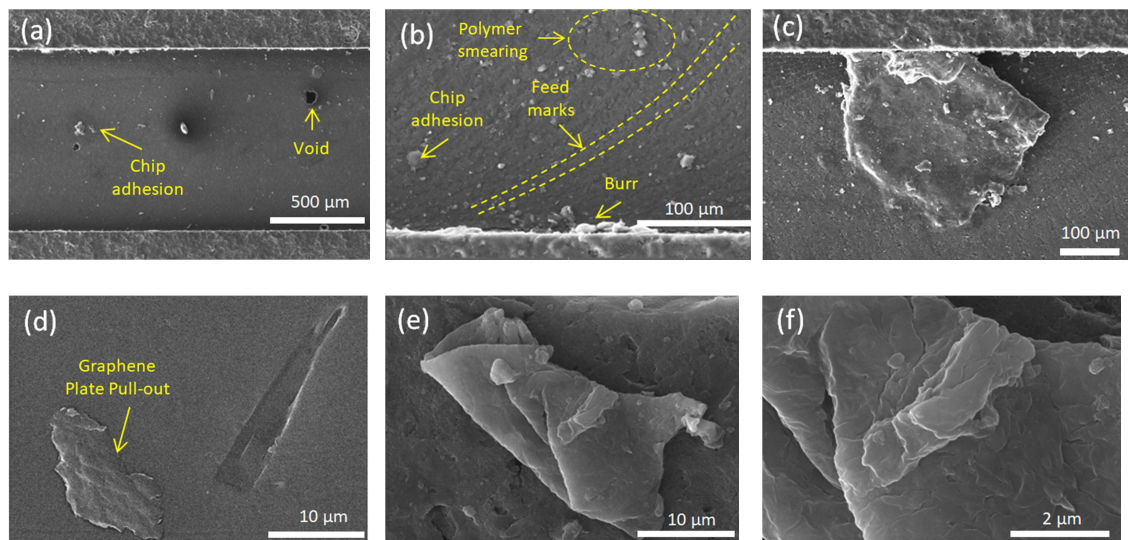


Figure 4.1: SEM images for a machined slot in graphene/epoxy specimens (at FPT of  $5\mu\text{m}$  and cutting speed of  $62.8\text{ m/min}$ )

### 4.3 Cutting force

#### 4.3.1 ANOVA analysis

ANOVA analysis from Minitab18 software was employed in this study to statistically identify the distributions of input variables (i.e., cutting speed) and their effect on the cutting force variation. The methods and formulas can be found in [383]. Table 4.3 represents the ANOVA analysis of the resultant cutting force that considers the influences of three main input factors. Generally, all filler content, FPT, and cutting speed showed significant influences on the cutting force. Among these variables, the cutting speed significantly influenced the cutting force with its contribution of around 43% followed by FPT and filler content (19% and 11%, respectively).

Table 4.3: ANOVA result for the resultant cutting force when micromilling epoxy/graphene nanocomposites

Source	DF	Seq SS	Contribution	Adj SS	Adj MS	F-Value	P-Value
Filler Content	3	5.244	18.91%	5.244	1.7479	6.61	0.002
Cutting Speed	2	11.958	43.12%	11.958	5.9788	22.59	< 0.001
FPT	2	3.121	11.25%	3.121	1.5605	5.90	0.007
Error	28	7.409	26.72%	7.409	0.2646		
Total	35	27.732	100.00%				

*DF: Degrees of Freedom, Seq SS: Sequential sums of squares, Adj SS: Adjusted sums of square, Adj MS: Adjusted mean square*

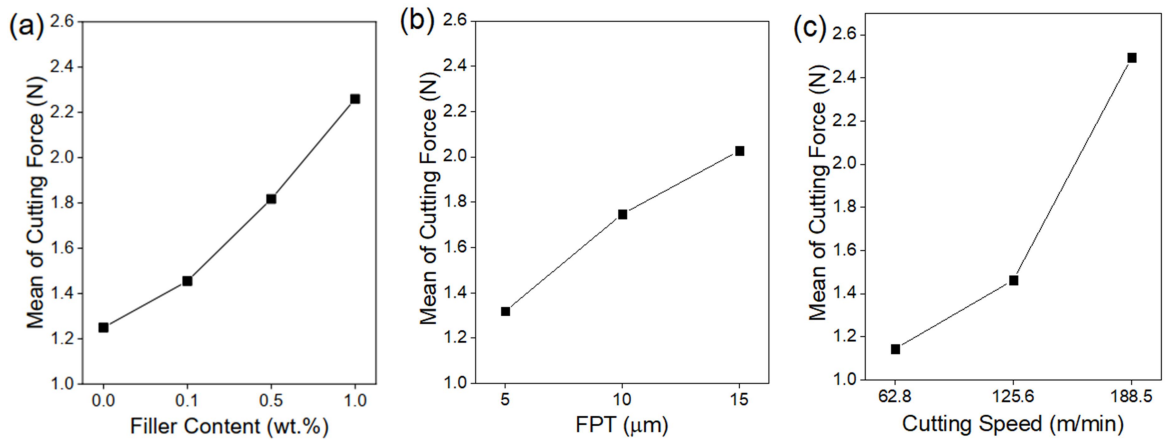


Figure 4.2: Main effect plots for the resultant cutting forces when micromilling epoxy/graphene nanocomposites: (a) Filler content, (b) FPT, and (c) Cutting speed

### 4.3.2 Cutting force analysis

Figure 4.3(a-c) show the average cutting force's variations at a function of FPT at different filler contents and cutting speeds. In general, the cutting force's magnitude when micromilling of epoxy/graphene nanocomposites and plain epoxy ranged between 0.72 and 4.54 N with a generally rising trend as FPT increased due to the increased chip load. This indicated the dominance of the feed rate effect on the cutting force variations by the formation of feed marks. Among different workpiece materials, plain epoxy and 0.1 wt.% graphene showed relatively low cutting forces compared to those of the high-filler-content nanocomposites. It was due to the low mechanical properties of these compositions compared to those of other materials (0.5 wt.% and 1 wt.%).

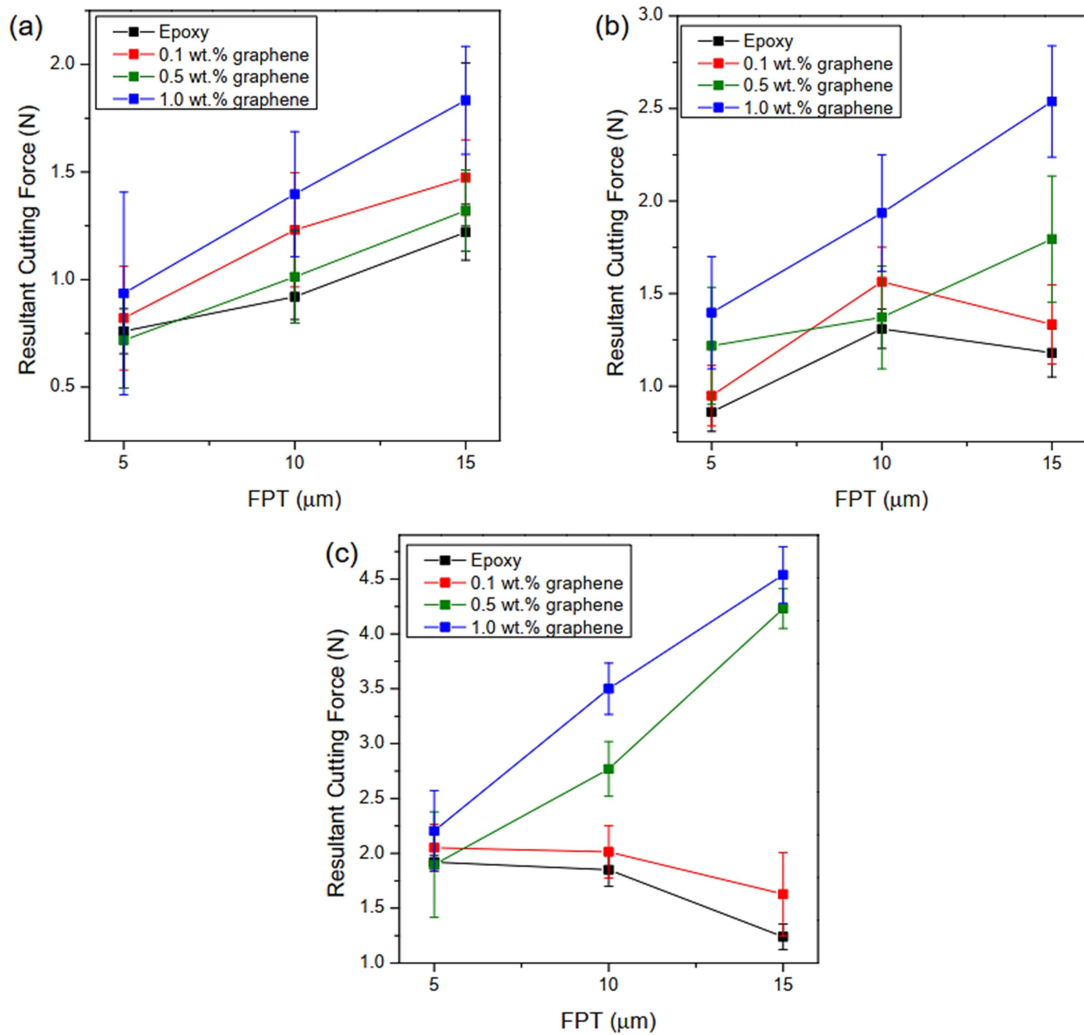


Figure 4.3. Cutting force results when micromilling of graphene/epoxy nanocomposites at different filler contents: (a) 62.8 m/min, (b) 125.6 m/min, and (c) 188.5 m/min

The characterisation of these materials (Table 4.4) showed significant enhancements of tensile modulus and hardness of 0.5 and 1 wt.% compositions that are likely to increase the cutting forces when micromilling these nanocomposites. A decrease of the cutting force variation of both plain epoxy and 0.1 wt.% graphene was observed at high cutting speeds. The thermal softening effect might appear while micromilling these materials due to their low glass transition temperature (Table 4.4), resulting in low cutting force generated. On the other hand, the dominance of the strengthening effect when



micromilling high-filler-content nanocomposites (0.5 wt.% and 1 wt.%) led to the significant increase of cutting force with FPT due to high chip load [384].

Table 4.4: Effect of filler content on mechanical properties of epoxy/graphene nanocomposites ([375, 385])

Content (wt.%)	Tensile strength (MPa)	Tensile modulus (GPa)	Fracture toughness (MPa.m <sup>1/2</sup> )	Hardness (GPa)	Glass transition temperature T <sub>g</sub> (°C)
0	57.24	0.868	0.687	0.216	93.37
0.1	60.51	1.030	0.761	0.225	97.15
0.3	64.44	1.169	0.831	0.235	99.08
0.5	63.84	1.219	0.805	0.246	98.35
1	58.53	1.360	0.734	0.255	97.12

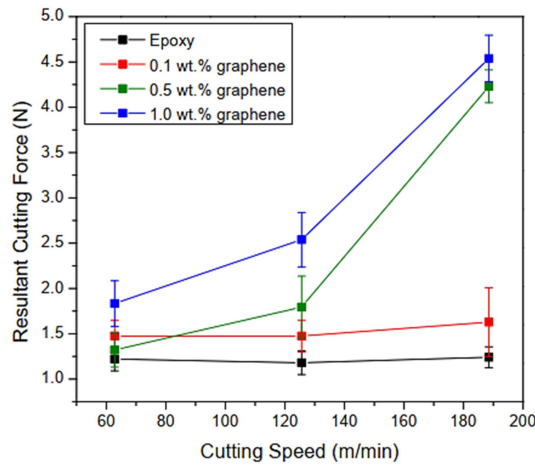


Figure 4.4: Effect of cutting speed on the cutting force when micromilling epoxy/graphene nanocomposites at different filler contents (FPT= 15 μm)

From Figure 4.4, it could be observed that the cutting force's increase of 0.5 wt.% and 1 wt.% nanocomposite showed higher sensitivity to FPT increment compared to those of other materials (epoxy and 0.1 wt.%). The increment of cutting speed could lead to higher cutting temperature due to the generated heat from tool-workpiece contact. It resulted in the presence of a thermal softening effect for the materials which inherently had low glass transition temperature (i.e., epoxy, 0.1 wt.%) [386]. On the other hand, strain hardening took place at high temperature for other which had higher T<sub>g</sub> (0.5 and 1 wt.%),

resulting in a higher cutting force required. There was an exception in the case of 1 wt.% material in which its  $T_g$  was relatively low but still exhibited the same cutting force's trend as 0.5 wt.% counterparts. This phenomenon might be contributed by the micro-structure effect at such a high filler loading. With high filler content of 1 wt.%, the micro-tool had a high tendency to contact with the rough and wrinkle surface texture of graphene platelets, hence increasing the cutting forces [384]. At the lowest cutting speed (62.8 m/min), there was no significant difference of cutting force's magnitudes between the various workpiece materials, indicating no effect of either thermal softening or strain hardening in this case.

#### 4.4 Surface roughness

##### 4.4.1 ANOVA analysis

Statistical analysis of ANOVA was applied to identify the level of input factor's distributions including filler content, FPT, and cutting speed on the machined surface roughness. The results from Table 4.5 indicated that both filler content and FPT were the most influential factors in Ra variation with their contributions of around 32% and 36%, respectively. On the contrary, the cutting speed seemed not to have a considerable effect on Ra.

Table 4.5: ANOVA result for the average surface roughness when micromilling epoxy/graphene nanocomposites

Source	DF	Seq SS	Contribution	Adj SS	Adj MS	F-Value	P-Value
Filler Content	3	0.071559	31.79%	0.071559	0.023853	9.29	< 0.001
Cutting Speed	2	0.000846	0.38%	0.000846	0.000423	0.16	0.849
FPT	2	0.080766	35.88%	0.080766	0.040383	15.72	< 0.001
Error	28	0.071911	31.95%	0.071911	0.002568		
Total	35	0.225082	100.00%				

##### 4.4.2 Surface roughness analysis

Figure 4.5(a-c) shows the effect of FPT on the machined surface roughness when micromilling epoxy/graphene nanocomposites. Generally, Ra showed an upward trend as FPT increases from 5 to 10 $\mu\text{m}$ , regardless of the cutting speed and the filler content. It indicated the dominance of cutting chip load in increasing the surface roughness due to plastic deformation increased. Ra hit a peak of  $\sim 0.45\mu\text{m}$  at cutting speed of 62.8 m/min and FPT of 15 $\mu\text{m}/\text{tooth}$  when machining 1 wt.% graphene/epoxy nanocomposites.

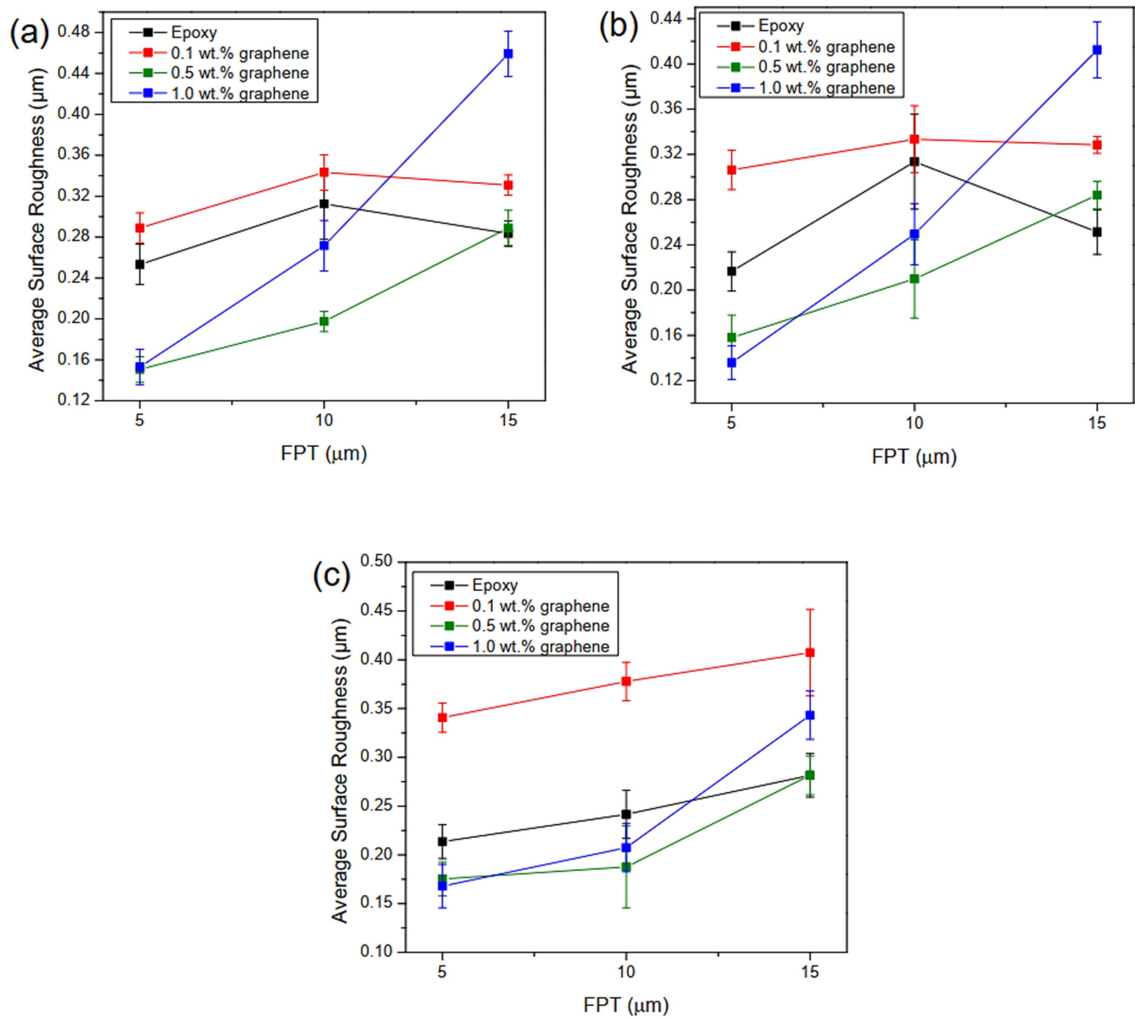


Figure 4.5 The average surface roughness as a function of FPT when micromilling epoxy/graphene nanocomposites at different filler contents: (a) 62.8 m/min, (b) 125.6 m/min, and (c) 188.5 m/min

On the other hand, the relatively high surface quality was obtained when micromilling epoxy/ 1 wt.% graphene at FPT of 5  $\mu\text{m}$  regardless of the used cutting speed. It was due to the lubricant effect of graphene at this filler content that improved the surface quality. The formation of tribofilm layer on the machined surface that resulted in the reduction of friction coefficient was addressed in the literature [387]. Additionally, the low fracture toughness of 1 wt.% composition compared to other nanocomposites (0.1 and 0.5 wt.%) [388] resulted in less plastic deformation on the machined surface at low chip load (FPT of 5 $\mu\text{m}$ ), hence reducing its surface roughness.

The surface roughness increases of 0.5 wt.% and 1 wt.% exhibited higher sensitivity with FPT than those of 0.1 wt.% and plain epoxy. It indicated the dominance of strengthening effect of these materials [388] that resulted in higher plastic deformation on the machined surfaces (or higher feed marks) as FPT increased. Additionally, the cutting force significantly increased with FPT when the micromilling of these two materials (Figure 4.4). It implied that these high cutting forces generated more tool vibration, hence resulting in the reduction of the surface quality of these high-filler-content compositions [389]. Given such high filler loading and small cutting tools, Ra tended to show high tool-vibration sensitivity in the micromilling of heterogeneous nanocomposites. This vibration was produced due to the microstructure effect of the workpiece. As the micro-tools moving through different phases (matrix and filler phase), the cutting force magnitude varied from low (when cutting polymer matrix phase) to high (when cutting filler phase). Given a small diameter of micro-tool (1mm), the micro-cutting process of these heterogeneous nanocomposites (0.5 and 1 wt.%) had a high tendency of generating high tool vibration compared to other compositions (epoxy and 0.1 wt.%). It resulted to the higher values of the surface roughness when micro-milling epoxy/ 1 wt.% graphene at 62.8 and 125.6 m/min (FPT of 15 $\mu\text{m}$ ) (Figure 4.5a and b) compared to epoxy and 0.1 wt.% composition. These results indicated the dominance of FPT effect in increasing the surface roughness over the lubricant of graphene (in reducing Ra) at the highest FPT.

It was also noticed a slight decrease of Ra when micromilling of epoxy and 0.1 wt.% materials at FPT of 15 $\mu\text{m}$  at low cutting speeds (62.8 and 125.6 m/min) (Figure 4.5a, b). Under high chip load and low cutting speed, the viscoelastic epoxy phase in these

materials was smeared (Figure 4.1b), hence slightly reduced the surface roughness. These slight reductions of Ra at high chip load and low cutting speed could be seen in the literature [390].

Figure 4.6 shows the effect of filler on the machined surface roughness when micromilling of epoxy/graphene nanocomposites at FPT 10 $\mu$ m. Ra generally showed the highest magnitude at 0.1 wt.%, followed by plain epoxy. As the filler content increased further, the surface roughness appeared to be reduced at 0.5 wt.% but slightly increased at 1wt.%. The rise of Ra as the filler content increased from 0 (epoxy) to 0.1 wt.% was contributed by the strengthening effect of graphene, as can be seen from Table 4.4.

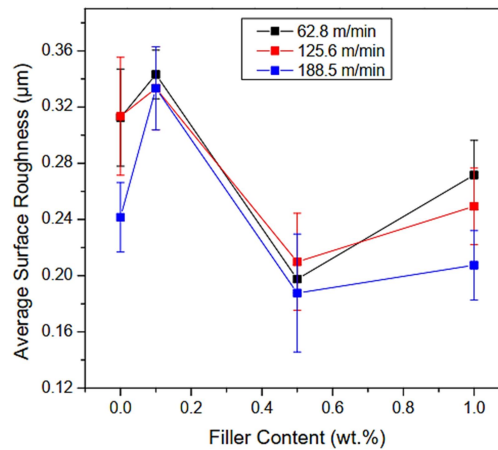


Figure 4.6 The effect of filler content on the average surface roughness at different filler cutting speeds when micromilling epoxy/graphene nanocomposites at FPT of 10 $\mu$ m

The higher the stiffness of the workpiece material led to more plastic deformation on the machined surface, hence increasing the surface roughness [391]. As the filler content reached 0.5 wt.%, the Ra was significantly reduced. Given this relatively high filler loading, the presence of graphene could reduce the tool-chip friction due to its low friction coefficient, hence improving the surface quality [392]. However, further addition of filler loading up to 1 wt.% resulted in a slight increase of Ra, which was due to more graphene deflection, resulting in more crack propagation on the machined surface [393].

#### **4.5 Summary**

The investigation on the micro-machinability of graphene reinforced nanocomposites in chapter 4-part I revealed the significant effects of cutting conditions (i.e., FPT, cutting speed) and workpiece materials on the cutting force and surface roughness variations. The ANOVA identified that the cutting force was influenced by all filler content, FPT, and cutting speed. On the other hand, only filler content and FPT were the most influential factors affecting the surface roughness. In general, the machinability of epoxy/graphene nanocomposites when micromilling at micro-cutting chip load showed a relatively similar trend to those of macro-cutting as both the cutting forces and the surface roughness increased with FPT. However, when the other input factors were taken into consideration including filler content and cutting speed, the machining behaviour of these materials became more sensitive to the microstructure effect and thermomechanical properties of the workpiece materials. It was indicated by the reduction of cutting force at high cutting speeds when micromilling epoxy and epoxy/0.1 wt.% graphene due to thermal softening. Also, the influences of lubricating graphene at high filler loadings (0.5 and 1wt.%) on the surface roughness reduction at low FPT (5 $\mu$ m) also represented the effect of workpiece materials. On the other hand, the microstructure effect increased the surface roughness of epoxy/1 wt.% graphene when high FPTs were employed (10-15 $\mu$ m) due to more tool vibration when moving between different phases of the nanocomposites' structure. The cutting condition at low cutting speeds and FPTs were recommended for micromilling epoxy/graphene nanocomposites to generate low cutting force and surface roughness, respectively.

## Part II: Tool wear

### 4.6 Tool wear analysis

Figure 4.7a shows an SEM image of a typical tool diameter reduction of the uncoated tool, whilst Figure 4.7b shows a comparison between three tools diameters (Uncoated, DLC and diamond) after cutting 500 slots (at two different cutting speeds). The initial diameters of the three tools were different because of the coating layer. In general, the uncoated micro end-mill showed the most considerable reduction of tool diameter following by the DLC counterpart. In contrast, the diamond tool exhibited the opposite trend with a slight increase in this category due to the adhesion of melted chip as can be seen from Figure 4.8c, f.

The rapid tool wear of uncoated tools was contributed by the highly abrasive nature of strong workpiece material (Table 4.4) combined with the tool material's high friction of coefficient. The SEM images from Figure 4.8a, d with noticeable edge rounding of the uncoated, regardless of the cutting speed, were revealed. However, the uncoated tool diameter variation was different from the other two tool types (DLC and diamond) with a non-linear trend. Unexpectedly, the uncoated tool diameter increased when the cutting speed reaches 188.4 m/min instead of further reduced. In a close investigation, Figure 4.8d shows more obvious chip adhesion on the uncoated tool surfaces at the high cutting speed that unlikely to appear at the lower cutting speed (Figure 4.8a).

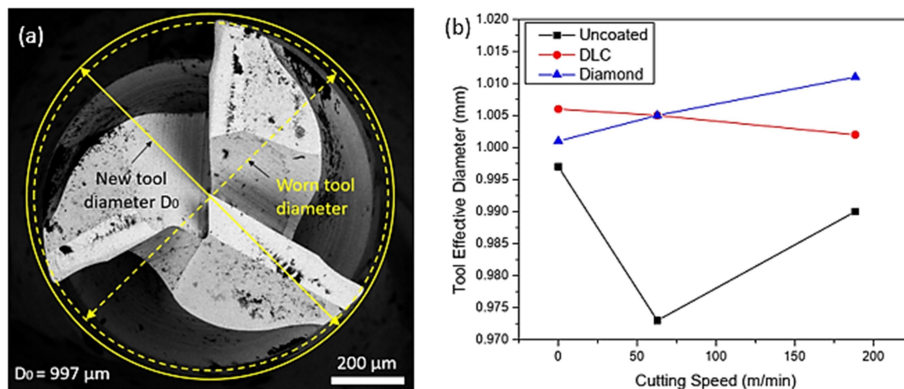
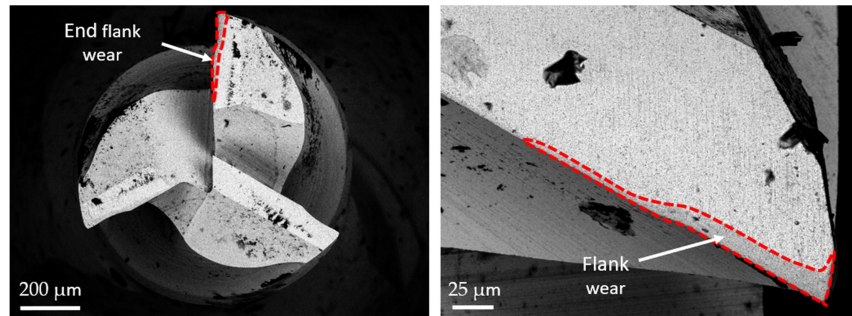
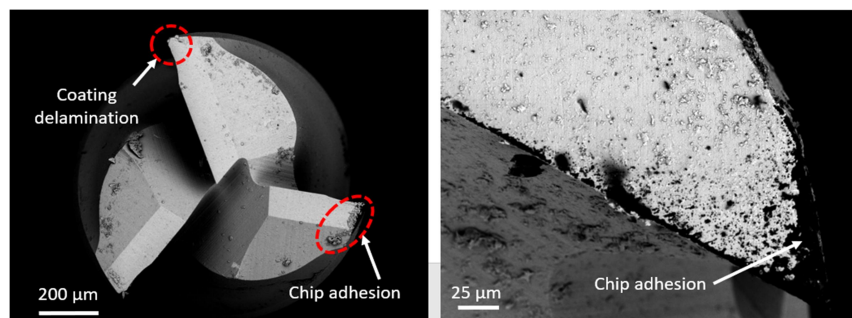


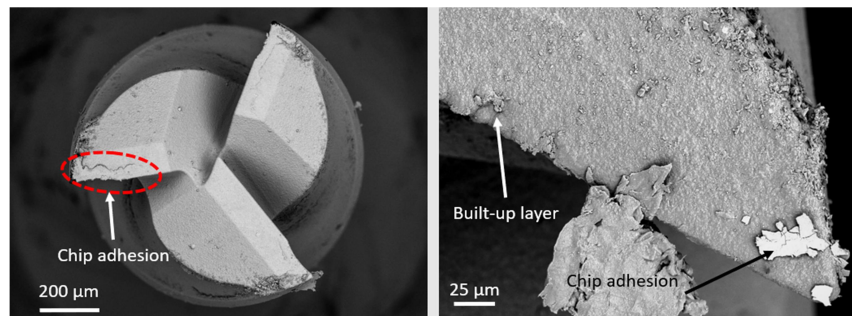
Figure 4.7: (a) SEM image of tool diameter reduction of the uncoated tool; (b) Effect of tool type and cutting speed on reducing the effective tool diameter.



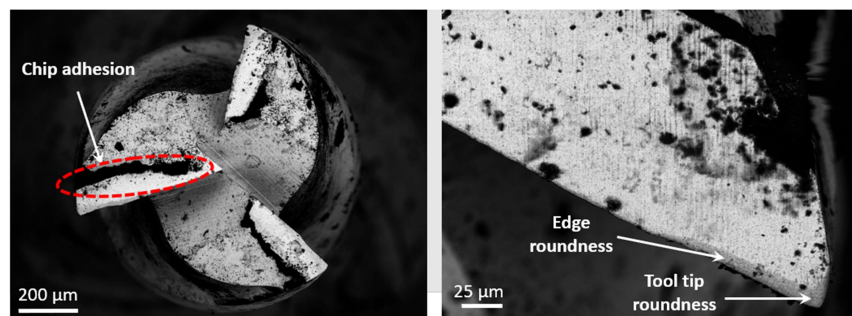
(a) Uncoated tool at cutting speed of 62.8 m/min



(b) DLC tool at cutting speed of 62.8 m/min



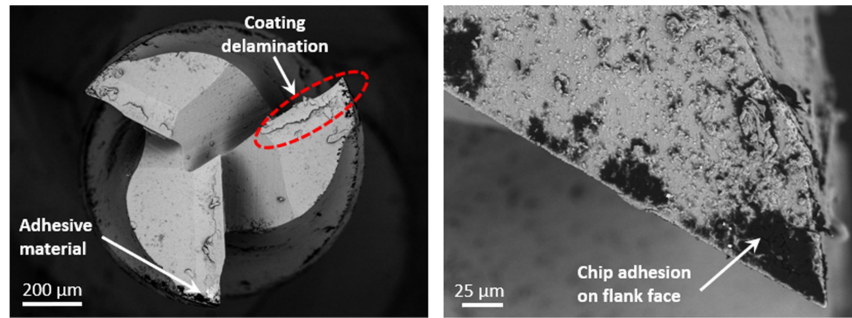
(c) Diamond tool at cutting speed of 62.8 m/min



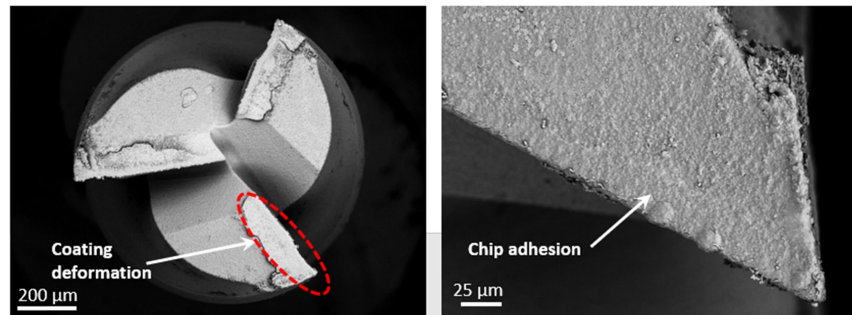
(d) Uncoated tool at cutting speed of 188.4 m/min

Figure 4.8: SEM images of tool wear of different micro-end mills under various cutting speed (after removing  $650 \text{ mm}^3$  of material or 500 slots) (left: top view, right: side view)





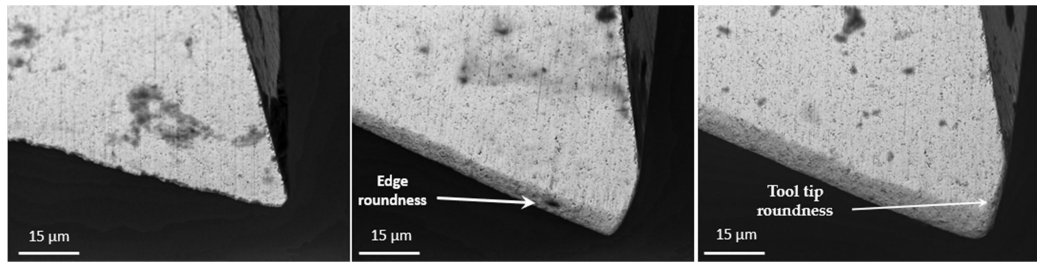
(e) DLC tool at cutting speed of 188.4 m/min



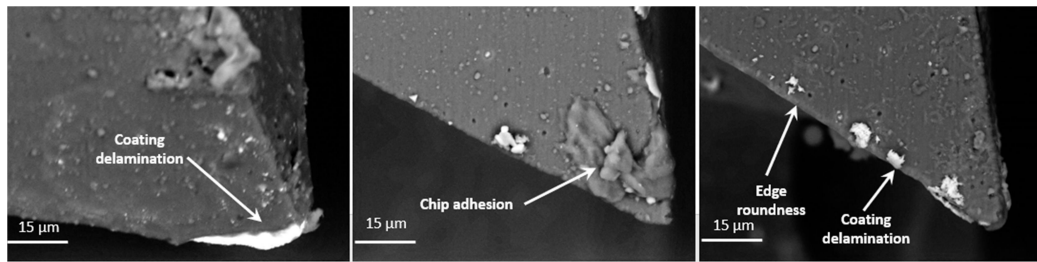
(f) Diamond tool at cutting speed of 188.4 m/min

Figure 4.8: continued.

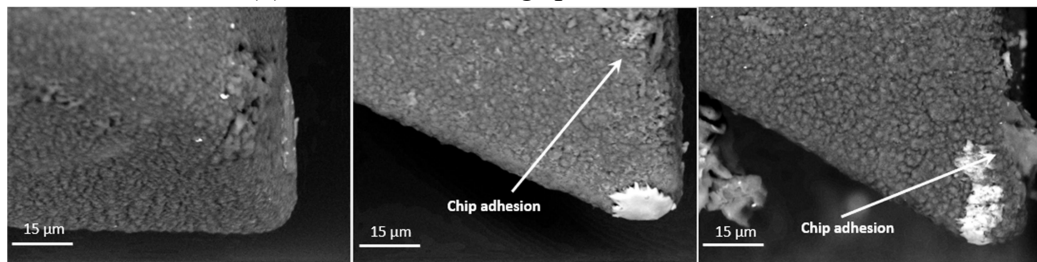
However, the apparent uncoated tool tip rounding can also be seen in Figure 4.9d, contributing to this cutting condition's highest cutting force (Figure 4.10). The mechanism that explained the tool radius's effect on cutting force in micromachining has been described [380]. It detailed that (i) the increase of tool radius due to tool tip roundness made the micro-tools blunt, consequently, generating high shear angle in cutting area or high plastic deformation of the workpiece, hence increasing cutting force, (ii) the tool tip roundness increased the contact area between flank face and workpiece, therefore, accelerating flank wear rate. It generated high cutting temperature [394], especially when micro-cutting inhomogeneous nanocomposites using uncoated tools with a high friction coefficient at high cutting speed. Thus, the thermal softening effect seemed dominant in this case, causing more chip adhesion on the flank face of the uncoated tool (Figure 4.8d), hence increasing the tool diameter at the cutting speed of 188.4 m/min.



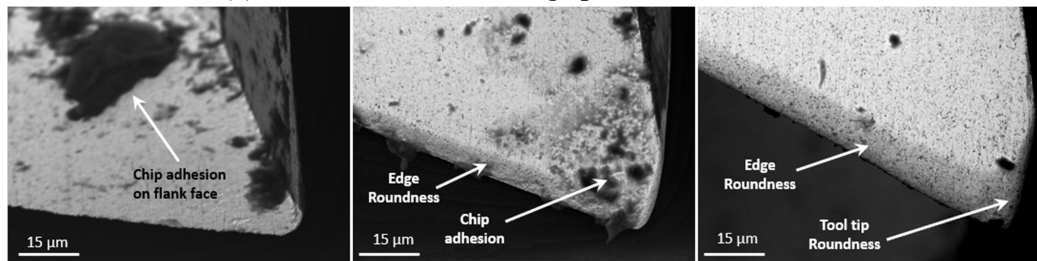
(a) Uncoated tool at cutting speed of 62.8 m/min



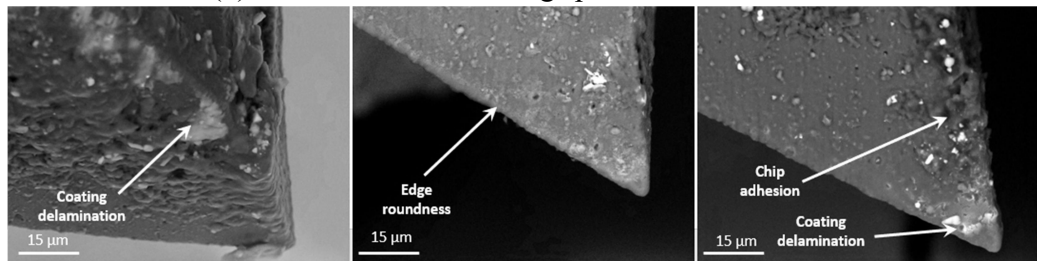
(b) DLC tool at cutting speed of 62.8 m/min



(c) Diamond tool at cutting speed of 62.8 m/min

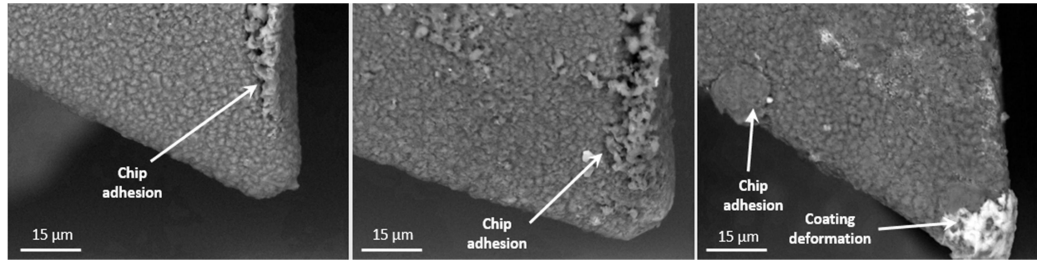


(d) Uncoated tool at cutting speed of 188.4 m/min



(e) DLC tool at cutting speed of 188.4 m/min

Figure 4.9: SEM images showing tool wear progression of different micro-end mills under the various cutting speed (From left to right: 10 slots, 300 slots and 500 slots)



(f) Diamond tool at cutting speed of 188.4 m/min

Figure 4.9: continued.

In the DLC case, the tool diameter reduction trend showed almost linear relation with cutting speed that indicated the dominance of cutting force influence on accelerating the tool wear of this type of micro-cutting tools. However, this trend was less severe than those of the uncoated tool. It was due to the high wear resistance and low friction of the DLC coating layer [395].

The use of DLC micro end-mill has shown a remarkable reduction of flank wear [396]. This reduction can be seen from Figure 4.8b and e with unobvious tool flank wear or less tool tip rounding from Figure 4.9b, e compared to those of uncoated tool. Coating delamination seemed to be the primary tool to wear a pattern in this case. The tool flank surfaces also showed material adhesion that might also contribute to a slighter reduction in a DLC tool's diameter than an uncoated tool. On the contrary, an opposite trend of the tool diameter after cutting 500 slots was reported when applying diamond tool with an increase in diameter of 10µm (at 188.4 m/min) and 4µm (at 62.8 m/min) compared to the new tool. Edge rounding was hardly observed for diamond tools (Figure 4.8c, f).

Moreover, aggressive workpiece material adhesions were seen on all diamond tools used at both cutting speeds. The layers of chip adhesion on tool surfaces could protect cutting tools from edge chipping and severe edge rounding [397]. It was also necessary to address low cutting forces' role when using diamond tools to reduce the tool wear compared to those of uncoated tools (Section 4.7).

The analysis of tool wear revealed the interaction between tool wear and cutting force. Micromachining polymer nanocomposites with high mechanical properties (i.e., fracture toughness, hardness) and thermal properties (i.e., thermal conductivity)

compared to plain matrix material at high cutting speed could lead to a higher tool wear rate. At an increased tool wear rate, the micro-tools became blunt, hence increasing the cutting force. This interaction was shown in micromilling using the uncoated tool in this study, exhibiting severe tool wear progress (Figure 4.9) and high cutting force at high cutting speed (Figure 4.7b). It also highlighted the essential roles of coating material such as DLC or diamond to reduce both cutting force and tool wear during the micro-cutting process.

#### **4.7 Effect of tool wear on cutting force**

In general, measured cutting forces were relatively higher at high cutting speed regardless of the tool material and the cutting progress (Figure 4.10). This phenomenon was opposed to those when micromilling PC/CNT [398] or epoxy/graphene nanocomposites [399]. However, the mechanism was identically based on strengthening or thermal softening dominant regimes of the workpiece materials. Micromachining of nanocomposites at high cutting speed could generate high heat concentration in the cutting zone that consequently led to softening. The thermal softening effect resulted in the reduction of mechanical properties of the workpiece (i.e., stiffness, strength), hence reducing the cutting force. However, for epoxy/0.3 wt.% nanocomposite, this phenomenon unlikely appeared due to its high glass transition temperature compared to epoxy [375]. The strengthening effect seemed to be dominant in this case that resulted in the increased cutting force. Therefore, the rising trend of cutting forces as the cutting speed increased, in this case, indicating the dominance of strengthening over thermal softening effects. Based on epoxy/graphene nanocomposites' characterisations from the previous study [375, 385], the addition of 0.3 wt.% of graphene into the epoxy matrix provided significant enhancements in terms of tensile strength, tensile modulus, fracture toughness, and hardness. The high strength of graphene led to the improvements of nanocomposites' tensile properties. Moreover, this addition also increased the polymer nanocomposites' fracture toughness as graphene nanoplatelets enhanced the energy absorbing capacity of the epoxy matrix

system [388]. These nano-platelets also restrained the epoxy molecules' mobility, hence improving the hardness and the glass transition temperature  $T_g$  of the nanocomposites.

The high mechanical properties of 0.3 wt.% epoxy/graphene nanocomposites (Table 4.4) compared to other compositions (epoxy, 0.1, 0.5, and 1 wt.%) contributed to the rising trend of cutting force at cutting speed from 62.8 m/min to 188.4 m/min. Figure 4.10 also shows the higher cutting force when using uncoated micro-tools at high cutting speed over the other two tool types (DLC and diamond). This trend became more evident as cutting volume increased and reached a peak at the end of the cutting process (500 slots). These results were similar to other studies when micromilling aluminium [400]. Micromilling polymer nanocomposites, using uncoated tools with high friction coefficient could accelerate the tool wear rate due to high frictional contact between micro-tools and the workpieces, leading to cutting edge roundness, hence increasing the cutting force. This claim was validated by the tool wear analysis using SEM imaging in section 4.6.

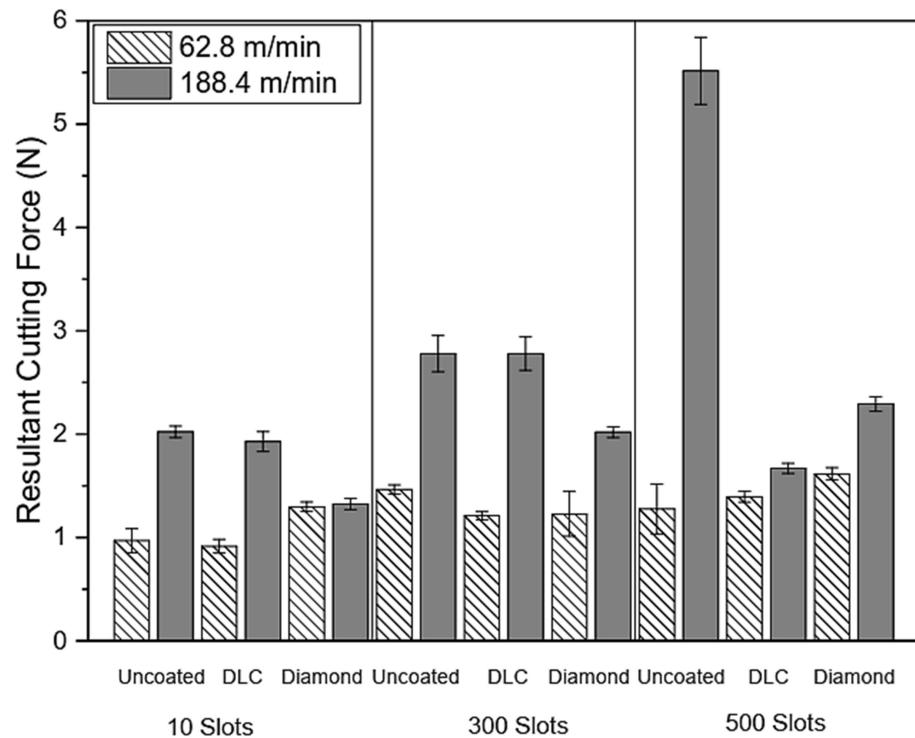


Figure 4.10: Effects of cutting speed and tool coating type on the average cutting force at different cutting stages (from 10 to 500 slots)

#### **4.8 Effect of tool wear on surface roughness**

Average surface roughness (Ra) was measured at an interval of 100 slots for a set of conditions till 500 slots ( $650 \text{ mm}^3$ ). It would also be necessary to identify Ra when new tools are used (up to 10 slots or  $13 \text{ mm}^3$ ). Figure 4.11 shows the progress of Ra values concerning tool wear (represented in terms of material removal volume). The Ra magnitudes of coated tools (DLC and diamond) at the beginning of the cutting processes (up to  $13 \text{ mm}^3$  removed material) were higher than those of uncoated counterpart. The thickness of coating layers might reduce these coated tools' sharpness, consequently increasing surface roughness [401]. Only uncoated tools exhibited a gradual rise in Ra, especially for high cutting speed (188.4 m/min).

In contrast, diamond and DLC coated tools mostly showed constant Ra values of  $650 \text{ mm}^3$  removed material. The considerable reduction in sharpness of cutting edges for the uncoated tools due to its higher tool wear rate than those of the coated tools (DLC and diamond) was the main reason for this phenomenon. The surface roughness results showed a good agreement with the tool wear analysis (Figure 4.9).

For uncoated tool, the surface roughness magnitudes of uncoated tool tended to be higher when high cutting speed was employed. Following the analysis in section 4.7 (Figure 4.10), the cutting force generated by the uncoated tool was always higher at high cutting speed, indicating the effect of rising cutting forces on the deterioration of the surface quality. The surface roughness's rising trend was mostly linear with the cutting volume in this cutting condition (uncoated tool at 188.4 m/min) (Figure 4.11b) indicating the significant effect of high tool wear rate of uncoated tool (compared to DLC and diamond tools) on reducing the surface roughness. It was due to the high plastic deformation on the machined surface generated by the blunt uncoated tool. Moreover, material adhered on uncoated tool surfaces at high cutting speed (Figure 4.7b and Figure 4.8a) further blunt the micro-tools, hence also contributing to the surface roughness increase. However, the improved surface quality generated from using the uncoated tool was observed at the beginning (from 13 to  $130 \text{ mm}^3$  of material removal volume) and the end of the tool wear progress (from 520 to  $650 \text{ mm}^3$  of material removal volume) at the cutting speed of 62.8 m/min (Figure 4.11a). The initial

tool wear at the beginning ( $130 \text{ mm}^3$ ) seemed to make the uncoated tool slightly shaper compared to the new tool (Figure 4.9a), hence resulting in a slight improvement of Ra at this stage. At the last stage ( $650 \text{ mm}^3$ ), the reduced surface roughness was contributed by the epoxy smearing on the machined surface. Given a low cutting speed ( $62.8 \text{ m/min}$ ), the worn tool produced a high shearing load (due to high plastic deformation compared to the new tool), hence smearing epoxy on the machined surface. It resulted in the reduction of the surface roughness at this stage.

For DLC and diamond tools, the cutting speed showed unobvious influences on the surface roughness. Ra had a noticeable rise in the diamond tool's case when increasing cutting speed from  $62.8 \text{ m/min}$  to  $188.4 \text{ m/min}$  (around 20%). It was also related to the influence of chip adhesion as seen by the increase of diamond tool diameter at the end of the cutting process (Figure 4.7b).

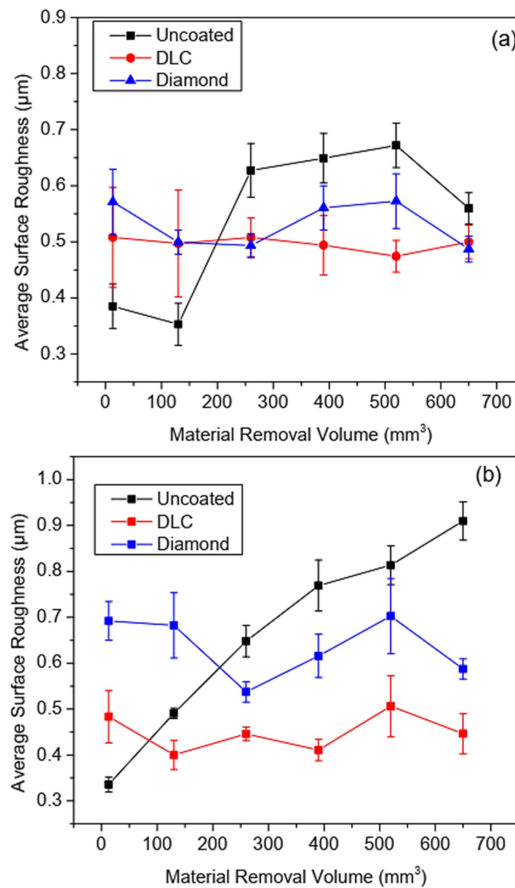


Figure 4.11: Average surface roughness (Ra) variation as a function of material removal volume at various cutting speeds: (a)  $62.8 \text{ m/min}$ ; (b)  $188.4 \text{ m/min}$

Figure 4.11 also reveals that using the DLC tool during the micromilling process provided higher machined surface quality than others (uncoated and diamond tools), regardless of the cutting speed. Low cutting forces and tool wear rate from using DLC tools were the two main factors that contributed to this phenomenon. The better performance of DLC (in terms of generating higher surface finish) than uncoated tools have been investigated by other researchers [395, 402, 403]. However, their applications in the micromilling of polymer nanocomposites have been minimal and lack sufficient analysis of their performance.

Therefore, DLC coated tools seemed to be more appropriate for micromachining graphene reinforced epoxy nanocomposites compared to the diamond and uncoated tools to improve surface finish. Figure 4.12 provides the quantitative data of the average surface roughness generated using different tools to consider the cutting speed effect. It reinforced the role of using DLC tools in reducing surface roughness compared to the diamond and uncoated tools, especially at high cutting speed (188.4 m/min).

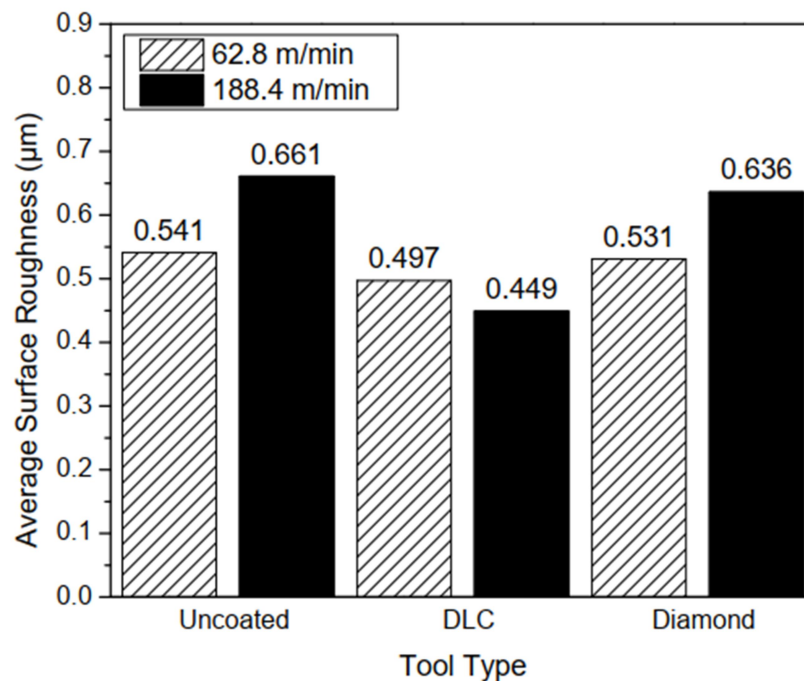


Figure 4.12: Effect of cutting speed and tool coating type on average surface roughness (in µm) at all cutting stages (from 10 to 500 slots)



#### 4.9 Effect of tool wear on machined surface morphology

Figure 4.13 shows SEM micrographs for the bottom surfaces of the machined slots. Intensive smearing (because of melting the matrix material) took place on specimens machined at higher cutting speeds (188.4 m/min).

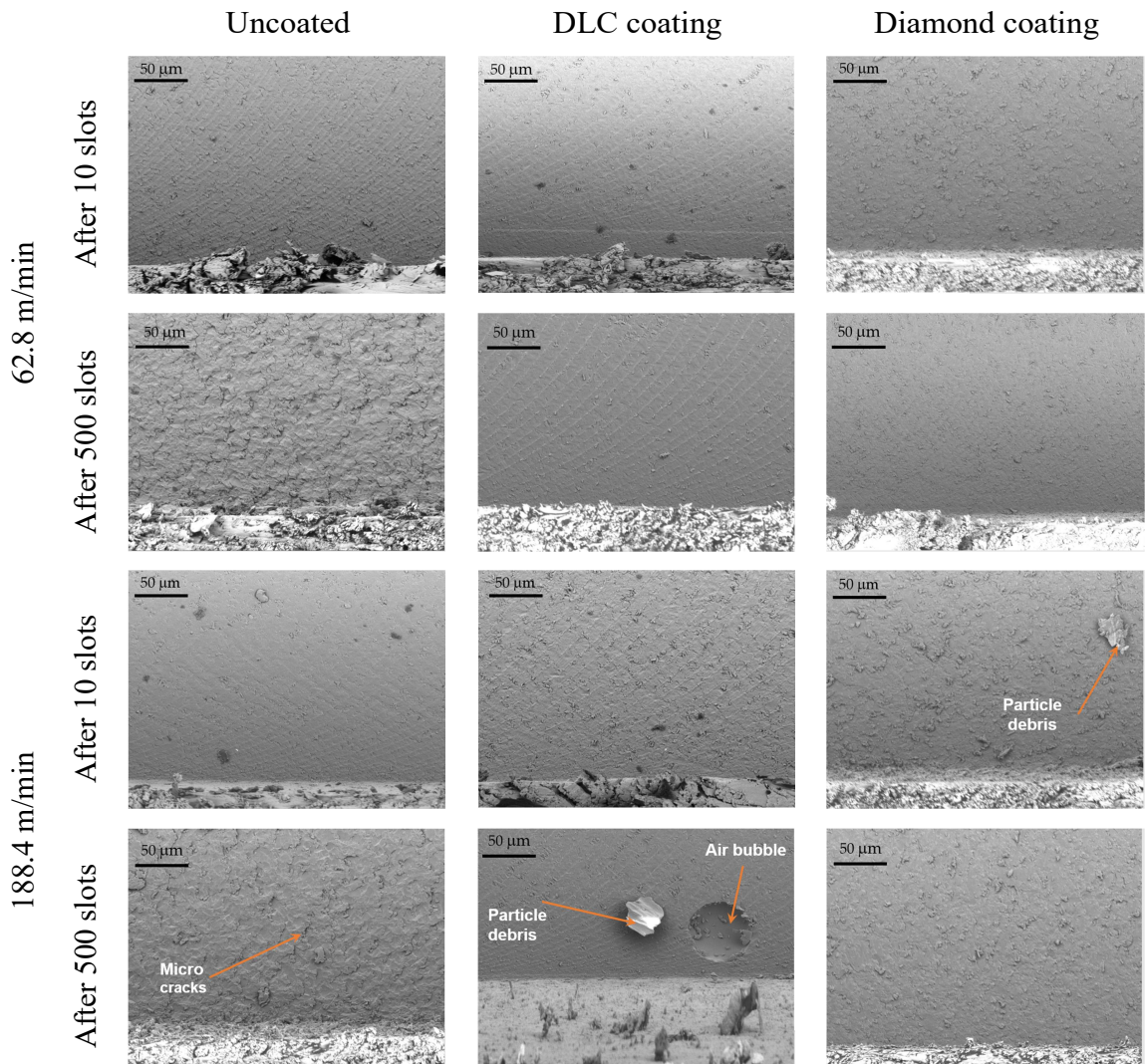


Figure 4.13: SEM images of machined surface morphology at two cutting stages (after 10 and 500 slots) using different micro-end mills under various cutting speeds

Additionally, the SEM analysis revealed that internal defects such as air bubbles (internal cavities) exist that were likely to be formed during the nanocomposite

samples' fabrication process. Feed marks were also observed in most machined surfaces that cut at low cutting speed (62.8 m/min). Deterioration in workpiece surface quality with machining time was apparent for surfaces cut using the uncoated cutting tools compared with the DLC and diamond coated counterparts. This could be the result of severe cutting edge rounding observed only on the uncoated tools. It was also supported by the observed increase in surface roughness values versus material removal volume, as shown in Figure 4.11.

#### 4.10 Effect of tool wear on dimensional accuracy

The presence of a 0.3% weight of graphene nanofiller in an epoxy resin/matrix was expected to improve the heat dissipation throughout the cutting process, enhancing the dimensional accuracy of the produced feature. Figure 4.14 shows the average slot width against cutting speed and cutting tool type. The results agreed with the original diameter of the cutting tools, as shown in Figure 4.7a. Marginal shrinkages in the machined slots were observed in all slots produced due to the residual stress and elasticity of the polymer nanocomposites [404]. This phenomenon explained slot width was always marginally smaller than the cutting tool's initial diameter for this test.

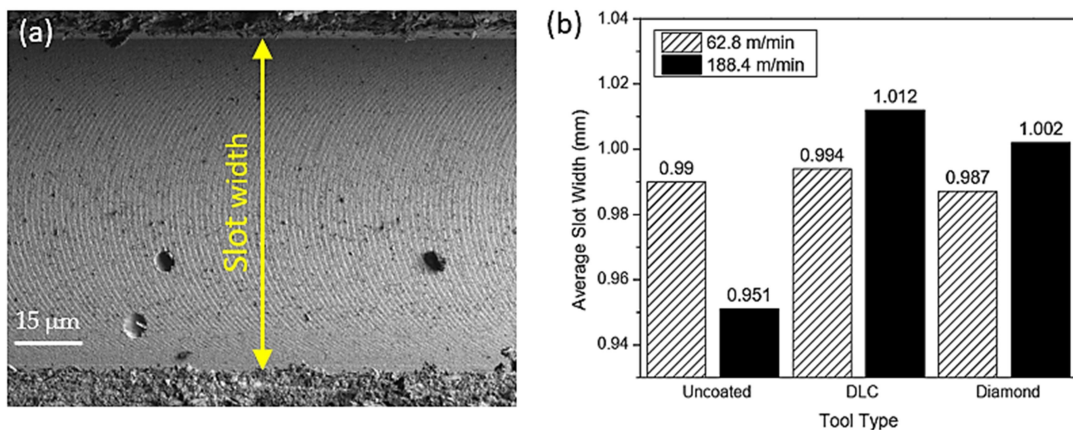


Figure 4.14: (a) SEM image of a slot generated by DLC coated tool at 62.8 m/min after 500 slots; (b) Effect of cutting speed and tool coating type on average slot width (in mm) at all cutting stages (from 10 to 500 slots)

As shown in Figure 4.14b, the tool coating led to less width channel reduction. The operation of suitable coating with adequate adhesion supported the tool for wear resistance and slowed down the acceleration of the edge roundness [401]. The remarkable width reduction could be assigned to tool wear enhancement of uncoated tool at 188.4 m/min cutting speed.

#### **4.11 Summary**

In this part of chapter 4, micromilling 0.3 wt.% graphene reinforced epoxy nanocomposites have been performed in dry cutting conditions. The corresponding tooling performances between three different tool types including tool wear, cutting force, dimensional accuracy surface roughness and surface integrity have been addressed and analysed. It has been observed that the micro-tool wear behaviour depended upon the thermomechanical properties of the polymer nanocomposites, cutting speed and cutting force. The uncoated micro-end mills exhibited the highest tool wear rate compared to that of DLC and diamond coated counterparts. This high tool wear rate significantly reduced the machinability of epoxy/graphene nanocomposites in terms of increasing the cutting force and surface roughness as well as reducing the dimensional accuracy. On the contrary, the influences of tool wear on the machinability of the workpiece materials were less significant when using DLC and diamond coated micro-tools due to their lower tool wear rate compared to the uncoated tool. In particular, it has been further observed that the use of DLC micro end-mill in micromachining of graphene reinforced epoxy nanocomposites was recommended.

## Chapter 5: Machinability of carbon nanofiller reinforced epoxy nanocomposites at nano-micro cutting chip load

### 5.1 Introduction

This chapter aimed to provide a comprehensive investigation on the micro-machinability of carbon nanofiller reinforced epoxy nanocomposite at nano/micro-chip load. The content was divided into two parts.

Part I examined the micro-machinability of epoxy/MWCNT nanocomposite including chip formation, cutting force, tool wear, machined surface morphology and roughness. The micromachining experiments were conducted on different cutting conditions including FPTs (0.2, 0.5, 1, 2, and 4  $\mu\text{m}$ ), cutting speeds (62.8, 125.6, and 188.5 m/min) and filler loadings (neat epoxy, 0.1, 0.3, 0.7 and 1 wt.%). The low chip loads of 0.2 and 0.5  $\mu\text{m}$  were employed to investigate the size effect in micromachining of polymer nanocomposites. A constant axial cutting depth (DoC) of 200  $\mu\text{m}$  was applied for all micro-cutting trials. The micro-end milling uncoated tools used in this study had some main features as follows: micro-grain tungsten carbide, two flutes, cutting diameter of 0.5 mm and helix angle of  $20^{\circ}$ . Also, material properties such as tensile mechanical properties and thermal conductivity were believed to have an impact on chip formation, cutting force and machined, hence tested before the micromachining trials. The details of experimental works including cutting parameters, tool and workpiece material are summarised in Table 5.1.

Table 5.1: Experimental settings

Specimen	Material	MWCNT reinforced epoxy and plain epoxy
	Filler loading (wt%)	0, 0.1, 0.3, 0.7 and 1
Cutting tool	Material	Micro-grain tungsten carbide
	Type	Uncoated micro-end mill
	Number of flutes	2
	Flute length (mm)	1.5
	Cutting diameter (mm)	0.5
	Helix angle	$20^{\circ}$
Cutting conditions	Cutting speed (m/min)	62.8, 125.6 and 188.5
	Feed per tooth ( $\mu\text{m}$ )	0.2, 0.5, 1, 2, and 4

In part II, the machinability of (epoxy/CNF) in micromachining was presented. Different cutting conditions and nanofiller contents were applied to identify the micromachining behaviours of this polymer nanocomposite during the micromilling process. Based on the literature and machine tool's capability, the main cutting parameters including cutting speed (31.41, 78.54, and 125.67 m/min) and FPT (0.2, 0.5, 1, 2, and 5  $\mu\text{m}$ ), as well as nano-filler content (0, 0.1, 0.3, 0.7 and 1 wt.%), were chosen as the main input factors. The titanium-carbon-nitride (TiCN) coated micro-end milling tools used in this study had some main features as follows: micro-grain tungsten carbide, two flutes, cutting diameter of 0.5 mm and helix angle of  $20^\circ$ . A constant DoC of 100  $\mu\text{m}$  was applied for all micro-cutting trials. The main objectives of the investigation were cutting force and surface roughness. Additionally, chip formation and machined surface morphology were also characterised to support the machinability analyses. It was also necessary to provide thermomechanical characterisations of the workpiece materials as these properties could affect the micromachining process. In this study, tensile and DMA tests were applied. Moreover, CNF distribution was also an important factor that could influence the mechanical properties of workpiece materials and consequently, their machinability. Therefore, it was also investigated using SEM analysis. The details of experimental works including cutting parameters, tool and workpiece material are summarised in Table 5.2.

Table 5.2: Experimental settings

Specimen	Material	CNF reinforced epoxy and plain epoxy
	Filler loading (wt%)	0, 0.1, 0.3, 0.7 and 1
Cutting tool	Material	TiCN coating
	Number of flutes	2
	Flute length (mm)	1.5
	Cutting diameter (mm)	0.5
	Helix angle	$20^\circ$
Cutting conditions	Cutting speed (m/min)	31.41, 78.54, and 125.67
	Feed per tooth ( $\mu\text{m}$ )	0.2, 0.5, 1, 2, and 5

## **Part I: Machinability of carbon nanotube reinforced epoxy nanocomposites**

### **5.2 Tensile properties**

The tensile properties of nanocomposites with different MWCNT contents are shown in Figure 5.1(a-c). The addition of varying filler contents, from 0.1 to 1 wt.%, showed certain effects on the tensile behaviour of epoxy-based nanocomposites. It could be observed an obvious improvement of tensile strength at 0.7 wt.% filler loading (Figure 5.1a). This indicated a sufficient load transfer from matrix to filler at this filler content. However, its further increase (up to 1 wt.%) led to a reduction of tensile strength due to CNT agglomeration. On the other hand, Young's modulus (Figure 5.1b) showed unobvious improvements when adding more MWCNT into the epoxy matrix compared to the plain epoxy. The highest value of modulus could be seen at 1 wt.% indicated an effective restraint of polymer chain sliding due to the dense network formed by the nano-fibres.

Furthermore, it could also be seen that the fracture strain of these nanocomposites (Figure 5.1c) increased when incorporating MWCNT from 0 to 0.3 wt.%. However, it started to decrease when the filler loading reached 0.7 wt.%, indicating a ductile-to-brittle transition. This phenomenon was possibly due to more agglomerations of MWCNT at high filler content, generating more stress concentration, hence leading to crack propagations under tensile loadings. Some similar findings could be found in [405, 406]. The improvements of tensile strength and modulus combined with the decrease of strain failure could be used to explain the effects of filler content on the machinability of these nanocomposites [407]. Furthermore, the thermal conductivity of these nanocomposites should also be considered since it could also influence the micromachining process in particular when the thermal softening phenomenon was dominant (at high cutting speed).

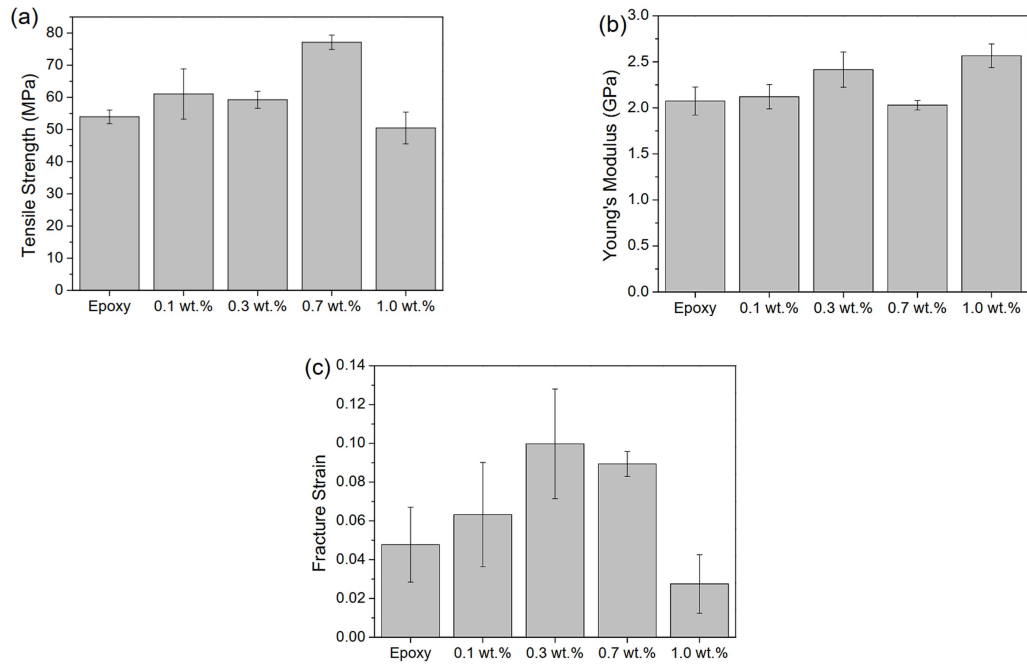


Figure 5.1: Tensile properties of epoxy/MWCNT nanocomposites: (a) Tensile strength, (b) Young's modulus, and (c) Fracture strain

### 5.3 Thermal conductivity

Since the cutting process generated high temperature in the cutting zone, causing workpiece material softening and chip adhesion that affected the surface quality and surface roughness. In micromachining, high cutting speed is preferred, so this phenomenon was expected to be more severe. Therefore, micromachining low-thermal-conductivity materials, such as polymers, required the investigation of their thermal conductivity. The thermal conductivity of epoxy/MWCNT nanocomposites is shown in Figure 5.2. The additions of low filler contents (0.1 and 0.3 wt.% MWCNT) showed insignificant improvement of thermal conductivity compared to epoxy. When the filler content reached 0.7 wt.%, a slight improvement could be observed. The highest thermal conductivity improvement of around 17% was found at 1 wt.% MWCNT, which showed agreement with the literature [408]. These enhancements of thermal conductivity was possibly due to the heat flow formed by dense MWCNTs network inside epoxy matrix at high filler contents (0.7 and 1 wt.%) as reported in the literature [409].

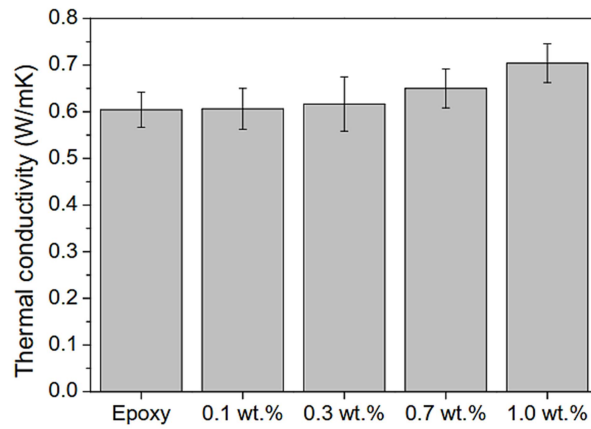


Figure 5.2: Thermal conductivity of MWCNT/epoxy nanocomposites at different filler contents

#### 5.4 Chip morphology

The chip morphology in micromachining plays a vital role in identifying the cutting mechanism as well as the behaviours of workpiece materials under the cutting process. Additionally, more details of chip morphology at low feed rates were also analysed to identify MUCT. This was indicated by a transition point from ploughing to the shearing-dominated regime and was an essential indicator of size effect when micromachining.

Figure 5.3 shows the chip morphology at a cutting speed of 62.8 m/min with the consideration of filler content and feed rate effects. For all compositions, the chips were transferred from discontinuous to continuous forms when increasing the feed rate. It indicated the transition of the cutting mechanism from ploughing into the shearing regime. However, this trend seemed to be different between each composition. For epoxy, 0.1 wt.% and 0.3wt.% MWCNT nanocomposites, the chips were crushed with fracture debris at the lowest FPT of 0.2  $\mu\text{m}$  and became more noticeable but still was in discontinuous form when FPT reached 1  $\mu\text{m}$ . For 0.7 wt.% and 1 wt.% MWCNT nanocomposites, the chips were much more apparent, even at 0.2  $\mu\text{m}$  FPT. The chip transition points from discontinuous to continuous form in these higher filler content nanocomposites were between 0.5  $\mu\text{m}$  and 1  $\mu\text{m}$ , which were smaller than those of lower filler contents and plain counterparts. Since the chip formation was characterised



at the lowest cutting speed (62.8 m/min), the effect of thermal softening could be eliminated. Tensile behaviour of these materials would be considered as the main reason for the change of MUCT between them. Based on the results in Figure 5.1c, it could be seen that the reduction of failure strain led to low plastic deformation when cutting high-filler-content nanocomposites (0.7 and 1 wt.%), allowing the chip formation at low cutting chip loads (0.5 to 1  $\mu\text{m}$ ) due to dominant shearing regime.

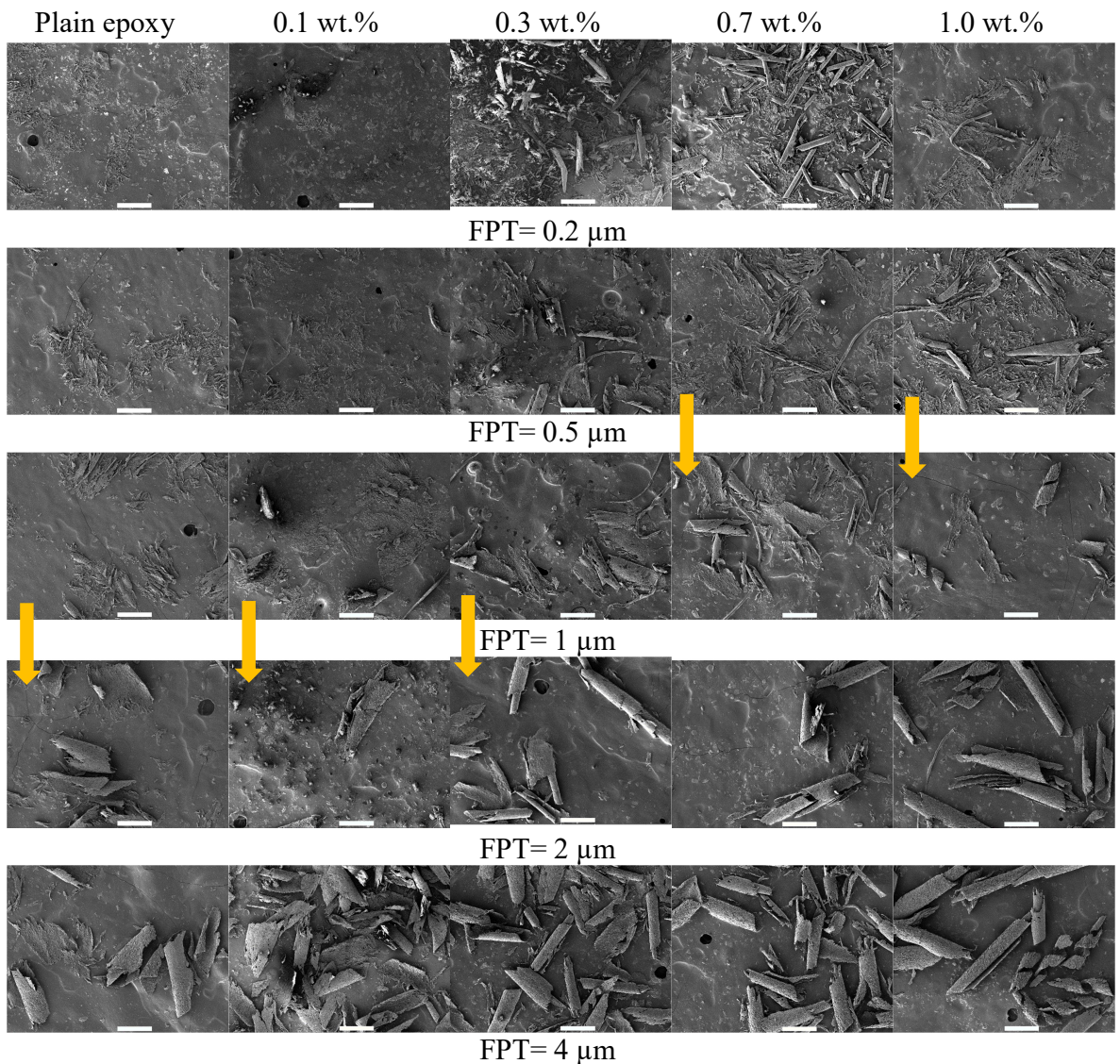


Figure 5.3: Chip formations when micromilling at different FPTs and CNT weight contents (Cutting speed = 62.8 m/min; Scale bar is 200  $\mu\text{m}$ )

On the contrary, ploughing predominated when micromachining lower-filler-content nanocomposites (0.1 and 0.3 wt.% and epoxy) due to their viscoelastic behaviour, resulting in higher MUCT (1 to 2  $\mu\text{m}$ ). Therefore, the addition of different MWCNT contents likely changed the MUCT thresholds when micromilling epoxy/MWCNT nanocomposites, owing to their various fracture strains. In this case, MUCTs of 0.7 wt.% and 1 wt.% MWCNT nanocomposites were in the range of 0.5 - 1  $\mu\text{m}$ ) while these values were from 1 to 2  $\mu\text{m}$  in case of low-filler-content nanocomposites. On closer observation of chip formations at low feed rates (Figure 5.4), it could be seen that chip formation of 0.7 and 1 wt.% MWCNT nanocomposites was continuous and partly discontinuous at the lowest FPT of 0.2  $\mu\text{m}$  indicating a partial shearing-dominant regime. At the same time, a completed ploughing mechanism was dominant at lower filler contents. At FPT of 1  $\mu\text{m}$ , the chips of higher filler content nanocomposites were likely to curl and become thicker. However, their chip surfaces were rough with the presence of micro-cracks, due to the low tensile strain-to-failure behaviour of nanocomposites at high filler contents that has been confirmed from the tensile results (Figure 5.1).

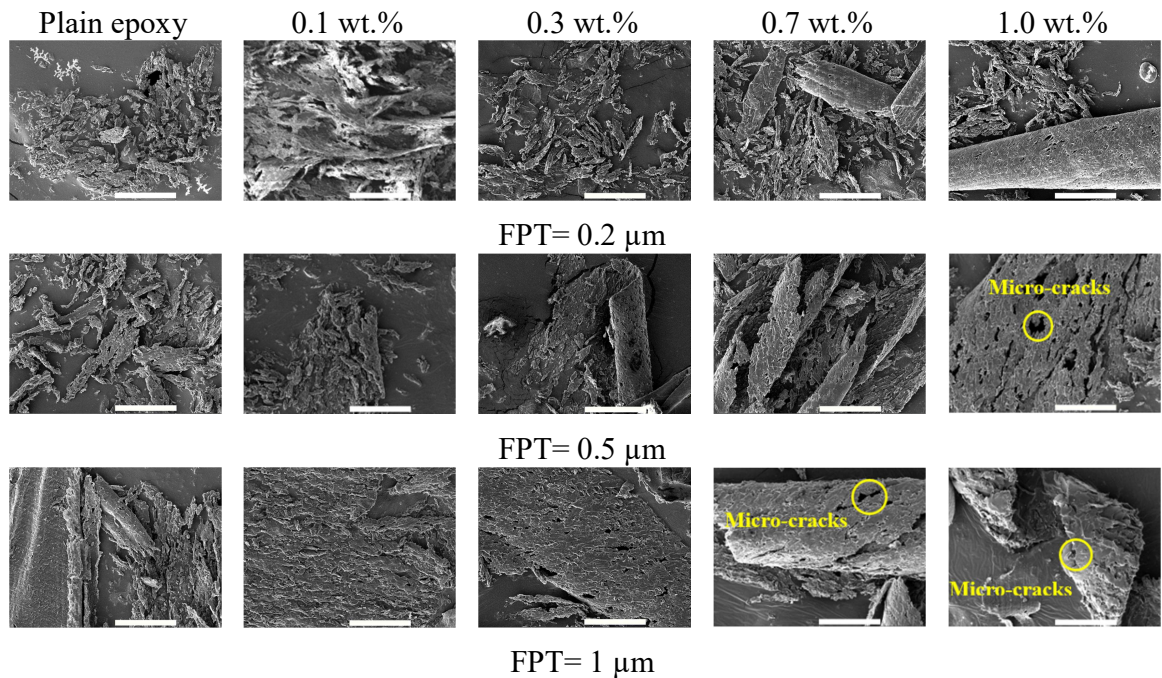


Figure 5.4: Chip formations at low FPTs at different CNT weight contents (Cutting speed = 62.8 m/min; Scale bar is 50  $\mu\text{m}$ )

## 5.5 Cutting force

### 5.5.1 ANOVA analysis

ANOVA was applied based on the cutting force results from all cutting conditions and filler contents. Table 5.3 depicts all uncertain input factors, including filler content (wt.%), cutting speed (V) and FPT with their effects on cutting force representing as contribution indicators. The filler content and FPT showed the most significant influences with their contributions to cutting force variation of ~ 30% and ~ 32%, respectively. The cutting speed only marginally influenced cutting force (2.76%).

Table 5.3: ANOVA result for cutting force when micromilling epoxy/MWCNT nanocomposites

Source	DF	Seq SS	Contribution	Adj SS	Adj MS	F-Value	P-Value
FPT	4	3.8542	32.37%	3.8542	0.96356	14.86	< 0.001
Cutting Speed	2	0.3285	2.76%	0.3285	0.16425	2.53	0.087
Filler Content	4	3.5764	30.03%	3.5764	0.89409	13.79	< 0.001
Error	64	4.1491	34.84%	4.1491	0.06483		
Total	74	11.9082	100.00%				

### 5.5.2 Cutting force analysis

Figure 5.5 shows the variations of cutting force as a function of FPT when a micromilling epoxy/MWCNT nanocomposite at different cutting speeds. A general increase of cutting force as a function of feed rate was observed for all cutting speeds and filler contents.

Regarding the effect of filler content on the cutting force, micromilling 1 wt.% MWCNT nanocomposite generated the highest cutting force regardless of the cutting conditions compare to other compositions (epoxy, 0.1, 0.3 and 0.7 wt.%). This phenomenon indicated the dominance of the microstructure effect in increasing the cutting force. The high MWCNT loading (1 wt.%) led to more physical contact between micro-tools and nano-fillers, resulting in higher cutting force. Moreover, the



sharper increase of cutting force with higher magnitude could be observed when micromilling 1 wt.% MWCNT nanocomposites at 62.8 m/min (Figure 5.5a) compared to those at 188.5 m/min (Figure 5.5b). These results indicated the dominance of the thermal softening effect at high cutting speed. This dominance of the thermal softening effect was also exhibited by the high sensitivity of filler content in varying cutting force at the high cutting speed (Figure 5.5b). The rising trend of cutting force with more added fillers at the high cutting speed of 188.5 m/min showed high consistency with the thermal conductivity of the workpiece materials (Figure 5.2). The lower added filler led to the lower thermal conductivity of the nanocomposites, consequently resulted in the reduction of cutting force, owing to the effect of thermal softening.

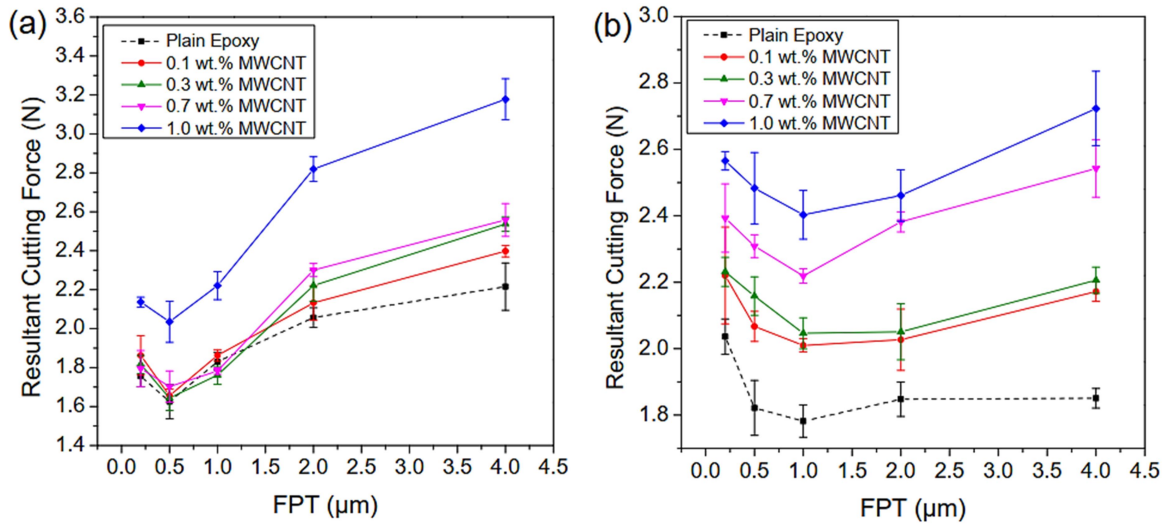


Figure 5.5: Cutting force when micromilling epoxy based nanocomposites at different MWCNT contents and FPTs: a) Cutting speed = 62.8 m/min (20,000 rpm); b) Cutting speed = 188.5 m/min (60,000 rpm)

In the consideration of the effect of FPT, the cutting force increased when chip load increased from 2 to 4  $\mu\text{m}$  regardless of the cutting speeds and filler content (Figure 5.5). It indicated the significant effect of chip load on cutting force increase due to the high plastic deformation and subsequently, high feed mark formation on the machined surface that was similar to macromachining.

However, the cutting force fluctuations at low FPTs (up to 1  $\mu\text{m}$  at 62.8 m/min and 2  $\mu\text{m}$  at 188.5 m/min) indicated the MUCT effect. These fluctuations of cutting

force were contributed by the transition of the cutting mechanism from ploughing (below MUCT) into shearing regime (above MUCT). At a cutting speed of 62.8 m/min, when the micro-tool ploughed the workpiece, high elastic deformation due to shear zone expanding was produced, resulting in high cutting force at FPT of 0.2  $\mu\text{m}$ . This phenomenon became less obvious as FPT increased and the shearing mechanism occurred, leading to a reduction of cutting force (from 0.2 to 0.5  $\mu\text{m}$ ) (Figure 5.5a). A further increase of FPT up to 1  $\mu\text{m}$  increased cutting force due to higher chip load. The fluctuation of cutting force could also be seen at the high cutting speed of 188.5 m/min (Figure 5.5b). However, it occurred in a larger range of FPT (from 0.2 to 2  $\mu\text{m}$ ) compared to those of low cutting speed (from 0.2 to 1  $\mu\text{m}$ ). It was due to the thermal softening effect that increased the MUCT boundary at high cutting speed (188.5 m/min).

Figure 5.6 depicts some specific cutting profiles on feed direction ( $F_y$ ) at a cutting speed of 62.8 m/min to clarify the MUCT effect on cutting force variation for FPT of 0.5 and 1  $\mu\text{m}$ . The influence of the thermal softening effect could be eliminated at such a low cutting speed. The cutting force profile appeared to be irregular at the filler contents of 0.1 (Figure 5.6b), 0.3 wt.% (Figure 5.6c) and epoxy (Figure 5.6a). It indicated an unstable cutting condition generated from the ploughing mechanism (below MUCT) that caused the cutting force to fluctuate.

On the contrary, cutting profiles at 0.7 (Figure 5.6d) and 1 wt.% MWCNT (Figure 5.6e) appeared to have more regular fluctuations compared to other compositions (epoxy, 0.1, and 0.3 wt.%) that indicated a stable cutting condition due to dominant-shearing regime, even at low FPT of 0.5  $\mu\text{m}$ . These results confirmed the MUCT identification that was analysed in the chip morphology section (section 5.4).

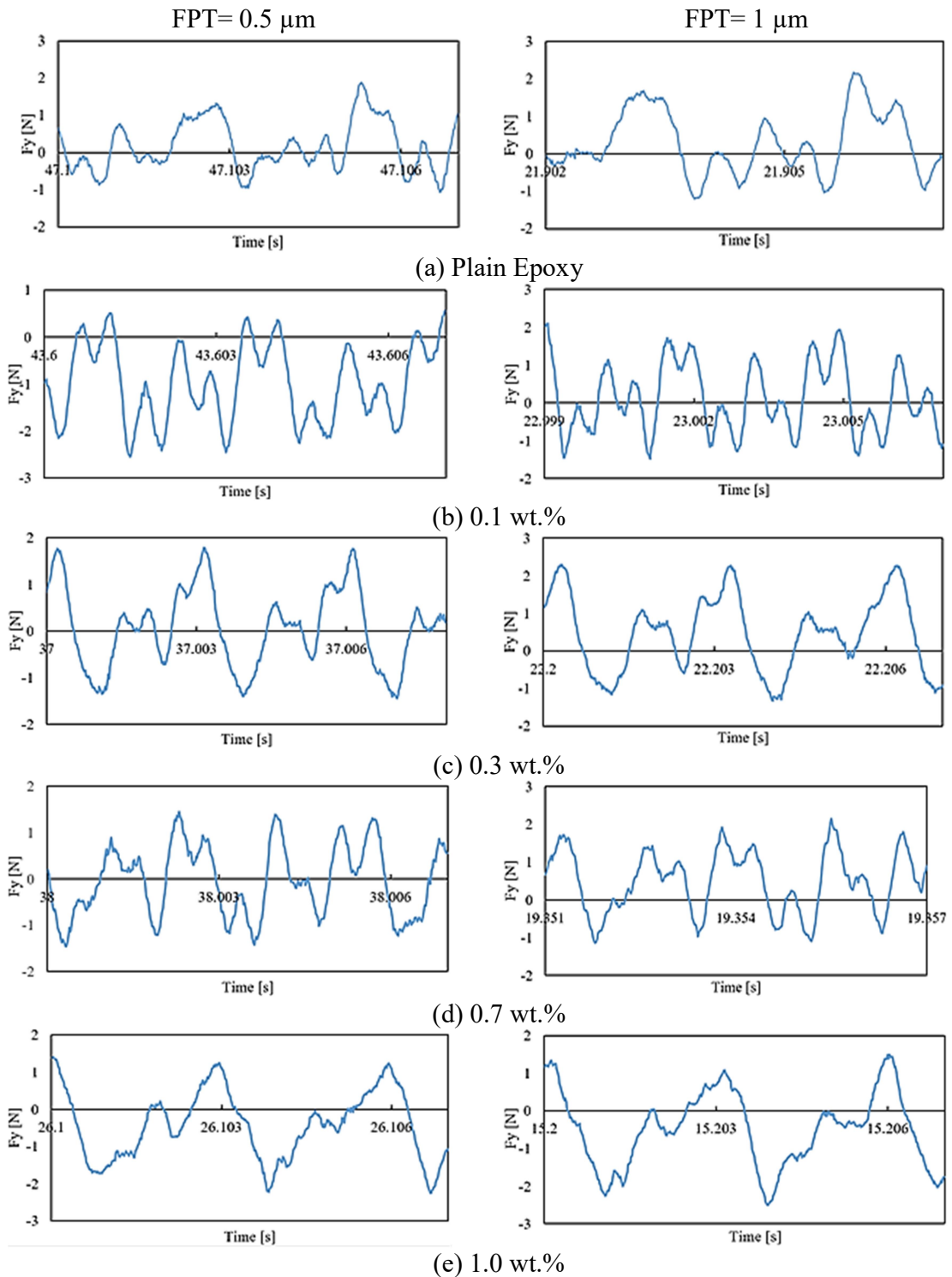


Figure 5.6: Cutting force profiles in feed direction at low FPT (0.5 and 1  $\mu\text{m}$ ) (Cutting speed= 62.8 m/min)

## 5.6 Machined surface morphology

Figure 5.7 shows general views of machined surface morphology at low magnification of 750x (cutting speed of 62.7 m/min and FPT of 4  $\mu\text{m}$ ). These SEM images have been captured at the central area of each slot. It was observed that the presence of feed marks becomes more pronounced when micromilling high-filler-content nanocomposites (0.7 and 1 wt.%). It was due to lower failure strain at high filler loadings (Figure 5.1). The feed marks on machined surfaces of plain epoxy and lower filler content nanocomposites seemed to be smeared by the matrix material due to their visco-elastic characteristic. It was likely compatible with the tensile characterisation of these materials.

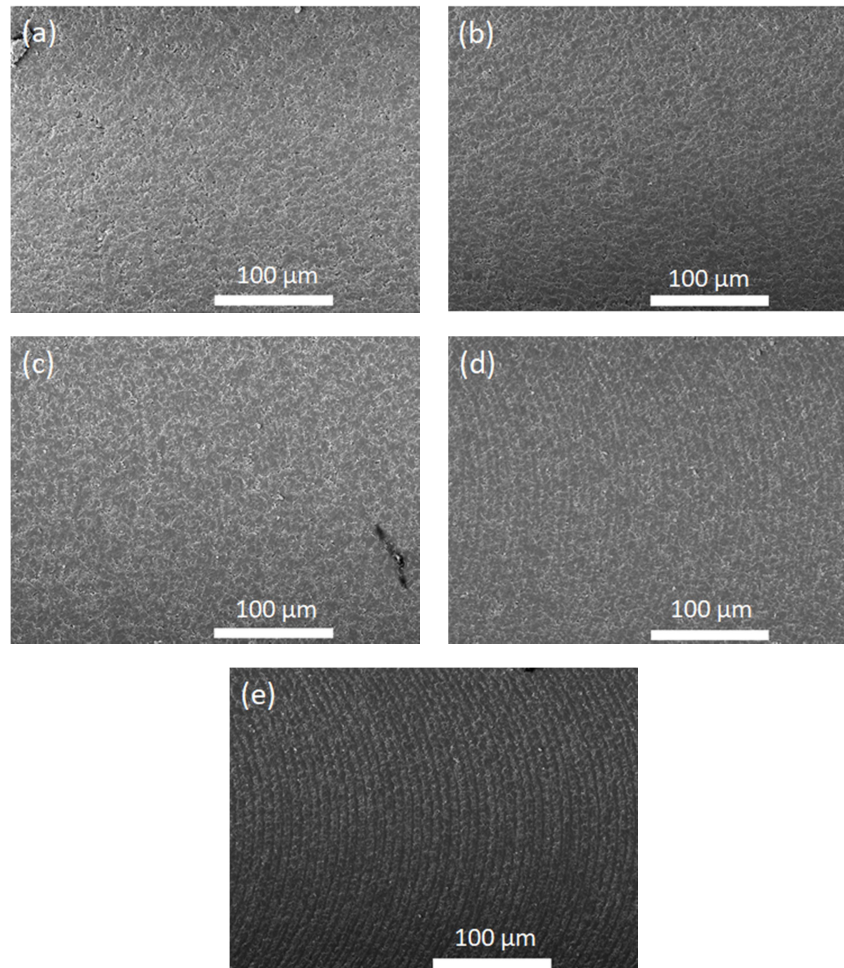


Figure 5.7: Surface morphology of machined surface at different CNT weight contents: (a) Epoxy, (b) 0.1 wt.%, (c) 0.3 wt.%, (d) 0.7 wt.%, and (e) 1 wt.% (FPT = 4  $\mu\text{m}$ ; Cutting speed = 62.8 m/min)



Chapter 5: Machinability of carbon nanofiller reinforced epoxy nanocomposites at nano-  
micro cutting chip load

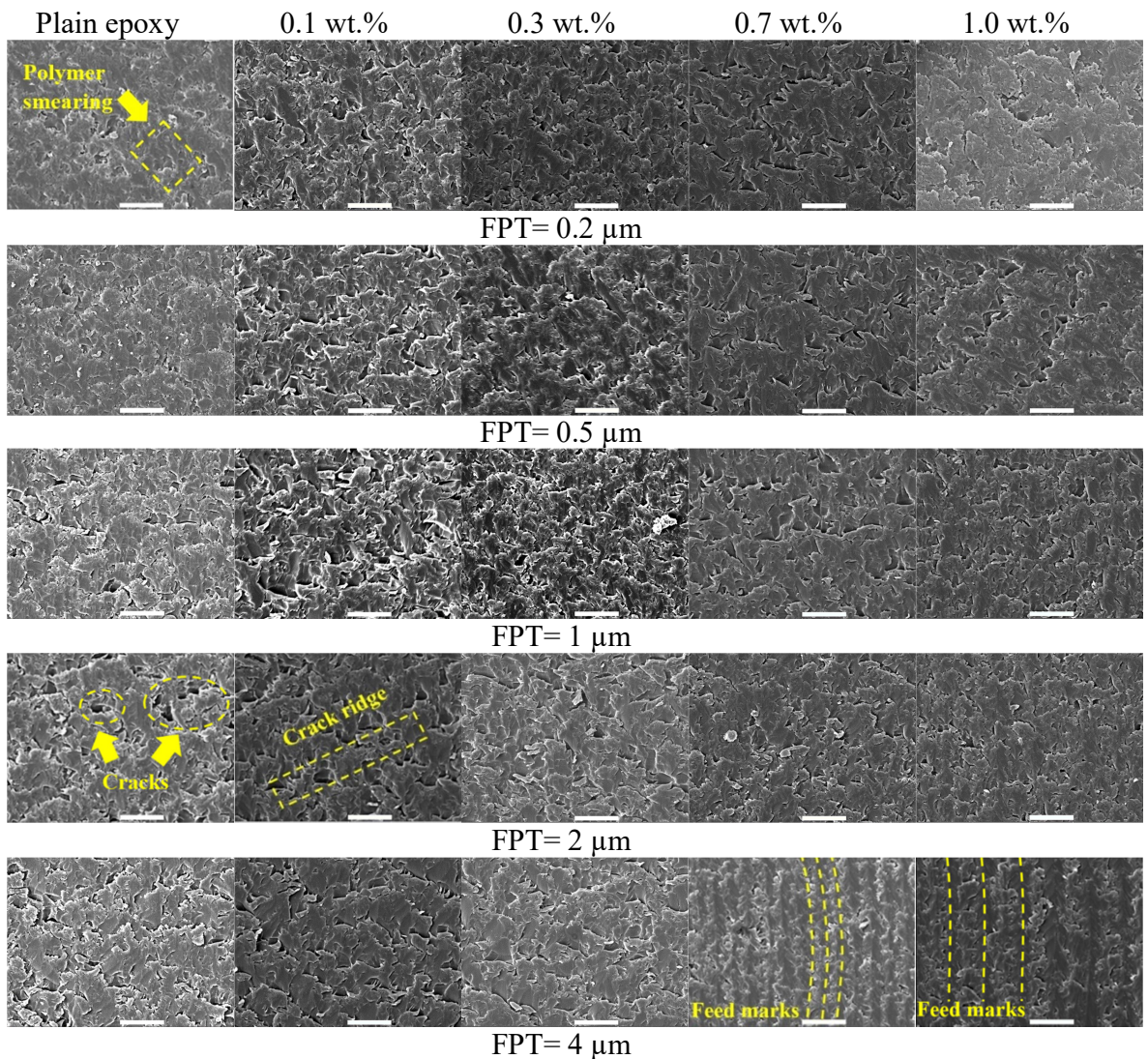


Figure 5.8: Surface morphology of machined surface at different CNT weight contents and FPTs (Cutting speed = 62.8 m/min; Scale bar is 10 μm)

On closer investigation (Figure 5.8), other SEM images for all FPTs were taken at a higher magnification of 5kx. It was generally observed that the surface morphology from micromilling higher filler content nanocomposites (0.7 wt.% and 1 wt.% MWCNT) tended to be smoother than those of the other compositions. The presences of cracks and crack ridges on their machined surfaces were also less frequent and prominent. It was likely due to MWCNT bridging the cracks that seemed to occur when high filler contents were employed. It has been confirmed by Samuel et al. [330] when micromachining



PC/CNT nanocomposites. For epoxy, 0.1 and 0.3 wt.% MWCNT nanocomposites, machined surfaces seemed to be relatively smooth at the beginning (FPT from 0.2 to 0.5  $\mu\text{m}$ ) but became rougher with clear micro-cracks along with the feed marks as FPT increased, especially for 0.1 wt.% nanocomposites. Polymer smearing of plain epoxy and CNT bridging of 0.3 wt.% MWCNT nanocomposites might contribute to their smoother surfaces compared to 0.1 wt.% counterparts. However, feed rate seems to inconsiderably affect surface morphology while only clear feed marks are found at the highest FPT.

## 5.7 Surface roughness

### 5.7.1 ANOVA analysis

Before investigating surface roughness variation, ANOVA was first applied based on the experiment results from all cutting conditions and filler contents. Table 5.4 shows all input factors, including filler content, cutting speed, and FPT with their effects on surface roughness representing as contribution indicators. It could be seen that filler content significantly affected the surface roughness with its contribution of ~30% followed by cutting speed (contribution of 25.69%) while FPT showed the least effect (2.46%). These statistical results seemed to be consistent with the surface morphology analysis (section 5.6).

Table 5.4: ANOVA result for surface roughness when micromilling epoxy/ MWCNT nanocomposites

Source	DF	Seq SS	Contribution	Adj SS	Adj MS	F-Value	P-Value
Filler Content	4	0.061	30.50%	0.061	0.015	11.80	< 0.001
Cutting Speed	2	0.051	25.69%	0.051	0.026	19.87	< 0.001
FPT ( $\mu\text{m}$ )	4	0.005	2.46%	0.005	0.001	0.95	0.440
Error	64	0.082	41.36%	0.082	0.001		
Total	74	0.199	100.00%				

### 5.7.2 Surface roughness analysis

Figure 5.9 depicts the surface roughness variation as a function of FPT at different filler contents. Surface roughness from micromachining 0.7 wt.% and 1 wt.% MWCNT nanocomposites were lower than the other composition regardless of the cutting conditions. It showed a firm agreement with the ANOVA analysis above. The Ra magnitudes of plain epoxy and other low-filler-content nanocomposites seemed to be comparable with each other, and their trends with FPT variations were also unclear indicating the minor effect of feed rate on surface roughness. However, from Figure 5.9), the effect of MUCT could be identified. In conventional machining, the increase of feed rate leads to the rise of surface roughness due to the effect of feed marks formation. In micromachining, when cutting below the MUCT threshold, the ploughing mechanism occurs that may have negative impacts on machined surface generation. From this study, surface roughness fluctuated along with FPT. As FPT increasing from 0.2 to 1  $\mu\text{m}$  which was below MUCT (as indicated by chip morphology and cutting force discussion), there was a fluctuation of surface roughness with high magnitudes at the beginning due to ploughing. It then reached the bottom at  $\text{FPT} = 0.5 \mu\text{m}$  with ploughing-shearing and then increased again as FPT reached 1  $\mu\text{m}$  when a shearing regime becomes more dominant.

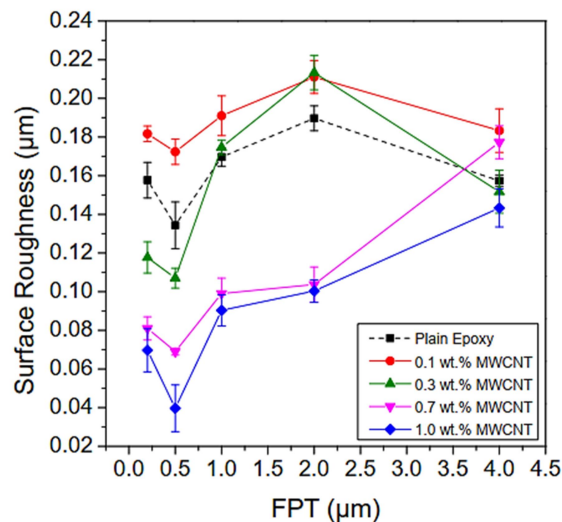


Figure 5.9: Surface roughness (Ra) when micromilling epoxy-based nanocomposites at different MWCNT contents and FPTs (cutting speed = 62.8 m/min)

A fluctuation of Ra could be seen for all materials as FPT increasing up to 1  $\mu\text{m}$ . As indicated by chip morphology investigation, this range of FPT was still below MUCT (below 2  $\mu\text{m}$ ) for these nanocomposites, hence showing the impact of the size effect. High magnitudes of Ra at the low FPTs (from 0.2 to 1  $\mu\text{m}$ ) were contributed by the ploughing mechanism. When the FPT kept increasing to 4  $\mu\text{m}$ , the dominance feed mark effect was now responsible for the significant increase of Ra due to higher chip load and consequently, higher plastic deformation. However, the surface roughness of epoxy and low filler content nanocomposites (0.1 wt.% and 0.3 wt.%) started to decrease when FPR reached 2  $\mu\text{m}$ . More polymer smearing due to high cutting temperature at high feed rates might be the reason for this phenomenon.

## **5.8 Tool wear**

Figure 5.10 shows the side and top views of the machined micro-end mill for all material compositions to depict the effect of workpiece properties on the flank wear and the face wear, respectively. These two wear patterns seemed to be only visible at high filler contents (0.7 and 1 wt.%). This phenomenon was confirmed by the results of tool wear measurements in Figure 5.11. For low filler content compositions (0.1 and 0.3 wt.%) and plain epoxy, there was an unobvious effect of filler contents on the tool wear. However, an increase from 0.7 to 1 wt.% MWCNT content exhibited considerable tool wear acceleration, especially flank wear. It was exhibited by the visible scratches on the tool flank face when micromilling these compositions (Figure 5.10). Given such high filler loadings of MWCNT, it likely indicated more physical contact between the tools and nanofibres, hence resulting in more tool wear. Additionally, MWCNT agglomeration at high filler loadings might also contribute to more trapping between tool and workpiece, caused more tool wear due to rubbing. This claim was supported by the stack of MWCNTs adhered on the tool surfaces when machined 0.7 and 1 wt.% nanocomposites (Figure 5.10).

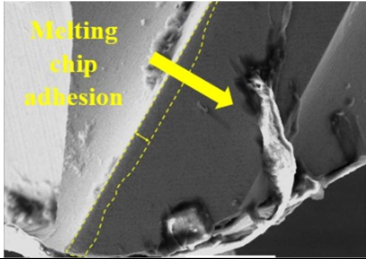
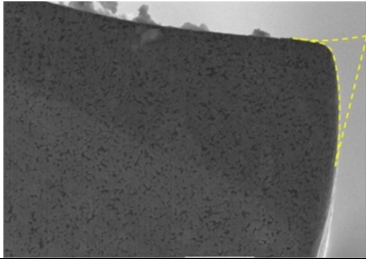
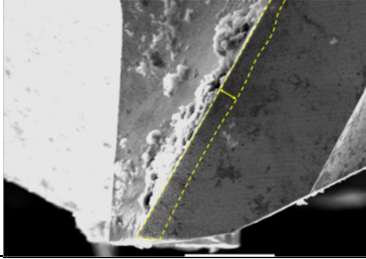
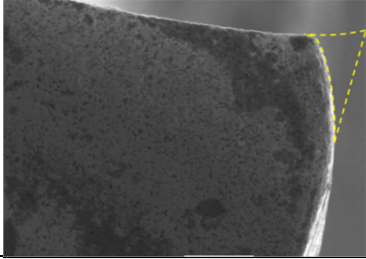
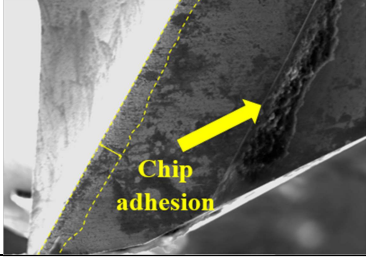
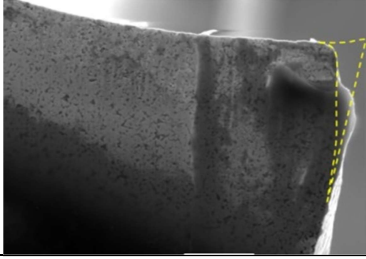
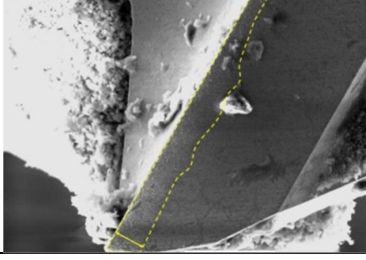
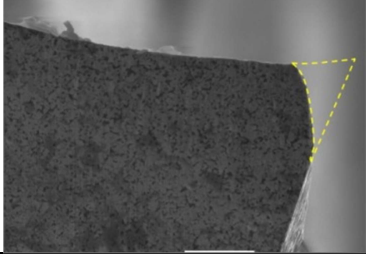
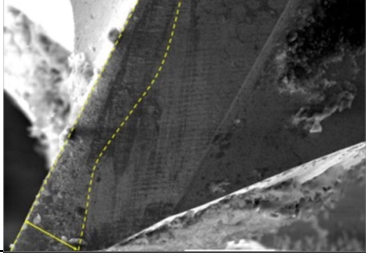
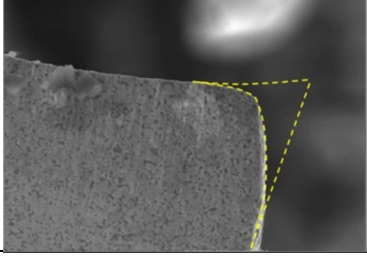
Filler content	Side view (Scale bar is 50 $\mu\text{m}$ )	Top View (Scale bar length 10 $\mu\text{m}$ )
Plain epoxy		
0.1 wt%		
0.3 wt%		
0.7 wt%		
1.0 wt%		

Figure 5.10: SEM images of tool wear at the end of the micromilling process for each composition (cutting volume of 58.5 mm<sup>3</sup>) (Yellow dashed line indicating wear area)

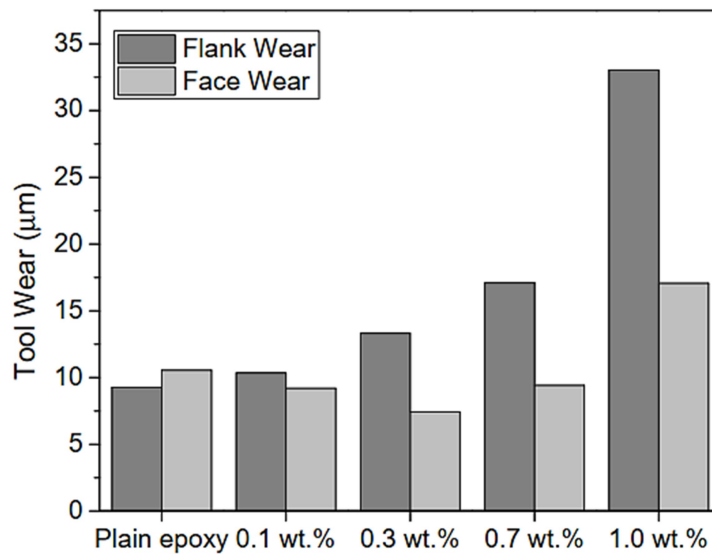


Figure 5.11: Effect of MWCNT content on tool wear when micromilling MWCNT/epoxy nanocomposites

In addition, the apparent melting chip adhesion on the flank face could be seen for the micro-tools which machined epoxy and low filler-content nanocomposites (0.1 and 0.3 w.t%). It indicated the effect of thermal softening when micromachining these low-thermal-conductivity materials. On the other hand, the chips adhered on the tool surfaces when machined high-filler-content compositions (0.7 and 1 w.t%) were in discontinuous form, implying the high brittleness of these nanocomposites. Also, their high thermal conductivity might contribute to the reduction of thermal softening, hence resulting in less melting chip adhesion.

## 5.9 Summary

The micro-machinability of multi-walled carbon nanotube reinforced epoxy nanocomposites (epoxy/MWCNT) was experimentally investigated and compared to those of plain epoxy. The cutting force and surface roughness were investigated with the validation from chip formation, surface morphology as well as workpiece material properties (mechanical tensile properties and thermal conductivity). Additionally, the influences of other factors including thermal softening, mechanical strengthening, microstructure, MUCT effects were also addressed. MWCNT content significantly

influenced the machinability of epoxy/MWCNT nanocomposites in terms of cutting force, surface roughness and tool wear. It indicated the dominant effects of thermomechanical and microstructure on the machinability of these nanocomposites. Chip load appeared to be the most influential factor affecting the cutting force while cutting speed showed the most significant effect on surface roughness variation. Additionally, the size effect appeared when the micromilling of epoxy/MWCNT nanocomposites at FPT below the MUCT threshold. It exhibited by the fluctuations of both cutting force and surface roughness at low chip loads due to the transition from ploughing to the shearing cutting regime.

## Part II: Machinability of carbon nanofibre reinforced epoxy nanocomposites

### 5.10 Tensile properties

Figure 5.12 shows tensile properties of epoxy/CNF nanocomposites at different contents including tensile strength, Young's modulus, and fracture strain. Generally, these tensile properties appeared to be improved with the addition of 0.1 and 0.3 wt.% CNF (0.1 and 0.3 wt.%) but started to decrease at higher filler loadings.

For tensile strength (Figure 5.12a), epoxy/0.1 wt.% CNF showed the highest improvement followed by epoxy/ 0.3 wt.% CNF, which were 6.4% and 5.3%, respectively compared to neat epoxy. These results were contributed by CNF fibres that could bear a fraction of the load from the epoxy matrix, hence improving the tensile strength of the nanocomposites. However, the degree of reinforcement depended on the distribution of fibres within the matrix. The more uniform distribution led to the higher possibility of fibre-matrix interaction instead of fibre agglomeration (fibre-fibre interaction).

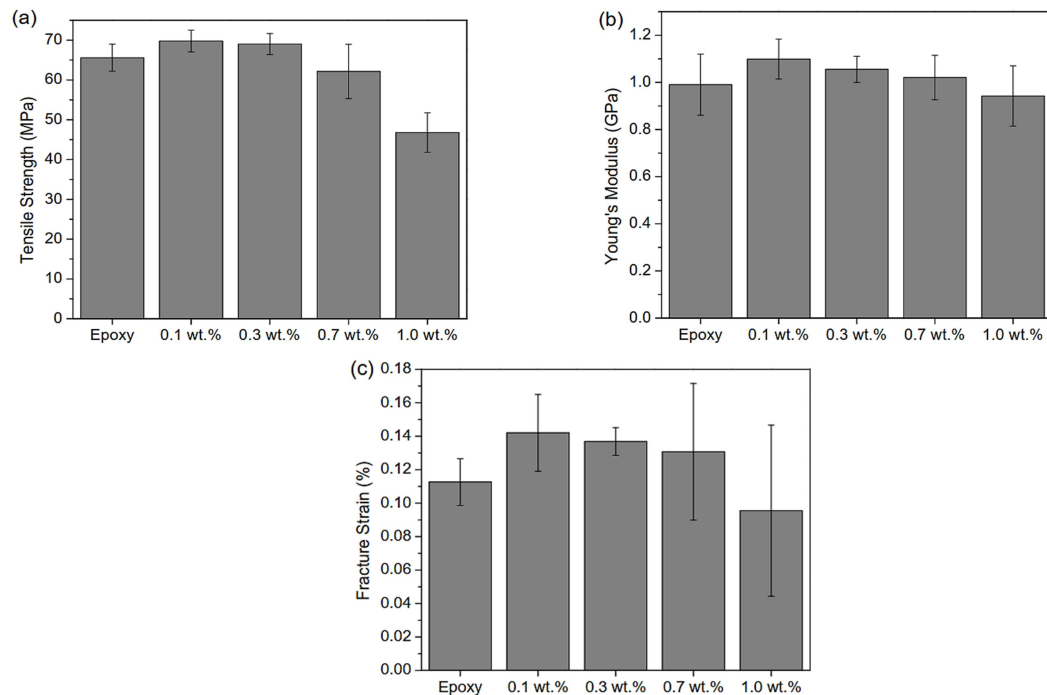


Figure 5.12: Tensile properties of epoxy/CNF nanocomposites at different filler contents: (a) Tensile strength, (b) Young's modulus, (c) Fracture strain

Based on that, these homogeneously dispersed CNFs could form a continuous network inside the epoxy matrix. It resulted in the efficient transfer of the tensile load from the epoxy matrix, hence improving the tensile strength of the nanocomposites. However, the tensile strength started to decrease as higher filler contents were incorporated and hit the lowest value at 46.8 MPa, which was around 28.6 % lower than neat epoxy. It was possibly due to the uneven distribution of CNF in the epoxy matrix that led to the presence of the stress concentration, hence reducing the tensile strength at such high filler loadings.

Young's modulus showed a similar trend with tensile strength with the highest value of 1.1 GPa at 0.1 wt.% and the lowest of 0.94 GPa at 1.0 wt.% (Figure 5.12b). This phenomenon could also be explained by the transform from homogenous to inhomogeneous distribution of CNFs as their loading increased. A uniform network formed by CNF fibres at the low filler loadings (0.1 wt.% and 0.3 wt.%) could efficiently restrain the movement of the polymer chains. As a consequence, Young's modulus or the stiffness of these materials was enhanced [375]. Similarly, the fracture strain also showed a ductile-to-brittle transition as the filler loading increases (Figure 5.12c). The well-dispersed CNF nano-fibres at low filler contents appeared to improve the fracture strain of the nanocomposites [410].

### **5.11 SEM analysis of tensile fracture surfaces**

The analysis of the tensile fracture surfaces was performed to investigate the toughening mechanisms as well as filler distribution when adding different CNT loadings into the epoxy matrix (Figure 5.13). Generally, the fracture samples showed a river-like pattern of radiating crack lines, regardless of the filler contents that indicated a typical failure pattern of brittle materials. However, a gradual change from irregularly dendritic (Figure 5.13a, b, and e) to radially straight cracks (Figure 5.13e and d) could be observed when more CNF was added. It indicated the toughening effect provided by CNF additions that restricted the free crack propagation (as could be seen in neat epoxy samples). Based on that, the higher filler contents seemed to provide better toughening efficiency for the nanocomposites.



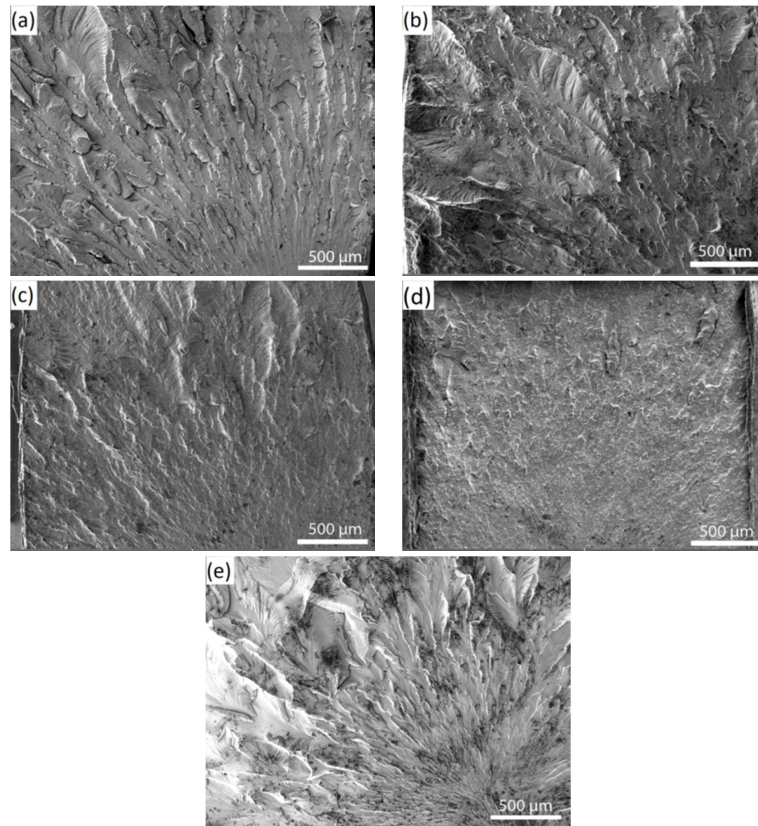


Figure 5.13: SEM micrographs of the tensile fracture surfaces of: (a) epoxy/0.1 wt.% CNF, (b) epoxy/0.3 wt.% CNF, (c) epoxy/0.7 wt.% CNF, (a) epoxy/1 wt.% CNF, (e) epoxy

Figure 5.14 shows the tensile fracture surfaces of epoxy/CNF nanocomposites at high magnification to exhibit the filler distributions. The fracture morphology of 0.1 and 0.3 wt.% nanocomposites appeared to be smooth with uniform distribution of CNFs (Figure 5.14a and b). It resulted in the enhancements of the tensile strength (Figure 5.12a) and Young's modulus (Figure 5.12b) of these compositions. Additionally, crack spinning, and crack deflection could also be observed on the fracture surfaces of 0.1 and 0.3 wt.% nanocomposites that indicated the high efficient toughening mechanism of these materials [411]. It resulted in the improvements of fracture strain at these materials compared to epoxy. On the contrary, clear CNF bundles and rough fracture surfaces were observed for 0.7 and 1.0 wt.% CNF nanocomposites (Figure 5.14c, d) that implied the poor distribution of the fillers at such high loadings.

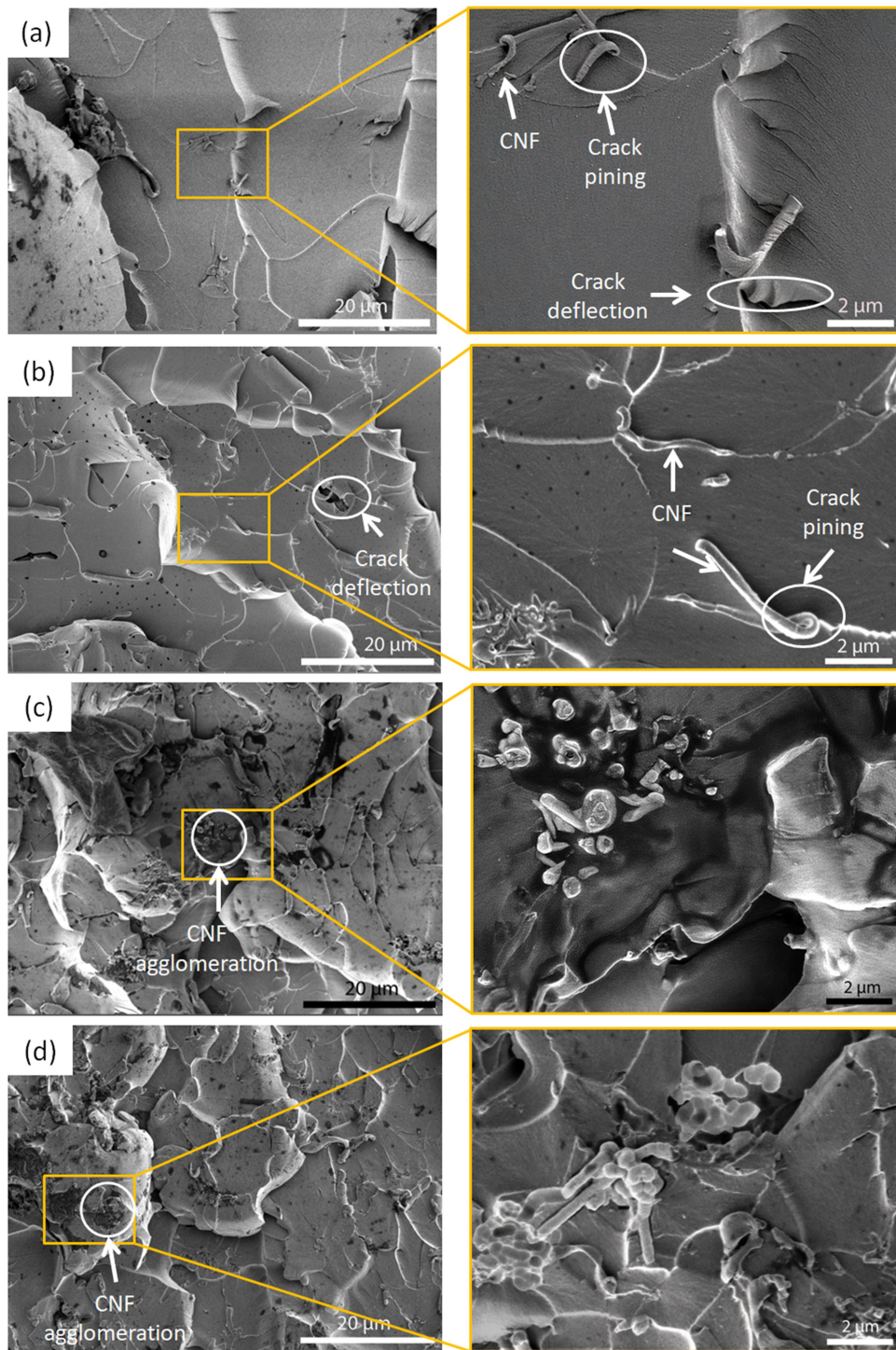


Figure 5.14: SEM micrographs at high magnifications of the tensile fracture surfaces of:  
(a) Epoxy/0.1 wt.% CNF, (b) Epoxy/0.3 wt.% CNF, (c) Epoxy/0.7 wt.% CNF, (a) Epoxy/1  
wt.% CNF

These poor-dispersed CNFs led to stress concentration, hence reducing the tensile strength of the materials (Figure 5.12a). Additionally, coarse fracture surfaces, large crack lines, and CNF agglomerates at this high-filler-content group (Figure 5.14c, d) indicated a low degree of toughening effect, resulting in low fracture strain of these materials.

### 5.12 DMA analysis – Glass transition temperature

Figure 5.15 illustrates a typical variation of epoxy/CNF nanocomposites'  $\tan \delta$  (ratio of loss modulus to storage modulus) as a function of temperature. The average glass transition temperature was identified based on the peak values of  $\tan \delta$  and is shown in Table 5.5. The gradual growth of the glass transition temperature at low filler was observed which reached the peak of 70.6°C at 0.3 wt.% CNF. Tg was then reduced for the filler content above 0.3 wt.%. The homogenous distribution of CNF at 0.1 and 0.3 wt.% (Figure 5.14a, b) contribute to their high magnitudes of Tg. It was due to the well-dispersed nanofibres at such low contents that could form a continuous network to restrict the polymer chains' mobility or increased the immobilization of macromolecules [412], hence stabilizing the material structure in response to accelerated thermal energy.

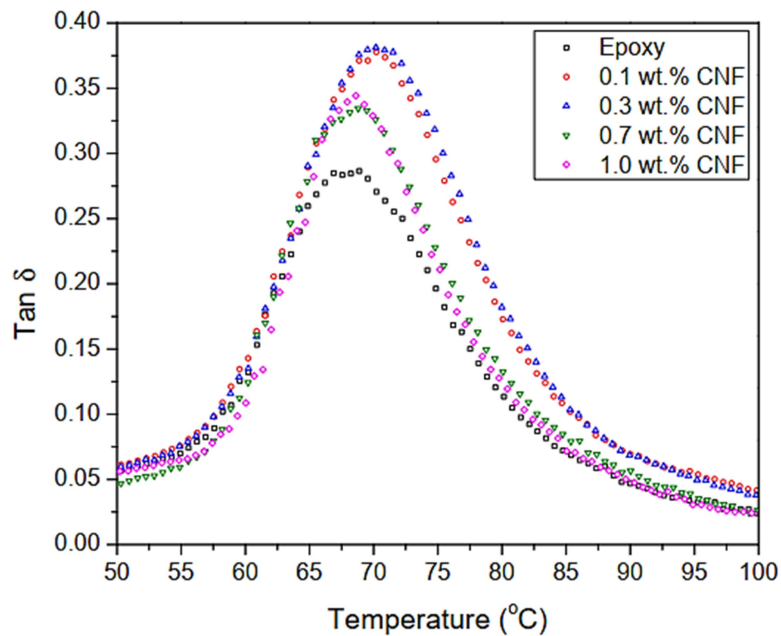


Figure 5.15:  $\tan \delta$  of epoxy/CNF nanocomposites at different filler contents from DMA analysis

Table 5.5: Glass transition temperature of epoxy/CNF nanocomposites at different filler contents

CNF concentration (wt.%)	Glass Transition Temperature $T_g$ (°C)
0	69.5 ( $\pm 0.55$ )
0.1	70.5 ( $\pm 0.47$ )
0.3	70.6 ( $\pm 0.76$ )
0.7	68.7 ( $\pm 0.07$ )
1	67.3 ( $\pm 1.82$ )

On the contrary, more agglomerations of CNFs at higher filler contents (Figure 5.14c, d) led to the reduction of  $T_g$  by 3% lower than plain epoxy at 1 wt.% CNF. These aggregations of the nano-fibres resulted in less matrix-filler interaction and left the more free volume of polymer chains, hence making the polymer's structure unstable at high temperature. The poor dispersion of nano-fillers also contributed to the degradation of polymer's mechanical properties as it impeded the curing and reduces the crosslinking density [413]. The effect of filler concentration on the transition temperature of epoxy/CNF nanocomposites from Table 5.5 showed high agreement with other investigations on various polymer nanocomposites such as epoxy/graphene [375] or PU/graphene oxide (PU/GO) [414]. This result was also identical to the tensile properties (section 5.10) that re-confirmed the obvious effect of fillers' distribution on the thermomechanical properties of epoxy/CNF nanocomposites.

### 5.13 Chip morphology

Figure 5.16 depicts the chip morphology for different polymer nanocomposites and plain epoxy at a cutting speed of 78.54 m/min. As a general trend, chip morphology tended to change from debris/discontinuous into continuous form as FPT increasing from 0.2 to 5  $\mu\text{m}$ . This transition point (denoted by horizontal arrows) was supposed to be the MUCT and it depended on the mechanical properties of workpiece materials. The chips when micromilling 0.1 wt.% nanocomposite (Figure 5.16a) started to form somewhere between 0.2 to 0.5  $\mu\text{m}$  of FPT that likely indicated the lowest MUCT compared of these materials to other compositions. The MUCTs of both 0.3 and 0.7 wt.% CNF nanocomposites were in the range from 0.5 to 1  $\mu\text{m}$  (Figure 5.16b, c).



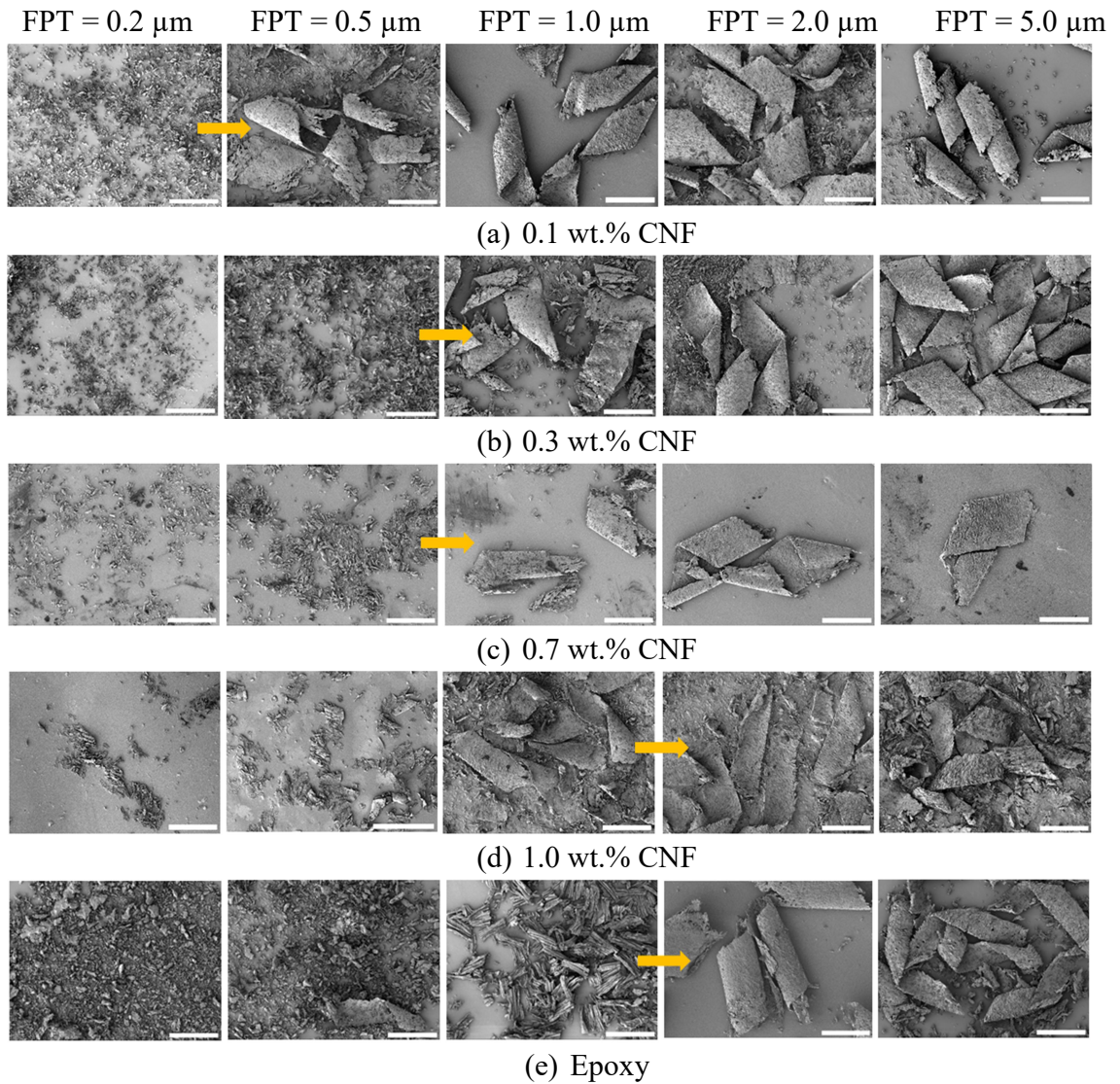


Figure 5.16: Chip morphology of epoxy/CNF nanocomposites at different filler contents (Cutting speed= 78.54 m/min) (Scale bar is 200  $\mu\text{m}$ )

The highest value of the MUCT was observed at 1 wt.% CNF and plain epoxy from 1 to 2  $\mu\text{m}$  (Figure 5.16d, e). The reduction of MUCT as the filler content increased was likely due to the ductility of the nanocomposites. Based on the tensile results from section 5.10, the addition of 0.1 wt.% CNF provided the highest improvement of the fracture strain, followed by 0.3 and 0.7 wt.%. However, there was a ductile-to-brittle transition as the filler content increased to 1 wt.% (Figure 5.12a), even lower than the epoxy (Figure 5.12c).

Chapter 5: Machinability of carbon nanofiller reinforced epoxy nanocomposites at nano-  
micro cutting chip load

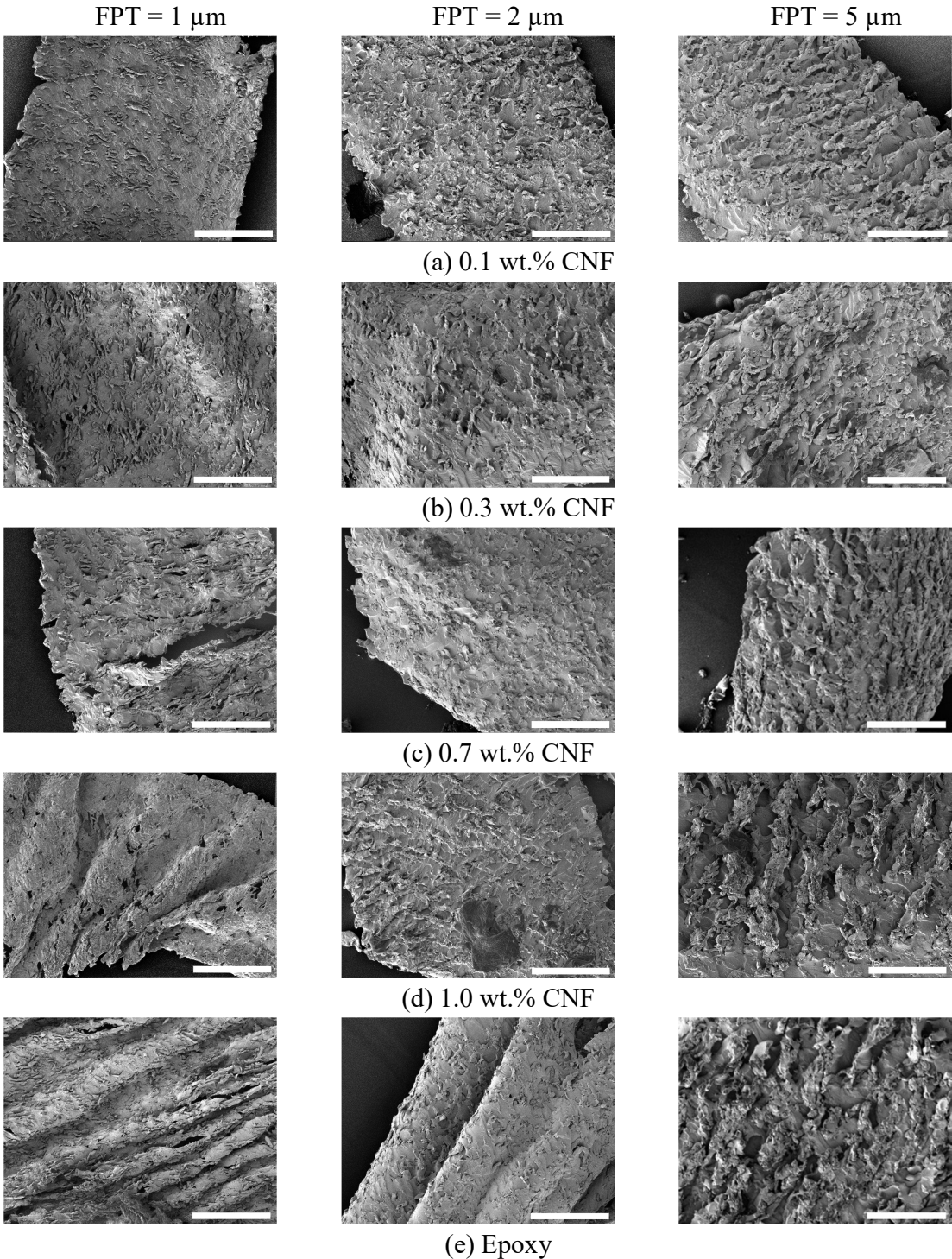


Figure 5.17: Chip morphology of epoxy/CNF nanocomposites at different filler contents (Cutting speed= 78.54 m/min) (Scale bar is 50 μm)



It led to the chip formation at higher FPT or higher MUCT compared to those of ductile nanocomposites (0.1, 0.3, and 0.7 wt.%). On closer observation of chip morphology, Figure 5.17 illustrates the effects of both FPT and filler content on the chip morphology at the cutting speed of 78.54 m/min. At the first glance, the chip surface appeared to be coarser at a high feed rate as FPT increasing. The broad shear zone at high feeds made the chip segments more obvious, hence roughening the chip surfaces. The chip morphology showed an obvious difference between compositions at FPT of 1 $\mu$ m. At this feed, the chip thickness was low enough to show the sensitivity of chip formation to the thermomechanical properties of nanocomposites. In detail, the well-enhanced thermomechanical properties of 0.1 and 0.3 wt. % CNF nanocomposites exhibited high integrity chip formation with flat and smooth surfaces and fewer cracks at FPT of 1 $\mu$ m (Figure 5.17a, b) compared to those other materials (0.7 and 1 wt.% and epoxy). On the contrary, the chip morphology showed more cracks for 0.7 and 1 wt.% as a result of the low fracture strain of these materials (Figure 5.12c). Moreover, the chips at 1 wt.% and epoxy appeared to be wrinkle (Figure 5.17d, e), especially for epoxy (Figure 5.17e). This was due to the thermal softening at the high cutting speed that was contributed by the low transition temperature of these nanocomposites (Table 5.5).

## **5.14 Cutting force**

### **5.14.1 ANOVA analysis**

ANOVA analysis was applied to statistically identify the level of input factor's distributions.

Table 5.6 represents the ANOVA analysis of the resultant cutting force that considered the influences of three main input factors. All filler content, FPT, and cutting speed showed a significant effect on cutting force. The cutting speed exhibited the most significant influence on the cutting force with its contribution of around 74.5%.

Table 5.6: ANOVA result for the resultant cutting force when micromilling epoxy/CNF nanocomposites

Source	DF	Seq SS	Contribution	Adj SS	Adj MS	F-Value	P-Value
Filler Content	4	2.146	11.09%	2.146	0.53641	33.75	< 0.001
Cutting Speed	2	14.426	74.53%	14.426	7.21316	453.86	< 0.001
FPT	4	1.766	9.12%	1.766	0.44154	27.78	< 0.001
Error	64	1.017	5.26%	1.017	0.01589		
Total	74	19.355	100.00%				

#### 5.14.2 Cutting force analysis

Figure 5.18 illustrates the cutting force's variations at the different cutting speeds (from 31.41 to 125.67 m/min). Generally, the cutting force gradually increased along with FPT increment regardless of the workpiece materials. It implied the significant effect of chip load on the feed mark formation due to the increased plastic deformation of the workpiece on the machined surfaces. This trend was more obvious at the lowest cutting speed of 31.41 m/min (Figure 5.18a) where the thermal softening effect was unlikely to occur.

At the high cutting speeds, the cutting force of 1 wt.% CNF nanocomposite and epoxy showed a fluctuation at the low range of FPT (0.2 – 2  $\mu\text{m}$ ) at 78.54 m/min (Figure 5.18b) and 125.67 m/min (Figure 5.18c). This phenomenon indicated the effect of MUCT on cutting force at these high cutting speeds. As discussed in section 5.13, 1 wt.% CNF nanocomposites and epoxy showed the highest MUCT (from 1 to 2 $\mu\text{m}$ ). It led to the occurrence of the ploughing regime at the FPT below 2 $\mu\text{m}$ , resulting in the high cutting force at FPT of 0.2  $\mu\text{m}$ . The cutting force was decreased as FPT increased (up to 1 $\mu\text{m}$ ) due to the reduction of the ploughing mechanism. As the occurrence of the dominant-shearing regime at higher FPT (from 1 to 2 $\mu\text{m}$ ), the cutting force increased as a result of increased chip load. On the contrary, the cutting force at 0.1, 0.3, and 0.7 wt.% CNF exhibited a



linear increase of cutting force in this FPT range (0.2 to 2  $\mu\text{m}$ ) (Figure 5.18b and c). It could be interpreted by considering the fracture strain and Young's modulus of the workpiece materials. As shown in Figure 5.1b and c, both fracture strain and Young's modulus of 0.1, 0.3, and 0.7 wt.% nanocomposites were higher than epoxy and 1 wt.% composition. It resulted in the higher resistance of the workpiece against the tool advance at high cutting speeds (78.54 and 125.67 m/min), hence leading to the linear raise of cutting force at FPT from 0.2 to 1  $\mu\text{m}$ . The rising portion of cutting force variation at higher feed rates (2 to 5  $\mu\text{m}$ ) for all compositions was attributed to the increased chip load and shear area or larger plastic deformation that was similar to those of conventional cutting (at macro scale).

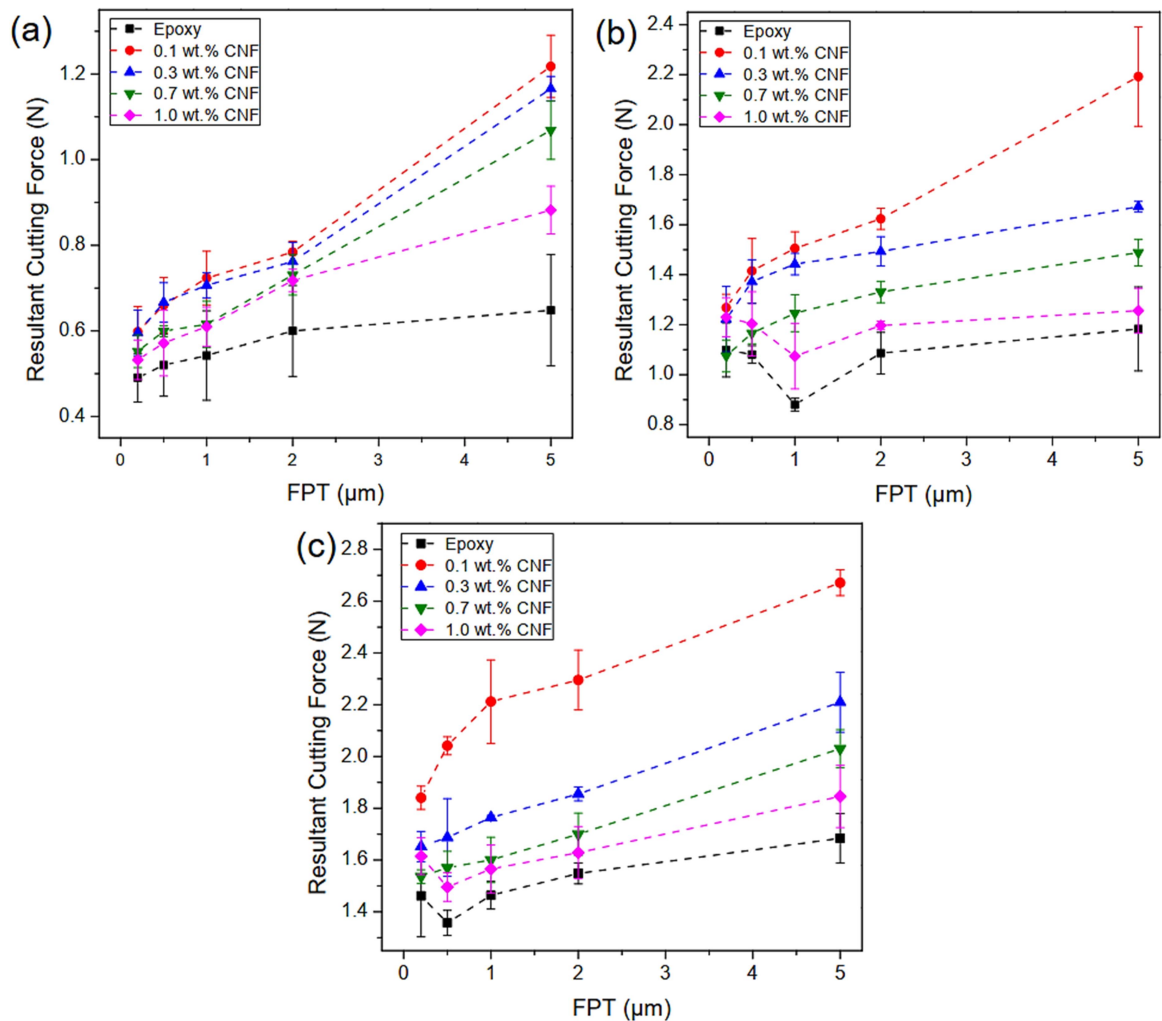


Figure 5.18: Cutting force when micromilling epoxy/CNF nanocomposites at different cutting speeds: (a) 31.41 m/min, (b) 78.54 m/min, (c) 125.67 m/min

The cutting force variation showed significant dependence on the filler content, exhibited by the higher cutting force magnitudes as the filler content increased (Figure 5.18). It was likely to imply the considerable effect of thermomechanical properties of materials. With the incorporation of CNFs, the epoxy-based nanocomposites showed higher cutting force magnitudes than epoxy due to the strengthening effect (Figure 5.12). From Figure 5.18a-c, it appeared that the cutting force for 0.1 wt.% CNF nanocomposite showed the highest values, followed by 0.3 wt.% counterparts. This could be attributed by the improvements of the stiffness (Figure 5.12b) and the failure strain (Figure 5.12c), owing to the uniform distribution of nano-fibres (Figure 5.14a, b) of these materials. On the contrary, the low cutting forces when micromilling high-filler-content nanocomposites (0.7 and 1 wt.% CNF) were contributed by the low mechanical properties compared to 0.1 and 0.3 wt.% CNF due to the agglomeration of the nano-fibres (Figure 5.14c, d). Also, 0.1 wt.% nanocomposites exhibited significantly high cutting force magnitudes at the highest cutting speed of 125.67 m/min that was distinct from those of other materials. At such a high cutting speed, the thermal softening effect seemed to appear. The high cutting force magnitudes when micromilling 0.1 wt.% nanocomposite was due to its low thermal sensitivity that was contributed by the high glass transition temperature of this composition (Table 5.5). It resulted in the stability of the mechanical properties of this material at a high cutting speed, hence increasing the cutting force.

Figure 5.19 shows the significant effect of cutting speed on the cutting force, regardless of the filler content. The cutting force showed only the rise trend as the cutting speed increased. It was commonly known that cutting speed increase could lead to high cutting temperature due to the generated heat from tool-workpiece contact [415]. This high cutting temperature led to two opposite mechanisms:

- The thermal softening effect reduced the mechanical properties of workpiece materials (i.e., stiffness), hence reducing the required cutting force.
- The strain hardening effect enhanced the mechanical properties of workpiece materials (stronger and harder to deform), increasing by cutting force.

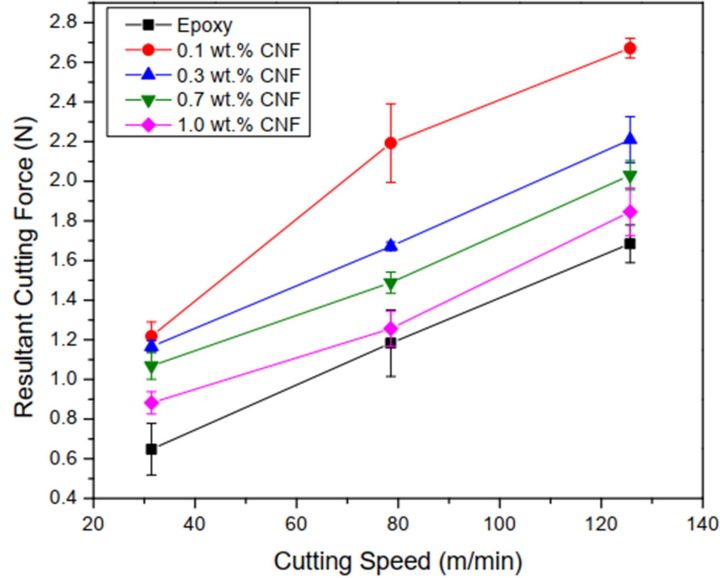


Figure 5.19: Effect of cutting speed on the cutting force when micromilling epoxy/CNF nanocomposites at different filler contents (FPT= 5  $\mu\text{m}$ )

The stress-strain behaviour of all materials showed no strain-hardening phenomenon (Figure 5.12) at room temperature. However, it has been investigated that this effect would take place at a higher temperature (right below the glass transition temperature) [386]. Therefore, the only upward trends of the cutting force from Figure 5.19 indicated the subservience of the thermal softening effect and the dominance of the strain hardening effect. In the case of 1 wt.% and 0.7 wt.% materials, the micro-structure effect might also contribute to the cutting force increment at high cutting speeds, owing to more contact between tool and CNFs at high filler contents.

### 5.15 Machined surface morphology

The characterisations of the machined surface morphology when micromilling of epoxy/CNF nanocomposites and epoxy at a cutting speed of 125.67 m/min are shown in Figure 5.20. The SEM imaging has been performed in the middle area of the machined slot. Generally, the feed marks became clearer as the FPT increased, regardless of the material type. Among different compositions, 0.1 wt.% nanocomposites showed the machined

surfaces (Figure 5.20a) with the most obvious feed marks, even at the low chip load (0.5  $\mu\text{m}$ ). It was attributed to the high MUCT at this filler concentration, hence making feed marks the main pattern of surface morphology for this material. However, feed marks appeared to be blurred at the higher filler content of 0.3 wt.% CNF (Figure 5.20b).

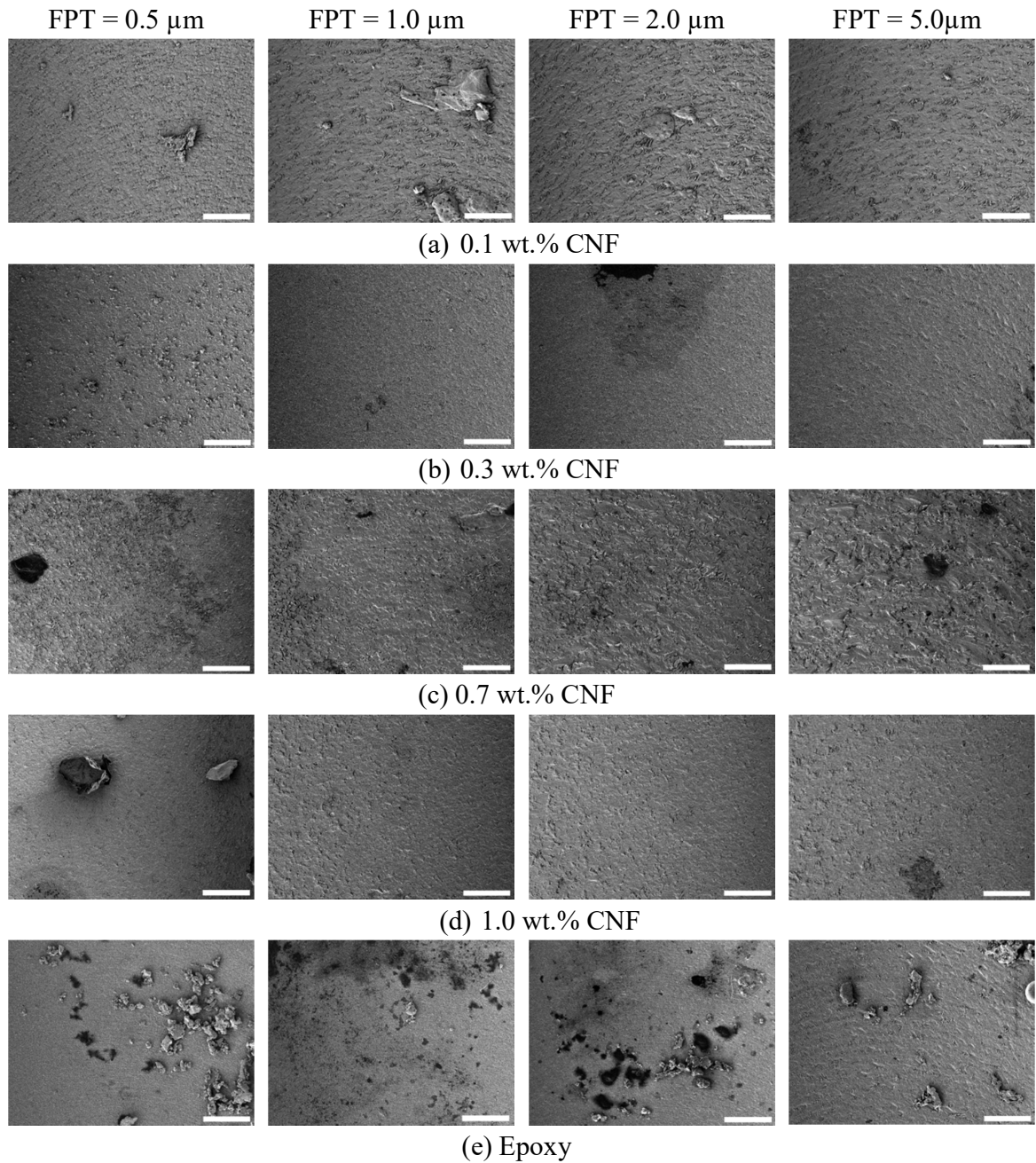


Figure 5.20: Machined surfaces when micromilling epoxy/CNF nanocomposites at the cutting speed of 125.67 m/min (Scale bar is 50  $\mu\text{m}$ )

Given the relatively high filler loading, the nano-fibres appeared to be bridging the cracks along with the feed marks, hence smoothing the machined surfaces. For a further increase of filler content to 0.7 wt.% CNF, the machined surface morphology appeared to be coarse with obvious cracks cover by material adhesion (Figure 5.20c). On the other hand, the machined surface morphology of 1 wt.% CNF nanocomposite (Figure 5.20d) tended to be relatively smooth that was similar to that of plain epoxy (Figure 5.20e). It might be attributed to the brittle failure of these two materials (Figure 5.12c). The machined surface of epoxy also showed more chip adhesion at every FPT, owing to their low thermal transition temperature that consequently leads to thermal softening at high cutting speeds.

## 5.16 Machined surface roughness

### 5.16.1 ANOVA analysis

Statistical analysis of ANOVA was used to identify the level of input factor's distributions on the machined surface roughness. The results from Table 5.7 revealed that all filler content, FPT, and cutting speed exhibited significant effects on Ra variation. In detail, the high contribution was found of around 29% for filler content, followed by FPT with around 25%. However, the cutting speed appeared to show the least effect at only 9%.

Table 5.7: ANOVA result for surface roughness when micromilling epoxy/CNF nanocomposites

Source	DF	Seq SS	Contribution	Adj SS	Adj MS	F-Value	P-Value
Filler Content	4	0.016096	29.21%	0.016096	0.004024	12.82	< 0.001
Cutting Speed	2	0.005011	9.10%	0.005011	0.002506	7.98	0.001
FPT	4	0.013896	25.22%	0.013896	0.003474	11.06	< 0.001
Error	64	0.020096	36.47%	0.020096	0.000314		
Total	74	0.055100	100.00%				



### **5.16.2 Surface roughness analysis**

The machined surface roughness exhibited a generally upward trend as the chip load increased, regardless of the cutting speed and the workpiece material's type (Figure 5.21). However, an initial decrease of the cutting force could be observed at the low FPTs for all materials, except 0.1 wt.% nanocomposite. Given such a low chip load, this phenomenon was likely attributed to the MUCT effect that implied a ploughing-dominated mechanism at this stage. The ploughing regime led to strong plastic deformation and large compressive residual stress of the top layer of the workpiece (machined surface) [416], resulting in high surface roughness (at FPT of 0.2  $\mu\text{m}$ ). These ploughing-based cutting force variations could be divided into two groups based on their similar trends: (i) 0.3 and 0.7 wt.% and (ii) 1 wt.% and plain epoxy.

At the lowest cutting speed (Figure 5.21a), the first group (0.3 and 0.7 wt.%) exhibited a drop of the cutting force at the FPT below 0.5  $\mu\text{m}$  while this threshold was shifted to 1  $\mu\text{m}$  in the case of the second group. This phenomenon correlated with the MUCTs of these materials from section 5.13 (Figure 5.16). Additionally, there was an enlargement of the cutting force's drop portion from 1 to 2  $\mu\text{m}$  for 1 wt.% and plain epoxy as higher cutting speeds (Figure 5.21b, c). It was likely to indicate the increase of MUCT of these materials at higher cutting speeds. Due to their low glass transition temperature (Table 5.5), these materials had a high tendency to be softened at high temperature, resulting in more chip adhesion on the micro-tool. It might lead to the decrease of the cutting edge radius (tool bluntness), hence increasing the MUCT. The machined surface roughness tended to exhibit higher MUCT sensitivity compared to that of the cutting force. For 0.1 wt.% material, the cutting force still showed a steady increase at the low FPTs, owing to its extremely low MUCT (0.2 to 0.5  $\mu\text{m}$ ) (Figure 5.16).

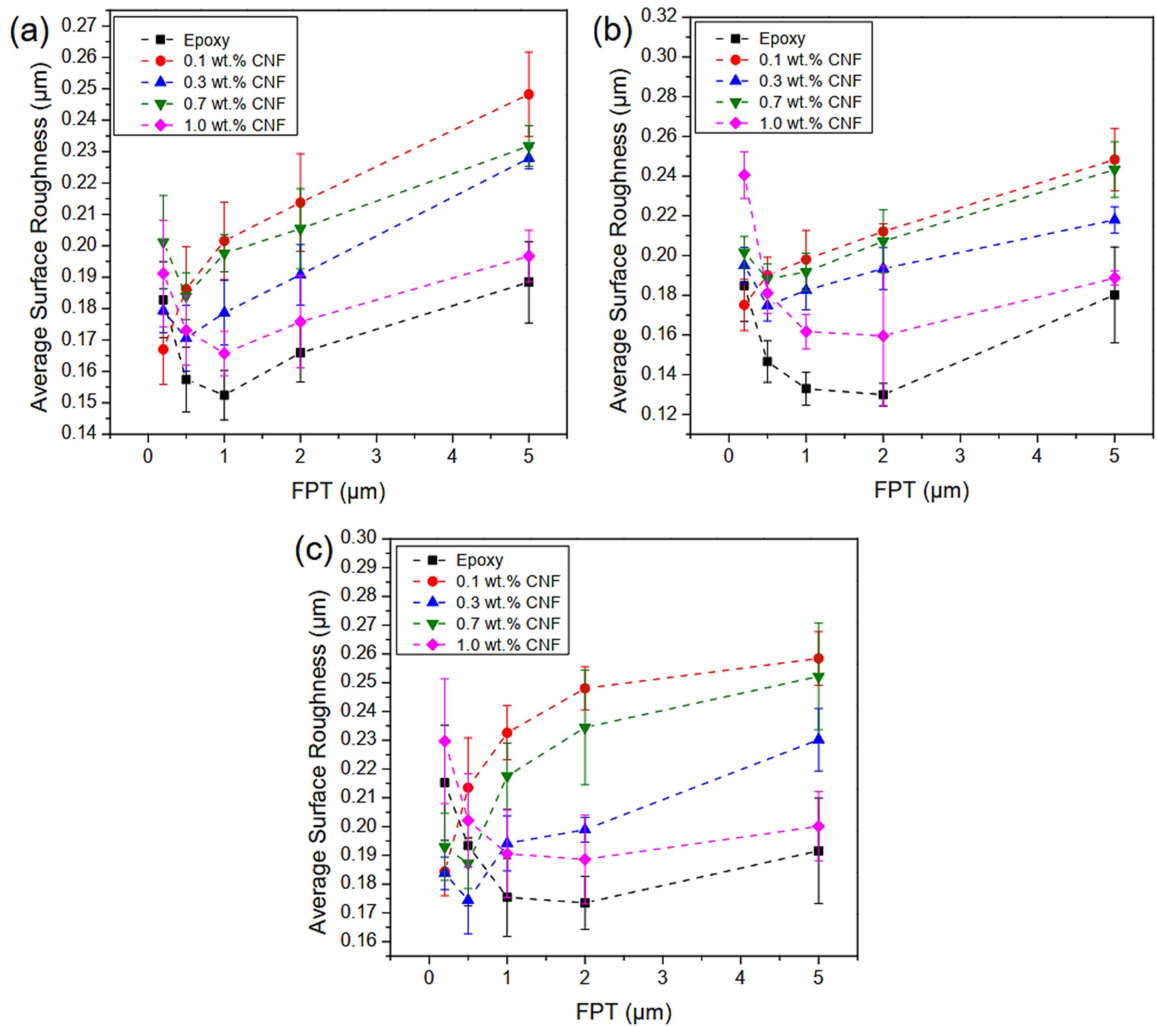


Figure 5.21: Effect of the filler content and feed rate on the average surface roughness when micromilling epoxy/CNF nanocomposites at different cutting speeds: (a) 31.41 m/min, (b) 78.54 m/min, (c) 125.67 m/min

As the FPT exceeded the MUCT boundary, the machined surface roughness showed a gradual increase with FPT. It was likely to indicate the dominant effect of FPT on Ra at this stage that was contributed by the formation of feed marks at high FPTs (Figure 5.20). The increase in feed rate led to higher plastic deformation, resulting in rougher surfaces and higher feed marks compared to those at low feed rates.

Figure 5.21(a-c) also exhibited the obvious effect of filler content on the surface roughness variation at the different cutting speeds despite some disorder at the lower feed

rates due to the MUCT thickness. Generally, the highest values of Ra could be observed at the machined surfaces of 0.1 wt.% CNF nanocomposite and appeared to be reduced as the filler content increased (Figure 5.22). This result seemed to be relatively identical with the mechanical properties (i.e., Young's modulus, fracture strain) of different compositions (Figure 5.12) that indicated the effect of strengthening effect on the surface roughness. The role of cutting force in machining was to generate stress that exceeds the strength of work material, hence resulting in the separation of material layers (UCT) or fracture. In that way, it was understood that a higher cutting force was needed to cut a stronger material's layers. As a consequence, the high cutting force generated tool vibration which was responsible for the increase of Ra [389]. Given such a high cutting speed and small tool in micro-machining, Ra was likely to exhibit high tool-vibration sensitivity. Therefore, the highest cutting force when micromilling of 0.1 wt.% material (Figure 5.18) might contribute to the highest Ra that can be seen in Figure 5.21. This mechanism could be used to explain the order of Ra magnitudes for other materials. From that point of view, the surface roughness of 0.7 wt.% nanocomposite was supposed to be lower than that of 0.3 wt.% counterparts due to its lower cutting force magnitudes (compared to that of 0.3 wt.%). As a matter of fact, these values were observed to be higher than those of 0.3 wt.% material. This unusual result might be explained based on two reasons. The first one was the contribution of the microstructure effect. Given such a high filler content of 0.7 wt.%, the CNFs tended to form a dense network, leading to the high tendency of tool-fibre interaction [331]. Secondly, the stiffness and fracture strain of 0.7 wt.% and 0.3 wt.% nanocomposites were comparable (Figure 5.12). These two factors likely resulted in more tool vibration, hence leading to rougher machined surfaces at 0.7 wt.% compared to those of 0.3 wt.% material that could be visually recognised from the SEM images in Figure 5.20.



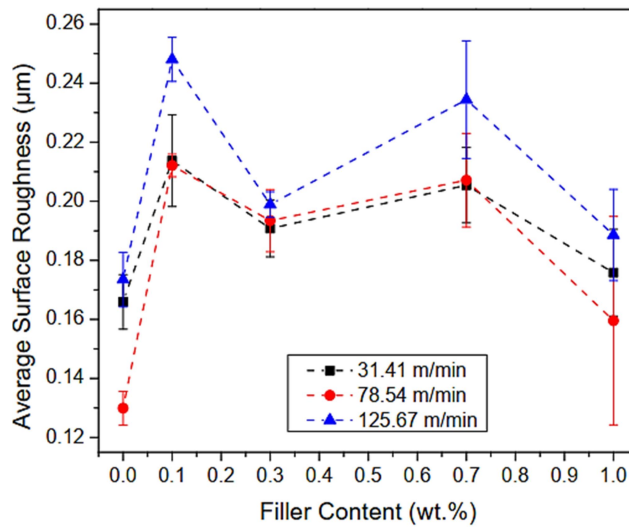


Figure 5.22: Effect of the filler content on the average surface roughness when micromilling epoxy/CNF nanocomposites (FPT= 2 µm)

Apart from the effect of tool vibration, it was also worthwhile to notice the negative effect of plastic deformation on the surface roughness. The SEM analysis of the machined morphology from section 5.16 (Figure 5.20) revealed the most obvious feed marks at 0.1 wt.% CNF but became unclear as the filler content reached 1 wt.% as well as plain epoxy. Given the high cutting force required to machine strong materials (i.e., 0.1 and 0.3 wt.%), the machined surface tended to be deformed severely, causing high plastic deformation. It resulted in more work material's residue left on the finished surface that contributed to higher feed marks (higher surface roughness).

### 5.17 Summary

The investigation on the machinability of CNF reinforced epoxy nanocomposites using micromilling revealed the significant effect of cutting conditions and workpiece material on the cutting force and surface roughness variations. From the ANOVA analysis, it was observed that cutting force was significantly affected by cutting speed whereas FPT and filler content were the two main influential factors in the surface roughness variation. Based on that, epoxy/CNF nanocomposites at the filler contents of 0.3 and 1 wt.% CNF showed good performances in terms of low cutting force and high surface finish when

micromilling at low cutting speeds of 31.41 m/min and low FPT (from 0.5 to 1  $\mu\text{m}$ ). Also, the size effect on both cutting force and surface roughness was revealed when micromilling these nanocomposites and plain epoxy at the FPTs below MUCT. The machinability behaviours of these materials also showed high agreement with the characterisation results (tensile properties, glass transition temperature, and SEM analysis of fracture surface) when the thermal-mechanical and micro-structure effects were taken into consideration.

## **Chapter 6: Conclusions and future work**

### **6.1 Conclusions**

In this research, the machinability of carbon nano-filler reinforced epoxy nanocomposites through the micromilling process was investigated. The micromachining experiments were conducted on epoxy-based nanocomposites reinforced by various types of carbon nano-filler (in terms of filler geometry and size) at different chip loads (from nano to micro). Based on that, a comprehensive study on the micromachining behaviours of carbon nano-filler reinforced epoxy nanocomposites was addressed. Due to the important roles of thermomechanical properties and micro-structure effect of workpiece materials on their micromachining behaviours, some relevant characterisations were made prior to micromilling experiments. They included tensile, thermal conductivity, DMA and SEM analysis. The workpiece materials were prepared by mould casting at different filler loadings (up to 1 wt.%). Due to the distinct nature of each carbon nano-filler's type, different mixing methods were applied during the fabrication including solution mixing and three roll milling to attain homogenous distributions of the nano-fillers. The addition of carbon nano-fillers in the epoxy matrix led to the improvements of tensile properties (strength, stiffness, ductility) as well as thermal properties (thermal conductivity, glass transition temperature) compared to epoxy.

From this research, some important results were identified that can be applied in the advancement of knowledge in the field of micromachining nanocomposites:

- Micromachining of polymer nanocomposites at micro-chip loads generally showed the similar role of FPT in increasing cutting force and surface roughness. However, the significant influences of cutting speed, filler loading on cutting force and surface roughness, respectively indicated the high sensitivity of these nanocomposites' machinability to thermomechanical and microstructure effect. This feature highlighted the key difference compared to macromachining of nanocomposites.

- The significant effects of thermomechanical properties and micro-structure of these epoxy-based nanocomposites also exhibited on the rapid tool wear of uncoated micro-tools during the micromilling process compared to those of coated tools (DLC and diamond). It was further suggested to use DLC micro-tool in micromachining of carbon nano-fillers reinforced epoxy nanocomposites to attain low tool wear, cutting force, and surface roughness.
- The micromilling experiments performed at nano-to-micro-chip loads (0.2 to 5 $\mu\text{m}$ ) showed two different trends of cutting force and surface roughness variations (as a function of FPT). At micro-cutting conditions (chip load from 1 to 5 $\mu\text{m}$ ), these trends were generally similar to those at the higher range of chip load (5 to 15 $\mu\text{m}$ ) with the increase of both cutting forces (F) and surface roughness (Ra) with FPT. However, the size effect took place in nano-cutting regimes at chip load below MUCT (around 1 $\mu\text{m}$ ), exhibited by the fluctuations of their values (F and Ra). It was contributed by the ploughing-dominated cutting mechanism, resulting in high magnitudes of both F and Ra at such low chip loads. Throughout the chip load range, the micro-structure and thermomechanical properties had dominant influences on the micromachining behaviours (cutting force, surface roughness, tool wear) of these epoxy-based nanocomposites.

Based on the analysis of the machinability of carbon nano-fillers reinforced epoxy nanocomposites, it was found that the manipulation of the cutting speed in micromachining can be an effective way to attain low cutting force generated that consequently reduce tool wear rate and surface roughness. Additionally, a machining regime at chip load beyond the MUCT was suggested to avoid negative influences from the size effect. Therefore, a pre-identification of the ratio of cutting edge radius to FPT is deemed to be necessary to achieve an optimal cutting condition.

The results from this research presented a comprehensive investigation on the machinability of carbon nano-fillers reinforced epoxy nanocomposites that can be applied in industry due to the growing demands of micro-manufacturing nanocomposites. Based on the study, the optimal micro-cutting conditions can be recommended to obtain high tool life, low cutting force and surface roughness. Also, these results from this study can contribute to further research in advanced machining of nanocomposites.

## **6.2 Future work**

In this research, the tool wear behaviour in micromachining of epoxy-based nanocomposites has been addressed in chapter 4-part II and chapter 5-part I. However, the cutting parameters (i.e., cutting speed, feed) need to be employed in a larger range to provide more in-depth investigations on this machinability response.

Due to the limitation of material models of nanocomposites, the researches on modelling of micromachining of nanocomposites have been still limited in metal matrix nanocomposites only. The ongoing study has been building the model of carbon nanofibre to reinforce epoxy nanocomposites. Therefore, the modelling of micromilling these nanocomposites is expected to be feasible in future work to provide real-time simulations. Based on that, more comprehensive investigation will be provided.

Due to the huge potential applications of nanocomposites in many industrial areas, future research trends may suggest that micromachining of metal and ceramic matrix nanocomposites should be addressed to provide comprehensive knowledge of advanced micromachining of nanocomposites and expand the applications of micromachining of nanocomposites.

The state of the art of micromachining of nanocomposites has shown very limited applications and most of the researches have been in the prototyping stage. Therefore, the future work also focuses on commercial applications of micromachining of nanocomposites such as micromachining of micro-products made from nanocomposites (i.e., micro-gear, micro-electronic components)

## References

- [1] A. Blumstein, "Erude Des Polymerisations en couche adsorbee. 1," *Bulletin de la Societe Chimique de France*, pp. 899-905, 1961.
- [2] Q. Cheng, B. Wang, C. Zhang, and Z. Liang, "Functionalized carbon-nanotube sheet/bismaleimide nanocomposites: mechanical and electrical performance beyond carbon-fiber composites," *Small*, vol. 6, pp. 763-767, 2010.
- [3] I. Srikantha, P. Ghosalb, A. Kumara, and R. Jaina, "Nanocomposites for Aerospace Applications," *Nanotech*, vol. 5, p. 52, 2014.
- [4] J. M. Garces, D. J. Moll, J. Bicerano, R. Fibiger, and D. G. McLeod, "Polymeric nanocomposites for automotive applications," *Advanced Materials*, vol. 12, pp. 1835-1839, 2000.
- [5] D. Feldman, "Polymer nanocomposites in medicine," *Journal of Macromolecular Science, Part A*, vol. 53, pp. 55-62, 2016.
- [6] I. Dinca, C. Ban, A. Stefan, and G. Pelin, "Nanocomposites as advanced materials for aerospace industry," *Incas Bulletin*, vol. 4, p. 73, 2012.
- [7] A. Leszczyńska, J. Njuguna, K. Pielichowski, and J. Banerjee, "Polymer/montmorillonite nanocomposites with improved thermal properties: Part I. Factors influencing thermal stability and mechanisms of thermal stability improvement," *Thermochimica acta*, vol. 453, pp. 75-96, 2007.
- [8] J. Bai and A. Allaoui, "Effect of the length and the aggregate size of MWNTs on the improvement efficiency of the mechanical and electrical properties of nanocomposites—experimental investigation," *Composites Part A: applied science and manufacturing*, vol. 34, pp. 689-694, 2003.
- [9] N. Dong, M. Zhong, P. Fei, Z. Lei, and B. Su, "Magnetic and electrochemical properties of PANI-CoFe<sub>2</sub>O<sub>4</sub> nanocomposites synthesized via a novel one-step solvothermal method," *Journal of Alloys and Compounds*, vol. 660, pp. 382-386, 2016.
- [10] H. Kim, Y. Miura, and C. W. Macosko, "Graphene/polyurethane nanocomposites for improved gas barrier and electrical conductivity," *Chemistry of Materials*, vol. 22, pp. 3441-3450, 2010.
- [11] H. Tang and H. A. Sodano, "High energy density nanocomposite capacitors using non-ferroelectric nanowires," *Applied Physics Letters*, vol. 102, p. 063901, 2013.
- [12] D. Kumar, T. Goyal, V. Kumar, P. Mohite, S. Kamle, and V. Verma, "Development and modal analysis of bioinspired CNT/epoxy nanocomposite MAV flapping wings," *J. Aerosp. Sci. Technol*, vol. 67, pp. 88-93, 2015.
- [13] J. Chae, S. Park, and T. Freiheit, "Investigation of micro-cutting operations," *International Journal of Machine Tools and Manufacture*, vol. 46, pp. 313-332, 2006.
- [14] A. Blumstein, "Polymerization of adsorbed monolayers. II. Thermal degradation of the inserted polymer," *Journal of Polymer Science Part A: General Papers*, vol. 3, pp. 2665-2672, 1965.

## References

- [15] I. Arora, J. Samuel, and N. Koratkar, "Experimental investigation of the machinability of epoxy reinforced with graphene platelets," *Journal of Manufacturing Science and Engineering*, vol. 135, p. 041007, 2013.
- [16] Y. Liu, W. Xiong, L. Jiang, Y. Zhou, and Y. Lu, "Precise 3D printing of micro/nanostructures using highly conductive carbon nanotube-thiol-acrylate composites," in *Laser 3D Manufacturing III*, 2016, p. 973808.
- [17] D. Kumar, P. M. Mohite, and S. Kamle, "Dragonfly Inspired Nanocomposite Flapping Wing for Micro Air Vehicles," *Journal of Bionic Engineering*, vol. 16, pp. 894-903, 2019.
- [18] M. Imboby and K. Jiang, "Fabrication of free standing 316-L stainless steel–Al<sub>2</sub>O<sub>3</sub> composite micro machine parts by soft moulding," *Acta Materialia*, vol. 57, pp. 4751-4757, 2009.
- [19] N. Oya, K. Nishiyabu, T. Yanagisawa, S. Higaki, and S. Tanaka, "Physical Properties of Carbon Nanotube/Polypropylene Compounds," in *Proceeding of the 11th European Conference on Composite Materials (ECCM-11)*.
- [20] Q. Y. Tang, Y. C. Chan, N. B. Wong, and R. Cheung, "Surfactant-assisted processing of polyimide/multiwall carbon nanotube nanocomposites for microelectronics applications," *Polymer International*, vol. 59, pp. 1240-1245, 2010.
- [21] F.-C. Chen, C.-W. Chu, J. He, Y. Yang, and J.-L. Lin, "Organic thin-film transistors with nanocomposite dielectric gate insulator," *Applied physics letters*, vol. 85, pp. 3295-3297, 2004.
- [22] P. M. Raj, H. Sharma, G. P. Reddy, N. Altunyurt, M. Swaminathan, R. Tummala, *et al.*, "Cobalt–polymer nanocomposite dielectrics for miniaturized antennas," *Journal of electronic materials*, vol. 43, pp. 1097-1106, 2014.
- [23] E. Goossen, "Vertical take off and landing unmanned aerial vehicle airframe structure," ed: Google Patents, 2012.
- [24] D. J. Pines and F. Bohorquez, "Challenges facing future micro-air-vehicle development," *Journal of aircraft*, vol. 43, pp. 290-305, 2006.
- [25] R. Vijayanandh, N. Kumar, S. Kumar, R. Kumar, and N. Kumar, "Material Optimization of High Speed Micro Aerial Vehicle using FSI Simulation," *Procedia Computer Science*, vol. 133, pp. 2-9, 2018.
- [26] X. Sun and J. Li, "Friction and wear properties of electrodeposited nickel–titania nanocomposite coatings," *Tribology Letters*, vol. 28, pp. 223-228, 2007.
- [27] M. Imboby and K. Jiang, "Stainless steel–titania composite micro gear fabricated by soft moulding and dispersing technique," *Microelectronic Engineering*, vol. 87, pp. 1650-1654, 2010.
- [28] J. i. Masuda and J. M. Torkelson, "Dispersion and major property enhancements in polymer/multiwall carbon nanotube nanocomposites via solid-state shear pulverization followed by melt mixing," *Macromolecules*, vol. 41, pp. 5974-5977, 2008.
- [29] J. Roul, S. K. Sahoo, and R. Mohapatra, "Design and characterization of biodegradable polymer-clay nanocomposites prepared by solution mixing technique," *International Journal of Nano Dimension*, vol. 4, pp. 135-139, 2013.

## References

- [30] Q. Zeng, D. Wang, A. Yu, and G. Lu, "Synthesis of polymer–montmorillonite nanocomposites by in situ intercalative polymerization," *Nanotechnology*, vol. 13, p. 549, 2002.
- [31] M. Lee, B. Kim, J. Nam, Y. Lee, Y. Son, and S. Seo, "In-situ formation of gold nanoparticle/conducting polymer nanocomposites," *Molecular Crystals and Liquid Crystals*, vol. 407, pp. 1-6, 2003.
- [32] I. A. Rahman and V. Padavettan, "Synthesis of silica nanoparticles by sol-gel: size-dependent properties, surface modification, and applications in silica-polymer nanocomposites—a review," *Journal of Nanomaterials*, vol. 2012, p. 8, 2012.
- [33] Y.-H. Choa, J.-K. Yang, B.-H. Kim, Y.-K. Jeong, J.-S. Lee, T. Nakayama, *et al.*, "Preparation and characterization of metal/ceramic nanoporous nanocomposite powders," *Journal of Magnetism and Magnetic Materials*, vol. 266, pp. 12-19, 2003.
- [34] S.-m. Zhou, X.-b. Zhang, Z.-p. Ding, C.-y. Min, G.-l. Xu, and W.-m. Zhu, "Fabrication and tribological properties of carbon nanotubes reinforced Al composites prepared by pressureless infiltration technique," *Composites Part A: Applied Science and Manufacturing*, vol. 38, pp. 301-306, 2007.
- [35] X. Li, Y. Yang, and X. Cheng, "Ultrasonic-assisted fabrication of metal matrix nanocomposites," *Journal of Materials Science*, vol. 39, pp. 3211-3212, 2004.
- [36] D. Ying and D. Zhang, "Processing of Cu–Al<sub>2</sub>O<sub>3</sub> metal matrix nanocomposite materials by using high energy ball milling," *Materials Science and Engineering: A*, vol. 286, pp. 152-156, 2000.
- [37] Y. Cao, Q. Su, R. Che, G. Du, and B. Xu, "One-step chemical vapor synthesis of Ni/graphene nanocomposites with excellent electromagnetic and electrocatalytic properties," *Synthetic Metals*, vol. 162, pp. 968-973, 2012.
- [38] M. Joseph, C. Tsotsos, M. Baker, P. Kench, C. Rebholz, A. Matthews, *et al.*, "Characterisation and tribological evaluation of nitrogen-containing molybdenum–copper PVD metallic nanocomposite films," *Surface and Coatings Technology*, vol. 190, pp. 345-356, 2005.
- [39] P. V. Kamat, M. Flumiani, and A. Dawson, "Metal–metal and metal–semiconductor composite nanoclusters," *Colloids and Surfaces A: Physicochemical and Engineering Aspects*, vol. 202, pp. 269-279, 2002.
- [40] S. Roy, D. Das, D. Chakravorty, and D. Agrawal, "Magnetic properties of glass-metal nanocomposites prepared by the sol-gel route and hot pressing," *Journal of applied physics*, vol. 74, pp. 4746-4749, 1993.
- [41] Y. Choa, S. Yoo, J. Yang, J. Park, S. Oh, K. Kang, *et al.*, "PART 2-C-05 Ceramic Materials-Effect of Powder Synthesis Processing on the Microstructure and Electrical Conductivity of Sintered CNTs/Fe/Al<sub>2</sub>O<sub>3</sub> Nanocomposites," in *Materials Science Forum*, 2007, p. 1021.
- [42] W. R. Schmidt, D. M. Narsavage-Heald, D. M. Jones, P. S. Marchetti, D. Raker, and G. E. Maciel, "Poly (borosilazane) precursors to ceramic nanocomposites," *Chemistry of materials*, vol. 11, pp. 1455-1464, 1999.
- [43] G. Ennas, A. Mei, A. Musinu, G. Piccaluga, G. Pinna, and S. Solinas, "Sol–gel preparation and characterization of Ni–SiO<sub>2</sub> nanocomposites," *Journal of non-crystalline solids*, vol. 232, pp. 587-593, 1998.



## References

- [44] I. Timoshkov, V. Kurmashev, and V. Timoshkov, *Electroplated nanocomposites of high wear resistance for advanced systems application* vol. 3, 2011.
- [45] R. N. Das, F. D. Egitto, J. M. Lauffer, and V. R. Markovich, "Laser micromachining of nanocomposite-based flexible embedded capacitors," in *2007 Proceedings 57th Electronic Components and Technology Conference*, 2007, pp. 435-441.
- [46] E. N. Udofia and W. Zhou, "A guiding framework for microextrusion additive manufacturing," *Journal of Manufacturing Science and Engineering*, vol. 141, 2019.
- [47] T. Bartkowiak and C. A. Brown, "A Characterization of Process–Surface Texture Interactions in Micro-Electrical Discharge Machining Using Multiscale Curvature Tensor Analysis," *Journal of Manufacturing Science and Engineering*, vol. 140, 2018.
- [48] J. Li, J. Liu, J. Liu, Y. Ji, and C. Xu, "Experimental investigation on the machinability of SiC nano-particles reinforced magnesium nanocomposites during micro-milling processes," *International Journal of Manufacturing Research*, vol. 8, pp. 64-84, 2013.
- [49] E. Brinksmeier, R. Gläbe, O. Riemer, and S. Twardy, "Potentials of precision machining processes for the manufacture of micro forming molds," *Microsystem Technologies*, vol. 14, p. 1983, 2008.
- [50] I. Ahmad, M. Islam, T. Subhani, and Y. Zhu, "Toughness enhancement in graphene nanoplatelet/SiC reinforced Al<sub>2</sub>O<sub>3</sub> ceramic hybrid nanocomposites," *Nanotechnology*, vol. 27, p. 425704, 2016.
- [51] J. Samuel, R. E. DeVor, S. G. Kapoor, and K. J. Hsia, "Experimental investigation of the machinability of polycarbonate reinforced with multiwalled carbon nanotubes," *Journal of Manufacturing Science and Engineering*, vol. 128, pp. 465-473, 2006.
- [52] H. Gustafsson, S. Isaksson, A. Altskär, and K. Holmberg, "Mesoporous silica nanoparticles with controllable morphology prepared from oil-in-water emulsions," *Journal of colloid and interface science*, vol. 467, pp. 253-260, 2016.
- [53] M. Huang and Z. Li, "Influences of particle size and interface energy on the stress concentration induced by the oblate spheroidal particle and the void nucleation mechanism," *International journal of solids and structures*, vol. 43, pp. 4097-4115, 2006.
- [54] W. Zhou, D. Yu, C. Wang, Q. An, and S. Qi, "Effect of filler size distribution on the mechanical and physical properties of alumina-filled silicone rubber," *Polymer Engineering & Science*, vol. 48, pp. 1381-1388, 2008.
- [55] N. Chisholm, H. Mahfuz, V. K. Rangari, A. Ashfaq, and S. Jeelani, "Fabrication and mechanical characterization of carbon/SiC-epoxy nanocomposites," *Composite structures*, vol. 67, pp. 115-124, 2005.
- [56] W. D. Callister, D. G. Rethwisch, A. Blicblau, K. Bruggeman, M. Cortie, J. Long, *et al.*, *Materials science and engineering: an introduction*: wiley, 2021.
- [57] Q. Zhang, M. Tian, Y. Wu, G. Lin, and L. Zhang, "Effect of particle size on the properties of Mg (OH) 2-filled rubber composites," *Journal of Applied Polymer Science*, vol. 94, pp. 2341-2346, 2004.
- [58] K. Radford, "The mechanical properties of an epoxy resin with a second phase dispersion," *Journal of Materials Science*, vol. 6, pp. 1286-1291, 1971.
- [59] J. Spanoudakis and R. Young, "Crack propagation in a glass particle-filled epoxy resin," *Journal of Materials Science*, vol. 19, pp. 473-486, 1984.

## References

- [60] Y. Nakamura, M. Yamaguchi, M. Okubo, and T. Matsumoto, "Effect of particle size on mechanical properties of epoxy resin filled with angular-shaped silica," *Journal of applied polymer science*, vol. 44, pp. 151-158, 1992.
- [61] A. Lazzeri, Y. Thio, and R. Cohen, "Volume strain measurements on CaCO<sub>3</sub>/polypropylene particulate composites: the effect of particle size," *Journal of applied polymer science*, vol. 91, pp. 925-935, 2004.
- [62] N. Suprapakorn, S. Dhamrongvaraporn, and H. Ishida, "Effect of CaCO<sub>3</sub> on the mechanical and rheological properties of a ring-opening phenolic resin: Polybenzoxazine," *Polymer composites*, vol. 19, pp. 126-132, 1998.
- [63] R. Singh, M. Zhang, and D. Chan, "Toughening of a brittle thermosetting polymer: effects of reinforcement particle size and volume fraction," *Journal of materials science*, vol. 37, pp. 781-788, 2002.
- [64] A. Roulin-Moloney, W. Cantwell, and H. Kausch, "Parameters determining the strength and toughness of particulate-filled epoxy resins," *Polymer composites*, vol. 8, pp. 314-323, 1987.
- [65] G. C. Onuegbu and I. O. Igwe, "The effects of filler contents and particle sizes on the mechanical and end-use properties of snail shell powder filled polypropylene," *Materials Sciences and Applications*, vol. 2, p. 810, 2011.
- [66] R. Kitey and H. Tippur, "Role of particle size and filler–matrix adhesion on dynamic fracture of glass-filled epoxy. I. Macromechanisms," *Acta Materialia*, vol. 53, pp. 1153-1165, 2005.
- [67] D. Devaprakasam, P. Hatton, G. Möbus, and B. Inkson, "Effect of microstructure of nano- and micro-particle filled polymer composites on their tribo-mechanical performance," in *Journal of Physics: Conference Series*, 2008, p. 012057.
- [68] J. Douce, J.-P. Boilot, J. Biteau, L. Scodellaro, and A. Jimenez, "Effect of filler size and surface condition of nano-sized silica particles in polysiloxane coatings," *Thin Solid Films*, vol. 466, pp. 114-122, 2004.
- [69] D. Edwards, "Polymer-filler interactions in rubber reinforcement," *Journal of Materials Science*, vol. 25, pp. 4175-4185, 1990.
- [70] O. Kamigaito, "What can be improved by nanometer composites?," *Journal of the Japan Society of Powder and Powder Metallurgy*, vol. 38, pp. 315-321, 1991.
- [71] S. Mishra, S. Sonawane, and R. Singh, "Studies on characterization of nano CaCO<sub>3</sub> prepared by the in situ deposition technique and its application in PP-nano CaCO<sub>3</sub> composites," *Journal of Polymer Science Part B: Polymer Physics*, vol. 43, pp. 107-113, 2005.
- [72] R. M. Kumar, S. K. Sharma, B. M. Kumar, and D. Lahiri, "Effects of carbon nanotube aspect ratio on strengthening and tribological behavior of ultra high molecular weight polyethylene composite," *Composites Part A: Applied Science and Manufacturing*, vol. 76, pp. 62-72, 2015.
- [73] S. Chowdhury and T. Okabe, "Computer simulation of carbon nanotube pull-out from polymer by the molecular dynamics method," *Composites Part A: Applied Science and Manufacturing*, vol. 38, pp. 747-754, 2007.

## References

- [74] K. Yazdchi and M. Salehi, "The effects of CNT waviness on interfacial stress transfer characteristics of CNT/polymer composites," *Composites Part A: Applied Science and Manufacturing*, vol. 42, pp. 1301-1309, 2011.
- [75] K. Xiao and L. Zhang, "The stress transfer efficiency of a single-walled carbon nanotube in epoxy matrix," *Journal of Materials Science*, vol. 39, pp. 4481-4486, 2004.
- [76] K. Li and S. Saigal, "Micromechanical modeling of stress transfer in carbon nanotube reinforced polymer composites," *Materials Science and Engineering: A*, vol. 457, pp. 44-57, 2007.
- [77] H. Cox, "The elasticity and strength of paper and other fibrous materials," *British journal of applied physics*, vol. 3, p. 72, 1952.
- [78] S. Yoo, S. Han, and W. Kim, "Strength and strain hardening of aluminum matrix composites with randomly dispersed nanometer-length fragmented carbon nanotubes," *Scripta Materialia*, vol. 68, pp. 711-714, 2013.
- [79] H. Choi, B. Min, J. Shin, and D. Bae, "Strengthening in nanostructured 2024 aluminum alloy and its composites containing carbon nanotubes," *Composites Part A: Applied Science and Manufacturing*, vol. 42, pp. 1438-1444, 2011.
- [80] K. M. Youssef, R. O. Scattergood, K. L. Murty, J. A. Horton, and C. C. Koch, "Ultrahigh strength and high ductility of bulk nanocrystalline copper," *Applied Physics Letters*, vol. 87, p. 091904, 2005.
- [81] D. H. Nam, S. I. Cha, B. K. Lim, H. M. Park, D. S. Han, and S. H. Hong, "Synergistic strengthening by load transfer mechanism and grain refinement of CNT/Al-Cu composites," *Carbon*, vol. 50, pp. 2417-2423, 2012.
- [82] M. Ashby, "The deformation of plastically non-homogeneous materials," *The Philosophical Magazine: A Journal of Theoretical Experimental and Applied Physics*, vol. 21, pp. 399-424, 1970.
- [83] C.-W. Nan and D. Clarke, "The influence of particle size and particle fracture on the elastic/plastic deformation of metal matrix composites," *Acta materialia*, vol. 44, pp. 3801-3811, 1996.
- [84] D. Lloyd, "Particle reinforced aluminium and magnesium matrix composites," *International materials reviews*, vol. 39, pp. 1-23, 1994.
- [85] P. Barai and G. J. Weng, "A theory of plasticity for carbon nanotube reinforced composites," *International Journal of Plasticity*, vol. 27, pp. 539-559, 2011.
- [86] S. Dong, J. Zhou, D. Hui, Y. Wang, and S. Zhang, "Size dependent strengthening mechanisms in carbon nanotube reinforced metal matrix composites," *Composites Part A: Applied Science and Manufacturing*, vol. 68, pp. 356-364, 2015.
- [87] B. Han, S. Sun, S. Ding, L. Zhang, X. Yu, and J. Ou, "Review of nanocarbon-engineered multifunctional cementitious composites," *Composites Part A: Applied Science and Manufacturing*, vol. 70, pp. 69-81, 2015.
- [88] X.-L. Xie, Y.-W. Mai, and X.-P. Zhou, "Dispersion and alignment of carbon nanotubes in polymer matrix: a review," *Materials science and engineering: R: Reports*, vol. 49, pp. 89-112, 2005.
- [89] S. Iijima, "Helical microtubules of graphitic carbon," *nature*, vol. 354, pp. 56-58, 1991.

## References

- [90] S. Iijima and T. Ichihashi, "Single-shell carbon nanotubes of 1-nm diameter," *nature*, vol. 363, pp. 603-605, 1993.
- [91] B. Singh, C. Baburao, V. Pispati, H. Pathipati, N. Muthy, S. Prassana, *et al.*, "Carbon nanotubes. A novel drug delivery system," *International Journal of Research in Pharmacy and Chemistry*, vol. 2, pp. 523-532, 2012.
- [92] S. Kumar, R. Rani, N. Dilbaghi, K. Tankeshwar, and K.-H. Kim, "Carbon nanotubes: a novel material for multifaceted applications in human healthcare," *Chemical society reviews*, vol. 46, pp. 158-196, 2017.
- [93] L.-M. Peng, Z. Zhang, and S. Wang, "Carbon nanotube electronics: recent advances," *Materials today*, vol. 17, pp. 433-442, 2014.
- [94] M. F. De Volder, S. H. Tawfick, R. H. Baughman, and A. J. Hart, "Carbon nanotubes: present and future commercial applications," *science*, vol. 339, pp. 535-539, 2013.
- [95] H. Cebeci, R. G. de Villoria, A. J. Hart, and B. L. Wardle, "Multifunctional properties of high volume fraction aligned carbon nanotube polymer composites with controlled morphology," *Composites Science and Technology*, vol. 69, pp. 2649-2656, 2009.
- [96] S. S. Samal and S. Bal, "Carbon nanotube reinforced ceramic matrix composites-a review," 2008.
- [97] N. Silvestre, "State-of-the-art review on carbon nanotube reinforced metal matrix composites," *International Journal of Composite Materials*, vol. 3, pp. 28-44, 2013.
- [98] W. Lu, M. Zu, J. H. Byun, B. S. Kim, and T. W. Chou, "State of the art of carbon nanotube fibers: opportunities and challenges," *Advanced materials*, vol. 24, pp. 1805-1833, 2012.
- [99] J. Zhu, H. Peng, F. Rodriguez-Macias, J. L. Margrave, V. N. Khabashesku, A. M. Imam, *et al.*, "Reinforcing epoxy polymer composites through covalent integration of functionalized nanotubes," *Advanced functional materials*, vol. 14, pp. 643-648, 2004.
- [100] R. Hagenmueller, W. Zhou, J. Fischer, and K. Winey, "Production and characterization of polymer nanocomposites with highly aligned single-walled carbon nanotubes," *Journal of nanoscience and nanotechnology*, vol. 3, pp. 105-110, 2003.
- [101] W. Tang, M. H. Santare, and S. G. Advani, "Melt processing and mechanical property characterization of multi-walled carbon nanotube/high density polyethylene (MWNT/HDPE) composite films," *Carbon*, vol. 41, pp. 2779-2785, 2003.
- [102] J. Zeng, B. Saltysiak, W. Johnson, D. A. Schiraldi, and S. Kumar, "Processing and properties of poly (methyl methacrylate)/carbon nanofiber composites," *Composites Part B: Engineering*, vol. 35, pp. 245-249, 2004.
- [103] S. Kumar, T. D. Dang, F. E. Arnold, A. R. Bhattacharyya, B. G. Min, X. Zhang, *et al.*, "Synthesis, structure, and properties of PBO/SWNT Composites," *Macromolecules*, vol. 35, pp. 9039-9043, 2002.
- [104] M. Paiva, B. Zhou, K. Fernando, Y. Lin, J. Kennedy, and Y.-P. Sun, "Mechanical and morphological characterization of polymer-carbon nanocomposites from functionalized carbon nanotubes," *Carbon*, vol. 42, pp. 2849-2854, 2004.
- [105] Z. Roslaniec, G. Broza, and K. Schulte, "Nanocomposites based on multiblock polyester elastomers (PEE) and carbon nanotubes (CNT)," *Composite Interfaces*, vol. 10, pp. 95-102, 2003.

## References

- [106] P. Pötschke, A. R. Bhattacharyya, A. Janke, and H. Goering, "Melt mixing of polycarbonate/multi-wall carbon nanotube composites," *Composite Interfaces*, vol. 10, pp. 389-404, 2003.
- [107] O. Meincke, D. Kaempfer, H. Weickmann, C. Friedrich, M. Vathauer, and H. Warth, "Mechanical properties and electrical conductivity of carbon-nanotube filled polyamide-6 and its blends with acrylonitrile/butadiene/styrene," *Polymer*, vol. 45, pp. 739-748, 2004.
- [108] T. Liu, I. Y. Phang, L. Shen, S. Y. Chow, and W.-D. Zhang, "Morphology and mechanical properties of multiwalled carbon nanotubes reinforced nylon-6 composites," *Macromolecules*, vol. 37, pp. 7214-7222, 2004.
- [109] D. Bikiaris, "Microstructure and properties of polypropylene/carbon nanotube nanocomposites," *Materials*, vol. 3, pp. 2884-2946, 2010.
- [110] P. Zhang, D. Qiu, H. Chen, J. Sun, J. Wang, C. Qin, *et al.*, "Preparation of MWCNTs grafted with polyvinyl alcohol through Friedel-Crafts alkylation and their composite fibers with enhanced mechanical properties," *Journal of Materials Chemistry A*, vol. 3, pp. 1442-1449, 2015.
- [111] J. Shin, C. Kim, and K. E. Geckeler, "Single-walled carbon nanotube-polystyrene nanocomposites: dispersing nanotubes in organic media," *Polymer international*, vol. 58, pp. 579-583, 2009.
- [112] A. M. Esawi, H. G. Salem, H. M. Hussein, and A. R. Ramadan, "Effect of processing technique on the dispersion of carbon nanotubes within polypropylene carbon nanotube-composites and its effect on their mechanical properties," *Polymer composites*, vol. 31, pp. 772-780, 2010.
- [113] J. Gao, M. E. Itkis, A. Yu, E. Bekyarova, B. Zhao, and R. C. Haddon, "Continuous spinning of a single-walled carbon nanotube-nylon composite fiber," *Journal of the American Chemical Society*, vol. 127, pp. 3847-3854, 2005.
- [114] J. C. Kearns and R. L. Shambaugh, "Polypropylene fibers reinforced with carbon nanotubes," *Journal of Applied Polymer Science*, vol. 86, pp. 2079-2084, 2002.
- [115] T. Fornes, J. Baur, Y. Sabba, and E. Thomas, "Morphology and properties of melt-spun polycarbonate fibers containing single- and multi-wall carbon nanotubes," *Polymer*, vol. 47, pp. 1704-1714, 2006.
- [116] X. Chen, J. Wang, M. Lin, W. Zhong, T. Feng, X. Chen, *et al.*, "Mechanical and thermal properties of epoxy nanocomposites reinforced with amino-functionalized multi-walled carbon nanotubes," *Materials Science and Engineering: A*, vol. 492, pp. 236-242, 2008.
- [117] H. G. Chae, M. L. Minus, and S. Kumar, "Oriented and exfoliated single wall carbon nanotubes in polyacrylonitrile," *Polymer*, vol. 47, pp. 3494-3504, 2006.
- [118] J. Vacha and M. Boruka, "Mechanical Properties of Acrylonitrile Butadiene Styrene Thermoplastic Polymer Matrix with Carbon Nanotubes," ed: NANOCON, 2015.
- [119] J. Chen, B. Liu, X. Gao, and D. Xu, "A review of the interfacial characteristics of polymer nanocomposites containing carbon nanotubes," *RSC Advances*, vol. 8, pp. 28048-28085, 2018.
- [120] M. Sennett, E. Welsh, J. Wright, W. Li, J. Wen, and Z. Ren, "Dispersion and alignment of carbon nanotubes in polycarbonate," *MRS Online Proceedings Library Archive*, vol. 706, 2001.

## References

- [121] J. Jang, J. Bae, and S.-H. Yoon, "A study on the effect of surface treatment of carbon nanotubes for liquid crystalline epoxide–carbon nanotube composites," *Journal of Materials Chemistry*, vol. 13, pp. 676-681, 2003.
- [122] W. Feng, X. Bai, Y. Lian, J. Liang, X. Wang, and K. Yoshino, "Well-aligned polyaniline/carbon-nanotube composite films grown by in-situ aniline polymerization," *Carbon*, vol. 41, pp. 1551-1557, 2003.
- [123] P. Ajayan, O. Stephan, C. Colliex, and D. Trauth, "Aligned carbon nanotube arrays formed by cutting a polymer resin—nanotube composite," *Science*, vol. 265, pp. 1212-1214, 1994.
- [124] T. Kimura, H. Ago, M. Tobita, S. Ohshima, M. Kyotani, and M. Yumura, "Polymer composites of carbon nanotubes aligned by a magnetic field," *Advanced materials*, vol. 14, pp. 1380-1383, 2002.
- [125] R. Sen, B. Zhao, D. Perea, M. E. Itkis, H. Hu, J. Love, *et al.*, "Preparation of single-walled carbon nanotube reinforced polystyrene and polyurethane nanofibers and membranes by electrospinning," *Nano letters*, vol. 4, pp. 459-464, 2004.
- [126] M. D. Lynch and D. L. Patrick, "Organizing carbon nanotubes with liquid crystals," *Nano letters*, vol. 2, pp. 1197-1201, 2002.
- [127] F. H. Gojny, M. H. Wichmann, B. Fiedler, and K. Schulte, "Influence of different carbon nanotubes on the mechanical properties of epoxy matrix composites—a comparative study," *Composites Science and Technology*, vol. 65, pp. 2300-2313, 2005.
- [128] S. U. Khan, J. R. Pothnis, and J.-K. Kim, "Effects of carbon nanotube alignment on electrical and mechanical properties of epoxy nanocomposites," *Composites Part A: Applied Science and Manufacturing*, vol. 49, pp. 26-34, 2013.
- [129] S. Jangam, S. Raja, and K. H. Reddy, "Effect of multiwalled carbon nanotube alignment on the tensile fatigue behavior of nanocomposites," *Journal of Composite Materials*, vol. 52, pp. 2365-2374, 2018.
- [130] K. S. Khare, F. Khabaz, and R. Khare, "Effect of carbon nanotube functionalization on mechanical and thermal properties of cross-linked epoxy–carbon nanotube nanocomposites: role of strengthening the interfacial interactions," *ACS applied materials & interfaces*, vol. 6, pp. 6098-6110, 2014.
- [131] J. Zhu, J. Kim, H. Peng, J. L. Margrave, V. N. Khabashesku, and E. V. Barrera, "Improving the dispersion and integration of single-walled carbon nanotubes in epoxy composites through functionalization," *Nano letters*, vol. 3, pp. 1107-1113, 2003.
- [132] C. Wang, J. Xu, J. Yang, Y. Qian, and H. Liu, "In-situ polymerization and multifunctional properties of surface-modified multiwalled carbon nanotube-reinforced polyimide nanocomposites," *High Performance Polymers*, vol. 29, pp. 797-807, 2017.
- [133] J. Shiju, F. Al-Sagheer, A. Bumajdad, and Z. Ahmad, "In-Situ Preparation of Aramid-Multiwalled CNT Nano-Composites: Morphology, Thermal Mechanical and Electric Properties," *Nanomaterials*, vol. 8, p. 309, 2018.
- [134] F. Buffa, G. A. Abraham, B. P. Grady, and D. Resasco, "Effect of nanotube functionalization on the properties of single-walled carbon nanotube/polyurethane composites," *Journal of Polymer Science Part B: Polymer Physics*, vol. 45, pp. 490-501, 2007.

## References

- [135] W. Leininger, X. Wang, and X. Tangpong, "Effects of MWCNT reinforcement on quasi-static and dynamic tensile properties of epoxy," *Journal of Composite Materials*, vol. 48, pp. 2049-2057, 2014.
- [136] Z.-K. Chen, J.-P. Yang, Q.-Q. Ni, S.-Y. Fu, and Y.-G. Huang, "Reinforcement of epoxy resins with multi-walled carbon nanotubes for enhancing cryogenic mechanical properties," *Polymer*, vol. 50, pp. 4753-4759, 2009.
- [137] F. Gojny, M. Wichmann, U. Köpke, B. Fiedler, and K. Schulte, "Carbon nanotube-reinforced epoxy-composites: enhanced stiffness and fracture toughness at low nanotube content," *Composites science and technology*, vol. 64, pp. 2363-2371, 2004.
- [138] R. Andrews and M. Weisenberger, "Carbon nanotube polymer composites," *Current Opinion in Solid State and Materials Science*, vol. 8, pp. 31-37, 2004.
- [139] J. Cha, G. H. Jun, J. K. Park, J. C. Kim, H. J. Ryu, and S. H. Hong, "Improvement of modulus, strength and fracture toughness of CNT/Epoxy nanocomposites through the functionalization of carbon nanotubes," *Composites Part B: Engineering*, vol. 129, pp. 169-179, 2017.
- [140] Y. Chen, B. Liu, X. He, Y. Huang, and K. Hwang, "Failure analysis and the optimal toughness design of carbon nanotube-reinforced composites," *Composites Science and Technology*, vol. 70, pp. 1360-1367, 2010.
- [141] C. Ma, H.-Y. Liu, X. Du, L. Mach, F. Xu, and Y.-W. Mai, "Fracture resistance, thermal and electrical properties of epoxy composites containing aligned carbon nanotubes by low magnetic field," *Composites Science and Technology*, vol. 114, pp. 126-135, 2015.
- [142] B. Coto, I. Antia, J. Barriga, M. Blanco, and J.-R. Sarasua, "Influence of the geometrical properties of the carbon nanotubes on the interfacial behavior of epoxy/CNT composites: a molecular modelling approach," *Computational materials science*, vol. 79, pp. 99-104, 2013.
- [143] M. Ayatollahi, S. Shadlou, M. Shokrieh, and M. Chitsazzadeh, "Effect of multi-walled carbon nanotube aspect ratio on mechanical and electrical properties of epoxy-based nanocomposites," *Polymer Testing*, vol. 30, pp. 548-556, 2011.
- [144] F. Inam, T. Vo, J. P. Jones, and X. Lee, "Effect of carbon nanotube lengths on the mechanical properties of epoxy resin: An experimental study," *Journal of Composite Materials*, vol. 47, pp. 2321-2330, 2013.
- [145] R. Hollertz, S. Chatterjee, H. Gutmann, T. Geiger, F. Nüesch, and B. Chu, "Improvement of toughness and electrical properties of epoxy composites with carbon nanotubes prepared by industrially relevant processes," *Nanotechnology*, vol. 22, p. 125702, 2011.
- [146] S.-G. Cho and K.-C. Ko, "Surface free energy and super-hydrophobic coating of multi-walled carbon nanotubes by 3: 1 TMCS/toluene glow discharge plasma under low pressure," *Thin solid films*, vol. 518, pp. 6619-6623, 2010.
- [147] S. Nuriel, L. Liu, A. Barber, and H. Wagner, "Direct measurement of multiwall nanotube surface tension," *Chemical Physics Letters*, vol. 404, pp. 263-266, 2005.
- [148] L. Zhang, J. Wang, C. A. Fuentes, D. Zhang, A. W. Van Vuure, J. W. Seo, *et al.*, "Wettability of carbon nanotube fibers," *Carbon*, vol. 122, pp. 128-140, 2017/10/01/ 2017.
- [149] R. Atif and F. Inam, "Reasons and remedies for the agglomeration of multilayered graphene and carbon nanotubes in polymers," *Beilstein journal of nanotechnology*, vol. 7, p. 1174, 2016.

## References

- [150] C. He, N. Zhao, C. Shi, and S. Song, "Mechanical properties and microstructures of carbon nanotube-reinforced Al matrix composite fabricated by in situ chemical vapor deposition," *Journal of Alloys and Compounds*, vol. 487, pp. 258-262, 2009.
- [151] K. Kondoh, T. Threrujirapong, J. Umeda, and B. Fugetsu, "High-temperature properties of extruded titanium composites fabricated from carbon nanotubes coated titanium powder by spark plasma sintering and hot extrusion," *Composites science and technology*, vol. 72, pp. 1291-1297, 2012.
- [152] H. Fukuda, K. Kondoh, J. Umeda, and B. Fugetsu, "Interfacial analysis between Mg matrix and carbon nanotubes in Mg-6 wt.% Al alloy matrix composites reinforced with carbon nanotubes," *Composites Science and Technology*, vol. 71, pp. 705-709, 2011.
- [153] F. Ostovan, K. A. Matori, M. Toozandehjani, A. Oskoueian, H. M. Yusoff, R. Yunus, *et al.*, "Effects of CNTs content and milling time on mechanical behavior of MWCNT-reinforced aluminum nanocomposites," *Materials Chemistry and Physics*, vol. 166, pp. 160-166, 2015.
- [154] H. Kwon and M. Leparoux, "Hot extruded carbon nanotube reinforced aluminum matrix composite materials," *Nanotechnology*, vol. 23, p. 415701, 2012.
- [155] J. Wu, H. Zhang, Y. Zhang, and X. Wang, "Mechanical and thermal properties of carbon nanotube/aluminum composites consolidated by spark plasma sintering," *Materials & Design*, vol. 41, pp. 344-348, 2012.
- [156] J. Nguyen, H. Wen, Z. Zhang, F. Yaghmaie, and E. Lavernia, "Surfactant assisted dispersion and adhesion behavior of carbon nanotubes on Cu-Zr and Cu-Zr-Al amorphous powders," *Journal of Materials Science & Technology*, vol. 30, pp. 847-853, 2014.
- [157] M. H. Nai, J. Wei, and M. Gupta, "Interface tailoring to enhance mechanical properties of carbon nanotube reinforced magnesium composites," *Materials & Design*, vol. 60, pp. 490-495, 2014.
- [158] Y. Park, K. Cho, I. Park, and Y. Park, "Fabrication and mechanical properties of magnesium matrix composite reinforced with Si coated carbon nanotubes," *Procedia Engineering*, vol. 10, pp. 1446-1450, 2011.
- [159] H.-p. Li, J.-w. Fan, J.-l. Kang, N.-q. Zhao, X.-x. Wang, and B.-e. Li, "In-situ homogeneous synthesis of carbon nanotubes on aluminum matrix and properties of their composites," *Transactions of Nonferrous Metals Society of China*, vol. 24, pp. 2331-2336, 2014.
- [160] W. M. Daoush, B. K. Lim, C. B. Mo, D. H. Nam, and S. H. Hong, "Electrical and mechanical properties of carbon nanotube reinforced copper nanocomposites fabricated by electroless deposition process," *Materials Science and Engineering: A*, vol. 513, pp. 247-253, 2009.
- [161] K. Vishwanath, G. Raji, A. Shakiba, and S. K. Murthy, "Mechanical properties of copper nanocomposites reinforced with uncoated and nickel coated carbon nanotubes," *FME Transactions*, vol. 46, pp. 623-630, 2018.
- [162] C. Deng, Y. Ma, P. Zhang, X. Zhang, and D. Wang, "Thermal expansion behaviors of aluminum composite reinforced with carbon nanotubes," *Materials Letters*, vol. 62, pp. 2301-2303, 2008.
- [163] D. Chunfeng, X. ZHANG, M. Yanxia, and W. Dezun, "Fabrication of aluminum matrix composite reinforced with carbon nanotubes," *Rare Metals*, vol. 26, pp. 450-455, 2007.
- [164] A. M. Esawi and M. A. El Borady, "Carbon nanotube-reinforced aluminium strips," *Composites Science and Technology*, vol. 68, pp. 486-492, 2008.



## References

- [165] T. Laha, Y. Chen, D. Lahiri, and A. Agarwal, "Tensile properties of carbon nanotube reinforced aluminum nanocomposite fabricated by plasma spray forming," *Composites Part A: Applied Science and Manufacturing*, vol. 40, pp. 589-594, 2009.
- [166] S. R. Bakshi, V. Singh, S. Seal, and A. Agarwal, "Aluminum composite reinforced with multiwalled carbon nanotubes from plasma spraying of spray dried powders," *Surface and Coatings Technology*, vol. 203, pp. 1544-1554, 2009.
- [167] C. He, N. Zhao, C. Shi, X. Du, J. Li, H. Li, *et al.*, "An approach to obtaining homogeneously dispersed carbon nanotubes in Al powders for preparing reinforced Al-matrix composites," *Advanced Materials*, vol. 19, pp. 1128-1132, 2007.
- [168] K. T. Kim, S. I. Cha, S. H. Hong, and S. H. Hong, "Microstructures and tensile behavior of carbon nanotube reinforced Cu matrix nanocomposites," *Materials Science and Engineering: A*, vol. 430, pp. 27-33, 2006.
- [169] J. Tu, Y. Yang, L. Wang, X. Ma, and X. Zhang, "Tribological properties of carbon-nanotube-reinforced copper composites," *Tribology Letters*, vol. 10, pp. 225-228, 2001.
- [170] H. Deng, J. Yi, C. Xia, and Y. Yi, "Mechanical properties and microstructure characterization of well-dispersed carbon nanotubes reinforced copper matrix composites," *Journal of Alloys and Compounds*, vol. 727, pp. 260-268, 2017.
- [171] G.-R. Shen, Y.-T. Cheng, and L.-N. Tsai, "Synthesis and characterization of Ni-P-CNT's nanocomposite film for MEMS applications," *IEEE Transactions on Nanotechnology*, vol. 4, pp. 539-547, 2005.
- [172] J. Nguyen, T. B. Holland, H. Wen, M. Fraga, A. Mukherjee, and E. Lavernia, "Mechanical behavior of ultrafine-grained Ni-carbon nanotube composite," *Journal of materials science*, vol. 49, pp. 2070-2077, 2014.
- [173] C. Li, X. Wang, W. Liu, K. Wu, H. Shi, C. Ding, *et al.*, "Microstructure and strengthening mechanism of carbon nanotubes reinforced magnesium matrix composite," *Materials Science and Engineering: A*, vol. 597, pp. 264-269, 2014.
- [174] C. Goh, J. Wei, L. Lee, and M. Gupta, "Simultaneous enhancement in strength and ductility by reinforcing magnesium with carbon nanotubes," *Materials Science and Engineering: A*, vol. 423, pp. 153-156, 2006.
- [175] M. Zhou, X. Qu, L. Ren, L. Fan, Y. Zhang, Y. Guo, *et al.*, "The effects of carbon nanotubes on the mechanical and wear properties of AZ31 alloy," *Materials*, vol. 10, p. 1385, 2017.
- [176] F. Bonaccorso, L. Colombo, G. Yu, M. Stoller, V. Tozzini, A. C. Ferrari, *et al.*, "Graphene, related two-dimensional crystals, and hybrid systems for energy conversion and storage," *Science*, vol. 347, p. 1246501, 2015.
- [177] C. Lee, X. Wei, J. W. Kysar, and J. Hone, "Measurement of the elastic properties and intrinsic strength of monolayer graphene," *science*, vol. 321, pp. 385-388, 2008.
- [178] A. A. Balandin, "Thermal properties of graphene and nanostructured carbon materials," *Nature materials*, vol. 10, pp. 569-581, 2011.
- [179] J. R. Potts, D. R. Dreyer, C. W. Bielawski, and R. S. Ruoff, "Graphene-based polymer nanocomposites," *Polymer*, vol. 52, pp. 5-25, 2011.
- [180] R. S. Edwards and K. S. Coleman, "Graphene synthesis: relationship to applications," *Nanoscale*, vol. 5, pp. 38-51, 2013.

## References

- [181] Y. Zhang, J. E. Mark, Y. Zhu, R. S. Ruoff, and D. W. Schaefer, "Mechanical properties of polybutadiene reinforced with octadecylamine modified graphene oxide," *Polymer*, vol. 55, pp. 5389-5395, 2014.
- [182] S. Wu, R. B. Ladani, J. Zhang, E. Bafekrpour, K. Ghorbani, A. P. Mouritz, *et al.*, "Aligning multilayer graphene flakes with an external electric field to improve multifunctional properties of epoxy nanocomposites," *Carbon*, vol. 94, pp. 607-618, 2015.
- [183] Z. Li, J. Chu, C. Yang, S. Hao, M. A. Bissett, I. A. Kinloch, *et al.*, "Effect of functional groups on the agglomeration of graphene in nanocomposites," *Composites Science and Technology*, vol. 163, pp. 116-122, 2018.
- [184] H. Kim and C. W. Macosko, "Processing-property relationships of polycarbonate/graphene composites," *Polymer*, vol. 50, pp. 3797-3809, 2009.
- [185] K. Wakabayashi, C. Pierre, D. A. Dikin, R. S. Ruoff, T. Ramanathan, L. C. Brinson, *et al.*, "Polymer– Graphite Nanocomposites: Effective Dispersion and Major Property Enhancement via Solid-State Shear Pulverization," *Macromolecules*, vol. 41, pp. 1905-1908, 2008.
- [186] T. Fornes and D. Paul, "Modeling properties of nylon 6/clay nanocomposites using composite theories," *polymer*, vol. 44, pp. 4993-5013, 2003.
- [187] D. R. Paul and L. M. Robeson, "Polymer nanotechnology: nanocomposites," *Polymer*, vol. 49, pp. 3187-3204, 2008.
- [188] L. Schadler, S. a. Giannaris, and P. Ajayan, "Load transfer in carbon nanotube epoxy composites," *Applied physics letters*, vol. 73, pp. 3842-3844, 1998.
- [189] M. A. Rafiee, J. Rafiee, I. Srivastava, Z. Wang, H. Song, Z. Z. Yu, *et al.*, "Fracture and fatigue in graphene nanocomposites," *small*, vol. 6, pp. 179-183, 2010.
- [190] P. Pötschke, M. Abdel-Goad\*, S. Pegel, D. Jehnichen, J. E. Mark, D. Zhou\*\*, *et al.*, "Comparisons among electrical and rheological properties of melt-mixed composites containing various carbon nanostructures," *Journal of Macromolecular Science, Part A*, vol. 47, pp. 12-19, 2009.
- [191] X. Zhao, Q. Zhang, D. Chen, and P. Lu, "Enhanced mechanical properties of graphene-based poly (vinyl alcohol) composites," *Macromolecules*, vol. 43, pp. 2357-2363, 2010.
- [192] I. Zaman, T. T. Phan, H.-C. Kuan, Q. Meng, L. T. B. La, L. Luong, *et al.*, "Epoxy/graphene platelets nanocomposites with two levels of interface strength," *Polymer*, vol. 52, pp. 1603-1611, 2011.
- [193] J. Wei, R. Atif, T. Vo, and F. Inam, "Graphene nanoplatelets in epoxy system: dispersion, reaggregation, and mechanical properties of nanocomposites," *Journal of Nanomaterials*, vol. 16, p. 374, 2015.
- [194] Z. Li, R. Wang, R. J. Young, L. Deng, F. Yang, L. Hao, *et al.*, "Control of the functionality of graphene oxide for its application in epoxy nanocomposites," *Polymer*, vol. 54, pp. 6437-6446, 2013.
- [195] C. Salom, M. Prolongo, A. Toribio, A. Martínez-Martínez, I. A. de Cárcer, and S. Prolongo, "Mechanical properties and adhesive behavior of epoxy-graphene nanocomposites," *International Journal of Adhesion and Adhesives*, vol. 84, pp. 119-125, 2018.

## References

- [196] C. E. Corcione, F. Freuli, and A. Maffezzoli, "The aspect ratio of epoxy matrix nanocomposites reinforced with graphene stacks," *Polymer Engineering & Science*, vol. 53, pp. 531-539, 2013.
- [197] L.-C. Tang, Y.-J. Wan, D. Yan, Y.-B. Pei, L. Zhao, Y.-B. Li, *et al.*, "The effect of graphene dispersion on the mechanical properties of graphene/epoxy composites," *Carbon*, vol. 60, pp. 16-27, 2013.
- [198] M. A. Rafiee, J. Rafiee, Z. Wang, H. Song, Z.-Z. Yu, and N. Koratkar, "Enhanced mechanical properties of nanocomposites at low graphene content," *ACS nano*, vol. 3, pp. 3884-3890, 2009.
- [199] J. Wei and F. Inam, "Processing of epoxy/graphene nanocomposites: Effects of surfactants," *Journal of Polymer Science & Applications*, vol. 1, p. 1000101, 2017.
- [200] N. Hong, J. Zhan, X. Wang, A. A. Stec, T. R. Hull, H. Ge, *et al.*, "Enhanced mechanical, thermal and flame retardant properties by combining graphene nanosheets and metal hydroxide nanorods for Acrylonitrile–Butadiene–Styrene copolymer composite," *Composites Part A: Applied Science and Manufacturing*, vol. 64, pp. 203-210, 2014.
- [201] J. R. Potts, S. H. Lee, T. M. Alam, J. An, M. D. Stoller, R. D. Piner, *et al.*, "Thermomechanical properties of chemically modified graphene/poly (methyl methacrylate) composites made by in situ polymerization," *Carbon*, vol. 49, pp. 2615-2623, 2011.
- [202] E. Lago, P. S. Toth, G. Pugliese, V. Pellegrini, and F. Bonaccorso, "Solution blending preparation of polycarbonate/graphene composite: boosting the mechanical and electrical properties," *RSC Advances*, vol. 6, pp. 97931-97940, 2016.
- [203] M. El Achaby and A. Qaiss, "Processing and properties of polyethylene reinforced by graphene nanosheets and carbon nanotubes," *Materials & Design*, vol. 44, pp. 81-89, 2013.
- [204] H. Kim, S. Kobayashi, M. A. AbdurRahim, M. J. Zhang, A. Khusainova, M. A. Hillmyer, *et al.*, "Graphene/polyethylene nanocomposites: effect of polyethylene functionalization and blending methods," *Polymer*, vol. 52, pp. 1837-1846, 2011.
- [205] F. Piana and J. Pionteck, "Effect of the melt processing conditions on the conductive paths formation in thermoplastic polyurethane/expanded graphite (TPU/EG) composites," *Composites science and technology*, vol. 80, pp. 39-46, 2013.
- [206] N. Domun, H. Hadavinia, T. Zhang, T. Sainsbury, G. Liaghat, and S. Vahid, "Improving the fracture toughness and the strength of epoxy using nanomaterials—a review of the current status," *Nanoscale*, vol. 7, pp. 10294-10329, 2015.
- [207] M. A. Rafiee, W. Lu, A. V. Thomas, A. Zandiatashbar, J. Rafiee, J. M. Tour, *et al.*, "Graphene nanoribbon composites," *ACS nano*, vol. 4, pp. 7415-7420, 2010.
- [208] R. Pérez-Bustamante, D. Bolaños-Morales, J. Bonilla-Martínez, I. Estrada-Guel, and R. Martínez-Sánchez, "Microstructural and hardness behavior of graphene-nanoplatelets/aluminum composites synthesized by mechanical alloying," *Journal of alloys and compounds*, vol. 615, pp. S578-S582, 2014.
- [209] P. Ashwath and M. A. Xavier, "The effect of ball milling & reinforcement percentage on sintered samples of aluminium alloy metal matrix composites," *Procedia Engineering*, vol. 97, pp. 1027-1032, 2014.

## References

- [210] S. F. Bartolucci, J. Paras, M. A. Rafiee, J. Rafiee, S. Lee, D. Kapoor, *et al.*, "Graphene–aluminum nanocomposites," *Materials Science and Engineering: A*, vol. 528, pp. 7933-7937, 2011.
- [211] Z. Li, G. Fan, Z. Tan, Q. Guo, D. Xiong, Y. Su, *et al.*, "Uniform dispersion of graphene oxide in aluminum powder by direct electrostatic adsorption for fabrication of graphene/aluminum composites," *Nanotechnology*, vol. 25, p. 325601, 2014.
- [212] M. Rashad, F. Pan, A. Tang, M. Asif, J. She, J. Gou, *et al.*, "Development of magnesium–graphene nanoplatelets composite," *Journal of composite materials*, vol. 49, pp. 285-293, 2015.
- [213] D. Kuang, L. Xu, L. Liu, W. Hu, and Y. Wu, "Graphene–nickel composites," *Applied Surface Science*, vol. 273, pp. 484-490, 2013.
- [214] W. Zhai, X. Shi, J. Yao, A. M. M. Ibrahim, Z. Xu, Q. Zhu, *et al.*, "Investigation of mechanical and tribological behaviors of multilayer graphene reinforced Ni3Al matrix composites," *Composites Part B: Engineering*, vol. 70, pp. 149-155, 2015.
- [215] R. Arsenault and N. Shi, "Dislocation generation due to differences between the coefficients of thermal expansion," *Materials Science and Engineering*, vol. 81, pp. 175-187, 1986.
- [216] M. Rashad, F. Pan, H. Hu, M. Asif, S. Hussain, and J. She, "Enhanced tensile properties of magnesium composites reinforced with graphene nanoplatelets," *Materials Science and Engineering: A*, vol. 630, pp. 36-44, 2015.
- [217] M. Bastwros, G.-Y. Kim, K. Zhang, and S. Wang, "Fabrication of graphene reinforced aluminum composite by semi-solid processing," in *ASME 2013 International Mechanical Engineering Congress and Exposition*, 2013, pp. V02BT02A030-V02BT02A030.
- [218] D. Lin, C. R. Liu, and G. J. Cheng, "Single-layer graphene oxide reinforced metal matrix composites by laser sintering: Microstructure and mechanical property enhancement," *Acta materialia*, vol. 80, pp. 183-193, 2014.
- [219] Y. Song, W. Liu, and Y. Chen, "Strengthening in a copper composite containing graphene nanofillers," in *IOP Conference Series: Materials Science and Engineering*, 2017, p. 012017.
- [220] L.-Y. Chen, H. Konishi, A. Fehrenbacher, C. Ma, J.-Q. Xu, H. Choi, *et al.*, "Novel nanoprocessing route for bulk graphene nanoplatelets reinforced metal matrix nanocomposites," *Scripta Materialia*, vol. 67, pp. 29-32, 2012.
- [221] J. Hwang, T. Yoon, S. H. Jin, J. Lee, T. S. Kim, S. H. Hong, *et al.*, "Enhanced mechanical properties of graphene/copper nanocomposites using a molecular-level mixing process," *Advanced materials*, vol. 25, pp. 6724-6729, 2013.
- [222] Y. Tang, X. Yang, R. Wang, and M. Li, "Enhancement of the mechanical properties of graphene–copper composites with graphene–nickel hybrids," *Materials Science and Engineering: A*, vol. 599, pp. 247-254, 2014.
- [223] B. Lim, C.-j. Kim, B. Kim, U. Shim, S. Oh, B.-h. Sung, *et al.*, "The effects of interfacial bonding on mechanical properties of single-walled carbon nanotube reinforced copper matrix nanocomposites," *Nanotechnology*, vol. 17, p. 5759, 2006.
- [224] Z. Xu and M. J. Buehler, "Interface structure and mechanics between graphene and metal substrates: a first-principles study," *Journal of Physics: Condensed Matter*, vol. 22, p. 485301, 2010.

## References

- [225] M. Rashad, F. Pan, A. Tang, Y. Lu, M. Asif, S. Hussain, *et al.*, "Effect of graphene nanoplatelets (GNPs) addition on strength and ductility of magnesium-titanium alloys," *Journal of Magnesium and alloys*, vol. 1, pp. 242-248, 2013.
- [226] Z. Ren, N. Meng, K. Shehzad, Y. Xu, S. Qu, B. Yu, *et al.*, "Mechanical properties of nickel-graphene composites synthesized by electrochemical deposition," *Nanotechnology*, vol. 26, p. 065706, 2015.
- [227] S.-j. Yan, C. Yang, Q.-h. Hong, J.-z. Chen, D.-b. Liu, and S.-l. Dai, "Research of graphene-reinforced aluminum matrix nanocomposites," *Journal of Materials Engineering*, vol. 1, pp. 1-6, 2011.
- [228] C.-H. Jeon, Y.-H. Jeong, J.-J. Seo, H. N. Tien, S.-T. Hong, Y.-J. Yum, *et al.*, "Material properties of graphene/aluminum metal matrix composites fabricated by friction stir processing," *International Journal of Precision Engineering and Manufacturing*, vol. 15, pp. 1235-1239, June 01 2014.
- [229] J. Li, Y. Xiong, X. Wang, S. Yan, C. Yang, W. He, *et al.*, "Microstructure and tensile properties of bulk nanostructured aluminum/graphene composites prepared via cryomilling," *Materials Science and Engineering: A*, vol. 626, pp. 400-405, 2015.
- [230] T. S. Koltsova, L. I. Nasibulina, I. V. Anoshkin, V. V. Mishin, E. I. Kauppinen, O. V. Tolochko, *et al.*, "New hybrid copper composite materials based on carbon nanostructures," *Journal of Materials Science and Engineering B*, vol. 2, pp. 240-246, 2012.
- [231] C. L. Pavithra, B. V. Sarada, K. V. Rajulapati, T. N. Rao, and G. Sundararajan, "A new electrochemical approach for the synthesis of copper-graphene nanocomposite foils with high hardness," *Scientific reports*, vol. 4, p. 4049, 2014.
- [232] M. Li, H. Che, X. Liu, S. Liang, and H. Xie, "Highly enhanced mechanical properties in Cu matrix composites reinforced with graphene decorated metallic nanoparticles," *Journal of materials science*, vol. 49, pp. 3725-3731, 2014.
- [233] D.-B. Xiong, M. Cao, Q. Guo, Z. Tan, G. Fan, Z. Li, *et al.*, "Graphene-and-copper artificial nacre fabricated by a preform impregnation process: bioinspired strategy for strengthening-toughening of metal matrix composite," *Acs Nano*, vol. 9, pp. 6934-6943, 2015.
- [234] C. Zhao and J. Wang, "Fabrication and tensile properties of graphene/copper composites prepared by electroless plating for structural applications," *physica status solidi (a)*, vol. 211, pp. 2878-2885, 2014.
- [235] E. P. Giannelis, "A new strategy for synthesizing polymer-ceramic nanocomposites," *Jom*, vol. 44, pp. 28-30, 1992.
- [236] Y. Kojima, A. Usuki, M. Kawasumi, A. Okada, T. Kurauchi, and O. Kamigaito, "Sorption of water in nylon 6-clay hybrid," *Journal of applied polymer science*, vol. 49, pp. 1259-1264, 1993.
- [237] R. A. Vaia, H. Ishii, and E. P. Giannelis, "Synthesis and properties of two-dimensional nanostructures by direct intercalation of polymer melts in layered silicates," *Chemistry of materials*, vol. 5, pp. 1694-1696, 1993.
- [238] P. B. Messersmith and E. P. Giannelis, "Synthesis and characterization of layered silicate-epoxy nanocomposites," *Chemistry of materials*, vol. 6, pp. 1719-1725, 1994.
- [239] L. Biasci, M. Aglietto, G. Ruggeri, and F. Ciardelli, "Functionalization of montmorillonite by methyl methacrylate polymers containing side-chain ammonium cations," *Polymer*, vol. 35, pp. 3296-3304, 1994.

## References

- [240] G. Jimenez, N. Ogata, H. Kawai, and T. Ogihara, "Structure and thermal/mechanical properties of poly ( $\epsilon$ -caprolactone)-clay blend," *Journal of Applied Polymer Science*, vol. 64, pp. 2211-2220, 1997.
- [241] Y. Kurokawa, H. Yasuda, M. Kashiwagi, and A. Oyo, "Structure and properties of a montmorillonite/polypropylene nanocomposite," *Journal of materials science letters*, vol. 16, pp. 1670-1672, 1997.
- [242] Z. Wang and T. J. Pinnavaia, "Nanolayer reinforcement of elastomeric polyurethane," *Chemistry of Materials*, vol. 10, pp. 3769-3771, 1998.
- [243] Z. K. Zhu, Y. Yang, J. Yin, X. Y. Wang, Y. C. Ke, and Z. N. Qi, "Preparation and properties of organosoluble montmorillonite/polyimide hybrid materials," *Journal of applied polymer science*, vol. 73, pp. 2063-2068, 1999.
- [244] V. Agubra, P. Owuor, and M. Hosur, "Influence of nanoclay dispersion methods on the mechanical behavior of E-glass/epoxy nanocomposites," *Nanomaterials*, vol. 3, pp. 550-563, 2013.
- [245] R. N. Choi, C. I. Cheigh, S. Y. Lee, and M. S. Chung, "Preparation and properties of polypropylene/clay nanocomposites for food packaging," *Journal of food science*, vol. 76, pp. N62-N67, 2011.
- [246] S. Abbasi, P. J. Carreau, A. Derdouri, and M. Moan, "Rheological properties and percolation in suspensions of multiwalled carbon nanotubes in polycarbonate," *Rheologica acta*, vol. 48, pp. 943-959, 2009.
- [247] M.-J. Khalaj, H. Ahmadi, R. Lesankhosh, and G. Khalaj, "Study of physical and mechanical properties of polypropylene nanocomposites for food packaging application: Nano-clay modified with iron nanoparticles," *Trends in Food Science & Technology*, vol. 51, pp. 41-48, 2016.
- [248] T. Fornes, P. Yoon, H. Keskkula, and D. Paul, "Nylon 6 nanocomposites: the effect of matrix molecular weight," *Polymer*, vol. 42, pp. 09929-09940, 2001.
- [249] B. Finnigan, D. Martin, P. Halley, R. Truss, and K. Campbell, "Morphology and properties of thermoplastic polyurethane nanocomposites incorporating hydrophilic layered silicates," *Polymer*, vol. 45, pp. 2249-2260, 2004.
- [250] S. Peeterbroeck, M. Alexandre, R. Jérôme, and P. Dubois, "Poly (ethylene-co-vinyl acetate)/clay nanocomposites: Effect of clay nature and organic modifiers on morphology, mechanical and thermal properties," *Polymer degradation and stability*, vol. 90, pp. 288-294, 2005.
- [251] D. N. Bikiaris, A. Vassiliou, E. Pavlidou, and G. P. Karayannidis, "Compatibilisation effect of PP-g-MA copolymer on iPP/SiO<sub>2</sub> nanocomposites prepared by melt mixing," *European Polymer Journal*, vol. 41, pp. 1965-1978, 2005.
- [252] P. Mederic, F. Fneich, J. Ville, and T. Aubry, "Migration of clay and its role in droplet morphology establishment during melt mixing of clay polyethylene/polyamide nanocomposites," *Applied Clay Science*, vol. 165, pp. 257-263, 2018.
- [253] S. Aoyama, I. Ismail, Y. T. Park, Y. Yoshida, C. W. Macosko, and T. Ougizawa, "Polyethylene terephthalate/trimellitic anhydride modified graphene nanocomposites," *ACS Applied Nano Materials*, vol. 1, pp. 6301-6311, 2018.
- [254] J. Bitenicks, R. M. Meri, J. Zicans, M. Kalnins, J. Andzane, and K. Buks, "Electrical and mechanical properties of melt-processed polyethylene terephthalate/multi-wall carbon

## References

- nanotube nanocomposites for thermoelectric materials," *Mechanics of Composite Materials*, vol. 54, pp. 457-462, 2018.
- [255] M. Zamanian, M. Mortezaei, B. Salehnia, and J. Jam, "Fracture toughness of epoxy polymer modified with nanosilica particles: Particle size effect," *Engineering Fracture Mechanics*, vol. 97, pp. 193-206, 2013.
- [256] A. Khosravi, A. Vatani, and T. Mohammadi, "Application of polyhedral oligomeric silsesquioxane to the stabilization and performance enhancement of poly (4-methyl-2-pentene) nanocomposite membranes for natural gas conditioning," *Journal of Applied Polymer Science*, vol. 134, p. 45158, 2017.
- [257] B. Johnsen, A. Kinloch, R. Mohammed, A. Taylor, and S. Sprenger, "Toughening mechanisms of nanoparticle-modified epoxy polymers," *Polymer*, vol. 48, pp. 530-541, 2007.
- [258] P. Svoboda, C. Zeng, H. Wang, L. J. Lee, and D. L. Tomasko, "Morphology and mechanical properties of polypropylene/organoclay nanocomposites," *Journal of Applied Polymer Science*, vol. 85, pp. 1562-1570, 2002.
- [259] L. Wang, K. Wang, L. Chen, Y. Zhang, and C. He, "Preparation, morphology and thermal/mechanical properties of epoxy/nanoclay composite," *Composites Part A: applied science and manufacturing*, vol. 37, pp. 1890-1896, 2006.
- [260] S. K. Singh, A. Kumar, and A. Jain, "Improving tensile and flexural properties of SiO<sub>2</sub>-epoxy polymer nanocomposite," *Materials Today: Proceedings*, vol. 5, pp. 6339-6344, 2018.
- [261] T. Hsieh, A. Kinloch, K. Masania, A. Taylor, and S. Sprenger, "The mechanisms and mechanics of the toughening of epoxy polymers modified with silica nanoparticles," *Polymer*, vol. 51, pp. 6284-6294, 2010.
- [262] B. Blackman, A. Kinloch, J. S. Lee, A. Taylor, R. Agarwal, G. Schueneman, *et al.*, "The fracture and fatigue behaviour of nano-modified epoxy polymers," *Journal of Materials Science*, vol. 42, pp. 7049-7051, 2007.
- [263] N. Eustathopoulos, M. G. Nicholas, and B. Drevet, *Wettability at high temperatures* vol. 3: Elsevier, 1999.
- [264] R. Aikin, "The mechanical properties of in-situ composites," *JOM*, vol. 49, p. 35, 1997.
- [265] Y.-T. Zhao, S.-L. Zhang, G. Chen, X.-N. Cheng, and C.-Q. Wang, "In situ (Al<sub>2</sub>O<sub>3</sub>+ Al<sub>3</sub>Zr) np/Al nanocomposites synthesized by magneto-chemical melt reaction," *Composites Science and Technology*, vol. 68, pp. 1463-1470, 2008.
- [266] D. Stinton, T. Besmann, and R. Lowden, "Advanced ceramics by chemical vapor deposition techniques," *American ceramic society bulletin*, vol. 67, pp. 350-355, 1988.
- [267] S. Tjong and H. Chen, "Nanocrystalline materials and coatings," *Materials Science and Engineering: R: Reports*, vol. 45, pp. 1-88, 2004.
- [268] R. Alexandrescu, E. Borsella, S. Botti, M. Cesile, S. Martelli, R. Giorgi, *et al.*, "Synthesis of TiC and SiC/TiC nanocrystalline powders by gas-phase laser-induced reaction," *Journal of materials science*, vol. 32, pp. 5629-5635, 1997.
- [269] D. K. Koli, G. Agnihotri, and R. Purohit, "Properties and characterization of Al-Al<sub>2</sub>O<sub>3</sub> composites processed by casting and powder metallurgy routes," *International Journal of Latest Trends in Engineering and Technology (IJLTET)*, vol. 2, pp. 486-496, 2013.

## References

- [270] S. A. Sajjadi and S. M. Zebarjad, "Synthesis of Al-Al<sub>2</sub>O<sub>3</sub> nano-composite by mechanical alloying and evaluation of the effect of ball milling time on the microstructure and mechanical properties," in *ICMN08*, 2008.
- [271] X. Zeng, W. Liu, B. Xu, G. Shu, and Q. Li, "Microstructure and mechanical properties of Al-SiC nanocomposites synthesized by surface-modified aluminium powder," *Metals*, vol. 8, p. 253, 2018.
- [272] Y.-C. Kang and S. L.-I. Chan, "Tensile properties of nanometric Al<sub>2</sub>O<sub>3</sub> particulate-reinforced aluminum matrix composites," *Materials chemistry and physics*, vol. 85, pp. 438-443, 2004.
- [273] F. Tang, M. Hagiwara, and J. M. Schoenung, "Microstructure and tensile properties of bulk nanostructured Al-5083/SiCp composites prepared by cryomilling," *Materials Science and Engineering: A*, vol. 407, pp. 306-314, 2005.
- [274] C. Hsu, C. Chang, P. Kao, N. Ho, and C. Chang, "Al-Al<sub>3</sub>Ti nanocomposites produced in situ by friction stir processing," *Acta Materialia*, vol. 54, pp. 5241-5249, 2006.
- [275] R. Rai, S. Saha, G. Datta, and M. Chakraborty, "Studies on synthesis of in-situ Al-TiC metal matrix composites," in *IOP Conference Series: Materials Science and Engineering*, 2016, p. 012042.
- [276] G. Cao, J. Kobliska, H. Konishi, and X. Li, "Tensile properties and microstructure of SiC nanoparticle-reinforced Mg-4Zn alloy fabricated by ultrasonic cavitation-based solidification processing," *Metallurgical and Materials Transactions A*, vol. 39, pp. 880-886, 2008.
- [277] L. Poovazhagan, K. Kalaichelvan, and A. Rajadurai, "Preparation of SiC nano-particulates reinforced aluminum matrix nanocomposites by high intensity ultrasonic cavitation process," *Transactions of the Indian Institute of Metals*, vol. 67, pp. 229-237, 2014.
- [278] Y. Yang, J. Lan, and X. Li, "Study on bulk aluminum matrix nano-composite fabricated by ultrasonic dispersion of nano-sized SiC particles in molten aluminum alloy," *Materials Science and Engineering: A*, vol. 380, pp. 378-383, 2004.
- [279] M. M. Boopathi, K. Arulshri, and N. Iyandurai, "Evaluation of mechanical properties of aluminium alloy 2024 reinforced with silicon carbide and fly ash hybrid metal matrix composites," *American journal of applied sciences*, vol. 10, p. 219, 2013.
- [280] M. Vanarotti, S. Kori, B. Sridhar, and S. B. Padasalgi, "Synthesis and characterization of aluminium alloy A356 and silicon carbide metal matrix composite," in *International Conference on Industrial Technology and Management*, 2012, pp. 11-15.
- [281] N. R. Kumar and E. Dwarakadasa, "Effect of matrix strength on the mechanical properties of Al-Zn-Mg/SiCP composites," *Composites Part A: Applied Science and Manufacturing*, vol. 31, pp. 1139-1145, 2000.
- [282] H. Ferkel and B. Mordike, "Magnesium strengthened by SiC nanoparticles," *Materials Science and Engineering: A*, vol. 298, pp. 193-199, 2001.
- [283] W. E Wong and M. Gupta, "Simultaneously improving strength and ductility of magnesium using nano-size SiC particulates and microwaves," *Advanced Engineering Materials*, vol. 8, pp. 735-740, 2006.
- [284] C. Lee, J. Huang, and P. Hsieh, "Mg based nano-composites fabricated by friction stir processing," *Scripta Materialia*, vol. 54, pp. 1415-1420, 2006.



## References

- [285] G. Byrne, D. Dornfeld, and B. Denkena, "Advancing cutting technology," *CIRP Annals*, vol. 52, pp. 483-507, 2003.
- [286] N. Taniguchi, "Current status in, and future trends of, ultraprecision machining and ultrafine materials processing," *CIRP Annals-Manufacturing Technology*, vol. 32, pp. 573-582, 1983.
- [287] G. Byrne, D. Dornfeld, and B. Denkena, "Advancing cutting technology," *CIRP Annals-Manufacturing Technology*, vol. 52, pp. 483-507, 2003.
- [288] M. P. Groover, D. Belson, A. Kusiak, J. M. Sánchez, J. W. Priest, L. J. Burnell, *et al.*, "Handbook of design, manufacturing and automation," 1994.
- [289] A. Simoneau, E. Ng, and M. Elbestawi, "Chip formation during microscale cutting of a medium carbon steel," *International Journal of Machine Tools and Manufacture*, vol. 46, pp. 467-481, 2006.
- [290] T. Masuzawa and H. Tönshoff, "Three-dimensional micromachining by machine tools," *CIRP Annals-Manufacturing Technology*, vol. 46, pp. 621-628, 1997.
- [291] D. Huo, *Micro-cutting: fundamentals and applications*: John Wiley & Sons, 2013.
- [292] M. Camara, J. C. Rubio, A. Abrão, and J. Davim, "State of the art on micromilling of materials, a review," *Journal of Materials Science & Technology*, vol. 28, pp. 673-685, 2012.
- [293] F. Vollertsen, "Categories of size effects," *Production Engineering*, vol. 2, p. 377, 2008.
- [294] F. B. De Oliveira, A. R. Rodrigues, R. T. Coelho, and A. F. De Souza, "Size effect and minimum chip thickness in micromilling," *International Journal of Machine Tools and Manufacture*, vol. 89, pp. 39-54, 2015.
- [295] I. Kang, J. Kim, and Y. Seo, "Investigation of cutting force behaviour considering the effect of cutting edge radius in the micro-scale milling of AISI 1045 steel," *Proceedings of the Institution of Mechanical Engineers, Part B: Journal of Engineering Manufacture*, vol. 225, pp. 163-171, 2011.
- [296] A. Aramcharoen and P. Mativenga, "Size effect and tool geometry in micromilling of tool steel," *Precision Engineering*, vol. 33, pp. 402-407, 2009.
- [297] X. Lu, Z. Jia, S. Liu, K. Yang, Y. Feng, and S. Y. Liang, "Chatter Stability of Micro-Milling by Considering the Centrifugal Force and Gyroscopic Effect of the Spindle," *Journal of Manufacturing Science and Engineering*, vol. 141, 2019.
- [298] A. Mian, N. Driver, and P. Mativenga, "Identification of factors that dominate size effect in micro-machining," *International Journal of Machine Tools and Manufacture*, vol. 51, pp. 383-394, 2011.
- [299] X. Sun and K. Cheng, "Micro-/Nano-Machining through Mechanical Cutting," *Micromanufacturing Engineering and Technology*, pp. 24-38, 2010.
- [300] Z. Yuan, W. Lee, Y. Yao, and M. Zhou, "Effect of crystallographic orientation on cutting forces and surface quality in diamond cutting of single crystal," *CIRP Annals-Manufacturing Technology*, vol. 43, pp. 39-42, 1994.
- [301] M. P. Vogler, R. E. DeVor, and S. G. Kapoor, "Microstructure-level force prediction model for micro-milling of multi-phase materials," *Journal of Manufacturing Science and Engineering*, vol. 125, pp. 202-209, 2003.

## References

- [302] S. Venkatachalam, O. Fergani, X. Li, J. G. Yang, K.-N. Chiang, and S. Y. Liang, "Microstructure effects on cutting forces and flow stress in ultra-precision machining of polycrystalline brittle materials," *Journal of Manufacturing Science and Engineering*, vol. 137, p. 021020, 2015.
- [303] S. Shimada, N. Ikawa, H. Tanaka, and J. Uchikoshi, "Structure of micromachined surface simulated by molecular dynamics analysis," *CIRP Annals-Manufacturing Technology*, vol. 43, pp. 51-54, 1994.
- [304] H. Weule, V. Hüntrup, and H. Tritschler, "Micro-cutting of steel to meet new requirements in miniaturization," *CIRP Annals-Manufacturing Technology*, vol. 50, pp. 61-64, 2001.
- [305] Y. Furukawa and N. Moronuki, "Effect of material properties on ultra precise cutting processes," *CIRP Annals-Manufacturing Technology*, vol. 37, pp. 113-116, 1988.
- [306] A. J. Mian, N. Driver, and P. T. Mativenga, "A comparative study of material phase effects on micro-machinability of multiphase materials," *The International Journal of Advanced Manufacturing Technology*, vol. 50, pp. 163-174, 2010.
- [307] A. Simoneau, E. Ng, and M. Elbestawi, "Surface defects during microcutting," *International Journal of Machine Tools and Manufacture*, vol. 46, pp. 1378-1387, 2006.
- [308] M. P. Vogler, "On the Modeling and Analysis of Machining Performance in Microendmilling," University of Illinois at Urbana-Champaign, 2003.
- [309] E. Uhlmann, S. Piltz, and K. Schauer, "Micro milling of sintered tungsten–copper composite materials," *Journal of Materials Processing Technology*, vol. 167, pp. 402-407, 2005.
- [310] K. B. Popov, S. S. Dimov, D. T. Pham, R. Minev, A. Rosochowski, and L. Olejnik, "Micromilling: material microstructure effects," *Proceedings of the Institution of Mechanical Engineers, Part B: Journal of Engineering Manufacture*, vol. 220, pp. 1807-1813, 2006.
- [311] C. H. Lauro, S. L. M. Ribeiro Filho, A. L. Christoforo, and L. C. Brandão, "Influence of the austenite grain size variation on the surface finishing in the micromilling process of the hardened AISI H13steel," *Matéria (Rio de Janeiro)*, vol. 19, pp. 235-246, 2014.
- [312] R. Komanduri, N. Chandrasekaran, and L. Raff, "MD Simulation of nanometric cutting of single crystal aluminum–effect of crystal orientation and direction of cutting," *Wear*, vol. 242, pp. 60-88, 2000.
- [313] S. To, W. Lee, and C. Chan, "Ultraprecision diamond turning of aluminium single crystals," *Journal of materials processing technology*, vol. 63, pp. 157-162, 1997.
- [314] M. Zhou and B. Ngoi, "Effect of tool and workpiece anisotropy on microcutting processes," *Proceedings of the Institution of Mechanical Engineers, Part B: Journal of Engineering Manufacture*, vol. 215, pp. 13-19, 2001.
- [315] T. Moriwaki, "Machinability of copper in ultra-precision micro diamond cutting," *CIRP Annals-Manufacturing Technology*, vol. 38, pp. 115-118, 1989.
- [316] X. Liu, R. E. DeVor, S. Kapoor, and K. Ehmann, "The mechanics of machining at the microscale: assessment of the current state of the science," *Journal of manufacturing science and engineering*, vol. 126, pp. 666-678, 2004.

## References

- [317] C. K. Ng, S. N. Melkote, M. Rahman, and A. S. Kumar, "Experimental study of micro-and nano-scale cutting of aluminum 7075-T6," *International Journal of Machine Tools and Manufacture*, vol. 46, pp. 929-936, 2006.
- [318] F. Ducobu, E. Rivière-Lorphèvre, and E. Filippi, "Chip formation in Micro-cutting," *J Mech Eng Autom*, vol. 3, pp. 441-448, 2013.
- [319] N. Ikawa, S. Shimada, and H. Tanaka, "Minimum thickness of cut in micromachining," *Nanotechnology*, vol. 3, p. 6, 1992.
- [320] N. L'vov, "Determining the minimum possible chip thickness," *Machines & Tooling*, vol. 4, p. 45, 1969.
- [321] K. Liu and S. N. Melkote, "Finite element analysis of the influence of tool edge radius on size effect in orthogonal micro-cutting process," *International Journal of Mechanical Sciences*, vol. 49, pp. 650-660, 2007.
- [322] G. Bissacco, H. N. Hansen, and L. De Chiffre, "Size effects on surface generation in micro milling of hardened tool steel," *CIRP Annals-Manufacturing Technology*, vol. 55, pp. 593-596, 2006.
- [323] D. Lucca, R. Rhorer, and R. Komanduri, "Energy dissipation in the ultraprecision machining of copper," *CIRP Annals-Manufacturing Technology*, vol. 40, pp. 69-72, 1991.
- [324] C.-J. Kim, J. R. Mayor, and J. Ni, "A static model of chip formation in microscale milling," *Transactions of the ASME-B-Journal of Manufacturing Science and Engineering*, vol. 126, pp. 710-718, 2004.
- [325] X. Liu, R. DeVor, and S. Kapoor, "An analytical model for the prediction of minimum chip thickness in micromachining," *Journal of manufacturing science and engineering*, vol. 128, pp. 474-481, 2006.
- [326] P. Basuray, B. Misra, and G. Lal, "Transition from ploughing to cutting during machining with blunt tools," *Wear*, vol. 43, pp. 341-349, 1977.
- [327] Z. Yuan, M. Zhou, and S. Dong, "Effect of diamond tool sharpness on minimum cutting thickness and cutting surface integrity in ultraprecision machining," *Journal of Materials Processing Technology*, vol. 62, pp. 327-330, 1996.
- [328] S. Filiz, C. M. Conley, M. B. Wasserman, and O. B. Ozdoganlar, "An experimental investigation of micro-machinability of copper 101 using tungsten carbide micro-endmills," *International Journal of Machine Tools and Manufacture*, vol. 47, pp. 1088-1100, 2007.
- [329] B. Deng, L. Zhou, F. Peng, R. Yan, M. Yang, and M. Liu, "Analytical model of cutting force in micromilling of particle-reinforced metal matrix composites considering interface failure," *Journal of Manufacturing Science and Engineering*, vol. 140, 2018.
- [330] J. Samuel, A. Dikshit, R. E. DeVor, S. G. Kapoor, and K. J. Hsia, "Effect of carbon nanotube (CNT) loading on the thermomechanical properties and the machinability of CNT-reinforced polymer composites," *Journal of Manufacturing Science and Engineering*, vol. 131, p. 031008, 2009.
- [331] M. N. Kumar, M. Mahmoodi, M. TabkhPaz, S. Park, and X. Jin, "Characterization and micro end milling of graphene nano platelet and carbon nanotube filled nanocomposites," *Journal of Materials Processing Technology*, vol. 249, pp. 96-107, 2017.
- [332] J. Horne, "A new model for initial chip curl in continuous cutting," *International Journal of Mechanical Sciences*, vol. 20, pp. 739-745, 1978.

## References

- [333] K. Enomoto, T. Yasuhara, S. Kitakata, H. Murakami, and N. Ohtake, "Frictional Properties of Carbon Nanofiber Reinforced Polymer Matrix Composites," *New Diamond and Frontier Carbon Technology*, vol. 14, pp. 11-20, 2004.
- [334] B. Chu, J. Samuel, and N. Koratkar, "Micromilling responses of hierarchical graphene composites," *Journal of Manufacturing Science and Engineering*, vol. 137, p. 011002, 2015.
- [335] M. Mahmoudi, M. Malekian, J. Mueller, M. Jun, and S. Park, "Machinability of aligned CNT nanocomposites," in *Proc. of the 6th Int. Conf. on MicroManufacturing*, 2011, pp. 391-398.
- [336] H. Gopalakrishna, J. S. Rao, S. N. Kumar, V. V. Shetty, and K. Rai, "Effect of Friction on the Cutting Forces in High Speed Orthogonal Turning of Al 6061-T6."
- [337] Y. Gong, Y.-J. Baik, C. P. Li, C. Byon, J. M. Park, and T. J. Ko, "Experimental and modeling investigation on machined surfaces of HDPE-MWCNT polymer nanocomposite," *The International Journal of Advanced Manufacturing Technology*, vol. 88, pp. 879-885, 2017.
- [338] R. F. Zinati and M. Razfar, "Experimental and modeling investigation of surface roughness in end-milling of polyamide 6/multi-walled carbon nano-tube composite," *The International Journal of Advanced Manufacturing Technology*, vol. 75, pp. 979-989, 2014.
- [339] M. Mahmoodi, M. Mostofa, M. Jun, and S. S. Park, "Characterization and micromilling of flow induced aligned carbon nanotube nanocomposites," *Journal of Micro and Nano-Manufacturing*, vol. 1, p. 011009, 2013.
- [340] A. Marcon, S. Melkote, K. Kalaitzidou, and D. DeBra, "An experimental evaluation of graphite nanoplatelet based lubricant in micro-milling," *CIRP annals*, vol. 59, pp. 141-144, 2010.
- [341] I. Shyha, G. Y. Fu, D. H. Huo, B. Le, F. Inam, M. S. Saharudin, *et al.*, "Micro-machining of nano-polymer composites reinforced with graphene and nano-clay fillers," *Key Engineering Materials*, vol. 786, pp. 197-205, 2018.
- [342] I. Shyha, G. Y. Fu, D. H. Huo, B. Le, F. Inam, M. S. Saharudin, *et al.*, "Micro-machining of nano-polymer composites reinforced with graphene and nano-clay fillers," in *Key Engineering Materials*, 2018, pp. 197-205.
- [343] C. Gao and J. Jia, "Factor analysis of key parameters on cutting force in micromachining of graphene-reinforced magnesium matrix nanocomposites based on FE simulation," *The International Journal of Advanced Manufacturing Technology*, vol. 92, pp. 3123-3136, 2017.
- [344] J. Liu, J. Li, Y. Ji, and C. Xu, "Investigation on the effect of SiC nanoparticles on cutting forces for micro-milling magnesium matrix composites," in *ASME 2011 International Manufacturing Science and Engineering Conference*, 2011, pp. 525-536.
- [345] X. Teng, D. Huo, E. Wong, G. Meenashisundaram, and M. Gupta, "Micro-machinability of nanoparticle-reinforced Mg-based MMCs: an experimental investigation," *The International Journal of Advanced Manufacturing Technology*, vol. 87, pp. 2165-2178, 2016.
- [346] F. Zeller, C. Müller, P. Miranzo, and M. Belmonte, "Exceptional micromachining performance of silicon carbide ceramics by adding graphene nanoplatelets," *Journal of the European Ceramic Society*, vol. 37, pp. 3813-3821, 2017.

## References

- [347] Y. Xiong, W. Wang, R. Jiang, and K. Lin, "A study on cutting force of machining in situ TiB<sub>2</sub> particle-reinforced 7050Al alloy matrix composites," *Metals*, vol. 7, p. 197, 2017.
- [348] A. Pramanik, A. Basak, Y. Dong, S. Shankar, and G. Littlefair, "Milling of nanoparticles reinforced Al-based metal matrix composites," *Journal of Composites Science*, vol. 2, p. 13, 2018.
- [349] E. Lee and B. Shaffer, "The theory of plasticity applied to a problem of machining," 1951.
- [350] X. Teng, D. Huo, W. Chen, E. Wong, L. Zheng, and I. Shyha, "Finite element modelling on cutting mechanism of nano Mg/SiC metal matrix composites considering cutting edge radius," *Journal of Manufacturing Processes*, vol. 32, pp. 116-126, 2018.
- [351] Z. Huang, Z. Guo, X. Chen, T. M. Yue, S. To, and W. B. Lee, "Molecular dynamics simulation for ultrafine machining," *Materials and Manufacturing Processes*, vol. 21, pp. 393-397, 2006.
- [352] M. Field and M. Merchant, "Mechanics of formation of the discontinuous chip in metal cutting," *Trans. ASME*, vol. 71, p. 421, 1949.
- [353] H.-J. Fu, R. DeVor, and S. G. Kapoor, "A mechanistic model for the prediction of the force system in face milling operations," 1984.
- [354] Z.-C. Lin and J.-C. Huang, "A nano-orthogonal cutting model based on a modified molecular dynamics technique," *Nanotechnology*, vol. 15, p. 510, 2004.
- [355] M. M. Shokrieh and R. Rafiee, "On the tensile behavior of an embedded carbon nanotube in polymer matrix with non-bonded interphase region," *Composite Structures*, vol. 92, pp. 647-652, 2010.
- [356] S. Park, S. G. Kapoor, and R. E. DeVor, "Microstructure-level model for the prediction of tool failure in WC-Co cutting tool materials," *J. Manuf. Sci. Eng.*, vol. 128, 2006.
- [357] R. DeVor and S. Kapoor, "Microstructure-Level Machining Simulation of Carbon Nanotube Reinforced Polymer Composites—Part I: Model Development and Validation," *Urbana*, vol. 51, p. 61801, 2008.
- [358] A. Dikshit, J. Samuel, R. DeVor, and S. G. Kapoor, "Microstructure-level machining simulation of carbon nanotube reinforced polymer composites—Part II: Model interpretation and application," *J. Manuf. Sci. Eng.*, vol. 130, 2008.
- [359] R. P. Nimmer and J. T. Woods, "An investigation of brittle failure in ductile, notch-sensitive thermoplastics," *Polymer Engineering & Science*, vol. 32, pp. 1126-1137, 1992.
- [360] L. Jiang, "Development of an enhanced microstructure-level machining model for carbon nanotube reinforced polymer composites using cohesive zone interface," M.S., Mechanical Sci & Engineering, University of Illinois at Urbana-Champaign, 2013.
- [361] F. Müller and J. Monaghan, "Non-conventional machining of particle reinforced metal matrix composite," *International Journal of Machine Tools and Manufacture*, vol. 40, pp. 1351-1366, 2000.
- [362] D. C. Kyritsis, S. Roychoudhury, C. S. McEnally, L. D. Pfefferle, and A. Gomez, "Mesoscale combustion: a first step towards liquid fueled batteries," *Experimental Thermal and Fluid Science*, vol. 28, pp. 763-770, 2004.
- [363] A. Dikshit, J. Samuel, R. DeVor, and S. G. Kapoor, "Microstructure-level machining simulation of carbon nanotube reinforced polymer composites—Part I: Model development and validation," *Journal of manufacturing science and engineering*, vol. 130, 2008.

## References

- [364] G. R. Johnson, "A constitutive model and data for metals subjected to large strains, high strain rates and high temperatures," in *Proceedings of the 7th International Symposium on Ballistics, The Hague, Netherlands, 1983*, 1983.
- [365] A. Dikshit, J. Samuel, R. DeVor, and S. Kapoor, "Microstructure-level machining simulation of carbon nanotube reinforced polymer composites—Part II: Model interpretation and application," *Journal of manufacturing science and engineering*, vol. 130, p. 031115, 2008.
- [366] R. DeVor and W. Kline, "A mechanistic model for the force system in end milling with application to machining airframe structures," in *Manufacturing Engineering Transactions and North American Manufacturing Research Conference, 8th*, 1980, pp. 297-303.
- [367] A. Dwivedi, J. Bradley, and D. Casem, "Mechanical response of polycarbonate with strength model fits," DYNAMIC SCIENCE INC ABERDEEN MD2012.
- [368] J. A. King, D. R. Klimek, I. Miskioglu, and G. M. Odegard, "Mechanical properties of graphene nanoplatelet/epoxy composites," *Journal of Applied Polymer Science*, vol. 128, pp. 4217-4223, 2013.
- [369] W. Tiejun, K. Kishimoto, and M. Notomi, "Effect of triaxial stress constraint on the deformation and fracture of polymers," *Acta Mechanica Sinica*, vol. 18, p. 480, 2002.
- [370] X. Teng, W. Chen, D. Huo, I. Shyha, and C. Lin, "Comparison of cutting mechanism when machining micro and nano-particles reinforced SiC/Al metal matrix composites," *Composite Structures*, vol. 203, pp. 636-647, 2018.
- [371] P. Theilmann, D.-J. Yun, P. Asbeck, and S.-H. Park, "Superior electromagnetic interference shielding and dielectric properties of carbon nanotube composites through the use of high aspect ratio CNTs and three-roll milling," *Organic Electronics*, vol. 14, pp. 1531-1537, 2013.
- [372] I. D. Rosca and S. V. Hoa, "Highly conductive multiwall carbon nanotube and epoxy composites produced by three-roll milling," *Carbon*, vol. 47, pp. 1958-1968, 2009.
- [373] M. Kim, K. Rhee, J. Lee, D. Hui, and A. K. Lau, "Property enhancement of a carbon fiber/epoxy composite by using carbon nanotubes," *Composites Part B: Engineering*, vol. 42, pp. 1257-1261, 2011.
- [374] G. Gkikas, N.-M. Barkoula, and A. Paipetis, "Effect of dispersion conditions on the thermo-mechanical and toughness properties of multi walled carbon nanotubes-reinforced epoxy," *Composites Part B: Engineering*, vol. 43, pp. 2697-2705, 2012.
- [375] J. Wei, R. Atif, T. Vo, and F. Inam, "Graphene nanoplatelets in epoxy system: dispersion, reaggregation, and mechanical properties of nanocomposites," *Journal of Nanomaterials*, vol. 2015, 2015.
- [376] E. T. Thostenson and T.-W. Chou, "Processing-structure-multi-functional property relationship in carbon nanotube/epoxy composites," *Carbon*, vol. 44, pp. 3022-3029, 2006.
- [377] A. Kernin, K. Wan, Y. Liu, X. Shi, J. Kong, E. Bilotti, *et al.*, "The effect of graphene network formation on the electrical, mechanical, and multifunctional properties of graphene/epoxy nanocomposites," *Composites Science and Technology*, vol. 169, pp. 224-231, 2019.
- [378] S. Ganguli, A. K. Roy, and D. P. Anderson, "Improved thermal conductivity for chemically functionalized exfoliated graphite/epoxy composites," *Carbon*, vol. 46, pp. 806-817, 2008.

## References

- [379] "Tool Life Testing in Milling - Part 2: End Milling," *International Standards Organisation*, vol. ISO 8688-2, 1989.
- [380] B. Le, J. Khaliq, D. Huo, X. Teng, and I. Shyha, "A Review on Nanocomposites. Part 2: Micromachining," *Journal of Manufacturing Science and Engineering*, vol. 142, 2020.
- [381] S. Wojciechowski, M. Matuszak, B. Powalka, M. Madajewski, R. Maruda, and G. Królczyk, "Prediction of cutting forces during micro end milling considering chip thickness accumulation," *International Journal of Machine Tools and Manufacture*, vol. 147, p. 103466, 2019.
- [382] F. Wang, L. T. Drzal, Y. Qin, and Z. Huang, "Mechanical properties and thermal conductivity of graphene nanoplatelet/epoxy composites," *Journal of materials science*, vol. 50, pp. 1082-1093, 2015.
- [383] M. E. Support. (2021). *Methods and formulas for Two-way ANOVA*. Available: <https://support.minitab.com/en-us/minitab-express/1/help-and-how-to/modeling-statistics/anova/how-to/two-way-anova/methods-and-formulas/methods-and-formulas/>
- [384] G. Fu, D. Huo, I. Shyha, K. Pancholi, and B. Alzahrani, "Experimental investigation on micromachining of epoxy/graphene nano platelet nanocomposites," *The International Journal of Advanced Manufacturing Technology*, vol. 107, pp. 3169-3183, 2020.
- [385] J. Wei, "Graphene in epoxy system: dispersion, preparation and reinforcement effect," Northumbria University, 2017.
- [386] E. Kontou, "Viscoplastic deformation of an epoxy resin at elevated temperatures," *Journal of applied polymer science*, vol. 101, pp. 2027-2033, 2006.
- [387] B. Yazdani, F. Xu, I. Ahmad, X. Hou, Y. Xia, and Y. Zhu, "Tribological performance of Graphene/Carbon nanotube hybrid reinforced Al 2 O 3 composites," *Scientific reports*, vol. 5, pp. 1-11, 2015.
- [388] J. Wei, "Graphene in epoxy system: dispersion, preparation and reinforcement effect," PhD, Mechanical & Construction Engineering, University of Northumbria at Newcastle (United Kingdom), 2017.
- [389] H. K. Neto, A. E. Diniz, and R. Pederiva, "The influence of cutting forces on surface roughness in the milling of curved hardened steel surfaces," *The International Journal of Advanced Manufacturing Technology*, vol. 84, pp. 1209-1218, 2016.
- [390] E. Kuram, "Micro-machinability of injection molded polyamide 6 polymer and glass-fiber reinforced polyamide 6 composite," *Composites Part B: Engineering*, vol. 88, pp. 85-100, 2016.
- [391] G. F. Gao, Z. X. Fu, J. Z. Zhao, and Y. Wang, "Study on Surface Roughness of Milling Based on the Elastic-Plastic Deformation," *Applied Mechanics and Materials*, vol. 551, pp. 55-60, 2014.
- [392] B. Chu, J. Samuel, and N. Koratkar, "Micromilling responses of hierarchical graphene composites," *Journal of Manufacturing Science and Engineering*, vol. 137, 2015.
- [393] M. Rafiee, J. Rafiee, Z.-Z. Yu, and N. Koratkar, "Buckling resistant graphene nanocomposites," *Applied Physics Letters*, vol. 95, p. 223103, 2009.
- [394] T. Wu, K. Cheng, and R. Rakowski, "Investigation on tooling geometrical effects of micro tools and the associated micro milling performance," *Proceedings of the Institution of*

## References

- Mechanical Engineers, Part B: Journal of Engineering Manufacture*, vol. 226, pp. 1442-1453, 2012.
- [395] M. Folea, A. Roman, and N.-B. Lupulescu, "An overview of DLC coatings on cutting tools performance," *Academic journal of manufacturing engineering*, vol. 8, 2010.
- [396] T. Wu and K. Cheng, "Micro milling performance assessment of diamond-like carbon coatings on a micro-end mill," *Proceedings of the Institution of Mechanical Engineers, Part J: Journal of Engineering Tribology*, vol. 227, pp. 1038-1046, 2013.
- [397] X. Teng, D. Huo, I. Shyha, W. Chen, and E. Wong, "An experimental study on tool wear behaviour in micro milling of nano Mg/Ti metal matrix composites," *The International Journal of Advanced Manufacturing Technology*, vol. 96, pp. 2127-2140, 2018.
- [398] J. Samuel, A. Dikshit, R. E. DeVor, S. G. Kapoor, and K. J. Hsia, "Effect of carbon nanotube (CNT) loading on the thermomechanical properties and the machinability of CNT-reinforced polymer composites," *Journal of Manufacturing Science and Engineering*, vol. 131, 2009.
- [399] I. Arora, J. Samuel, and N. Koratkar, "Experimental investigation of the machinability of epoxy reinforced with graphene platelets," *Journal of Manufacturing Science and Engineering*, vol. 135, 2013.
- [400] Z. Niu, F. Jiao, and K. Cheng, "An innovative investigation on chip formation mechanisms in micro-milling using natural diamond and tungsten carbide tools," *Journal of Manufacturing Processes*, vol. 31, pp. 382-394, 2018.
- [401] A. Aramcharoen, P. Mativenga, S. Yang, K. Cooke, and D. Teer, "Evaluation and selection of hard coatings for micro milling of hardened tool steel," *International Journal of Machine Tools and Manufacture*, vol. 48, pp. 1578-1584, 2008.
- [402] M. Dai, K. Zhou, Z. Yuan, Q. Ding, and Z. Fu, "The cutting performance of diamond and DLC-coated cutting tools," *Diamond and Related Materials*, vol. 9, pp. 1753-1757, 2000.
- [403] V. F. Sousa and F. J. Silva, "Recent Advances on Coated Milling Tool Technology—A Comprehensive Review," *Coatings*, vol. 10, p. 235, 2020.
- [404] A. Dudarev, K. Volegov, and G. Kurzanov, "Rheonomic phenomenon shrinkage of holes drilled in fibreglass and carbon fibre-reinforced polymer composites," *Mechanics of Advanced Materials and Modern Processes*, vol. 3, pp. 1-9, 2017.
- [405] B. K. Satapathy, R. Weidisch, P. Pötschke, and A. Janke, "Tough-to-brittle transition in multiwalled carbon nanotube (MWNT)/polycarbonate nanocomposites," *Composites science and technology*, vol. 67, pp. 867-879, 2007.
- [406] A. T. Seyhan, M. Tanoğlu, and K. Schulte, "Tensile mechanical behavior and fracture toughness of MWCNT and DWCNT modified vinyl-ester/polyester hybrid nanocomposites produced by 3-roll milling," *Materials Science and Engineering: A*, vol. 523, pp. 85-92, 2009.
- [407] B. Le, J. Khaliq, D. Huo, X. Teng, and I. Shyha, "A Review on Nanocomposites. Part 1: Mechanical Properties," *Journal of Manufacturing Science and Engineering*, vol. 142, 2020.
- [408] V. Romano, C. Naddeo, L. Guadagno, and L. Vertuccio, "Thermal conductivity of epoxy resins filled with MWCNT and hydrotalcite clay: Experimental data and theoretical predictive modeling," *Polymer Composites*, vol. 36, pp. 1118-1123, 2015.



## References

- [409] S.-Y. Yang, C.-C. M. Ma, C.-C. Teng, Y.-W. Huang, S.-H. Liao, Y.-L. Huang, *et al.*, "Effect of functionalized carbon nanotubes on the thermal conductivity of epoxy composites," *Carbon*, vol. 48, pp. 592-603, 2010.
- [410] D. R. Bortz, C. Merino, and I. Martin-Gullon, "Carbon nanofibers enhance the fracture toughness and fatigue performance of a structural epoxy system," *Composites Science and Technology*, vol. 71, pp. 31-38, 2011.
- [411] M. Quaresimin, K. Schulte, M. Zappalorto, and S. Chandrasekaran, "Toughening mechanisms in polymer nanocomposites: From experiments to modelling," *Composites Science and Technology*, vol. 123, pp. 187-204, 2016.
- [412] O. A. Serenko, V. I. Roldughin, A. A. Askadskii, E. S. Serkova, P. V. Strashnov, and Z. B. Shifrina, "The effect of size and concentration of nanoparticles on the glass transition temperature of polymer nanocomposites," *RSC advances*, vol. 7, pp. 50113-50120, 2017.
- [413] B. Qi, S. Lu, X. Xiao, L. Pan, F. Tan, and J. Yu, "Enhanced thermal and mechanical properties of epoxy composites by mixing thermotropic liquid crystalline epoxy grafted graphene oxide," *Express Polymer Letters*, vol. 8, 2014.
- [414] H. J. Kim, J. Han, and Y. Son, "Effect of a Monomer Composition on the Mechanical Properties and Glass Transition Temperature of a Waterborne Polyurethane/Graphene Oxide and Waterborne Polyurethane/MWCNT Nanocomposite," *Polymers*, vol. 12, p. 2013, 2020.
- [415] M. Nasr, E. Ng, and M. Elbestawi, "Effects of workpiece thermal properties on machining-induced residual stresses-thermal softening and conductivity," *Proceedings of the Institution of mechanical engineers, Part B: journal of engineering manufacture*, vol. 221, pp. 1387-1400, 2007.
- [416] A. C. Ramos, H. Autenrieth, T. Strauß, M. Deuchert, J. Hoffmeister, and V. Schulze, "Characterization of the transition from ploughing to cutting in micro machining and evaluation of the minimum thickness of cut," *Journal of Materials Processing Technology*, vol. 212, pp. 594-600, 2012.

## **List of publications**

### **Journal papers:**

1. I. Shyha, G. Fu, D. Huo, B. Le, F. Inam, M. Saharudin, et al., "Micro-machining of nano-polymer composites reinforced with graphene and nano-clay fillers" *Key Engineering Materials*, 2018, pp. 197-205.
2. B. Le, J. Khaliq, D. Huo, X. Teng, and I. Shyha, "A Review on Nanocomposites. Part 1: Mechanical Properties," *Journal of Manufacturing Science and Engineering*, vol. 142, 2020.
3. B. Le, J. Khaliq, D. Huo, X. Teng, and I. Shyha, "A Review on Nanocomposites. Part 2: Micromachining," *Journal of Manufacturing Science and Engineering*, vol. 142, 2020.
4. N. Shakoory, G. Fu, B. Le, J. Khaliq, L. Jiang, D. Huo, et al., "An experimental investigation on tool wear behaviour of uncoated and coated micro-tools in micro-milling of graphene-reinforced polymer nanocomposites," *The International Journal of Advanced Manufacturing Technology*, vol. 113, pp. 2003-2015, 2021.
5. B. Le, A. Kernin, J. Khaliq, G. Fu, D. Huo, E. Bilotti, H. Zhang, and I. Shyha, "Micro-End-Milling of Carbon Nanotube Reinforced Epoxy Nanocomposites Manufactured using Three Roll Mill Technique", *Journal of Manufacturing Processes*, vol.70, 2021.

### **Conference papers:**

6. I. Shyha, D. Huo, B. Le, G. Fu, E. Soliman, and B. Alzahrani, "Investigation on Micro-Slotting of Polymer Nanocomposites: Cutting Forces" *Advances in Manufacturing Technology XXXII: Proceedings of the 16th International Conference on Manufacturing Research, incorporating the 33rd National Conference on Manufacturing Research*, September 11–13, 2018, University of Skövde, Sweden, 2018, p. 57.
7. I. Shyha, B. Le, H. Dehong, F. Guoyu, H. Arrowsmith, and A. Ahmed, "Analysis of Surface Quality when Micro-Milling Polymer Nanocomposites" *Advances in Manufacturing Technology XXXII: Proceedings of the 16th International Conference on Manufacturing Research, incorporating the 33rd National Conference on Manufacturing Research*, September 11–13, 2018, University of Skövde, Sweden, 2018, p. 51.

### **Book chapters:**

8. B. Le, I. Shyha, and D. Huo, "Machining of Nano-structured Polymer Composites", *Advances in Machining of Composite Materials – Conventional and Non-conventional processes*, I. Shyha, and D. Huo, Springer, 2021, ch. 14.